



**This electronic thesis or dissertation has been
downloaded from Explore Bristol Research,
<http://research-information.bristol.ac.uk>**

Author:
Gu, Yue

Title:
Diabetes mellitus causes adiposopathy in bone marrow
investigation of the underpinning cellular and molecular mechanisms

General rights

Access to the thesis is subject to the Creative Commons Attribution - NonCommercial-No Derivatives 4.0 International Public License. A copy of this may be found at <https://creativecommons.org/licenses/by-nc-nd/4.0/legalcode>. This license sets out your rights and the restrictions that apply to your access to the thesis so it is important you read this before proceeding.

Take down policy

Some pages of this thesis may have been removed for copyright restrictions prior to having it been deposited in Explore Bristol Research. However, if you have discovered material within the thesis that you consider to be unlawful e.g. breaches of copyright (either yours or that of a third party) or any other law, including but not limited to those relating to patent, trademark, confidentiality, data protection, obscenity, defamation, libel, then please contact collections-metadata@bristol.ac.uk and include the following information in your message:

- Your contact details
- Bibliographic details for the item, including a URL
- An outline nature of the complaint

Your claim will be investigated and, where appropriate, the item in question will be removed from public view as soon as possible.



**This electronic thesis or dissertation has been
downloaded from Explore Bristol Research,
<http://research-information.bristol.ac.uk>**

Author:
Gu, Yue

Title:
**Diabetes mellitus causes adiposopathy in bone marrow: investigation of the
underpinning cellular and molecular mechanisms**

General rights

Access to the thesis is subject to the Creative Commons Attribution - NonCommercial-No Derivatives 4.0 International Public License. A copy of this may be found at <https://creativecommons.org/licenses/by-nc-nd/4.0/legalcode> This license sets out your rights and the restrictions that apply to your access to the thesis so it is important you read this before proceeding.

Take down policy

Some pages of this thesis may have been removed for copyright restrictions prior to having it been deposited in Explore Bristol Research. However, if you have discovered material within the thesis that you consider to be unlawful e.g. breaches of copyright (either yours or that of a third party) or any other law, including but not limited to those relating to patent, trademark, confidentiality, data protection, obscenity, defamation, libel, then please contact collections-metadata@bristol.ac.uk and include the following information in your message:

- Your contact details
- Bibliographic details for the item, including a URL
- An outline nature of the complaint

Your claim will be investigated and, where appropriate, the item in question will be removed from public view as soon as possible.

Diabetes mellitus causes adiposopathy in bone marrow: investigation of the underpinning cellular and molecular mechanisms



YUE GU

A dissertation submitted to the University of Bristol in accordance with the
requirements for award of the degree of Philosophiae Doctor in the Faculty of Health

Sciences

School of Medical

Submitted in September 2023

54,693 words

ABSTRACT

Background: Lipotoxicity contributes to local and systemic damage. Senolytic drugs eliminate senescent preadipocytes. However, their effects on fat in heart and bone marrow (BM) remain unknown. Tyrosine kinase inhibitors (TKI) showed therapeutic potential for treating non-malignant disorders such as cardiac hypertrophy, atherosclerosis, and arthritis. Dasatinib is a second-generation TKI endowed with senolytic activity. It is unknown whether Dasatinib reduces adiposity in BM and the heart.

Hypothesis and Aims: Pericytes (PCs) are primary adipocyte sources among BM stromal cells. BM senescence causes the adipogenic commitment of PCs. Dasatinib reduces fat deposits in the BM and heart in a diabetic murine model, positively affecting organ function.

Methods and results: Human CD34^{neg} CD45^{neg} CD146^{pos} pericytes (hBM-PCs) were sorted from BM mesenchymal stromal cells (hBM-MSCs) by immunomagnetic beads. HBM-PCs showed a special propensity to differentiate into adipocytes. Dasatinib reduced hBM-PCs viability and adipocyte differentiation. In a randomised, operator-blinded study, Dasatinib (5 mg/kg) or vehicle (10% DMSO + 90% PEG300) was given by gavage to T2DM, obese 21-week-old male mice. Animals were sacrificed at 1 (Total administrations = 2) or 4 (Total administrations = 4) weeks thereafter. The short-term treatment reduced the fat content in heart and BM but did not improve heart anatomy and function. The long-term treatment reduced steatosis, fibrosis, and levels of senescence marker p16^{INK4a} in the heart. It also improved left ventricle diastolic indexes. Moreover, Dasatinib reduced BM adiposity but no other fat depots. *In vitro*, Dasatinib treatment of murine BM-MSCs reduced the expression of p21^{Waf1/Cip1}.

Conclusion: PCs are the primary source of adipocytes in human BM. Dasatinib reduces the PC adipogenesis commitment. Dasatinib prevented fat accumulation in the heart and BM and cell senescence in the heart of T2DM mice. Prolonged treatment reduced adiposity and improved cardiac function. These findings demonstrate that pulsed administration of Dasatinib benefits diabetic cardiomyopathy.

DEDICATION AND ACKNOWLEDGEMENTS

I sincerely want to thank my supervisors, Prof Paolo Madeddu and Prof Harry Mellor, for supporting me in completing this Ph.D. project. Thanks to Prof Paolo Madeddu for your passion, patience, and step-by-step supervision, which makes me grow quickly in all aspects. Even though the pandemic of COVID-19 severely influenced the progress of my study, your robust support and guidance inspired me to overcome all the difficulties. They made me feel confident about my Ph.D. project and personal future.

I would like to thank Elisa, Valeria, Anita, Sadie, and Michele for teaching me all the laboratory techniques and encouraging me to cover the stressful situation in both work and life. Your enthusiasm and support make me feel not lonely during this impressive Ph.D. journey!

Thanks to the core tech team, Jan, Hannah, Tom, and Simon, for the technical help with the multiplex assay, the processing of mouse histological samples, and support for other aspects.

Thanks to Gallia, Marianna, and Andrew for all the technical support on immunohistology, cell isolation, and flow cytometry.

Thank you to all my friends in Bristol for your accompany, especially in this tough time.

Finally, a huge thanks to my parents. We didn't meet in person for around four years, which is so long! Our remote video call is the power to inspire me during the whole Ph.D. study, and I can't wait to see you soon! Thank you!

AUTHOR'S DECLARATION

I declare that the work in this dissertation was carried out in accordance with the requirements of the University's Regulations and Code of Practice for Research Degree Programmes and that it has not been submitted for any other academic award. Except where indicated by specific references in the text, the work is the candidate's own work. Work done in collaboration with, or with the assistance of, others is indicated as such. Any views expressed in the dissertation are those of the author.

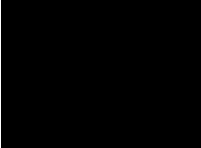
SIGNED:  DATE:.....26/09/2023.....

TABLE OF CONTENTS

Abstract	3
Dedication and Acknowledgements	5
Author's declaration	7
Table of contents	9
List of tables	14
List of figures	15
List of abbreviations	18
Publications arising from this work.....	25
Chapter 1. Introduction.....	27
1.1. Diabetes mellitus	27
1.1.1. Definition and classification of diabetes mellitus	27
1.1.2. Diagnosis of diabetes mellitus	28
1.1.3. Type 1 diabetes mellitus	28
1.1.4. Type 2 diabetes mellitus	28
1.1.5. Epidemiology of diabetes mellitus.....	29
1.1.6. Insulin resistance.....	30
1.1.7. Complications of type 2 diabetes mellitus.....	33
1.1.8. Therapy of type 2 diabetes mellitus	50
1.1.9. <i>In vitro</i> & <i>in vivo</i> models of type 2 diabetes mellitus.....	55
1.2. Bone marrow	59
1.2.1. Structure of bone marrow	59
1.2.2. Function of bone marrow	61
1.2.3. Bone marrow cells.....	63

1.3.	Senescence	69
1.3.1.	Characteristics and mechanisms of senescence	69
1.3.2.	Markers of senescence	71
1.3.3.	Senescence and type 2 diabetes mellitus	72
1.3.4.	Senescence and obesity	74
1.3.5.	Senescence and cardiovascular disease	74
1.4.	Senolytic agents.....	75
1.4.1.	Definition and classification	75
1.4.2.	Dasatinib	78
1.4.3.	Clinical trials of senolytic agents	80
1.5.	Hypothesis for this project	80
1.6.	Aims and objectives.....	81
Chapter 2. Cellular Source of adipocytes in human bone marrow.....		83
2.1.	Introduction.....	83
2.2.	Methods	84
2.2.1.	Ethics	84
2.2.2.	Human BM-MSCs isolation	84
2.2.3.	Human BM-PCs sorting	85
2.2.4.	Human BM-PCs culture conditions optimisation.....	87
2.2.5.	Induction of adipogenic differentiation on human BM-PCs & BM-SCs	87
2.2.6.	Immunocytochemistry	88
2.2.7.	Oil red O staining on cells	91
2.2.8.	Viability assay.....	91
2.2.9.	Proliferation assay.....	92
2.2.10.	Gene expression analysis	92
2.2.11.	Statistical analysis.....	94

2.3.	Results	94
2.3.1.	Sample collection and cell sorting	94
2.3.2.	Optimisation of human BM-PCs culture conditions	98
2.3.3.	Characterisation of human BM-PCs	100
2.3.4.	Phenotypic characteristics of human BM-SCs	102
2.3.5.	Propensity of human BM-PCs & BM-SCs differentiation into adipocytes 103	
2.4.	Conclusion	104
Chapter 3. Effects of senolytic agent Dasatinib on human BM-PCs & BM-SCs		107
3.1.	Introduction.....	107
3.2.	Methods	108
3.2.1.	Cell culture	108
3.2.2.	Dasatinib treatment on human BM-PCs	108
3.2.3.	Dasatinib treatment effects on human BM-PCs and BM-SCs adipose differentiation	108
3.2.4.	Immunocytochemistry	109
3.2.5.	Oil red O staining on cells.....	109
3.2.6.	Functional assays	109
3.2.7.	Gene expression analysis	110
3.2.8.	Western blot analysis.....	110
3.2.9.	ELISA assay	113
3.2.10.	Statistical analysis.....	113
3.3.	Results	113
3.3.1.	Effects of Dasatinib on human BM-PCs	113
3.3.2.	Dasatinib blunts the adipose differentiation of human BM-PCs and BM- SCs	115

3.4. Conclusion	119
Chapter 4. <i>In vivo</i> effects of Dasatinib treatment on T2DM obese mice	121
4.1. Introduction.....	121
4.2. Methods	122
4.2.1. Ethics	122
4.2.2. Experiment design	122
4.2.3. Echocardiography	125
4.2.4. Mouse BM cells isolation and expansion.....	128
4.2.5. Histology	128
4.2.6. Multiplex assay.....	132
4.2.7. <i>In vitro</i> Dasatinib treatment on mouse BM-SCs	133
4.2.8. Flow cytometry analyses on mouse BM cells	133
4.2.9. Statistical analysis	134
4.3. Results	135
4.3.1. <i>In vivo</i> effects of short-term Dasatinib treatment on T2DM obese mice 135	
4.3.2. <i>In vivo</i> effects of long-term Dasatinib treatment on T2DM obese mice	145
4.4. Conclusion	161
Chapter 5. Discussion.....	163
Chapter 6. Future perspectives.....	173
Chapter 7. Conclusion	177
Chapter 8. Appendix	181
8.1. Supplementary data	181
8.1.1. Positive control of cellular senescence.....	181
8.1.2. Optimisation of Dasatinib concentration for <i>in vitro</i> treatment of human BM-PCs	182

8.1.3. Optimisation of the Dasatinib concentration for <i>in vitro</i> induction of human BM-PC adipocyte differentiation	185
8.2. <i>In vitro</i> insulin resistance models	188
8.2.1. High glucose induced insulin resistance <i>in vitro</i>	188
8.2.2. High glucose and glucosamine induced insulin resistance <i>in vitro</i>	190
8.3. T2DM obese mice age selection	194
8.3.1. Experiment design	194
8.3.2. Results	194
Bibliography	196

LIST OF TABLES

Table 1-1 Pharmacotherapy of glycaemic control of T2DM.	53
Table 1-2 Positive and negative BM-MSCs' markers in different species.	66
Table 1-3 List of first and second generations senolytic therapies.	76
Table 2-1 Primary and secondary antibodies used in immuocytochemistry studies.	90
Table 2-2 TaqMan probes used in qPCR assays.	93
Table 2-3 Clinical characteristic of recruited patients and sample attribution to specific experiments.	97
Table 3-1 List of antibodies used for Western blot analyses.	112
Table 4-1 Representative views of PSLAX B-mode & M-mode; PSAX B-mode & M-mode; PW Doppler and tissue Doppler and the parameters acquired from the above views.	127
Table 4-2 Primary and secondary antibodies used in immunohistochemistry studies.	131
Table 4-3 List of antibodies used in mouse bone marrow cells flow cytometry analyses.	134
Table 7-1 Summary of the findings.	177

LIST OF FIGURES

Figure 1-1 Number of people with diabetes worldwide in 2021-2045 (20–79-year-olds).	30
Figure 1-2 The morphological difference between white, beige, and brown adipose tissue adipocytes.....	34
Figure 1-3 The anatomy distribution of epicardial and pericardial adipose tissue.	39
Figure 1-4 The mechanisms of adiposopathy induces T2DM.....	43
Figure 1-5 Progress of diabetes and hypertension induce cardiovascular disease.	45
Figure 1-6 Metabolic relationship between obesity, T2DM and CVD.	47
Figure 1-7 A potential mechanism linking aging, T2DM and CVD.	48
Figure 1-8 Scheme of bone marrow vascular system.....	60
Figure 1-9 Bone marrow architecture and cell types in niches.	61
Figure 1-10 Human bone marrow haematopoiesis cells and stromal cells.....	63
Figure 1-11 Markers of cellular senescence.	72
Figure 1-12 Potential mechanisms of cellular senescence and T2DM pathogenic positive feedback loops.....	73
Figure 1-13 Chemical structure of Dasatinib.	79
Figure 2-1 Scheme of human BM cell isolation and human BM-PCs & BM-SCs sorting.	86
Figure 2-2 Human BM-PCs and BM-SCs sorting flow chart and results.....	95
Figure 2-3 Morphology, phenotype, proliferation, and viability of human BM-PCs under different culture conditions.	99
Figure 2-4 Human BM-PCs phenotypes are assessed using immunocytochemistry....	100
Figure 2-5 Cellular senescence, proliferation ability and viability at different passages.	102
Figure 2-6 Phenotypic characteristics of the human BM-SCs populations (mixture of CD45 ^{neg} CD34 ^{pos} and CD45 ^{neg} CD34 ^{neg} CD146 ^{neg} cell populations) remaining after the human BM-PCs isolation.	103
Figure 2-7 Adipogenic potential of human BM-PCs and BM-SCs.	104
Figure 3-1 Effects of Dasatinib (1 μ M, 48 hours) or Vehicle (DMSO) treatment on human BM-PCs function and senescence.....	115

Figure 3-2 Effects of Dasatinib on the adipose differentiation of human BM-PCs and BM-SCs.	118
Figure 4-1 Scheme of short-term treatment of Dasatinib or Vehicle in T2DM obese mice.	124
Figure 4-2 Scheme of long-term treatment of Dasatinib or Vehicle on T2DM obese mice.	125
Figure 4-3 (A) Cartoon of short-term Dasatinib treatment on T2DM obese mice. (B) Table of glycosuria level in T2DM obese mice during the short-term Dasatinib treatment.	135
Figure 4-4 Cardiac function is evaluated by echocardiography in 21- and 22-week-old T2DM obese mice before and after the short-term Dasatinib treatment.	138
Figure 4-5 A short-term Dasatinib treatment does not alter the expression of plasma adipokines in T2DM obese mice.	139
Figure 4-6 Short-term treatment with Dasatinib reduces lipid droplet accumulation in T2DM obese mice hearts.	140
Figure 4-7 Short-term treatment with Dasatinib reduces lipid droplet accumulation in T2DM obese mice bone marrow.	141
Figure 4-8 Effects of short-term Dasatinib treatment on the expression of senescence markers in the hearts of T2DM obese mice.	142
Figure 4-9 Short-term Dasatinib treatment influences T2DM obese mice bone marrow senescence.	143
Figure 4-10 Effects of in vitro treatment with Dasatinib on mouse BM-SCs isolated from T2DM obese mice.	144
Figure 4-11 Confirmation of the diabetic status in T2DM obese mice used for the long-term treatment study with Dasatinib.	145
Figure 4-12 Long-term treatment with Dasatinib does not impact the body weight and fat pad weight of T2DM obese mice.	146
Figure 4-13 Results of echocardiography analysis in 25-week-old T2DM obese mice undergoing long-term treatment with Dasatinib.	151
Figure 4-14 Long-term treatment with Dasatinib does not affect the concentrations of adipokines in T2DM obese mice plasma.	152

Figure 4-15 Long-term treatment with Dasatinib reduces the lipid accumulation in the hearts of T2DM obese mice.	153
Figure 4-16 Long-term treatment with Dasatinib reduces the lipid accumulation in the bone marrow of T2DM obese mice.	154
Figure 4-17 Regression analysis of bone marrow and heart lipid accumulation and cardiac function.....	155
Figure 4-18 Long-term treatment with Dasatinib reduces the myocardial interstitial fibrosis of T2DM obese mice.....	157
Figure 4-19 Long-term treatment with Dasatinib reduces cardiac senescence of T2DM obese mice.	158
Figure 4-20 Effects of long-term treatment with Dasatinib on bone marrow senescence of T2DM obese mice.	159
Figure 4-21 Flow cytometry analysis of mouse bone marrow mesenchymal stromal cells.....	160
Figure 8-1 Etoposide-induced human CPs senescence as a positive control of cellular senescence.	182
Figure 8-2 Optimisation of Dasatinib concentration for in vitro treatment of human BM-PCs.	184
Figure 8-3 Optimisation of the Dasatinib concentration for experiments of adipogenesis differentiation of human BM-PCs.	187
Figure 8-4 In vitro model of high glucose-induced insulin resistance in human BM-PCs and HUVECs.....	190
Figure 8-5 In vitro model of high glucose and glucosamine-induced insulin resistance in human BM-PCs.....	193
Figure 8-6 Lipid droplet accumulation in T2DM obese mice hearts at different ages.	195

LIST OF ABBREVIATIONS

A

α MEM	Alpha minimum essential medium
α SMA	α -smooth muscle actin
ADIPOQ	Adiponectin
AET	Aortic ejection time
AMPK	AMP-activated protein kinase
ANOVA	Analysis of variance
AP4	Apical four chamber

B

B-mode	Brightness mode
BAT	Brown adipose tissue
BCA	Bicinchoninic acid protein assay
BCL-2	B cell lymphoma 2
BM	Bone marrow
BMAT	Bone marrow adipose tissue
BMI	Body mass index
BMP4	Bone morphogenetic protein 4
BSA	Bovine serum albumin

C

cDNA	Complementary deoxyribonucleic acid
C/EBP α	CCAAT/enhancer binding protein α
CD	Cluster of differentiation
CI	Cardiac index
CO	Cardiac output
CVD	Cardiovascular disease
CXCL	C-X-C motif chemokine ligand

D

DAPI	4',6-diamidino-2-phenylindole
Db/Db	BKS.Cg-+Lepr ^{db} /+Lepr ^{db} /OlaHsd
DDR	Deoxyribonucleic acid damage response
DM	Diabetes mellitus
DMEM	Dulbecco's modified eagle medium
DMSO	Dimethyl sulfoxide
DNA	Deoxyribonucleic acid
DPBS	Dulbecco's phosphate buffered saline
DPP4	Dipeptidyl peptidase-4
DSBs	Double-strand breaks
DT	Deceleration time

E

EAT	Epicardial adipose tissue
ECGM2	Endothelial cell growth medium 2
ECM	Extracellular matrix
EdU	5-ethynyl-2'-deoxyuridine
EDTA	Ethylenediaminetetraacetic acid
EF	Ejection fraction
ELISA	Enzyme-linked immunosorbent assay
ER	Endoplasmic reticulum
EthD-III	Ethidium homodimer III

F

FABP4	Fatty acid-binding protein 4
FACS	Fluorescence-activated cell sorting
FBS	Fetal bovine serum
FDA	The United States Food and Drug Administration
FFAs	Free fatty acids
FMO	Fluorescence minus one

FOXO4-DRI Forkhead box O transcription factor 4-D-retro-inverso
FS Fractional shortening

G

GADA Glutamic acid decarboxylase antibodies
GLP1 Glucagon-like peptide 1
GLUT4 Glucose transporter type 4
GTTs Glucose tolerance tests

H

hBM Human bone marrow
hCPS Human primary cardiac pericytes
HbA1c Haemoglobin A1c
HFpEF Heart failure with preserved ejection fraction
HG High glucose
HIF-1 α Hypoxia-inducible factor-1 alpha
HOMA2-B Homoeostasis model assessment 2 estimates of β -cell function
HOMA-IR Homeostasis model assessment-estimated insulin resistance
HR Heart rate
HSC Hematopoietic stem cell
HUVEC Human umbilical vein endothelial cell

I

ICC Immunocytochemistry
IDF International Diabetes Federation
IGFBP Insulin-like growth factor binding protein
IHC Immunohistochemistry
IL Interleukin
ITTs Insulin tolerance tests
IVCT Isovolumic contraction time
IVRT Isovolumic relaxation time

J

JNK c-Jun N-terminal kinase

L

LepR Leptin receptor

LN₂ Liquid nitrogen

LV Left ventricle

LVAW Left ventricular anterior wall thickness

LVID Left ventricular internal diameters

LVPW Left ventricular posterior wall thickness

M

mBM Mouse BM

mRNA Messenger ribonucleic acid

mTOR Mammalian target of rapamycin

M-mode Motion mode

MARD Mild age-related diabetes

MCP-1 Monocyte chemoattractant protein-1

MDR MitoTracker® deep red

MMPs Matrix metalloproteinases

MOD Mild obesity-related diabetes

MPI Myocardial performance index

MPP Multipotent progenitor cells

MSC Mesenchymal stromal cell

MW Molecular weight

N

NAFLD Non-alcoholic fatty liver disease

NASH Non-alcoholic steatohepatitis

NF-κB Nuclear factor kappa B

NFT Non-flow time

NG2 Neural/glial antigen 2
NDM-CTRL Non-diabetes mellitus control

O

Ob/Ob $Lep^{ob/ob}$
OCT Optimal cutting temperature compound
OD Optical density
ORO Oil red O

P

PAI-1 Plasminogen activator inhibitor-1
PAT Pericardial adipose tissue
PC Pericyte
PDGFR β Platelet-derived growth factor receptor beta
PEG300 polyethene glycol 300
PFA Paraformaldehyde
PGC Peroxisome proliferator-activated receptor gamma coactivator
PHT Pressure half time
PI3K Phosphatidylinositol 3-kinase
PPAR γ Peroxisome proliferator-activated receptor gamma
PSAX Parasternal short-axis
PSLAX Parasternal long-axis
PW Pulsed wave

Q

qPCR Quantitative reverse-transcription-polymerase chain reaction

R

RBC Red blood cell
RIPA buffer Radioimmunoprecipitation assay buffer
RNA Ribonucleic acid

ROS Reactive oxygen species

RT Room temperature

S

SA- β -gal Senescence-associated beta-galactosidase

SADS Senescence-associated distention of satellites

SAHF Senescence-associated heterochromatin foci

SAID Severe autoimmune diabetes

SASP Senescence-associated secretory phenotype

SAT Subcutaneous adipose tissue

Sca-1 Stem cells antigen-1

SCs Stromal cells

SDS Sodium dodecyl sulfate

SEM Standard error of the mean

SG Senescence green

SGLT2 Sodium-glucose cotransporter 2

SIDD Severe insulin-deficient diabetes

SIRD Severe insulin-resistant diabetes

SV Stroke volume

T

TAF Telomere-associated foci

TdT Terminal deoxynucleotidyl transferase

T1DM Type 1 diabetes mellitus

T2DM Type 2 diabetes mellitus

TGs Triglycerides

TGF- β Transforming growth factor β

TKI Tyrosine kinases inhibitor

TNF- α Tumour necrosis factor alpha

TUNEL Terminal deoxynucleotidyl transferase-mediated dUTP nick-end labelling

U

UBC	Ubiquitin C
UCP-1	Uncoupling protein 1

V

VAT	Visceral adipose tissue
-----	-------------------------

W

WAT	White adipose tissue
WB	Western blotting

Z

ZDF	Zucker Diabetic Fatty
-----	-----------------------

PUBLICATIONS ARISING FROM THIS WORK

Below is a list of publications from research undertaken throughout this Ph.D., along with the contributions section from each publication.

The following publication is based on Chapter 6 and also includes elements of Chapters 1, 4, 5, 7 and 9

Publication: The tyrosine kinase inhibitor Dasatinib reduces cardiac steatosis and fibrosis in obese, type 2 diabetic mice. *Cardiovascular Diabetology* 22, 214 (2023). <https://doi.org/10.1186/s12933-023-01955-9>

Authors: Yue Gu, Elisa Avolio, Valeria V Alvino, Anita C Thomas, Andrew Herman, Poppy J Miller, Niall Sullivan, Ashton Faulkner, and Paolo Madeddu

Author contributions: **YG:** research conception and design, in vivo procedures with mice (both short & long duration treatment models including echocardiography), histological, cellular, and molecular biology experiments, data analysis, manuscript writing. **EA:** mouse bone marrow cell isolation, molecular biology techniques support, manuscript writing. **VVA:** in vivo long-duration procedures with mice support. **ACT:** in vivo short-duration procedures with mice and echocardiography technique support. **AH:** flow cytometry experiment and data analysis. **PJM:** flow cytometry experiment. **NS:** patient recruitment and human bone marrow sample collection. **AF:** critical analysis and interpretation of experimental data. **PM:** research conception and design, research supervision, data analysis, manuscript writing, funding provision. All authors read and approved the final manuscript.

First author: Yue, Gu

Date: 26/09/2023

Last author: Paolo, Madeddu

Date: 26/09/2023

CHAPTER 1. INTRODUCTION

1.1. Diabetes mellitus

1.1.1. Definition and classification of diabetes mellitus

Diabetes mellitus (DM) is defined as “A series of metabolic diseases caused by lacking insulin production or insulin insensitivity or both factors”. The characteristic of DM is hyperglycemia which is related to multiple tissues’ long-time damage, dysfunction, and failure, such as heart, liver, kidney, eyes, blood vessels, and nerves [1].

There are four major classical types of DM: type 1 DM (T1DM), type 2 DM (T2DM), gestational DM, and some specific types of DM caused by other factors, such as genetic diabetes syndromes (e.g., neonatal diabetes and maturity-onset diabetes of the young), exocrine pancreas disease (e.g., pancreatitis), and drug- or chemical-induced DM (e.g., glucocorticoid using in the treatment of HIV/AIDs or organ transplantation) [2, 3].

In addition to the standard classification of T2DM, Ahlqvist et al. [4] reported a new category of T2DM. The authors proposed a classification that better predicts T2DM progression and risk of cardiovascular complications by including six variables (age at diagnosis, body mass index (BMI), Haemoglobin A1c (HbA1c), glutamic acid decarboxylase antibodies (GADA), and C-peptide to calculate homoeostasis model assessment 2 estimates of β -cell function (HOMA2-B) and HOMA-insulin resistance (HOMA-IR)). The significant difference from the older classification is that T2DM consists of five sub-groups.

1. SAID (severe autoimmune diabetes) is a sub-group that coincident with the current diagnosis of T1DM and latent autoimmune diabetes in the adult and shows the following characteristics: high morbidity at a younger age, reduction of metabolic control, the inability of insulin production, and the existence of GADA antibodies (a vital factor of insulin therapy prediction).

2. SIDD (severe insulin-deficient diabetes) is a sub-group characterised by patients who have high HbA1c levels, abnormal insulin production and show mild insulin resistance. SIDD individuals are at the highest risk of retinopathy.

3. SIRD (severe insulin-resistant diabetes) is a sub-group which shows serious obesity and heavy insulin resistance and has the highest incidence of nephropathy.

4. MOD (mild obesity-related diabetes) is a sub-group characterised by patients who are obesity without insulin resistance from a relatively low age.

5. MARD (mild age-related diabetes) is a sub-group that takes the primary part, about 40%, among all the five sub-groups and includes the oldest patients.

1.1.2. Diagnosis of diabetes mellitus

The clinical diagnosis of DM is based on the following parameters: fasting plasma glucose levels ≥ 7.0 mmol/L (126 mg/dL), random plasma glucose levels ≥ 11.1 mmol/L (200 mg/dL), two-hour plasma glucose levels after 75 grams of oral glucose intake ≥ 11.1 mmol/L (200 mg/dL), and HbA1c levels ≥ 48 mmol/mol (6.5%) [3].

1.1.3. Type 1 diabetes mellitus

T1DM is also denominated juvenile DM as it often manifests at a young age but can be diagnosed at any age. It is typically characterised by reduced insulin production and requires insulin treatment [5, 6].

1.1.4. Type 2 diabetes mellitus

T2DM is the most prevalent form of DM, occurring in 90% of all DM cases. It is characterised by ineffective insulin metabolisms, such as insulin resistance, and is regularly related to overweight and obesity. Some symptoms are common to T1DM and T2DM, such as polydipsia, polyuria, and fatigue [3]. To control hyperglycemia, T2DM can be initially treated with oral medications, such as metformin only, or combined with other drugs. However, if the blood glucose still resists at a high level, insulin administration is applied to improve metabolic control. Insulin production and sensitivity can be altered in some patients with T2DM. The promoters of T2DM are various, such as aging, environmental factors, physical inactivity, and obesity [7, 8].

1.1.5. Epidemiology of diabetes mellitus

DM is one of the most harmful non-communicable diseases, along with cancer, cardiovascular disease (CVD), and pulmonary disease. Compared with 2000, there was a 3% increase in age-standardized mortality rates in 2019 due to DM [9, 10]. The International Diabetes Federation (IDF) Diabetes Atlas (10th edition) reports that the global prevalence of DM in 20-79 years old is increasing fast worldwide. It is estimated that 537 million people have DM, which will increase 1.2 times by 2030 and 1.5 times by 2045 (**Figure 1-1**) [3]. DM is a disease but also a risk factor for other diseases. Risk factors are conditions (inherited or acquired) that make a subject more susceptible to an illness or complications. They can also accelerate the aging clock, making the whole organism or a single organ older than the actual age, thereby increasing the probability of death. Different risk factors can additively augment morbidity and mortality. DM increases the risk associated with non-communicable diseases. Moreover, patients with DM have a higher risk of adverse events associated with communicable diseases than non-diabetic patients, as reported during the recent COVID-19 epidemics [7].

The dysmetabolic condition and complications, including cardiovascular, renal, and hepatic disease, cause the high mortality of DM. In addition, quality of life is worsened by neuropathic and ischemic complications affecting the lower limbs [11]. Moreover, according to large meta-analyses, DM is highly linked to increased mortality risk of most cancers. In a prospective cohort study in the US, DM was associated with an increased approximately 7% mortality risk in male cancer patients and 11% in female cancer patients [12].

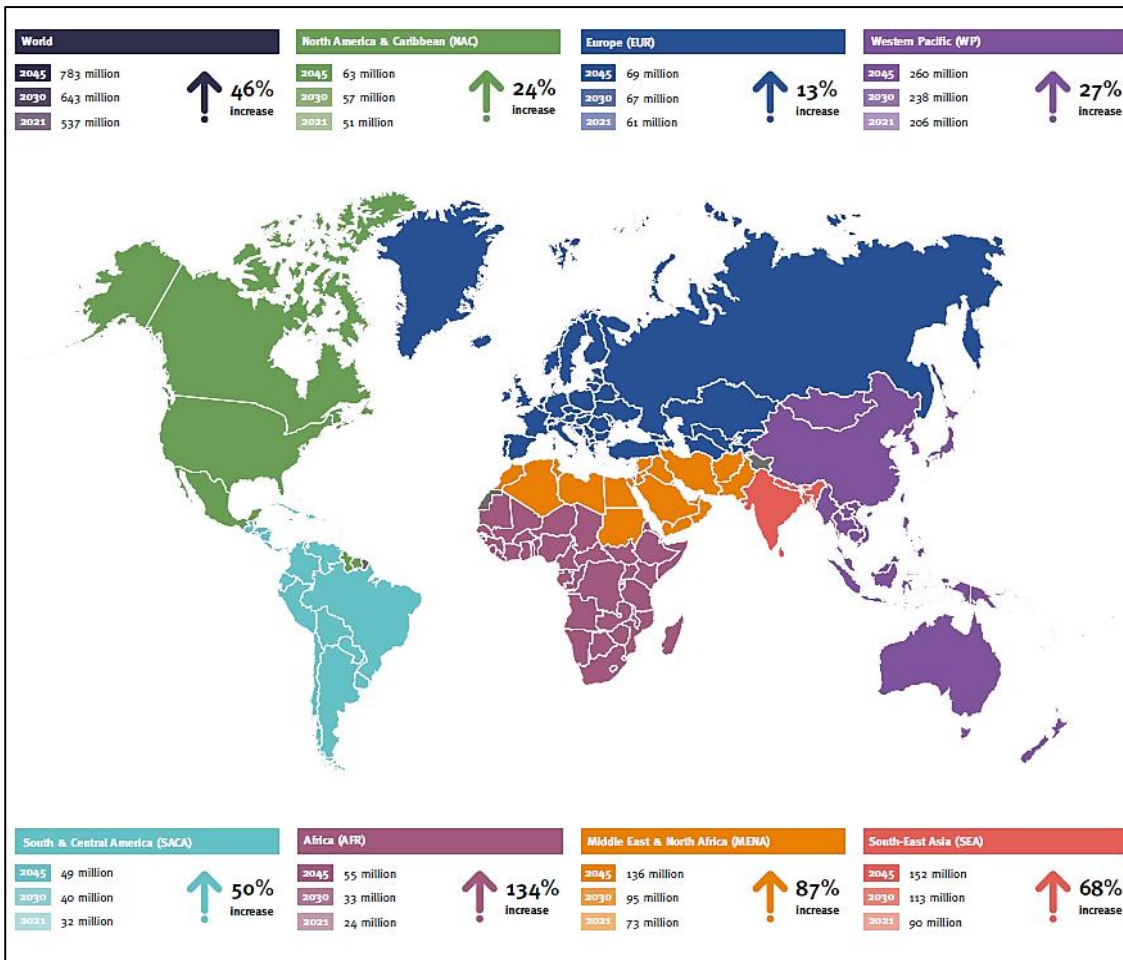


Figure 1-1 Number of people with diabetes worldwide in 2021-2045 (20–79-year-olds).
Figure source: the 10th edition of IDF Diabetes Atlas.

1.1.6. Insulin resistance

1.1.6.1. Insulin and its effects

Insulin, a peptide hormone secreted by pancreatic β -cells, was first discovered by Frederick Banting and Charles Best in 1921 [13]. Insulin is crucial in regulating blood glucose levels and inducing glucose storage in the liver, muscles, and adipose tissue. Under fasting, the liver secretes glucose through both breakdowns of glycogen and de novo glucose synthesis [14]. Glucose is vital for stimulating insulin secretion. Pancreatic β cells secrete 0.25–1.5 units of insulin per hour during fasting, thereby enabling glucose insulin-dependent entry into cells [15]. After a meal or glucose administration, insulin

synthesised and stored in secretory granules is initially released. The second phase represents the secretion of both accumulated and newly synthesised insulin.

1.1.6.2. Mechanisms of insulin resistance

Insulin resistance is defined as reduced tissue response to a normal level of insulin stimulation, characterised by decreased glucose uptake and oxidation, decreased glycogen synthesis, and partly inhibited oxidation of lipids [16]. Insulin resistance is associated with hyperglycemia, hypertension, dyslipidemia, visceral adiposity, hyperuricemia, increased inflammatory markers, dysfunction of endothelial, and a prothrombotic state [17]. Insulin resistance is also associated with excess lipid availability [18]. In 1963, Randle et al. [19] proposed that lipid-induced insulin resistance in skeletal muscle was attributable to the fatty acid oxidation elevation in the glucose-fatty acid cycle. However, the glucose-fatty acid cycle cannot explain all the characteristics of lipid-induced insulin resistance. The following studies suggest other potential pathways causing insulin resistance, such as the hexosamine biosynthesis pathway, a branch of glycolysis responsible for producing a critical substrate for protein glycosylation [18]. Ectopic lipid accumulation, especially in the liver and skeletal muscles is another risk factor contributing to insulin resistance (e.g., about 70% of obese, T2DM individuals have non-alcoholic fatty liver disease (NAFLD), and most of the NAFLD patients have T2DM and hepatic insulin resistance) [20]. Moreover, ceramide [21], endoplasmic reticulum (ER) stress [22], and inflammation [23] are reported as pivot mediators in inducing insulin resistance.

1.1.6.3. Diagnosis of insulin resistance

Insulin resistance is associated with many metabolic abnormalities, such as glucose tolerance, T2DM, obesity, and dyslipidemia [24, 25]. The commonly used diagnosis methods for insulin resistance include glucose tolerance tests (GTTs), insulin tolerance tests (ITTs), and hyperinsulinemic-euglycemic clamp [26]. GTT is a method to confirm the break speed of a quantity of exogenous glucose (e.g., oral, intraperitoneal, or intravenous administration) in the blood, which can help measure insulin sensitivity and

release [27]. ITT is used to assess the sensitivity of systemic insulin receptors via measuring blood glucose level changes before and after intravenous insulin injection [28]. The hyperinsulinemic-euglycemic clamp is a gold-standard way [26] to assess the tissue insulin sensitivity *in vivo* by continuous intravenous infusion of insulin at 120 mU/m² · min while blood glucose level is kept constant at basal levels via adjustable glucose infusion to achieve steady-state and calculate the glucose infusion rate [29].

1.1.6.4. Therapeutic strategies of insulin resistance

No specific treatment is approved to treat insulin resistance; the leading management consists of lifestyle changes, such as dietary, physical exercise, and disease prevention. In addition, some pharmacological medications are used to alleviate insulin insensitivity. For example, metformin treatment can improve insulin sensitivity by activating insulin receptor tyrosine kinase and glucose transporter type 4 (GLUT4), promoting glycogen synthesis, and re-esterifying the free fatty acid [30]. Thiazolidinediones are peroxisome proliferator-activated receptor gamma (PPAR γ) agonists, which can improve liver and skeletal muscles' insulin sensitivity and promote lipid storage and reduce ectopic lipid accumulation [26]. Glucagon-like peptide 1 (GLP1) is a hormone that can activate pancreatic islet β -cells GLP1 receptors to stimulate insulin release [31]. Therefore, the GLP1 agonists, such as Liraglutide, Semaglutide, and Dulaglutide, are also applied in T2DM treatment [26]. Dipeptidyl peptidase-4 (DPP4) is reported to degrade GLP1, mediate insulin resistance and inflammation in adipose tissues and the liver and reduce the activation of the downstream AKT signalling pathway [26, 32]. The DPP4 inhibitors (e.g., omarigliptin, sitagliptin and vildagliptin) are also approved to treat T2DM and increase insulin sensitivity [33, 34]. However, these drugs have limited effects on treatment due to their side effects, such as body weight gain, vomiting, bone fractures, and hypoglycemia [26]. So novel therapeutic strategies investigation is necessary.

1.1.7. Complications of type 2 diabetes mellitus

1.1.7.1. Adipose tissue accumulation in diabetes

Since T2DM and its various complications are highly associated with obesity. It is essential to understand the characteristics of adipose tissue accumulation and the influence of T2DM during this process.

1.1.7.1.1. Types and characteristics of adipose tissue

Adipocytes, fat cells, can be distinguished according to their structural and functional characteristics. The primary function of adipocytes is energy storage, which implies the accumulation of fatty acids as inert triacylglycerols into lipid droplets [35]. Conversely, adipocyte lipolysis allows energy release through the breakdown of triacylglycerols into fatty acids and glycerol. Lipolysis is regulated by lipases (e.g., patatin-like phospholipase domain containing-2 (PNPLA2)/adipocyte triglyceride lipase (ATGL) [36] and hormone-sensitive lipase [37]), hormones (e.g., catecholamines [38], insulin [39], and atrial natriuretic peptides [40]) and intracellular intermediary metabolites (e.g., oleoyl-CoA and oleic acid [41]) [35].

White adipocytes have a single large lipid droplet and low mitochondria density, and their function is as energy storage in specific tissue fat depots. Brown adipocytes consist of multiple tiny lipid droplets and have high mitochondria density. They participate in thermogenesis, i.e., heat production by lipolysis, which usually occurs in brown adipose tissue and skeletal muscle [42]. Beige adipocytes have both characteristics of white and brown adipocytes. They have multiple lipid droplets and mitochondria like brown adipocytes, but they also show similar plasticity (a capability of cells transforming into another cell type) as white adipocytes [43-45]. Based on the prevalent composition of different adipocyte subtypes, three main types of adipose tissues have been described, which differ in structure, function, and metabolism: white adipose tissue (WAT), brown adipose tissue (BAT), and beige adipose tissue [46]. The structure of adipocytes and adipose tissue is shown in **Figure 1-2** [47].

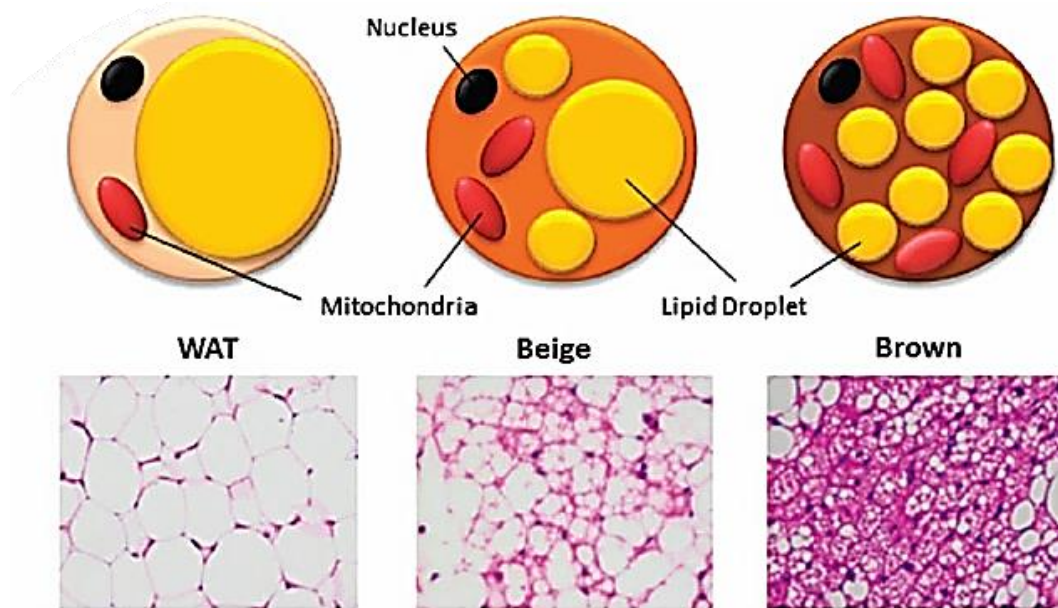


Figure 1-2 The morphological difference between white, beige, and brown adipose tissue adipocytes.

The structures of white, beige, and brown adipocytes and adipose tissue are demonstrated by cartoon and hematoxylin-eosin staining at 40x magnifications. Abbreviations: WAT = white adipose tissue. Figure source: Kwok, K et al., Heterogeneity of white adipose tissue: molecular basis and clinical implications. *Exp Mol Med* 48, e215 (2016).

White adipose tissue

WAT is considered an energy storage organ crucial in endocrine function and body weight regulation [48]. According to the distribution, WAT is distinguished into visceral adipose tissue (VAT) (e.g., pericardial and epididymal) and subcutaneous adipose tissue (SAT) (e.g., inguinal) [49]. Apart from mature adipocytes, WAT contains preadipocytes, macrophages, neutrophils, endothelial cells, and T and B immune cells [50, 51].

In non-obesity T2DM populations, WAT adipocytes appear hypertrophic, possibly due to an impaired adipogenic ability of stromal cells (SCs). Furthermore, the size of adipocytes shows a positive correlation with the ratio of M1/M2 macrophages, tumour necrosis factor alpha (TNF- α) level, insulin resistance, and lipolysis and a negative correlation with the expression level of adipogenesis regulator and adipose morphology genes (e.g., bone morphogenetic protein 4 (*BMP4*) and *PPARG*) [52].

WAT is also found altered and dysfunctional in individuals with obesity or aging, as shown by chronic low-grade inflammation, adipose tissue redistribution, and remodelling [53]. WAT is linked to obesity-related co-morbidities, such as insulin resistance and weak glycaemic control [54]. Since large adipocytes contribute more to insulin resistance and adipocyte size is more prominent in VAT than in SAT, the former is more significant in metabolic disorders. In contrast, the high avidity of free fatty acids (FFAs) and triglycerides (TGs) and insulin sensitivity of small adipocytes in SAT explain why increased SAT is associated with better metabolic status [55-57]. Since the number of adipocytes in individuals remains constant throughout life [58], obesity- and aging-induced hypertrophic adipocytes cause dysregulation of adipokines secretion [59], activate the ERK (extracellular signal-regulated kinase) and p38/MAPK (mitogen-activated protein kinase) signalling pathways, leading to upregulation of monocyte chemoattractant protein-1 (MCP-1) [60]. MCP-1 can promote macrophage recruitment following TGs release and activate the I κ B kinase (IKK)/ nuclear factor kappa B (NF- κ B) pathway and, consequently, promote TNF- α secretion. The TGs and TNF- α inhibit insulin receptor substrate 1 signalling reaction, influencing adipose tissue glucose uptake, and contributing to insulin resistance [61]. Moreover, inflamed adipocytes tend to undergo heightened apoptosis [62]. Cell debris attracts macrophage infiltration, which extends the inflammatory milieu [53, 62].

In obese individuals, the percentage of VAT is increased and correlated with the decrease in SAT, promoting the development of T2DM [53, 63, 64]. In high-fat diet feeding C57BL/6J mice, removing VAT can help prevent obesity-induced insulin resistance, ameliorate glucose tolerance, decrease liver TGs, increase circulating adiponectin (an essential insulin-sensitizing adipokine), and reduce the circulation of interleukin 6 (IL-6) (a pro-inflammatory adipokine) [65]. In obesity, the hypertrophy and hyperplasia of WAT promote local and systemic chronic low-grade inflammation, activating metabolic deterioration. WAT shows an increased inflammatory milieu, featuring increased expression and release of leptin, IL-6, TNF- α , C-reactive protein, MCP-1, and plasminogen activator inhibitor-1 (PAI-1). In contrast, the anti-inflammation cytokines adiponectin and IL-10 are inversely downregulated [57, 66, 67]. In addition,

studies in obese humans and mice found increased WAT collagen content, followed by fibrotic remodelling [68].

In addition to obesity, aging contributes to adipose tissue redistribution, upregulating the amount of adipose tissue in the trunk and visceral parts and inducing the SAT decrease in limbs [61, 69]. In Gabriely et al.'s study, after the surgical removal of VAT from aging Zucker Diabetic Fatty (ZDF) rats, the decrease of insulin action was prevented, and the onset of diabetes was delayed [63]. In senescent WAT, inflammatory factors are upregulated, transferring senescence to the neighbouring cells and recruiting immune cells. In aged WAT, inflammaging is associated with developing metabolic diseases, such as insulin resistance and lipid metabolism [61].

Brown adipose tissue

Unlike WAT, BAT mainly comprises brown adipocytes and only takes approximately 1-2% of adipose tissue's total weight in humans [46], located at the cervical, supraclavicular, axillary, and paravertebral [45]. BAT plays a vital role in mediating thermogenesis. This property of brown adipocytes is attributed to the abundance of multiple mitochondria and high expression of uncoupling protein 1 (UCP-1), an inner mitochondrial membrane protein promoting non-shiver thermogenesis [45, 70, 71]. BAT thermogenesis can be stimulated by cold [71]. β -adrenergic receptors are abundant in BAT and can be activated by cold stimulating on β 3-adrenoreceptor via circulating catecholamines [72]. Hence, β 3-adrenoreceptor agonists may activate BAT by upregulating UCP-1 expression level and promoting glucose metabolism [73-75]. Cold exposure promotes BAT activation increasing energy expenditure and glucose uptake [76].

Interestingly, WAT has browning potential, and in the browning WAT, the UCP-1-positive cells show similar features as brown adipocytes [77, 78]. BAT activation may reduce the risks of CVD by mediating relevant metabolic factors, such as glucose metabolism and lipoprotein cholesterol. For instance, BAT can produce heat against the cold by burning fatty acids. Triglyceride-rich lipoproteins play a role in transporting lipids in the blood, and part of the fatty acids can be released by lipoprotein lipase. The fatty acids can be

absorbed by muscle and adipose tissue, and the liver eliminates the remained cholesterol. However, over-accumulation of TGs and cholesterol in the circulation system prolongs the circulating time and overloads the liver, resulting in dyslipidemia, especially in people with diabetes, consequently increasing the risk of CVD. Bartelt et al. found that short-term cold exposure-induced BAT activation could increase the consumption of fatty acids and activation of lipoprotein lipase, consequently accelerating the plasma TGs clearance. Therefore, cold-induced BAT activation may contribute to decreasing plasma TGs levels, reducing the risk of hyperlipidemia and ameliorating insulin resistance, consequently delaying the formation of atherosclerotic [71, 79]. In the study of 10-day cold induction of BAT activation, insulin sensitivity was improved in the entire body in obese T2DM subjects [80]. However, BAT may also lose function under adiposopathy or aging conditions, showing transformation into WAT [81]. Within vascular dysfunction, whitened BAT was observed to start expressing leptin [46, 82], while mitochondria density decreased, disrupting thermogenesis progress and contributing to increasing insulin resistance [83].

Beige adipose tissue

Beige adipose tissue is mainly constituted by beige adipocytes, which are also termed “Brite” or “browened” fat tissue [72]. Beige adipose tissue has been proven to have similar morphology and function with BAT in humans and rodents [72, 84, 85]. As described above, beige fat cells have multiple lipid droplets and mitochondria, similar to brown adipocytes. The source of beige adipocytes is still unclear, but two highly supported hypotheses exist. The first is that the beige adipocyte is derived from trans-differentiation of WAT [45]; the second is a hypothesis that beige adipocyte originates from *de novo* adipogenesis from dormant special progenitor cells when stimulated by cold exposure, but this process is unstable [86-88]. Like BAT, beige adipose tissue is also essential for glucose homeostasis and lipid metabolism by promoting excessive glucose consumption to improve insulin sensitivity and increase thermogenesis [89-91]. BAT activation and WAT browning can encourage the uptake of glycolipids and decrease the requirement of insulin production, subsequently improving the insulin sensitivity in the tissues, which may become a novel therapeutic for ameliorating glycolipid metabolism and insulin resistance of obesity and T2DM [89, 92].

1.1.7.1.2. Important adipose depots

Adipose tissue is distributed variously in the whole body. The critical adipose depots include dermal, facial, mammary, joint, bone marrow (BM), planter and palmar, and cardiovascular and mesenteric adipose tissues [93]. The present introduction reviews the features and functions of BM and cardiovascular adipose tissues.

Bone marrow adipose tissue

BM adipose tissue (BMAT) is vital in energy metabolism and bone homeostasis. BMAT takes around 10% of total body fat and shows different characteristics from WAT and BAT [94]. In Scheller et al.'s study, BMAT was divided into constitutive and regulated BMAT [95]. Constitutive BMAT is defined as early-matured marrow adipose tissue, composed of dense adipocytes resembling WAT and distributed in the distal skeleton's yellow marrow without haematopoiesis activation. The regulated BMAT is defined as single adipocytes scattered and participating in active haematopoiesis, distributed in the red marrow of the proximal skeleton containing hematopoietic cells. [93, 95, 96].

BMAT is considered a complex endocrine fat depot. It responds to metabolic requirements by expansion, which can be observed under disorders, such as diabetes, aging, anorexia nervosa, or obesity [97-100]. BMAT plays a crucial role in energy metabolism. High-calorie diet and calorie restriction are known to increase BMAT, but the potential mechanism of caloric restriction on BMAT is still unclear [94]. Moreover, BMAT can regulate the skeleton homeostasis and energy metabolisms via producing adipokines (e.g., adiponectin) [101], growth factors (e.g., insulin-like growth factor binding protein 2 (IGFBP-2) and Wnt-10b) [102], proinflammatory factors (e.g., TNF- α , IL-6, and IL-1 β) [103], peptides (e.g., leptin) [104] and fatty acids [105]. In addition, aging is an essential factor in influencing bone homeostasis and inducing adipocyte accumulation in BM [94, 106]. The expression level of adipokines and proinflammatory cytokines is increased alongside BMAT expansion, thereby promoting the development of low-grade inflammation, and participating in cellular senescence [107, 108].

Cardiovascular adipose tissue

There are two crucial intrathoracic adipose depots surrounding the heart, the epicardial adipose tissue (EAT), located between the myocardium and visceral layer of the pericardium, and pericardial adipose tissue (PAT) around the surface of the parietal pericardium (**Figure 1-3**) [93, 109].

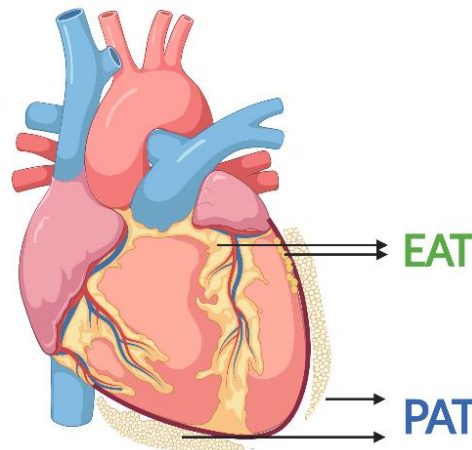


Figure 1-3 The anatomy distribution of epicardial and pericardial adipose tissue.

EAT is located between the myocardium and the visceral pericardium. PAT lies around the external surface of the parietal pericardium. Abbreviations: EAT = epicardial adipose tissue; PAT = pericardial adipose tissue.

Epicardial adipose tissue

EAT adipocyte has both characteristics of white and brown adipocytes. Although the adipocytes in EAT show a similar anatomical property to white adipocytes, they can produce UCP-1, like brown adipocytes, which means these EAT adipocytes may participate in the thermo-regulation of the heart [109-111]. Besides protecting the heart against cold, EAT also plays an important role in the mechanical support of the heart and coronary arteries. It participates in energy storage containing lipotoxic damage induced by high FFAs environment on the myocardium [112, 113]. EAT shows paracrine and vasocrine (signalling of cytokines access to the vascular system to restrain insulin-mediated capillary recruitment [114]) properties by producing cytokines or other factors, such as adiponectin, nitric oxide, leptin, NF- κ B, c-Jun N-terminal kinase (JNK), IL-1 β , TNF- α , IL-6 and MCP-1 [109, 115].

EAT dysfunction can induce coronary arteries inflammation by releasing proinflammatory factors [116, 117]. Furthermore, in obese individuals, the hypertrophy

of EAT increases the working pressure on heart contraction and may facilitate atrial fibrillation by filtering the posterior left atrial wall [93, 118, 119]. EAT is also found to increase in T2DM patients independently from BMI [120]. In obese diabetic subjects, the intra-myocardial fat increased alongside the infiltration of EAT into the myocardium [121-123].

Pericardial adipose tissue

Like EAT, PAT is also associated with developing atrial fibrillation. The potential mechanism of PAT-induced atrial fibrillation may correlate with increasing pro-fibrotic signalling [121, 124]. Moreover, PAT produces proinflammatory factors, induces cardiac fibrosis, regulates granulopoiesis after myocardial infarction [125], and contributes to atrial fibrillation [126]. PAT is increased in pre-diabetic and diabetic individuals, and the abundance and dysfunction of PAT are considered risk factors for CVD [121, 127]. In addition, the excess volume of EAT and PAT are all linked to left ventricular diastolic dysfunction and participate in heart failure with preserved ejection fraction (HFpEF) [109, 128, 129].

1.1.7.1.3. Definition of adiposopathy

Adiposopathy, also called “sick fat”, is an accumulation of dysfunctional fat that causes damage in distant tissues. Adipose tissue is an essential organ in energy storage and exerts endocrine functions by secreting factors that participate in glucose and lipid metabolisms and inflammation [130, 131]. Adiposopathy is a crucial promotor in inducing T2DM, hypertension, dyslipidemia, and other metabolic disorders, like CVD and atherosclerosis [131, 132].

The positive caloric balance and abnormal secreted levels of hormones (e.g., insulin, growth hormones, angiotensin II type 1 and 2), adipokines (e.g., leptin, IL-6 and TNF- α), coagulation factors (e.g., PAI-1), and enzymes (e.g., protein kinases and lipoprotein lipase) concur causing adiposopathy [133]. Pathologically enlarged adipocytes can induce irregular metabolic activity in the neighbour fat cells and affect the adipocytes' proliferation, recruitment, and adipogenic differentiation [134]. In sick fat, the lipolysis

is higher than in healthy adipose tissue, leading to the overproduction of FFAs and the redistribution of FFAs in other tissues (e.g., liver, muscle, and pancreatic islet) or other fat pads (e.g., pericardial and perivascular fat) [135, 136]. Moreover, adiposopathy crosstalk with other organs leads to disorders in other metabolic systems. For example, adiposopathy is reported to be associated with developing dementia in the central nervous system. Increased FFAs are toxic to cells, such as activating reactive oxygen species (ROS) and inducing liver and skeletal muscle insulin resistance. Adiposopathy causes the dysfunction of pancreatic β -cells reducing insulin production. An unbalance between sick adipocytes and osteoblasts causes a reduction in bone mineral density. Epicardial fat dysfunction is associated with cardiomyopathy [133, 137, 138].

1.1.7.1.4. Adiposopathy and type 2 diabetes mellitus

The link between adiposopathy and T2DM is complex. According to recent findings, adiposopathy induces lipotoxicity and unbalanced secretion of adipokines, thereby contributing to insulin resistance, pancreatic β cell dysfunction and T2DM [135]. The production of excessive FFAs or TGs by “sick fat” in the circulation and re-deposition in the liver or skeletal muscle could induce insulin resistance, mitochondrial dysfunction, and oxidative and ER stress, which is termed lipotoxicity [135].

Increased FFAs

FFAs play crucial roles in linking adiposopathy and T2DM. FFAs are usually stored in adipocytes. However, in T2DM obese individuals, the plasma FFAs level is significantly higher than in normal people [139]. Moreover, in nondiabetic but obese or pre-diabetic individuals, overaccumulation of FFAs in tissues increases the risk of T2DM [140, 141]. Short-term exposure to a low level of FFAs could stimulate insulin secretion and reduce insulin resistance. In contrast, long-term exposure to a higher level of FFAs leads to impairment of pancreatic β cells, affects insulin synthesis, and induces insulin resistance [135, 142]. The potential mechanism of FFAs-induced insulin resistance is associated with ectopic fat metabolism. The overaccumulation of FFAs in nonadipose tissues (e.g., heart, liver, muscle, and pancreas) promotes lipid accumulation, subsequently inducing ectopic fat depositions and finally resulting in insulin resistance. For example, muscle-

and liver-specific overexpression of lipoprotein lipase transgenic mice showed a reduction of insulin sensitivity and could develop into insulin resistance. [135, 143].

Abnormal adipokines, cytokines, hormones, and other factors

Adiposopathy is characterised by the increased expression level of inflammatory factor IL-6, which can interfere with the metabolism of glucose [144]. Adiponectin, which plays a vital role in anti-inflammatory, protecting pancreatic β cell and improving insulin sensitivity in the liver, is decreased in T2DM and insulin-resistant obese patients [145, 146]. Furthermore, IL-1 β , resistin, leptin, and TNF- α are all found to increase along with excessive body fat, contributing to pancreatic β cell dysfunction, insulin resistance, inflammation, and development of T2DM. The imbalance between insulin-desensitising and insulin-sensitising factors may become an essential predictor of T2DM [133, 135, 147]. In summary, the mechanisms of adiposopathy-induced T2DM are based on causing dysfunctional pancreatic β cells and increasing the inflammatory response and insulin resistance (**Figure 1-4**).

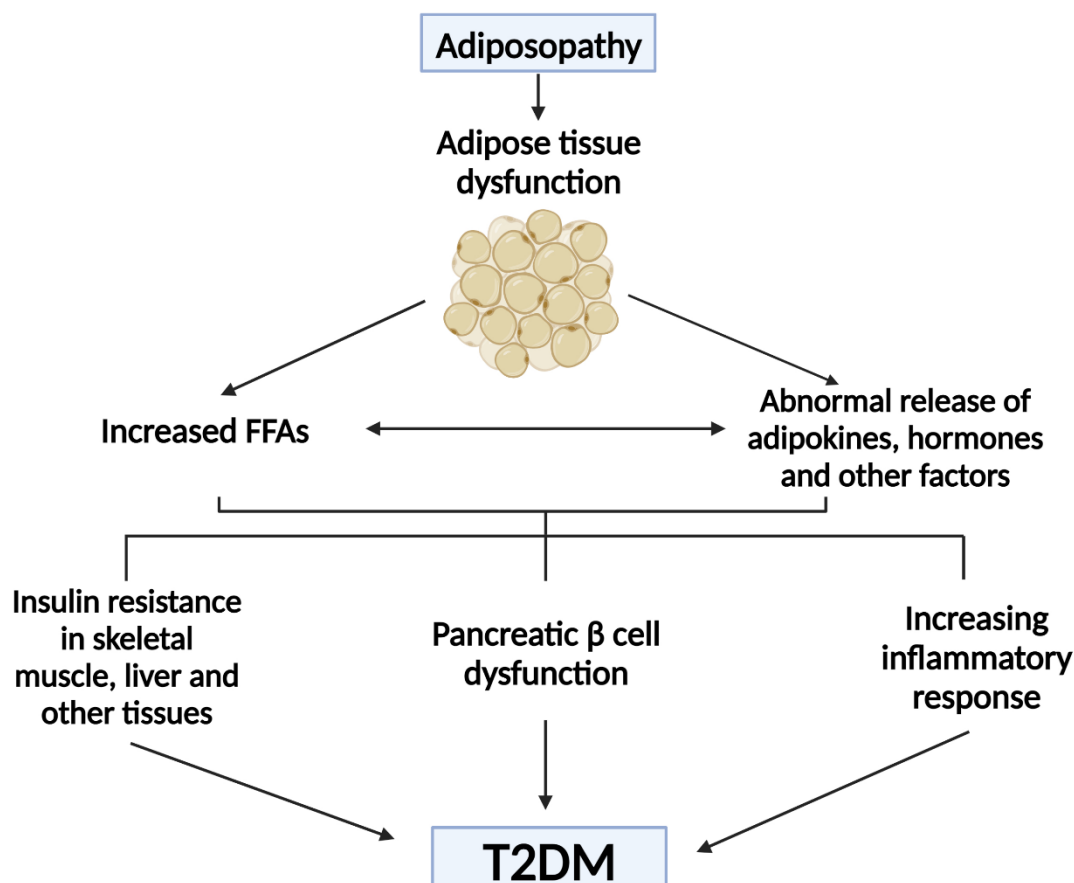


Figure 1-4 The mechanisms of adiposopathy induces T2DM.

In patients with adiposopathy, the dysfunctional adipose tissues abnormally produce excessive FFAs and adipokines, and other pathogenic factors into circulation, which induce peripheral tissue dysfunction. Upregulated FFAs, abnormal adipokines, and hormones lead to insulin resistance in liver, skeletal muscle, and other tissues, impair insulin biosynthesis and secretion in pancreatic β cells, increase the inflammatory response, and activate the development of T2DM. Abbreviations: T2DM = type 2 diabetes mellitus, FFAs = free fatty acids.

1.1.7.1.5. Adiposopathy and cardiovascular disease

Adiposopathy is also a risk factor for CVD as it is highly associated with inducing hypertension and atherosclerosis [133, 138, 148]. The pathophysiological mechanisms of adiposopathy causing CVD include positive caloric balance, ectopic fat deposition (e.g., liver, muscle, and heart) [149], increased epicardial fat [137], unbalanced between pro-inflammatory and anti-inflammatory factors, and abnormalities of hormones [133, 148]. With adipocyte dysfunction, adiposopathy causes insulin resistance and leads to hyperinsulinemia, which may contribute to hypertension via the renin-angiotensin system and hypothalamic–pituitary–adrenal axis [138, 150, 151]. Moreover,

adiposopathy-induced high blood pressure is correlated with the upregulated level of 11 β -hydroxysteroid dehydrogenase type 1 [152], angiotensinogen, angiotensin I and II [153, 154], and FFAs [155], besides downregulated the circulating level of adiponectin [156].

Adipose tissue dysfunction leads to dyslipidemia by reducing adiponectin levels and promoting excessive TG and cholesterol storage, which potentially induce lipid accumulation in the intima of the arterial wall [157]. In addition, the pro-inflammatory factors and anti-inflammatory factors play essential roles in contributing to CVD or preventing the progress of CVD. For example, the pro-inflammatory adipokine IL-6 can directly activate the expression of adhesion factors in endothelial cells and lymphocytes [131, 158]. TNF- α is associated with inducing endothelial dysfunction and calcification in coronary arteries [159, 160], and PAI-1 promotes thrombotic disorders within adipocyte dysfunction [161]. In contrast, the anti-inflammatory factor adiponectin has an athero-protective function to reduce the effects of adiposopathy [156, 162]. Overall, adiposopathy induces aberrant adipogenesis and adipocyte hypertrophy and promotes excessive circulating FFAs, abnormal adipose tissue metabolism, and unbalanced adipokines levels, thereby contributing to CVD.

1.1.7.2. Type 2 diabetes mellitus and cardiovascular disease

CVD is the primary frequent cause of morbidity and mortality in people with T2DM [163, 164]. Epidemiological studies indicate that patients with T2DM are at a higher risk of developing CVD than individuals without DM, and 52% of CVD deaths were caused by T2DM [165]. For instance, a pivotal CVD in T2DM is represented by peripheral arterial disease, which affects about 16.2% of people, and heart failure, which affects 14.7% [165]. The prevalence of myocardial infarction appears to be 2-7% higher in diabetic patients than non-diabetics [166]. Likewise, the prevalence of strokes in prediabetes was 7.8% and in diabetes was 11.2% [167].

Several comorbidities (diseases frequently associated with T2DM) are additive risk factors for CVD. They include arterial hypertension, obesity, aging, and atherosclerosis

[163, 168]. Underpinning molecular mechanisms impinge upon inflammatory, immune, oxidative stress, and mitochondrial pathways [169].

Hypertension

The American Heart Association/American College of Cardiology guideline defines hypertension as an adult systolic blood pressure level of 130-139 mm Hg or a diastolic blood pressure level of 80-89 mm Hg. [170, 171]. Hypertension reduces the elasticity of large arteries [172], causes endothelial cell dysfunction [173], accelerates atherosclerosis [174], and damages the microvasculature (**Figure 1-5**) [168, 175]. Diabetic subjects with hypertension are at a higher danger of developing retinopathy [176], renal disease [177], and peripheral neuropathy [163]. Moreover, the morbidity and mortality of stroke are increased in diabetic hypertensive patients than the nondiabetics [178]. Adequate blood pressure control could reduce the stroke risk in diabetic patients. In the Syst-Eur trial, 492 patients received antihypertensive treatment, and after five years, the stroke rate decreased by 26.6% in people with DM and 12.3% in nondiabetics [179].

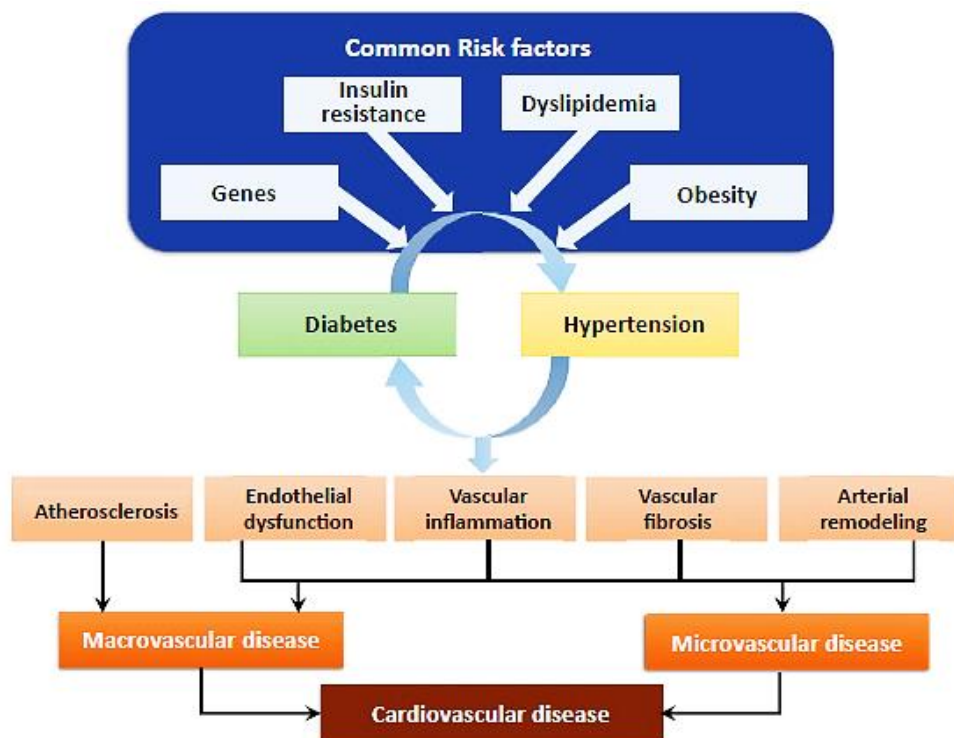


Figure 1-5 Progress of diabetes and hypertension induce cardiovascular disease.

Figure source: Petrie, J.R et al., *Diabetes, Hypertension, and cardiovascular disease: Clinical Insights and Vascular Mechanisms*. Can J Cardiol, 2018. **34**(5): p. 575-584.

Obesity

Obesity, excess body fat, is assessed by measuring the BMI, calculated with the formula: $\text{BMI (kg/m}^2\text{)} = (\text{Adult's weight}) / \text{height}^2$ [180]. A BMI between 25 - 29.9 kg/m² is known as overweight, while a BMI ≥ 30 kg/m² is identified as a condition of obesity. Epidemiological studies indicate that approximately 80% of T2DM patients are overweight or obese [163]. Severe obesity (BMI ≥ 40 kg/m²) is regularly correlated with left ventricular remodelling and heart failure [181]. Obese populations with DM are at high risk of CVD, including stroke, myocardial infarction, atherosclerosis, heart failure, and atrial fibrillation [182]. For example, the prevalence of stroke in obese, diabetic populations increased by about 20-30% [183]. Likewise, the meta-analysis results showed that obesity and overweight were positively correlated with acute myocardial infarction [184]. Obesity increases CVD risk by causing chronic low-grade inflammation (**Figure 1-6**) [185, 186]. Chronic inflammation worsens β cell dysfunction, insulin resistance, and metabolic control. The level of inflammatory factors, such as IL-1 β , NF- κ B, and NLR family pyrin domain containing 3, is increased in diabetic and obese individuals. Furthermore, these factors are found to induce heart failure and atherosclerosis [187]. The potential mechanisms of inflammation-causing vascular diseases include promoting atheroma progression [188], promoting clotting by reducing the activity of natural anticoagulants, and influencing the fibrinolytic system [189].

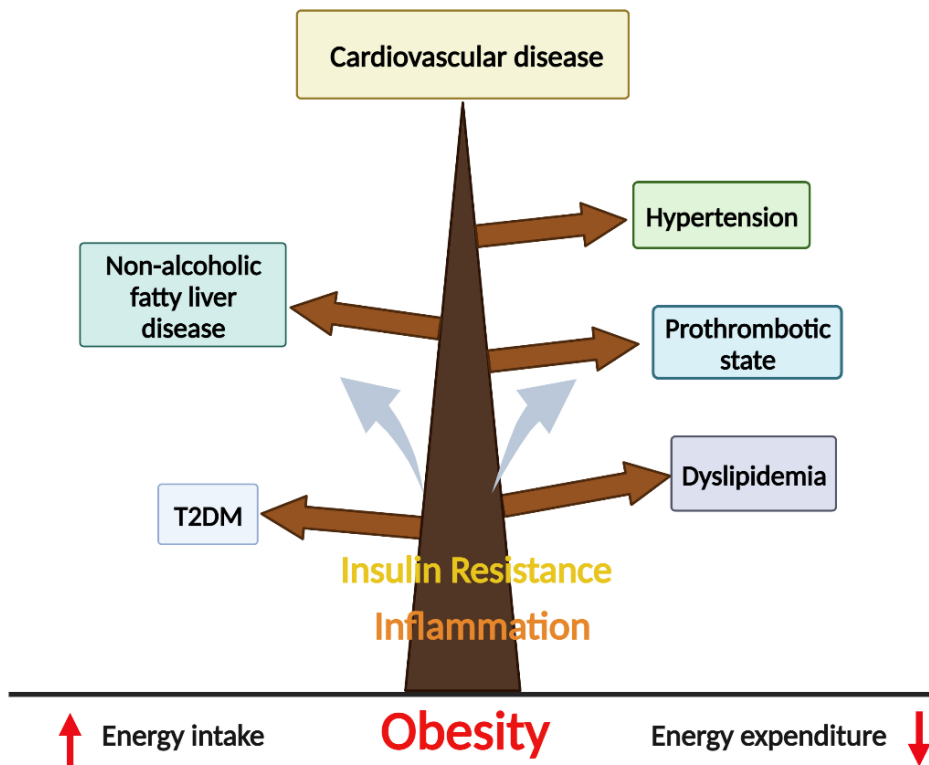


Figure 1-6 Metabolic relationship between obesity, T2DM and CVD.
Abbreviations: T2DM = type 2 diabetes mellitus.

Aging

Aging is a risk factor for T2DM and synergizes with T2DM in increasing the risk of CVD. The 10th edition of IDF Atlas shows that the prevalence of T2DM increases with age. It is estimated that 128 million (24%) T2DM individuals are aged between 75 and 79 years old, and this number is predicted to increase to 193 million (24.7%) in 2045 [3]. Public Health England reported data demonstrating the synergistic action of aging and obesity in favouring T2DM [190]. Statistical analysis results from Einarson et al.' review article showed that among 4.5 million diabetic patients, 47% were obese, aged 63.6 ± 6.9 years old, and 29.1% had atherosclerosis, 14.9% had heart failure, 10% had myocardial infarction and 7.6% had stroke [191]. In elderly patients, the accumulation level of ROS is increased, due to the alteration of mitochondrial function and decline of antioxidant mechanisms, resulting in oxidative stress, which is toxic to cardiovascular cells [192] (Figure 1-7).

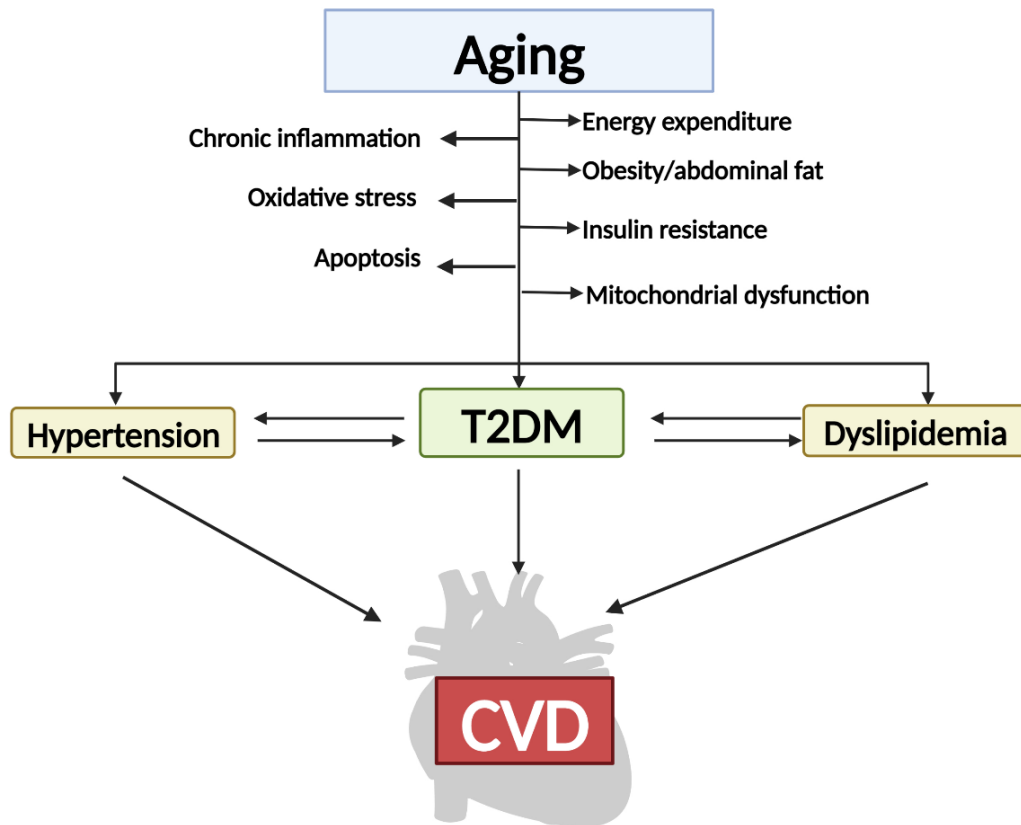


Figure 1-7 A potential mechanism linking aging, T2DM and CVD.

Abbreviations: T2DM = type 2 diabetes mellitus, CVD = cardiovascular disease.

1.1.7.3. Type 2 diabetes mellitus and bone marrow dysfunction

T2DM is a high-risk factor for bone dysfunction, inducing skeletal fragility [193]. Although some patients with T2DM have higher bone mineral density than nondiabetic individuals, they have still been found with skeletal fragility, possibly due to the increased body weight [194, 195]. Meantime, BM fat overaccumulation correlates with impaired skeletal health [196]. Furthermore, long-term T2DM plays an important role in the dysfunction of BM-derived progenitors and multiple BM microenvironmental imbalances, such as micro- and macroangiopathy [197]. Micro- and macroangiopathy are also accompanied by neuropathy and clinically by an increase in the risk of falls, responsible for bone fracture [197].

Bone marrow adiposity

BM adiposity is highly related to T2DM. BM adipocytes have the same precursor cells as osteocytes, which indicates a competitive relationship between adipogenesis and osteoblastogenesis differentiation. Therefore, the upregulation of BM adipocytes may lead to a decrease in the number of osteoblasts [195]. In Baum et al.'s study, the magnetic resonance spectroscopy results demonstrated that L1 - L3 marrow fat content in diabetic patients was significantly higher than in nondiabetic individuals. Furthermore, in female type 2 diabetic patients, a higher HbA1c was usually accompanied by a higher BM fat level, indicating a positive correlation between T2DM and BM adiposity [100]. Clinical and biochemical background factors contribute to fat deposition in the BM, such as aging, sex, PPARs over-expression, cytokines, oxidative stress, and hormone imbalance [195, 196, 198]. Within T2DM, BM adipocyte abundance is attributed to two mechanisms: firstly, increasing pre-existing fat cell size, e.g., adipocyte hypertrophy; secondly, BM adipocyte hyperplasia due to enhanced differentiation from progenitor cells [198]. Moreover, human BM adipocyte accumulation was negatively correlated with microvascular density in patients with diabetes, suggesting that BM adiposity may increase the risk of microangiopathy [199].

Aging

Aging is also associated with T2DM-induced bone fragility. In senescent BM-adipocytes from T2DM individuals, the expression levels of adipogenesis differentiation markers PPAR γ , fatty acid-binding protein 4 (FABP4) and CCAAT/enhancer binding protein α (C/EBP α) increased [198, 200]. This finding demonstrates the differentiation bias in T2DM-induced marrow fat accumulation and bone loss. As a crucial adipose tissue, diabetic and obese BM shows apparent senescence compared with nondiabetic [56, 201, 202]. Senescent cells express a higher level of senescence-associated secretory phenotype (SASP), including pro-inflammatory factors, chemokines, and matrix remodelling proteins [203]. SASP factors positively correlate with matrix metalloproteinases (MMPs) in senescent BM of T2DM [198, 202]. Moreover, T2DM, especially combined with obesity, has the propensity to lead to the senescence of osteocytes to cause bone fragility [204]. Consequently, cellular senescence affects bone health in T2DM by activating BM adiposity and inducing the aging of osteocytes.

1.1.8. Therapy of type 2 diabetes mellitus

Therapy approaches usually focus on (1) prevention and delay of T2DM, (2) non-pharmacological therapy, (3) pharmacological therapy [205, 206].

1.1.8.1. Precaution and Non-pharmacological therapy

Precautionary measures at an early stage for people under high risk effectively delay or prevent diabetes. Lifestyle interventions, such as calorie-restricted diets and physical exercises, help reduce body weight. They may be combined with drug therapies, including metformin, pioglitazone, and liraglutide [205].

Clinical evidence demonstrates that physical exercise is an essential non-pharmacological approach to promote body weight loss and improve HbA1c, thereby reducing the risk of obesity [207]. In addition, a balanced diet and avoidance of smoking and alcohol intake are essential lifestyle modifications, improving the efficacy of insulin, ameliorating mitochondrial function, reducing the production of radicals, and ultimately enhancing the quality of life of T2DM patients [208, 209].

1.1.8.2. Pharmacotherapy

Glycaemic management is a crucial target of all therapies. The consensus guidelines suggest that the target HbA1c $\leq 7\%$ is necessary to achieve strong endpoints such as survival (From the American Diabetes Association and the European Association for the Study of Diabetes) [205, 210]. The application of glucose-lowering drugs in clinical is targeted for glycaemic management and should have fewer side effects. Metformin is the first-line drug for glucose control in T2DM [211]. This treatment strategy is due to low cost, convenient administration, weight stability, and overall clinical experiences [212]. Sodium-glucose cotransporter 2 (SGLT2) inhibitors and GLP1 receptor agonists are crucial for the initial and combination of T2DM therapy to reduce the risks of micro- and macrovascular disease and renal disease [211, 213]. In addition, there are many other agents for clinical application (**Table1-1**), including sulfonylureas, thiazolidinediones,

DPP4 inhibitors, glimepiride, sitagliptin, liraglutide, basal insulin glargine and insulin therapy [205].

Types	Medications	Primary mechanism of action	Advantages	Common side-effects or disadvantages
Biguanide	Metformin	Decrease hepatic glucose production and output, insulin sensitiser	Long-term safety and efficacy data, no hypoglycaemia, weight neutral or loss, low cost, and can be combined safely with most other glucose-lowering therapies	Gastrointestinal symptoms, lactic acidosis (rare), and vitamin B12 deficiency
Sulfonylurea	Glibenclamide (also known as glyburide), glipizide, gliclazide, and glimepiride	Stimulate the release of insulin from β cells of pancreas (insulin secretagogues)	Extensive experience, widely available, low cost, and effective glucose-lowering properties	Risk of hypoglycaemia, weight gain, and no cardiovascular benefits
Thiazolidinedione (PPAR γ agonist)	Pioglitazone, lobeglitazone, and rosiglitazone	Insulin sensitiser	No hypoglycaemia, low cost, widely available, and effective in fatty liver disease	Weight gain, fluid retention, heart failure, and increased risk of fractures
Meglitinide	Repaglinide, nateglinide, and mitiglinide	Short-acting insulin secretagogues	Shorter duration of action, less hypoglycaemia than sulfonylureas, and flexible dosing	Hypoglycaemia and weight gain
α -glucosidase inhibitor	Acarbose, voglibose, and miglitol	Delays digestion and absorption of glucose from the gastrointestinal tract	Low hypoglycaemia, decrease the post-prandial rise in blood glucose, low cost, and cardiovascular safety	Gastrointestinal side-effects like diarrhoea and flatulence
DPP4 inhibitor (gliptin)	Sitagliptin, vildagliptin, saxagliptin, linagliptin, alogliptin, gemigliptin,	Increase insulin secretion and decrease glucagon secretion	No hypoglycaemia, weight neutral, good tolerability, and simple dose scheduling	Angioedema, acute pancreatitis, and

	teneligliptin, anagliptin, and evogliptin			increased risk of heart failure with saxagliptin
SGLT2 inhibitor (gliflozin)	Canagliflozin, dapagliflozin, empagliflozin, ertugliflozin, ipragliflozin, and sotagliflozin	Increase urinary excretion of glucose via kidneys.	No hypoglycaemia, weight reduction, heart failure benefits, CKD benefits including albuminuria, reduce blood pressure and decrease major adverse cardiovascular events in cardiovascular outcome trials.	Genital tract infection, risk of dehydration, euglycaemic ketoacidosis, Fournier's gangrene, and fracture and amputation (canagliflozin in CANVAS trial)
GLP1 receptor agonist	Exenatide, lixisenatide, albiglutide, liraglutide, semaglutide, dulaglutide, efpeglenatide, and tirzepatide	Increase insulin secretion and reduce glucagon secretion, reduce gastric emptying, and promote satiety mainly by binding to receptors in the hypothalamus and hindbrain	No hypoglycaemia, weight reduction, and cardiovascular benefits (except lixisenatide)	Gastrointestinal side-effects, acute pancreatitis, and contraindicated if medullary carcinoma of the thyroid
Fixed-dose combination of GLP1 receptor agonist and long-acting insulin	Lixisenatide plus insulin glargine, liraglutide plus insulin degludec	Combined benefit of GLP1 receptor agonist and basal insulin therapy	Less weight gain than insulin therapy alone	High cost, less flexibility in dosing, and risk of hypoglycaemia

Table 1-1 Pharmacotherapy of glycaemic control of T2DM.

Abbreviations: CKD = chronic kidney disease, DPP4 = dipeptidyl peptidase-4, GLP1 = glucagon-like peptide-1, PPAR γ = peroxisome proliferator-activated receptor- γ , SGLT2 = sodium-glucose cotransporter-2. Table source: Ahmad, E., et al., Type 2 diabetes. *Lancet*, 2022. 400(10365): p. 1803-1820.

1.1.8.3. Insulin therapy

Insulin therapy is an essential approach in the glycaemic management of T2DM. The insulin treatment regulates blood glucose levels dose-dependently and is easy to approach to any glycaemic target. However, compared with other glucose control agents, the disadvantages of insulin therapy are increasing body weight, increasing risks of hypoglycaemia, and the requirement for frequent glucose monitoring. GLP1 receptor agonists can be applied together with insulin to compensate for the shortage of insulin treatment, reducing the risk of hypoglycaemia and body-weight gain [205].

1.1.8.4. Obesity management

Obesity management is another vital approach for T2DM treatment. Since obesity is closely associated with T2DM and its complications, drugs target pathways common to T2DM and obesity have been found to efficiently improve T2DM and obesity. For instance, in Davies et al.'s study, treatment with Semaglutide 2.4 mg once weekly reduced body weight in type 2 diabetic, obese adults [214]. Furthermore, Roux-en-Y gastric bypass surgery to vertical sleeve gastrectomy improves metabolic function and reduces body weight in some diabetic and obese patients [205, 215].

In summary, the clinical treatment of T2DM is complex and individually variable but usually follows these four steps [208]:

- Step 1: Non-drug therapy: lifestyle modifications, physical exercise, dietary therapy.
- Step 2: Non-drug therapy and drug monotherapy.
- Step 3: Insulin therapy only or combined with one medication.
- Step 4: Intensified insulin and drug combination therapy.

1.1.9. *In vitro* & *in vivo* models of type 2 diabetes mellitus

1.1.9.1. *In vitro* insulin resistance models

Insulin resistance is a pivotal property of T2DM, which is related to obesity and metabolic disorders [216]. In individuals with T2DM, insulin resistance usually occurs in the insulin-sensitive tissues: the liver, adipose tissue, and skeletal muscle [217].

The pathogenesis of insulin resistance is highly associated with three main mechanisms:

1. FFA overaccumulation-induced liver glucose production and reduced glucose uptake [217].
2. Mitochondrial dysfunction and upregulation of ROS level [218].
3. PI3K/AKT signalling pathway dysfunction affected insulin metabolism [218].

Palmitic acid, high glucose, and chronic insulin exposure are the main factors widely used to induce insulin resistance *in vitro*.

Palmitic acid-induced in vitro insulin resistance.

Palmitic acid is one of the most popular agents for inducing insulin resistance *in vitro*. In Garg's study, the hepatocytes (HepG2 cells) were stimulated with 0.3 mM Palmitate for 48 hours to mimic insulin resistance [219]. In addition, after exposing to 0.75 mM Palmitate for 18 hours, HepG2 cells showed insulin resistance characteristics: decreased AKT phosphorylation and glycogen synthesis, accompanied by upregulation of glucose-6-phosphatase expression [220]. C2C12 myoblast is another cell line sensitive to palmitic acid stimulation. The C2C12 cells demonstrated insulin resistance after incubating with 0.75 mM palmitic acid in the medium without FFA for 16 hours or 0.25 mM palmitic acid for 24 hours. Within insulin resistance, C2C12 cells showed less glucose uptake, together with p-AKT, GLUT4, and GLUT2 decrease [221, 222].

High glucose-induced in vitro insulin resistance

High glucose is another crucial factor in setting up insulin resistance *in vitro*. High glucose, also known as glucose toxicity, can induce cellular damage [223]. Luo et al. found that the C2C12 cells exposed to 60 mM glucose for five days showed less

myogenesis, had lower expression levels of GLUT4 and glucose uptake and inhibited AKT activation [223]. In addition, high glucose (30 mM) or glucosamine (10 mM) stimulation could induce insulin resistance in human umbilical vein endothelial cells (HUVECs) after 72 hours of incubation by downregulating p-AKT activity [224]. Hyperglycemia-caused glucose toxicity harms many cell types, which can induce oxidative stress and ROS accumulation and accelerate the progression of insulin resistance [225].

Chronic insulin exposure-induced in vitro insulin resistance.

Continuously insulin induction can also lead to cellular insulin resistance *in vitro*. Insulin resistance subjects with normal β cell function can secrete more insulin to compensate for the blunted insulin response, but increased insulin circulation can aggravate insulin resistance. This phenomenon explained why diabetic patients receiving pulsatile insulin therapy had better glucose control than those receiving successive insulin treatment [217, 226]. Krako et al. used C2C12 myoblasts and Huh7 hepatocytes to mimic insulin resistance. These two cell types were incubated with 60 nM insulin for 24 hours, followed by acute insulin stimulation (120 nM, 15 minutes) to activate insulin-related pathways [218].

Other factors-induced insulin resistance in vitro

In addition to the above factors, *in vitro* insulin resistance model can be induced by glucocorticoid dexamethasone, TNF- α , and hydrogen peroxide (H₂O₂). The 3T3-L1 cells were treated with dexamethasone (20 nM) for eight days or recombinant mouse TNF- α (4 ng/ml) for four days to induce insulin resistance in 3T3-L1 adipocytes. The 3T3-L1 cells showed common features of insulin resistance: lower glucose uptake and significantly increased ROS level [227]. Furthermore, Tan et al. successfully mimicked insulin resistance on HL-1 adult cardiomyocytes by incubating with 100 μ M H₂O₂ for 16 hours [228].

1.1.9.2. *In vivo* animal models of T2DM

Although *in vitro* models can mimic some characteristics of insulin resistance, it is still challenging to substitute for the role of *in vivo* T2DM models. In-vivo models are

essential in studying the complicated pathogenesis of T2DM and helpful in identifying the targets for treatment. Mice and rats are the two most common models used in T2DM studies, as mice show similar genetic homology [229], and rats are extensively applied to understand the metabolic property and pathology at different stages of T2DM [230]. The typical feature of T2DM is insulin resistance, which cannot be adequately compensated by β cells [231]. T2DM animal models are generally induced by obesity since the high association between T2DM and obesity [231, 232]. The classical T2DM animal models are outlined below.

Genetically T2DM models

The most common monogenic T2DM models are the defective leptin model, $Lep^{ob/ob}$ (Ob/Ob) mouse, and leptin receptor-deficient model, BKS.Cg- $+Lepr^{db}/+Lepr^{db}$ /OlaHsd (Db/Db) mouse and ZDF rat [231].

Ob/Ob mouse model

The Ob/Ob mouse is a monogenic homozygous for leptin mutation, a phenotype based on a C57BL/6 background, first discovered by Jackson Laboratory in 1949. However, until 1994 the mutated protein was identified as leptin [233]. The Ob/Ob mouse shows the following characteristics: developing obesity, glucose intolerance, insulin resistance, hyperphagia, and transient hyperglycemia [231].

Db/Db mouse model

Unlike the Ob/Ob mouse, the Db/Db mouse is a monogenic spontaneous mutation in the leptin receptor. It was first reported by Hummel et al. in 1966 from Jackson Laboratory [234]. Like Ob/Ob mouse, the Db/Db model shows typical T2DM features: insulin resistance, hyperinsulinemic, hyperglycemic, and obesity. Furthermore, the Db/Db mouse is a robust T2DM model with progressing pancreatic islet damage, leading to its short lifespan, usually around ten months [235, 236].

ZDF rat model

The ZDF rat is a T2DM model that reflects for human diabetic form. This genetic model originated from Zucker rats in Walter Shaw's Laboratory [230, 237]. The ZDF rat model

shows obesity, insulin resistance, and glucose-intolerant characteristics and is usually used as a pancreatic exhaustion model to mimic the late stage of human diabetes. The male ZDF rat model has severe hyperglycemia compared with the female ZDF model [230, 235, 237].

High-fat diet-induced T2DM models

High-fat diet-induced *in vivo* T2DM model is another widely used obese-related diabetic model. Surwit et al. first reported high-fat diet-induced T2DM on C57BL/6 mice in 1988 [238]. High-fat diet leads to obesity, hyperinsulinaemia, and hyperglycemia [239]. Since most obese T2DM is induced by environmental manipulation rather than gene, the high-fat diet model is more accurate in mimicking human diabetic conditions than genetic models [231]. However, the high-fat diet models can vary according to the duration of the high-fat diet, the mouse strains, the sex and age of the mice, and diet compositions [229]. For instance, the earliest high-fat diet effects were observed on Day 3, which showed an increase in β cell proliferation. However, glucose and insulin tolerance and hyperinsulinemia only showed after 11 weeks of diet [240]. The MRL mice that received a high-fat diet showed a two to three weeks adaptation phase that became mild hyperglycemic and recovered after seven weeks, while high-fat diet-fed C57BL/6 mice did not have this early adaptation property [229]. Furthermore, male mice were easier to get hyperglycemia with the induction of a high-fat diet [241].

Other T2DM in-vivo models

In addition to monogenic obese T2DM and high-fat diet-induced models, other T2DM rodent models are also applied for diabetes studies. KK mouse [242] and the Otsuka Long-Evans Tokushima Fat rat are polygenic models of obesity and hyperglycaemia [231]. The New Zealand obese mouse is another polygenic model of obesity and hypertrophic, which shows impaired glucose tolerance [243]. The TallyHo mouse model is a polygenic, non-insulin-dependent T2DM and obese model. However, the characteristics of the TallyHo mouse are distinct to sex: only male mouse develops hyperglycaemia between ten to fourteen weeks old; the female mouse keeps normal blood glucose and does not become diabetic; both sex of mice display medium obesity [244, 245].

1.2. Bone marrow

1.2.1. Structure of bone marrow

BM locates in the spongy central medullary cavities of long and axial bones [246]. It is one of the largest organs in the body, taking around 3% of body weight in rats and 5% in humans [246]. The BM is the principal haematopoiesis organ, which produces red blood cells, platelets, and granulocytes [247]. It is constituted of hematopoietic cells, adipocytes, and SCs. Based on the ratio of hematopoietic cells and adipocytes and the function of marrow, there are two types of BM: red and yellow marrow.

In a normal adult, the red marrow comprises 50% fat. In comparison, the fat in yellow marrow takes approximately 80%, and the prevalence of fat in both red and yellow marrow is elevated alongside aging [247, 248]. However, the haematopoietically active red BM progressively regresses from newborn to late adolescence, which is the reverse of the haematopoietically inactive yellow marrow. Moreover, the fatty replacement in red marrow is related to age and shows reconversion capacity in response to an upregulated demand for blood cells [247, 248].

The blood supply in BM is mainly based on an endosteal network of vessels. By passing through the nutrient canal, the nutrient artery divides into ascending and descending medullary or central arteries via radial branches and penetrates to the inner face of the cortex. Then the arterioles reduced calibre to match the size of the capillary, and then anastomose with venous sinuses. The blood from the venous sinuses is mixed in the cortical capillary system back to the central sinus and is drained via an emissary vein (**Figure 1-8**) [246, 247, 249].

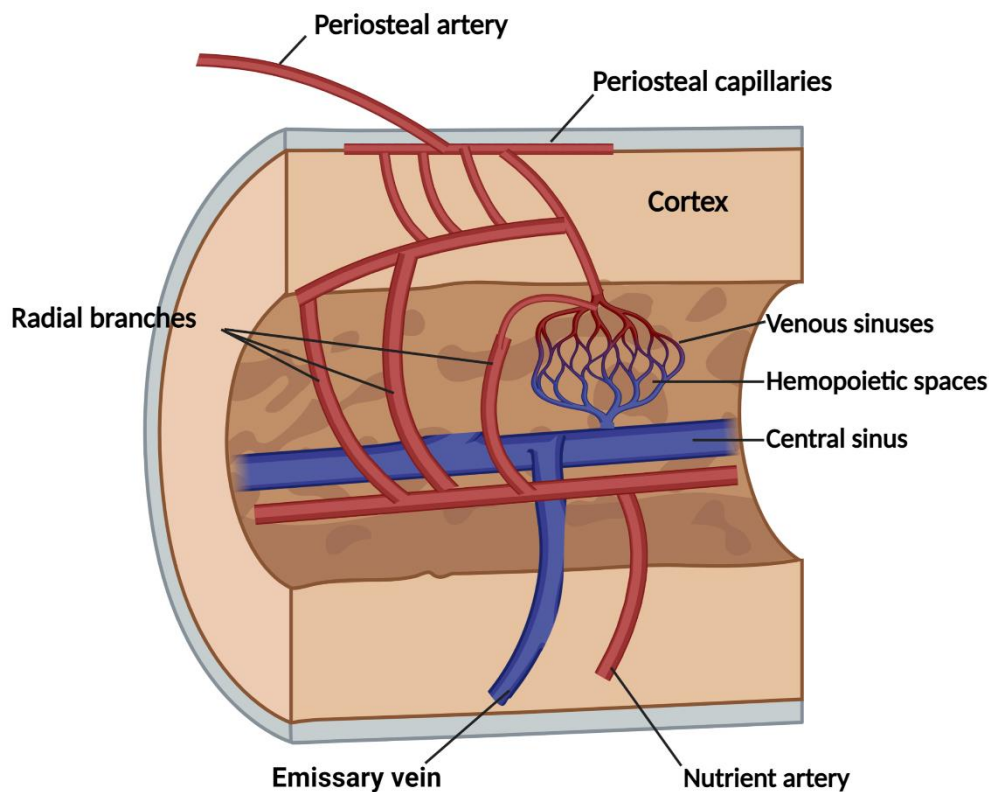


Figure 1-8 Scheme of bone marrow vascular system.

Although the hematopoietic stem cell (HSC) is an essential cell type in the BM, the composition of BM is complex. The BM-derived hematopoietic and non-hematopoietic cells are generally interlaced with the vascular and sympathetic nervous systems [247]. The BM niche supports HSC maintenance and function [250, 251]. The cell populations that contribute to the niche are varied, including both hematopoietic and non-hematopoietic cells, such as mesenchymal stromal cells (MSCs), osteoblasts, osteoclasts, adipocytes, macrophages, T lymphocytes, neutrophils, endothelial cells, pericytes, Schwann cells, nerve cells and Megakaryocytes (**Figure 1-9**) [251-253].

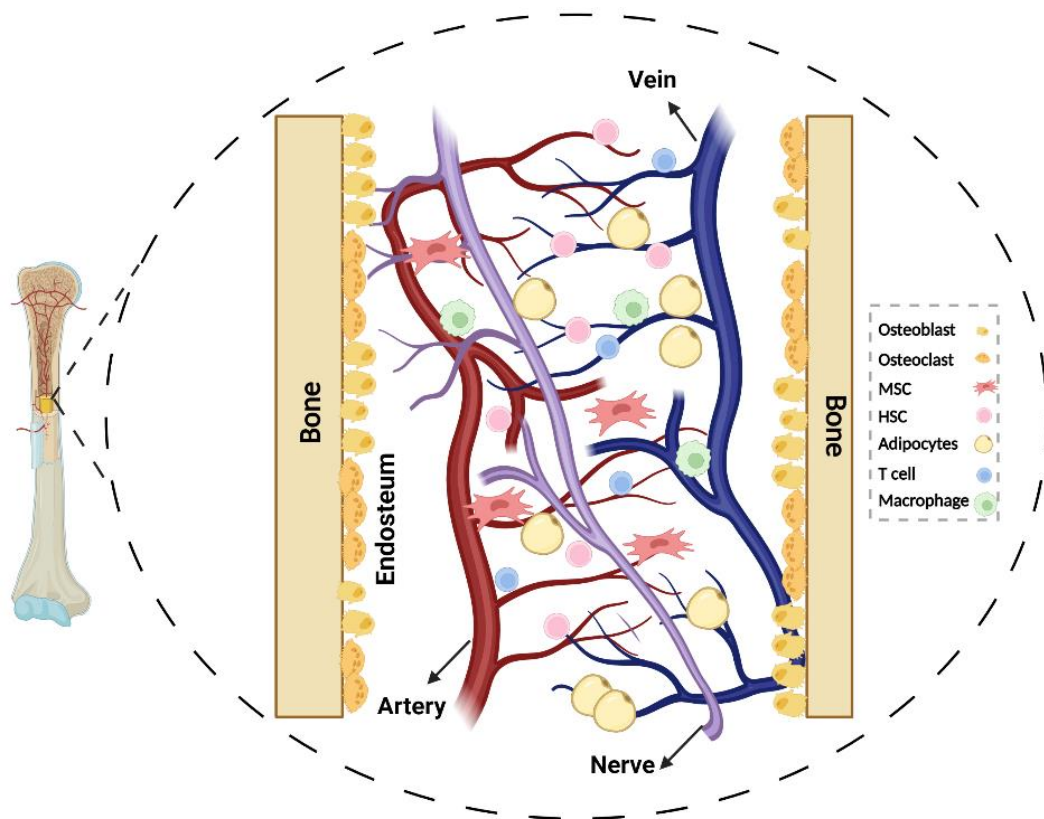


Figure 1-9 Bone marrow architecture and cell types in niches.

Abbreviations: MSC = mesenchymal stromal cell; HSC = hematopoietic stem cell.

For instance, MSCs are cells with self-renewal and multipotent abilities, which contribute to tissue repair and generate progeny cells, such as chondrocytes, osteoblasts, adipocytes, and fibroblasts [254]. The BM-derived adipocyte is a negative regulator of haematopoiesis [255]. In particular, the number of adipocytes increases as the individual ages, whereas the number and activity of HSCs decrease [256, 257]. In addition, endothelial and perivascular cells, and neuronal and glial cells maintain the BM vascular niche's stability [257-259].

1.2.2. Function of bone marrow

BM is essential in hematopoietic homeostasis and is associated with the nervous system and immunity [260, 261]. It is one of the most crucial organs for generating all the blood cell populations [260].

Haematopoiesis

The BM-derived HSC is vital in keeping BM homeostasis and blood cells productive. The regulation of HSCs maintenance, self-renewal, and differentiation depends on the BM niche [262]. Unlike general cells, the mitosis of HSCs is asymmetry, which means one HSC can be divided into two non-identical daughter cells, one remaining the features of a stem cell, the other turning into a differentiated cell [262]. The adult HSCs may be quiescent for a while. However, they can be directly reactivated to respond to the stress and injury or released to the circulation, recalling into haematopoiesis, migrating to the target tissues, such as the liver and spleen, and participating in the repair, and finally returning to the BM niches and quiescent again [262-264].

Nervous system and immunity

In BM, neuronal regulation is also essential in haematopoiesis and immunomodulation. Autonomic nerves are found in bone and widely distributed in BM [261]. The sympathetic nerve fibres and other neural crests are crucial for maintaining HSC function and regulating cell niche homeostasis, regeneration, and inflammatory response [265]. As described before (**Figure 1-9**), many immune cells are also shown in the niche. The sympathetic nervous system enhances the immune reaction to clear pathogens and adjusts the immune response to stop inflammation [266]. Moreover, the parasympathetic nervous system also participates in immune responses and is sensitive to inflammation [261].

BM is crucial in mediating haematopoiesis, immune response, and the nervous system. Since the BM niche is the main pool of HSC, which has the differentiation ability to all blood cell lineages, BM-derived cells are essential to keep homeostasis in heart tissue, and the dysfunction of these cells is also associated with various cardiac disease progression [267]. Moreover, the role of BM in interaction with the immune system and regulating inflammation is also remarkable, indicating that it contributes to diabetic cardiomyopathy, adiposopathy, and other types of metabolic disorders [267-269].

1.2.3. Bone marrow cells

The BM contains various types of cells, including haematopoiesis cells, their multipotent progenitor cells (MPP), and differentiated progeny cells, such as NK cells, T cells, B cells, macrophages, osteoclasts, megakaryocytes, neutrophils, and red blood cells. Furthermore, MSCs and their subpopulation PCs also reside in the BM, which arises the majority of SC lineages in BM, including chondrocytes, osteoblast, fibroblasts, adipocytes, myocytes, and endothelial cells (**Figure1-10**) [270].

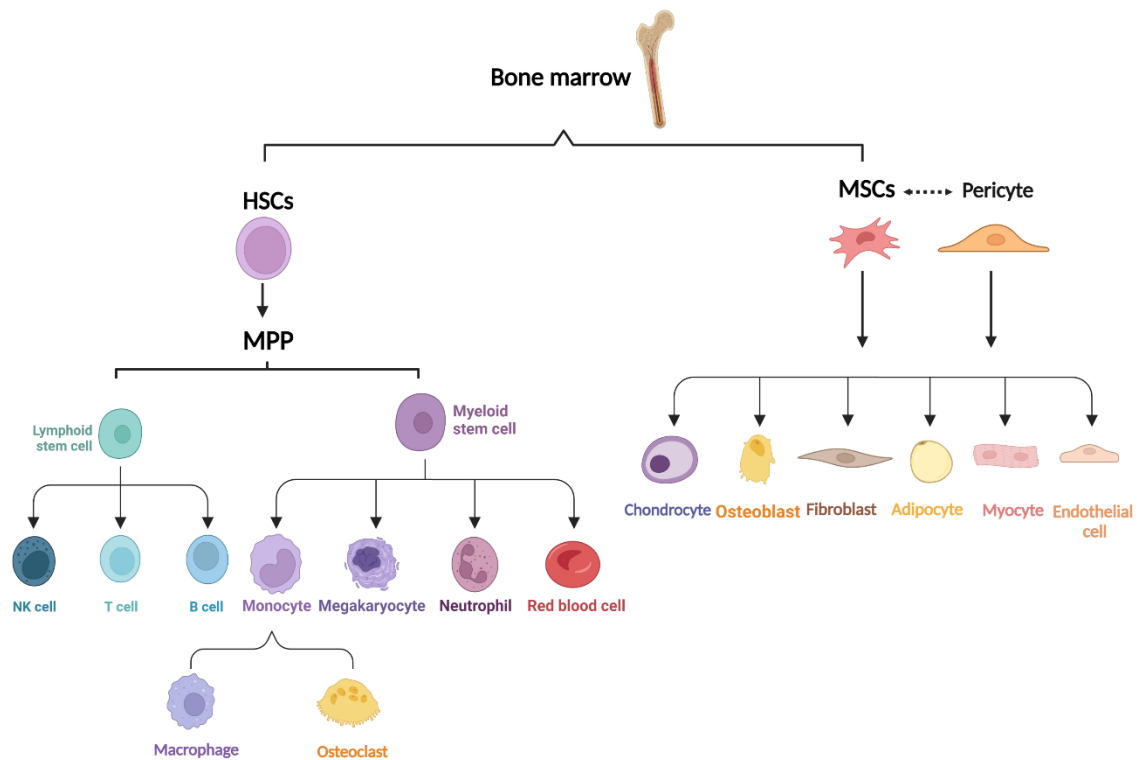


Figure 1-10 Human bone marrow haematopoiesis cells and stromal cells.

Abbreviations: HSCs = hematopoietic stem cells; MPP = multipotent progenitor stem cell; MSCs = mesenchymal stromal cells.

1.2.3.1. Bone marrow hematopoietic stem cells

Source of HSCs

BM-derived HSCs have been widely studied in the past. HSC produces all mature blood cells and keeps the haematopoiesis balance in vertebrates [259]. The concept of HSC was first posted by Ernst Neumann, who pointed out that a cell type might exist that was the progenitor of all blood cells [271].

Characteristics of HSCs

HSCs are located in a unique microenvironment in the BM niche, which plays a crucial role in maintaining the properties of HSC, such as multilineage repopulation capacity, self-renewal, quiescence, differentiation, and apoptosis [258]. HSCs are primarily found in hypoxic regions in BM, such as the endosteal area [272]. HSCs within this low cellular level of ROS environment demonstrate higher self-renewal propensity [273]. For example, the shortage of hypoxia-inducible factor-1 alpha (HIF-1 α) may induce dysfunction of HSC; reversely, stabilization of HIF-1 α could improve the repopulation activity and quiescence of HSCs [274, 275].

The markers or proteins that are used to identify HSCs and their subpopulations are multiple, such as stem cells antigen-1 (Sca-1, a murine cell membrane glycoprotein) [276], c-Kit (a tyrosine kinase receptor, also named as cluster of differentiation 117 (CD117)), and negative for several lineage markers (e.g., Gr-1, Ter119, CD4, and CD8) [277]. Furthermore, CD34 and CD41 are usually expressed at the early stage of embryonic HSCs, while CD45 and CD150 are generally expressed in mature HSCs [278].

1.2.3.2. Bone marrow mesenchymal stromal cells

Source of MSCs

MSCs were first found in BM by Friedenstein et al. and identified as fibroblast colony-forming units [279]. The source of MSCs varies, and MSCs not only remain in the BM, but are also found and isolated from other tissues, such as adipose tissue, vascular wall, synovium, lung, liver, skeletal muscle, umbilical cord, amniotic fluid, and foetal blood [280-282]. Furthermore, BM-derived MSCs are abundant in many species, including humans, rats, mice, canine, and ovine [280].

Characteristics of BM-MSCs

The International Society for Cellular Therapy terms the criteria characteristics of most MSCs from the following aspects: (1) in-vitro plastic-adherent capacity within standard culture conditions (alpha minimum essential medium (α MEM) supplementary with 20% fetal bovine serum (FBS)), (2) expression of CD105, CD73, and CD90, and lack of CD45,

CD14 or CD11b, CD34, CD79 α or CD19, and HLA-DR, (3) multiple *in vitro* differentiation potential (e.g., differentiation into chondrocytes, osteoblasts, and adipocytes) [283]. However, this is a basic standard to identify the MSCs, the phenotype of BM-derived MSCs is more complicated, which can be different *in vivo* and *in vitro* culture or due to the different distributions of MSCs in BM [284, 285].

BM-derived MSCs are in endosteal, stromal, and perivascular around perivascular niches [284, 286]. The endosteal-located BM-MSCs are linked to osteoblasts and HSCs, and vascular-located BM-MSCs show similar phenotypic features with both PCs and MSCs expressing Nestin and CD146 [284]. Among the BM-MSCs subpopulations, CD146^{pos}CD45^{neg} cells are enriched, demonstrating a high multipotent differentiation capability and self-renewal ability, and participating in osteogenesis [287].

In addition to meeting the standard phenotypic features of MSCs, different species show other surface markers, such as human BM-MSCs express CD271, CD146, CD49f, GD2, Stro-1 and some of them express NG2 [288, 289]; rat BM-MSCs express CD29, CD44, CD54, CD90, and CD166 [290, 291], and mouse BM-MSCs highly express CD29, CD9, CD24, Sca-1, CD44 and some of them also express CD73 and CD71 [292] (**Table 1-2**).

Species	Positive markers	Negative markers	References
Human	CD13, CD29, CD44, CD73 (SH3/SH4), CD90 (Thy-1), CD105 (SH2, endoglin), Stro-1, CD271, MSCA-1, CD146	CD235a, CD45, CD11b, CD14, CD79, HLA-DR, CD19, CD34	[293], [281], [288, 289]
Mouse	CD9, CD24, CD29, CD44, CD47, CD49e, CD81, CD98, CD106, CD147, Sca-1, CD71, CD73, CD51, CD140a, SSEA-4	CD45, CD11b, CD31, Vcam-1, CD34, C-Kit, CD135	[292], [294]
Rat	CD29, CD44, CD54, CD90, CD105, VLA-4, CD166, CD73, CD79, CD50	CD45, CD34, CD31, CD71	[290], [291], [295], [296],

Table 1-2 Positive and negative BM-MSCs' markers in different species.

Function and clinical application of BM-MSCs

BM-MSCs are crucial for maintaining haematopoiesis, which contributes to establishing perivascular niches and supporting the proliferation and differentiation of hematopoietic cells *in vitro* [281]. In addition, BM-MSCs can mediate the hematopoietic microenvironment by producing cytokines, growth factors, leukemia inhibitory factor, TNF- α , and stem cell factor [255, 280, 281]. Furthermore, BM-MSCs play essential roles in keeping the structure of bone by its self-renewal and osteogenesis capacity [280].

Since BM-MSCs can secrete many pro-inflammatory and anti-inflammatory cytokines and growth factors and have self-renewal and multipotency capacities, they are now considered for regenerative therapies to treat autoimmune, inflammatory, and vascular diseases [297].

1.2.3.3. Bone marrow pericytes

Source of pericytes

The PC was first described and named by Benjamin Rouget. It was identified enwrapping vessel wall [298] and formally called “pericyte” by Zimmerman in 1923 [299]. The precursor of PCs is still controversial. BM-derived PCs have some MSC activity and distinct types of PCs distributed around two different vessels: arterioles and sinusoids [300]. In the subpopulations of BM-derived MSCs, some populations (i.e., C-X-C motif chemokine ligand 12 (CXCL-12)⁺-Leptin receptor (LepR)⁺CD146⁺ (CAR) cells) [301] show the same characteristic of PCs, such as perivascular position, positivity for typical PC markers: NG2, platelet-derived growth factor receptor beta (PDGFR β), CD146 and negativity for CD45 [299]. In BM, about 10% of PCs around arterioles express NG2 antigen but no LepR, whereas 90% of PCs associated with sinusoids are positive for LepR but negative for NG2. Both arterioles and sinusoids PCs are crucial for maintaining the quiescence of HSC [300].

Characteristics and function of BM-PCs

The human BM-PCs (hBM-PCs) are reported to express adhesion molecule CD146 and they are positive for α -smooth muscle actin (α SMA), NG2, PDGFR β , but negative for the haematopoietic (CD34 and CD45) and endothelial (CD31) markers [302]. Like MSCs, PCs also have the multipotent ability for adipogenic, osteogenic, and myogenic lineages [288]. PCs are essential for tissue restoration, and several regenerative preclinical studies are using PCs [299, 303]. PCs can detach from the endothelium, move along the microvessels and target the injury sites [304]. Moreover, this PC flexibility allows them to respond to proinflammation quickly, identifying tissue trauma signals and participating in immune responses by cell-crosstalk and paracrine activity [299, 305, 306]. In addition to their regeneration and immune-modulating functions, PCs form the blood-brain barrier together with endothelial cells [307], modulate vascular permeability and vascular tone, and play roles in angiogenesis [299].

BM pericytes in pathological conditions

BM-PCs are reported to be dysfunctional in many pathological conditions. In the leukaemia model, two independent groups reported that leukaemia cells promoted BM-PCs to differentiate into osteolineages, resulting in altered normal HSCs that induced suppression of haematopoiesis [308, 309]. Leukaemia impairs nerves, changes the BM microenvironment to support tumour growth, and results in PC apoptosis [310]. In addition to leukaemia, Mangialardi et al. reported BM-PCs dysfunction in diabetic conditions. T2DM decreases the primary function of BM-PCs, such as reducing their proliferation, viability, and migration abilities, causing less support for *in vitro* angiogenesis, and reducing cellular apoptosis [302].

1.2.3.4. Bone marrow adipocytes

BM adipocyte is another essential cell type in maintaining BM stability and function. Distinct from WAT and BAT, BMAT participates in energy metabolism and endocrine and contributes to haematopoiesis and bone remodelling [311, 312]. The content of BMAT is continually changed alongside age, disease, and sex [313].

Characteristics of BM adipocytes

Although the specific markers of BMAT are still unclear, it has been documented highly expression of BAT makers, such as PR domain zinc finger protein 16, PPAR γ coactivator (PGC)-1 α , type 2 iodothyronine deiodinase, and low expression of WAT markers (i.e., leptin and adiponectin), whereas these characteristics can be altered along with aging and T2DM [311].

The structure characteristics of BM adipocytes generally show a single lipid droplet within the cytoplasm and a single nucleus enveloped by a lipid membrane. However, some BM adipocytes demonstrate beige adipocyte properties: multiple lipid droplets in the cytoplasm and middle expression of the *UCP1* gene (the characteristics details of beige adipocytes can be found in **section 1.1.7.1.1**) [314]. BM adipocytes are considered to share the same progenitors with osteogenic, which are differentiated from MSCs [315]. Many studies have approved this conclusion. For instance, Ambrosi et al. found that the CD45^{neg}CD31^{neg}Sca-1^{pos} MSC population showed high adipogenesis but limited osteogenesis potency. The CD45^{neg}CD31^{neg}Sca-1^{pos}CD24^{neg} subpopulation could differentiate into adipocytes, osteoblasts, and chondrocytes [98]. Moreover, BM adipocytes also express PCs and perivascular antigens CD146 and 3G5 [311].

BM adipocytes in pathological conditions

BM adipocytes participate in various pathological conditions. Aging and obesity can induce elevated ectopic adipocyte accumulation in BM [98]. BM adipocytes demonstrate endocrine function by secreting adipokines and cytokines [316]. They are crucial for mediating inflammation by regulating the levels of relative anti- or pro-inflammatory factors: IL-6, macrophage inflammatory protein-1 α , adiponectin, leptin, MCP-1, IL-1 β , TNF- α , CXCL2, CXCL1 and IL-10 [316, 317]. In addition to aging and obesity, T2DM also influences the differentiation and function of BM adipocytes. In mice diabetic models, BMAT was increased [316]. This conclusion is also identified in the human BM from T2DM individuals, the size and density of adipocytes are all elevated [200].

1.3. Senescence

1.3.1. Characteristics and mechanisms of senescence

Aging has become a root-cause contributor to many diseases, and the aging population is constantly increasing [318]. The standard definition of cellular senescence is a permanent cell cycle arrest state associated with morphology changes, secretory profile, cell death insensitivity, increased inflammation, and reduced proliferation [319-321]. Since cellular senescence markers are not specific and unique, a combination of several markers should be detected simultaneously to identify the senescent cells [319]. Cellular senescence can be considered as two types: replicative senescence and stress-induced premature senescence [322].

Replicative senescence

The characteristics of replicative cellular senescence focus on these aspects: (1) prolonged cell cycle; (2) increase the cell size; (3) cellular metabolic shifts; (4) telomere shortening or dysfunction; and (5) intracellular impairment [320].

Firstly, Hayflick et al. found that the proliferation ability of normal cells is limited, and cells will finally get into an irreversible growth arrest stage named “replicative senescence” [323]. At this stage, cells show less clonal capacity and longer cell cycle duration [324, 325].

Secondly, the senescent cells’ morphology shows an increasing size or hypertrophy. This phenomenon links to cell proliferation ability decreasing, as dividing cells must increase the mass of cells to compensate for the mass loss due to diversion. In other words, increasing cell size could induce decreasing proliferation rate and *vice versa* [326].

Thirdly, the metabolic of senescent cells highly shows lipid accumulation tendency [320, 327, 328]. Furthermore, senescent cells show mitochondrial dysfunction, including reducing oxidative phosphorylation, reduction of NAD⁺/NADH ratio, lower ATP content, and activating mammalian target of rapamycin (mTOR) [329-332].

Fourthly, telomere shortening is another critical feature of senescent cells. Within senescence, telomeres show double-strand breaks (DSBs), inducing deoxyribonucleic acid (DNA) damage response (DDR) and cell cycle arrest [333]. Finally, the senescent cells are usually found with two typical intracellular damages: DNA DSBs and lipofuscin. During replicative senescence, DSB-bearing cells increased, and the level of lipofuscin increased along with the passaging of cells [320, 334].

Stress-induced premature cellular senescence

In addition to replicative senescence, the other non-telomere shortening-induced cellular senescence is considered “stress-induced premature senescence” [322, 335]. The stress-induced premature senescence types focused on these three parts: oxidative stress-, genotoxic stress-, and oncogene-induced premature cellular senescence.

Oxidative stress-induced premature cellular senescence

Oxidative stress is one of the most common reasons that induce premature senescence. The stimulation factors include ultraviolet, H₂O₂, and hyperoxia [336-338]. With oxidative stress, ROS overexpression in cells can lead to DDR, subsequently inducing premature senescence [339, 340].

Genotoxic stress-induced premature cellular senescence

Genotoxic stress-induced premature senescence is usually caused by mitogenic oncogenes or genotoxic therapies, such as radiation and chemotherapy [322, 341, 342]. These genotoxic methods or agents can interact with DNA structure, lead to DNA repair program overload, and activate cellular fail-safe programs, for instance, apoptosis or senescence [343]. The chemotherapy drugs, such as Etoposide and Adriamycin are found to induce cellular senescence [344, 345].

Oncogene-induced premature cellular senescence

Furthermore, overexpression of oncogenes is another way to induce premature cellular senescence. Oncogenes are the mutations of normal genes that may promote cell transformation. Cells usually develop senescence to inhibit abnormal proliferation and prevent oncogenic transformation [322, 346, 347].

1.3.2. Markers of senescence

As I described before, the hallmarks of cellular senescence are not specificity and unique. Therefore, it becomes imperative to identify cellular senescence combined with different markers from different signalling pathways. The main signalling pathways as hallmarks of cellular senescence show in **Figure 1-11** [325]. Most cellular senescence can motivate the activation of cyclin-dependent kinase inhibitors during cell cycle arrest programs, such as p53/p21^{Waf1/Cip1} or p16^{INK4a}. P21^{Waf1/Cip1}, a downstream protein of the p53 signalling pathway, is crucial for inhibiting the activity of cyclin-dependent kinase and regulating cell cycle progress [348]. P16^{INK4a} is always considered a typical marker of senescence which is consistently expressed in senescent cells [349]. Meantime, p16^{INK4a} is essential to maintain the senescence state by inhibiting the phosphorylation of retinoblastoma protein (Rb) [350].

Some cytokines and chemokines are overexpressed in senescent cells, called “senescence-associated secretory phenotype (SASP)”. As a direct detection factor, senescence-associated beta-galactosidase (SA-β-gal) activity at pH = 6.0 is used to identify potential senescent cells [351]. DDR marker γH2AX demonstrates continuous and unrepaired DNA damage, which usually co-detects with cell cycle marker ki67 [352]. In addition, senescence-associated heterochromatin foci (SAHF), senescence-associated distention of satellites (SADS), and telomere-associated foci (TAF) are considered hallmarks of cellular senescence [325, 353-355].

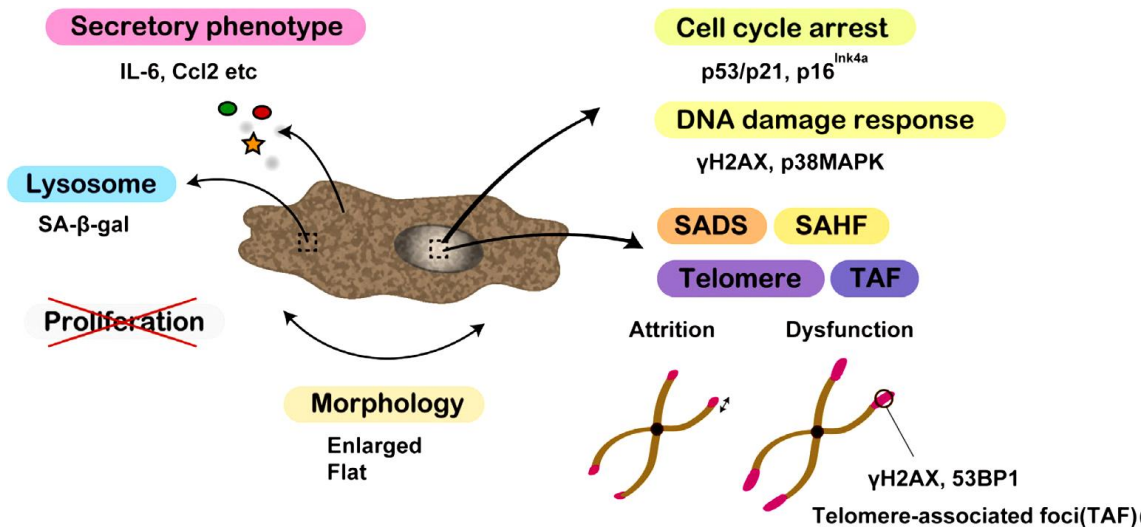


Figure 1-11 Markers of cellular senescence.

(1) Morphology changes to enlarge and flattening; (2) SASP; (3) lysosome: SA-β-gal; (4) limited proliferation; (5) cell cycle arrest; (6) DNA damage response; (7) SADS; (8) SAHF; (9) telomere and TAF. Abbreviations: SASP = senescence-associated secretory phenotype; SA-β-gal = senescence-associated beta-galactosidase; SADS = senescence-associated distention of satellites; SAHF = senescence-associated heterochromatin foci; TAF = telomere-associated foci. Figure source: Shimizu et al., Cellular senescence in cardiac diseases, Journal of Cardiology, Volume 74, Issue 4, 2019, Pages 313-319, ISSN 0914 5087.

1.3.3. Senescence and type 2 diabetes mellitus

Cellular senescence is one of the most critical factors that induce diabetes; in turn, T2DM is also found to lead to cellular senescence. Therefore, cellular senescence and T2DM are both causes and consequences of each other [356]. The potential mechanisms of senescence causing T2DM are the dysfunction of senescent pancreatic β cells, adipose tissue dysfunction, and SASP-induced tissue damage (**Figure 1-12**) [201, 356, 357]. Pancreatic β cell dysfunction is the key reason for unbalanced insulin secretion in T2DM, whereas chronic hyperglycemia and hyperlipidemia lead to β cell dysfunction [358]. Within T2DM conditions, senescent β cells accumulation is found in rodents and humans, which links to the lower proliferation ability of β cells leading to insulin secretion [356, 359-361]. High glucose in T2DM can cause premature senescence for many cells, including β cells [357]. Subsequently, the abundance of senescent β cells highly promotes the expression of SASP factors, increasing the risk of insulin resistance and inflammation [56, 362].

Furthermore, as one of the most crucial endocrine organs, adipose tissue dysfunction is related to obesity and aging associated with T2DM [356]. Increasing senescent preadipocytes leads to the decrease of adipogenic and lipogenic, causing lipodystrophy in adipose tissue to increase the potential of insulin resistance, inflammation, and oxidative stress [201, 357, 363]. Aging-related lipid overaccumulation in other peripheral tissues (e.g., BM, liver, heart, skeletal muscle, kidney, and pancreas) can lead to metabolic dysfunction, mitochondrial dysfunction, and tissue damage [216, 356, 364]. Although the causes of diabetic complications are complex, cellular senescence is highly related. Senescent cells are contributed to developing aging-related diseases, such as bone fragility, CVD, osteoporosis, and renal dysfunction [365].

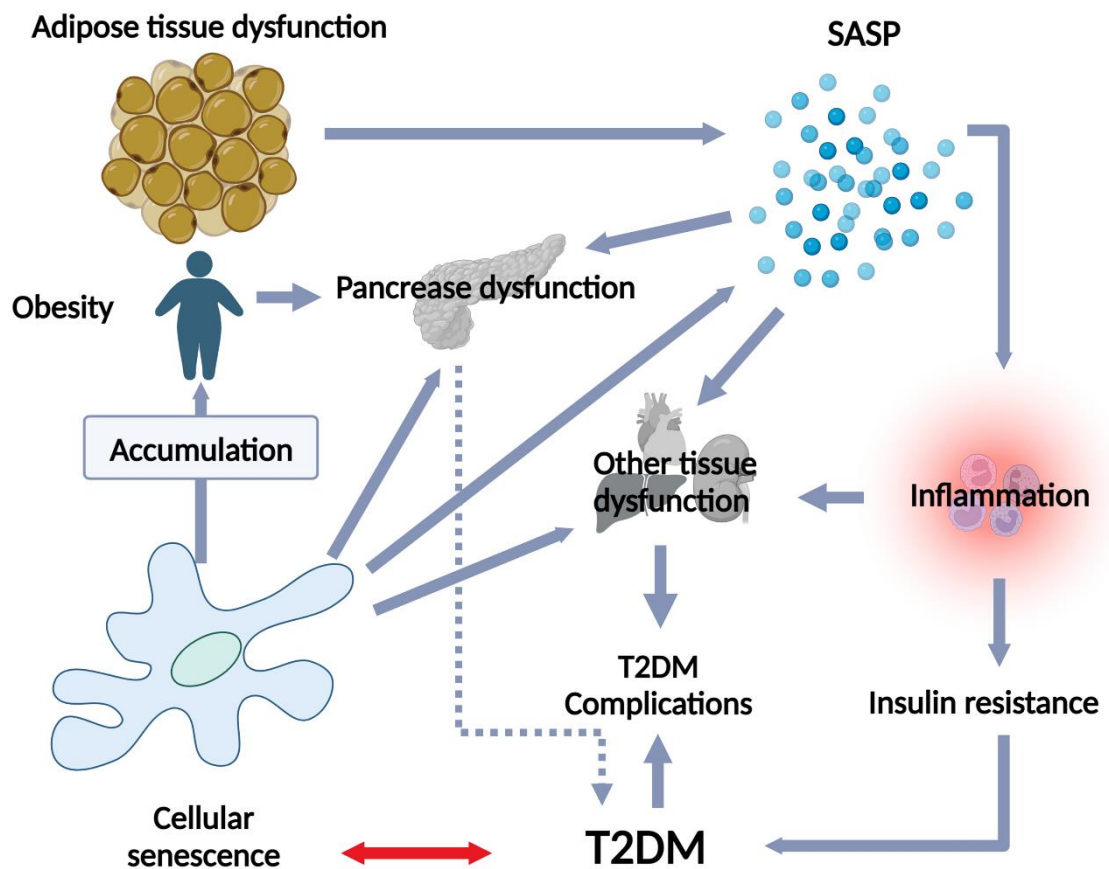


Figure 1-12 Potential mechanisms of cellular senescence and T2DM pathogenic positive feedback loops.

Cellular senescence overaccumulation can induce obesity, causing adipose tissue dysfunction, pancreas β cells, and whole tissue dysfunction, releasing SASP factors. The abundance of SASPs induces inflammation and dysfunction of other tissues and causes insulin resistance to induce T2DM and its complications. Meantime, T2DM plays an

important role in generating cellular senescence. Abbreviations: SASP = senescence-associated secretory phenotype; T2DM = type 2 diabetes mellitus.

1.3.4. Senescence and obesity

Obesity is positive correlated with cellular senescence in the adipose tissue, liver, and pancreatic β cells. Senescent cells secreted SASP factors can influence tissues' mitochondrial function and antioxidant ability. For instance, senescent hepatocytes lose oxidation capability for fatty acids, causing lipid deposition and β cell senescence, subsequently inducing insulin resistance and onset of T2DM [366]. Senescent cells accumulation in the adipose tissues can affect lipid storage and prevent adipogenesis [366]. Moreover, senescent adipose tissue leads to unbalanced adipokines expression, promoting inflammation and insulin resistance, inhibiting adipogenesis, and inducing vascular dysfunction [367, 368]. Oxidative stress [369], telomere shortening [370], growth hormone abnormal [371], mTOR activity [372], and altered microbiome [373] also have a high potential to induce senescence in obese individuals. Based on the correlation between obesity and cellular senescence, senescent cells are considered a therapeutic target for improving obesity. There are three main treatments: senolytic agents removing senescent cells, senomorphic agents suppressing the production and function of SASP factors, and physical exercise to alleviate metabolic dysfunction and reduce body weight [367, 374, 375].

1.3.5. Senescence and cardiovascular disease

Cellular senescence has been proven highly related to most CVDs. The typical hallmarks of cardiomyocyte senescence are multiple, including DNA damage and repair response, inflammation, ER stress, mitochondrial dysfunction, morphological changes, genomic instability, SASP, hypertrophic growth, and contractile dysfunction [376-379]. In senescent cardiomyocytes, overaccumulation of ROS is found in total cells and mitochondria, which leads to DNA damage and DSBs [319]. Moreover, DNA damage is found in telomere regions [377]. In cardiomyocytes, telomere-shortening is independent of senescence, and in postmitotic cardiomyocytes, senescence is regulated

by length-independent telomere damage, which promotes p21^{Waf1/Cip1} and p16^{INK4a} pathways [380].

In addition, senescent cardiomyocytes secrete SASP factors, including proinflammatory cytokines and cardiac remodelling molecules [381]. The ASK1-signalosome-p38MAPK and SAPK/JNK signalling mechanisms are reported to activate cellular senescence and aging in response to inflammation and oxidative stress in cardiomyopathies [378, 382-384]. ER stress is accumulated in senescent cardiomyocytes associated with inducing apoptosis, hypertrophic growth, and contractile dysfunction [376, 385, 386]. Mitochondrial dysfunction is one of the most crucial features of cardiomyocyte senescence [387]. The potential mechanisms of senescence-causing CVDs include unregulated nutrient and growth signalling, oxidative stress, extracellular matrix homeostasis defect, and impaired calcium handling [377]. Two therapeutic approaches: senolytics, agents that selectively remove senescent cells and senomorphics, small molecules that can inhibit SASP, are currently being explored to understand potential benefits on cardiac dysfunction by ameliorating cellular senescence [377].

1.4. Senolytic agents

1.4.1. Definition and classification

Senolytic agents are a type of drug that can selectively eliminate senescent cells. There are two classical senotherapeutics: first-generation senolytics, which are based on hypothesis-driven and mechanism-based; second-generation senolytic treatments, including traditional and other drug discovery methods (**Table 1-3**) [348, 388].

Generation of senolytics	Targets	Agents	References
1st generation senolytics (methods: hypothesis-driven, mechanism-based discovery)	Anti-apoptotic proteins	Navitoclax	[389]
		ABT-737	[348]
		A1331852	[390]
		A1155463	[390]

		Piperlongumine	[391]
	PI3K and other kinases	Dasatinib	[56]
		Quercetin	[392]
		Fisetin	[393]
		Luteolin	[394]
		Curcumin	[394]
	p53 pathway	FOXO4-DRI	[395]
	NF-κB pathway	Metformin	[396, 397]
		Rapamycin	[398, 399]
		Ruxolitinib	[400]
		Momelotinib	[400]
2nd generation senolytic treatments			
Methods			References
High-throughput compound library screens			[401]
Vaccines			[402, 403]
Toxin-loaded nanoparticles preferentially lysed by senescent cells			[404]
Immunomodulators			[405]

Table 1-3 List of first and second generations senolytic therapies.

Abbreviations: FOXO4-DRI = Forkhead box O transcription factor 4-D-retro-inverso.

1.4.1.1. First generation senolytic agents

The 1st generation senolytic drugs mostly target senescent cells, especially blocking their anti-apoptosis pathways, which protect cells from their own pro-apoptotic SASP [406]. The senolytic drugs generally target to inhibit the activity of anti-apoptotic pathways proteins (i.e., overexpression of B cell lymphoma 2 (BCL-2) protein family, p53, the phosphatidylinositol 3-kinase (PI3K)/ATK pathways and NF-κB from reducing senescent cells selectively [348].

Targeting anti-apoptotic proteins

Navitoclax (ABT263) and ABT-737 are the first small molecules that specifically remove senescent cells by inhibiting BCL-W, BCL-XL, and BCL-2 and then promote cellular

apoptosis [389, 407]. Watanabe et al. found that Navitoclax eliminated senescent mice hepatocytes *in vitro* via downregulating SASP factors and promoting mitochondrial function [408]. However, the first-generation BCL-2 family inhibitors are reported to have neutrophils and platelets toxic [409]; these side effects are solved by second-generation BCL-2 family inhibitors like A1331852 and A1155463 [348]. In the BCL-2 family, the BH4 domain is another essential anti-apoptotic target for senolytic drugs [410]. The alkaloid, Piperlongumine, is reported as a novel senolytic drug to reduce senescence by activating apoptosis without ROS stimulation [411].

Targeting PI3K and other kinases

Dasatinib, a type of tyrosine kinase inhibitor (TKI), is initially used as an anti-cancer drug (e.g., anti-chronic myelogenous leukaemia and acute lymphoblastic leukaemia) but also has selectively senolytic effects on targeting senescent adipocyte progenitors [56, 348]. Quercetin is a natural flavonoid compound with senolytic effects in adipocytes, pre-adipocytes, umbilical vein endothelial cells, and cancer cells by inducing cellular apoptosis [348, 392, 412]. The combination of Dasatinib and Quercetin is also widely applied for reducing senescence *in vitro* and *in vivo* [318, 388] and shows better overall senolytic effects [348]. The natural flavone Fisetin is another senolytic agent that can eliminate senescent cells by blocking PI3K/AKT/mTOR pathway [393, 413], suppress BCL-XL and diminish pro-inflammatory SASP factors expression [394, 414]. Moreover, Luteolin and Curcumin also performed well with Fisetin in senolytic therapy [390, 394].

Targeting p53 pathway

In addition to the BCL-2 protein family and PI3K/AKT pathway, the p53 pathway plays an essential role in cellular senescence. Forkhead box O transcription factor 4-D-retro-inverso (FOXO4-DRI), a senolytic peptide, is found to reduce senescent fibroblasts selectively [395] and can disturb the interaction between FOXO4 and p53 and resulting in excluding p53 from the nucleus [348].

Targeting NF-κB

Senolytic drugs can also directly inhibit the activation of NF-κB or its upstream mediators. Metformin is a type of classical oral glucose-lower medication used in T2DM treatment.

However, it is reported that Metformin has senolytic effects, which inhibit the SASP expression by blocking NF- κ B translocating to the nucleus [396] and stimulating autophagy to protect against cellular anti-apoptotic progress [397]. Rapamycin is a macrolide compound that reported to reduce senescent cells by suppressing SASP and NF- κ B signalling pathway and activating autophagy [398, 399]. Meantime, Ruxolitinib and Momelotinib are also found to decrease the expression level of SASP factors in senescent preadipocytes by inhibiting the JAK pathway [400].

1.4.1.2. Second generation senolytic treatments

In addition to first-generation senolytic drugs, which are identified by bioinformatics approaches, the second generation of senolytic agents are discovered by novel strategies: high-throughput compound library screens; vaccines; toxin-loaded nanoparticles preferentially lysed by senescent cells; and immunomodulators [415]. These discovery methods may accelerate the future development of senolytic therapies.

1.4.2. Dasatinib

Dasatinib is a potent, short-acting TKI. The structure of Dasatinib is N-(2-chloro-6-methyl-phenyl)-2-(6-(4-(2-hydroxyethyl)-piperazin-1-yl)-2-methylpyrimidin-4-ylamino)thiazole-5-carboxamide monohydrate (**Figure 1-13**). It is reported that Dasatinib can inhibit the activity of BCR-ABL, the SRC family, C-KIT, PDGFR α , PDGFR β , and the TEC family [416]. Dasatinib is a second generation of TKIs, generally applied in chronic myeloid leukaemia clinical treatment by targeting BCR-ABL [417]. Due to its senolytic potential by promoting apoptosis induced by dependence receptor ephrins or partly by inhibiting SRC kinase, Dasatinib has been applied as one of the senolytic drugs, especially in combination with Quercetin to reduce senescent cells abundant in adipose tissue [418, 419].

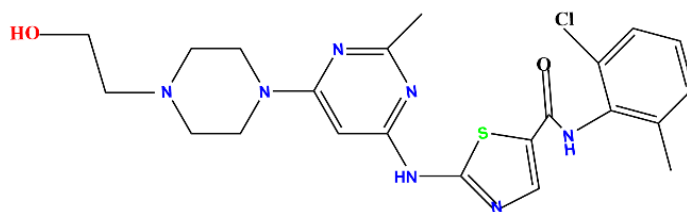


Figure 1-13 Chemical structure of Dasatinib.

The figure was created by using ChemDraw software.

1.4.2.1. Effects of Dasatinib in apoptosis and senescence

Dasatinib is found to induce apoptosis in-vitro and in-vivo. Gao et al., reported that Dasatinib caused keratinocyte apoptosis by inhibiting HMGB1-mediated mitophagy [420]. Dasatinib promotes cellular apoptotic effects via regulating multiple targets: SRC, JAK/STAT, Raf/MEK/Erk, and PI3K/AKT and caspase 9/3 and HIF-1 α [421, 422]. In the obese murine model, Dasatinib treatment reduced the expression of lipogenesis marker SREBP1, inflammation markers (e.g., iNOS), fibrosis markers (e.g., transforming growth factor β (TGF- β)), and apoptosis markers (e.g., caspase-3) [423]. In addition, Ohrodnik et al. reported that Dasatinib + Quercetin ameliorated NAFLD by eliminating p16^{INK4a}-expressing senescent hepatocytes and reducing hepatic steatosis [327].

1.4.2.2. Effects of Dasatinib in inflammation

In addition to inducing cellular apoptosis, Dasatinib is reported to downregulate inflammation. Saccon's study demonstrated that administration of Dasatinib + Quercetin on aged BALB/c mice reduced intestinal senescence and inflammation by reducing the expression of senescence markers p16^{INK4a} and p21^{Waf1/Cip1} and decreased the expression of inflammatory factors CXCL-1, IL-1 β , IL-6, MCP-1, and TNF- α [424]. Moreover, Dasatinib and Quercetin combination treatment could improve age-dependent disc degeneration in mice by eliminating p16^{INK4a}-, p19-positive senescent cells and decreasing SASP molecules IL-6 and MMP13 [425]. Both in-vitro and in-vivo studies showed that Dasatinib treatment ameliorated LPS-induced microglial and astrocytic neuroinflammation by inhibiting AKT/STAT3 pathway [426].

1.4.2.3. Effects of Dasatinib in fibrosis

Apart from activating apoptosis and inhibiting inflammation, Dasatinib also ameliorates fibrosis in some models. Li et al. found that Dasatinib + Quercetin treatment reduced renal interstitial fibrosis and downregulated the expression level of renal Fibronectin, Collagen I and α SMA, and decreased renal senescence on C57BL/6 mice chronic kidney disease post-acute kidney injury model [427]. These findings support that senolytic treatments have effects on reducing senescence and other disorders.

In summary, Dasatinib plays a crucial role in reducing senescence and their-related disorders by activating senescent cells apoptosis to eliminate senescent cells, regulating pro- and anti-inflammatory factors, and decreasing fibrosis progression.

1.4.3. Clinical trials of senolytic agents

To date, three senolytics: Dasatinib + Quercetin, Fisetin, and UBX0101, are approved for clinical trials by the United States Food and Drug Administration (FDA) [318]. Unfortunately, the trial results of UBX0101 on treating osteoarthritis are disappointing (<https://clinicaltrials.gov/ct2/show/NCT04229225>). However, the clinical trial using Dasatinib + Quercetin shows promising results in patients with diabetic renal disease (<https://clinicaltrials.gov/ct2/show/NCT02848131>). The abundance of adipose tissue senescent cells and blood SASP factors decreased after 11 days of treatment [415, 419]. Another trial of Dasatinib + Quercetin indicates the safety and efficiency of this treatment combination in subjects with idiopathic pulmonary fibrosis (<https://clinicaltrials.gov/ct2/show/NCT02874989>) [428]. Finally, the clinical trials of Fisetin are ongoing, but no results have been reported yet [415].

1.5. Hypothesis for this project

By studying the literature, I find several exciting and unstudied points to investigate. Based on these points, I raise three hypothesis outlines.

1. Human BM-MSC are multipotent cells that can differentiate into adipocytes. However, the specific subpopulation that is responsible for adipogenesis is unclear yet. Since the CD146-positive cell population is a key component of BM-MSCs and shows PC characteristics, it might be the potential adipogenesis subsets of BM-MSCs.
2. The senolytic agent Dasatinib belongs to the drug class of TKI and was shown to selectively eliminate senescent preadipocytes and mature adipocytes. It has been applied in clinical trials of senolytic therapy together with Quercetin. However, the single effects of Dasatinib on natural cellular senescence alone with adipogenesis are still uncertain. Therefore, I hypothesise that Dasatinib treatment could inhibit preadipocyte adipogenesis and eliminate senescent preadipocytes and adipocytes.
3. Since T2DM is closely connected with senescence and obesity and can also lead to cardiovascular and BM diseases. I hypothesise that *in vivo* Dasatinib treatment could ameliorate diabetes-induced cardiomyopathy and BM dysfunction by improving steatosis and senescence.

1.6. Aims and objectives

According to the hypothesis raised above in **section 1.5**, there are three aims for this study, which are shown in the following outlines.

1. Based on the first hypothesis, the present study aims to understand the adipogenic differentiation potential of human BM-derived CD146-positive PCs.
2. To identify the second hypothesis, the present project explores the effects of senolytic agent Dasatinib on human BM-derived CD146-positive PC adipogenesis and senescence.
3. To identify the third hypothesis, the present study explores the effects of *in vivo* administration of Dasatinib on T2DM obese mice heart and BM.

CHAPTER 2. CELLULAR SOURCE OF ADIPOCYTES IN HUMAN BONE MARROW

2.1. Introduction

This chapter aims to study whether hBM-PC is the population in charge of adipogenesis in human BM. Human BM-derived MSCs are reported to have multipotent differentiation ability and differentiate into adipocytes. However, there are many subpopulations in the hBM-MSCs, and the specific subset responsible for adipogenesis is unclear. It is worth exploring the cellular source of adipocytes, which might become a novel therapy target for T2DM and adiposity.

The isolation of hBM-MSCs is based on the definition from the International Society for Cellular Therapy, that most of the MSCs show *in vitro* plastic adherent characteristics expansion in the α MEM + 20% FBS media [283]. However, among all the markers that were described in **section 1.2.3.2**, the subpopulation with positive expression for CD146 is enriched in human BM-derived MSCs [429]. The enrichment of the CD146-positive population increases the adipogenic differentiation possibility of this subset from the quantitative aspect. Therefore, in the present study, I decided to explore whether human BM-derived CD146-positive PCs is the population in charge of adipogenesis in human BM. The hBM-PC was isolated according to Mangialardi, G et al.'s protocol [302].

Cellular senescence is a permanent cell cycle arrest state, which occurs along with aging (replicative senescence) or is induced by stress [322]. Due to the lack of typical hallmarks for senescence assessments, it's necessary to measure the cellular senescence combined with different markers from different signalling pathways, such as the expression level of cyclin-dependent kinase inhibitors (p16^{INK4a} and p21^{Waf1/Cip1}), SASP levels, SA- β -gal, and DDR marker γ H2AX, together with the morphology characteristics

of senescent cells, including enlarged and flat of cells, and decreasing of proliferation ability [325]. Since the average age of donors for this project is more than 67 years old, it's worth exploring the characteristics of the isolated hBM-PCs to understand the senescence of these cells for further studies.

Adipogenesis is the progress of precursors differentiating into mature adipocytes [430], that are regulated by both positive and negative effectors. For instance, PPAR γ and AP-1 (activator protein-1) family play crucial roles in promoting adipogenesis from preadipocytes, and other factors, like STATs (signal transducers and activators of transcription), KLF4 (kruppel-like factor 4), SREBP-1 (sterol response element-binding protein-1), and C/EBPs are efficient to facilitate adipocytes maturation. In contrast, Wnt signalling, GATA factors, KLF2, and Pref-1 (preadipocyte factor-1) are found to inhibit adipogenic differentiation [431]. To stimulate adipogenesis *in vitro*, dexamethasone [432, 433] and indomethacin [434] prime the adipocyte differentiation via increasing the expression of PPAR γ and C/EBP. In addition, isobutylmethylxanthine promotes adipogenesis by increasing the expression level of C/EBP β [435] and insulin also acts as an adipogenic hormone to promote the progress of adipocyte differentiation [436].

2.2. Methods

2.2.1. Ethics

The study was registered as an observational clinical study in the National Institute for Health Research Clinical Research Network Portfolio, UK Clinical Trials Gateway. The experimental procedures were covered by ethical approval from Wales Rec 4 (REC reference number: 14/WA/1005), which complied with the "Declaration of Helsinki" principles. Patients who received orthopaedic surgery for hip reconstruction were recruited by giving written informed consent at the Southmead Hospital, Bristol, UK.

2.2.2. Human BM-MSCs isolation

Human BM samples were harvested from the femoral head and removed following the standard steps of hip replacement surgery. BM was scooped into a sterile pot and

transferred into a sterile Falcon tube containing 5 mL 0.5M ethylenediaminetetraacetic acid (EDTA), pH = 8.0, stored at 4°C for cell isolation within 24 hours. Only material that would be otherwise discarded was collected for the study.

BM samples were washed three times with Dulbecco's phosphate buffered saline (DPBS, Thermo Fisher Scientific, CAT# 14190-094), passed through a 70 µm strainer (Fisher Scientific, CAT# 22-363-548) to remove bone fragments and cell clumps, centrifuged at 300 x *g* for 15 minutes at 25°C. After resuspension in DPBS, BM cells were stratified on Ficoll Histopaque 1077 (Sigma-Aldrich, CAT# 10771), centrifuged at 300 x *g* for 45 minutes with acceleration set at one and without deceleration at 25°C. BM mononuclear cells layered at the interphase were collected and washed with DPBS, and the viability was assessed using trypan blue staining. Trypan blue is a membrane-impermeable dye not taken up by viable cells; therefore, it only stains dead cells whose membranes are damaged and become permeable. A total of 1×10^7 cells were seeded into flasks in α MEM basal media (Thermo Fisher Scientific, CAT# 32561-029) supplemented with 20% (v/v) FBS (Thermo Fisher Scientific, CAT# 16000044), and incubated for 48 hours at 37°C, 5% CO₂. The adherent cells were considered BM-MSCs and further expanded with α MEM + 20% (v/v) FBS medium.

2.2.3. Human BM-PCs sorting

Once approximately 90% confluent, BM-MSCs were trypsinized with 1x 0.5% Trypsin-EDTA (10x stock solution diluted in 1x DPBS, Thermo Fisher Scientific, CAT# 15400) and sorted to isolate PCs using magnetic cell separation immunomagnetic beads, columns, and a manual magnetic cell separator, all from Miltenyi, Germany. Around 1×10^7 BM-MSCs were resuspended in pre-cooled column buffer containing 0.5% (w/v) bovine serum albumin (BSA) (Sigma-Aldrich, CAT# A9418-100G) and 2 mM EDTA in DPBS, labelled with CD45-conjugated microbeads (Miltenyi, CAT# 130-045-801). After incubation for 15 minutes at 4°C, cells were transferred to the magnetic separation system. CD45^{pos} cells were attracted by the magnet and thus retained in the column, while the flow-through represented the CD45^{neg} cells. These latter were collected, centrifuged, resuspended in column buffer, and labelled with CD34-conjugated

microbeads (Miltenyi, CAT# 130-046-702). A second sorting procedure was applied to obtain CD45^{neg} CD34^{neg} cells. After centrifugation and resuspension in column buffer, cells were finally labelled with CD146-conjugated microbeads (Miltenyi, CAT# 130-093-596). Through a third immunomagnetic sorting, CD45^{neg} CD34^{neg} CD146^{pos} cells were collected. This was the cell fraction retained within the magnetic column and flushed in a new tube. This cell population was considered hBM-PCs [302]. The remaining populations (CD45^{neg} CD34^{pos} and CD45^{neg} CD34^{neg} CD146^{neg} populations) were mixed and renamed non-pericyte stromal cells (hBM-SCs). hBM-PCs and hBM-SCs were stored in liquid nitrogen (LN₂) for further experiments. Cells were frozen using a freezing solution made of 90% (v/v) FBS + 10% (v/v) DMSO. This latter is a cryoprotective agent that prevents the formation of intracellular water crystals, thus avoiding cell death during cryopreservation. The purity of hBM-PCs was assessed using ICC staining (see below). Cell lines between passage 3 to passage 6 were used for subsequent experiments. The working flow of human BM-MSCs isolation and hBM-PCs and hBM-SCs sorting is shown in **Figure 2-1**.

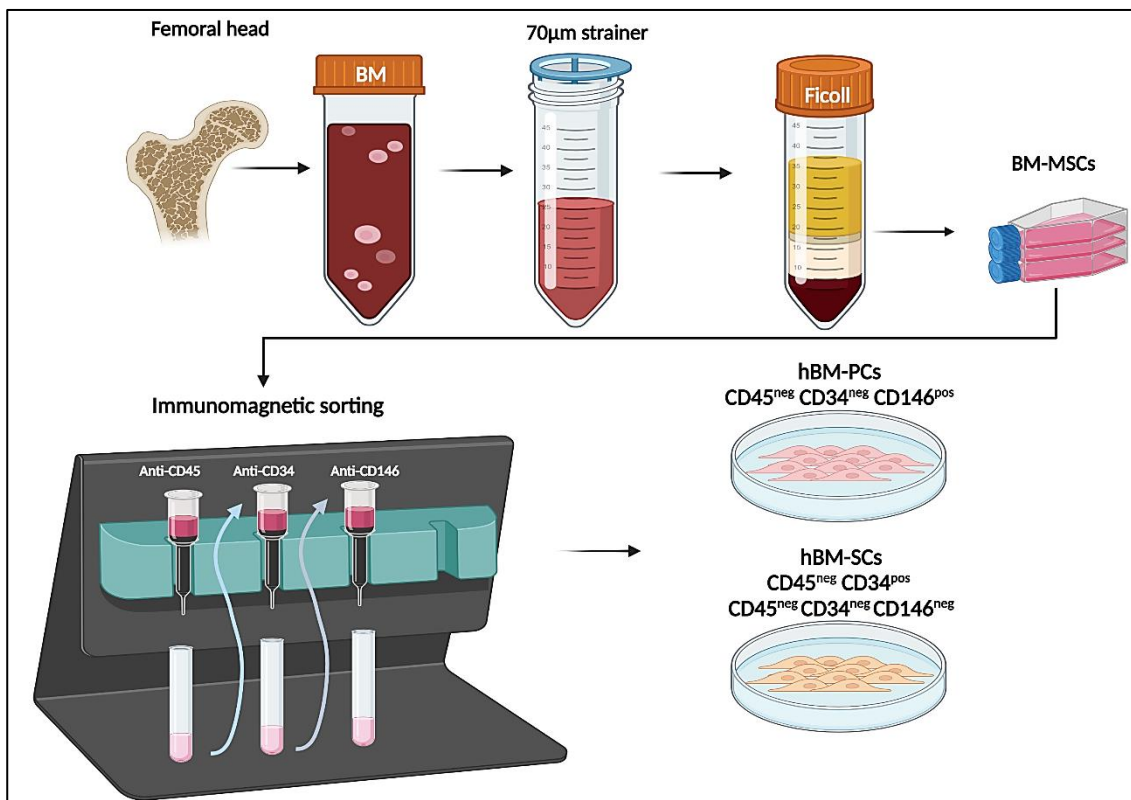


Figure 2-1 Scheme of human BM cell isolation and human BM-PCs & BM-SCs sorting.

2.2.4. Human BM-PCs culture conditions optimisation

HBM-PCs tended to detach from the culture surface and did not grow well using a previously established method [302], so I optimised the expansion condition. One hBM-PCs line was seeded onto a 6-well plate at a density of 1,500 cells/cm², cultured with four different conditions:

- (1) Uncoated culture flasks and cells cultured in endothelial cell growth medium 2 (ECGM2, PromoCell, CAT# C-39211);
- (2) Uncoated culture flasks and cells cultured in α MEM supplemented with 20% (v/v) FBS;
- (3) Culture flasks coated with 0.1% (w/v) gelatin solution (Sigma-Aldrich, CAT# G9391) and cells cultured in ECGM2;
- (4) Culture flasks coated with 0.1% (w/v) gelatin solution and cells cultured in α MEM supplemented with 20% (v/v) FBS.

The optimisation was evaluated by analysing cell viability and proliferation rate, morphological changes, and antigenic profile.

2.2.5. Induction of adipogenic differentiation on human BM-PCs & BM-SCs

HBM-PCs and hBM-SCs were isolated from the same subject and used at the same passage. Adipogenesis was induced by incubating cells with 1 μ M dexamethasone (Sigma-Aldrich, CAT# D4902-100mg), 0.5 mM isobutylmethylxanthine (Sigma-Aldrich, CAT# I5879-250mg), 10 μ g/mL insulin (Sigma-Aldrich, CAT# I9278), and 1 μ M indomethacin (Sigma-Aldrich, CAT# I7378-5g) in Dulbecco's Modified Eagle Medium (DMEM, Thermo Fisher Scientific, CAT# 21885025) supplemented with 10% (v/v) FBS for 7, 14 or 21 days, with media changed every three days. Cells cultured in DMEM + 10% (v/v) FBS medium only were used as undifferentiated controls. After treatment, extracted ribonucleic acid (RNA) was used for qPCR analyses to assess the expression level of relevant mRNAs: *PPARG*, *ADIPOQ* and *FABP4*. Moreover, ORO staining was

performed to identify the lipid droplets. Cells were washed once with 1x DPBS, fixed in 4% (w/v) paraformaldehyde (PFA) for 30 minutes, then washed with 60% (v/v) isopropanol and stained with ORO working solution for another 30 minutes, as described in **section 2.2.7**. A Leica DMI6000B microscope (Leica Microsystems, Wetzlar, Germany) was used to acquire images.

2.2.6. Immunocytochemistry

Cells were washed once in 1x PBS and fixed with 4% (w/v) PFA for 15 minutes at room temperature (RT). Cells were incubated with 0.1% (v/v) Triton X-100 (Sigma-Aldrich, CAT# X100-500ML) in 1x PBS for 5 minutes at RT to detect intracellular antigens. Triton is a non-ionic surfactant that permeabilises cellular membranes. After washing twice in 1x PBS, cellular non-specific binding sites were blocked with 5% (v/v) FBS in 1x PBS for 30 minutes at RT and then incubated with primary antibodies for 16 hours at 4°C. After washing three times with PBS, cells were incubated with appropriate secondary antibodies, diluted 1:200 in the blocking solution for one hour at RT and protected from light. The nuclei were counterstained with 3 µM 4',6-diamidino-2-phenylindole (DAPI) (Thermo Fisher Scientific, CAT# D3571) in 1x PBS for 2 minutes at RT, protected from light. Cells were preserved with Fluoromount-G and imaged by Zeiss Observer.Z1 microscope under 10x and 20x objectives. Secondary antibody controls omitting primary antibodies were performed for each cell line to rule out non-specific binding of the secondary antibodies to the cells (images not shown). Details of the primary and secondary antibodies used in ICC are listed in **Table 2-1**. All antigens were assayed in duplicates.

Antigen	Host	Technique	Reactivity	Dilution	Permeabilization	Supplier & CAT#	2 nd Abs
CD34	Mouse	ICC	Human	1:100	No	Dako, M7165	Invitrogen, Alexa568 goat anti-mouse, A11004
CD146	Rabbit	ICC	Human	1:100	Yes	Abcam, Ab75769	Invitrogen, Alexa488 goat anti-rabbit, A11008
NG2	Rabbit	ICC	Human	1:50	No	Millipore, AB5320	Invitrogen, Alexa488 goat anti-rabbit, A11008
PDGFR β	Goat	ICC	Human	1:50	No	R&D, AF385	Invitrogen, Alexa488 donkey anti-goat, A11005
PDGFR α	Mouse	ICC	Human	1:100	Yes	Santa cruze, SC-398206	Invitrogen, Alexa568 goat anti-mouse, A11004
P16 ^{INK4a}	Mouse	ICC, IHC	Human, Mouse	1:50	Yes	Santa cruze, SC-1661	Invitrogen, Alexa568 goat anti-mouse, A11004
P21 ^{Waf1/Cip1}	Rabbit	ICC	Human, Mouse	1:600	Yes	Cell signaling, 2947S	Invitrogen, Alexa488 goat anti-rabbit, A11008
γ H2AX	Mouse	ICC	Human, Mouse	1:125	Yes	Biologend, 613401	Invitrogen, Alexa568 goat anti-mouse, A11004
ki67	Rabbit	ICC	Human, Mouse	1:500	Yes	Abcam, ab16667	Invitrogen, Alexa488 goat anti-rabbit, A11008

Table 2-1 Primary and secondary antibodies used in immuocytochemistry studies.

2.2.7. Oil red O staining on cells

ORO is a fat-soluble diazole dye that identifies neutral lipids and cholesteryl esters but does not stain the biological membranes [437]. To identify lipids, ORO staining [438] was performed on mouse tissue sections and human BM cells. The ORO working solution was prepared as follows: 1.5 parts of ORO stock solution (0.5% w/v) (Sigma-Aldrich, CAT# O1391-500ML) were diluted into 1 part of distilled water, left to stand for 10 minutes at 4°C and then passed through a 0.2 µm filter to remove precipitates. The working solution was used within 6 hours [438].

Cells were fixed with 4% PFA (w/v) for 30 minutes at RT and washed once with DPBS and 60% (v/v) isopropanol (Sigma-Aldrich, CAT# I9516-1L). Cells were stained with ORO working solution for 30 minutes at RT and washed once with 60% (v/v) isopropanol and distilled water. The nuclei were counterstained with 3 µM DAPI in 1x PBS for 5 minutes at RT and protected from light. ORO-stained lipid droplets can easily identify their intense red colouration under a light microscope or show red fluorescence under fluorescence microscopy [439]. To confirm the accuracy of the data, I acquired both brightfield and fluorescent images for quantification. Brightfield images were taken at 50x, 100x and 200x magnification using a Leica DMI1 light microscope. The fluorescent images (images not shown) were acquired using a Zeiss Observer.Z1 microscope at 100x and 200x magnifications under DAPI and Cy5 channels. Cells were analysed in duplicates.

2.2.8. Viability assay

The cells were seeded in a dark 96-well plate at the density of 4,500 cells per well and cultured until 80% confluent. Cell viability was measured by using Viability/Cytotoxicity Assay kit for Animal Live & Dead cells (Biotium, CAT# 30002-T) according to the vendor protocol. In this assay, the membrane-permeant Calcein-AM is cleaved by esterase in live cells and labels the cytoplasm in green fluorescence. Dead cells lacking esterase activity are not labelled. Ethidium homodimer III (EthD-III) is a plasma membrane-impermeant DNA dye that is excluded by viable cells and only labels nuclei of dead cells in red fluorescence. After warming the reagents to RT, the staining solution was

prepared as follows: 4 mM Calcein-AM (1:2000) and 2 mM EthD-III (1:500) were diluted in serum-free α MEM medium. Cells were washed twice with 1x DPBS, incubated with the dye solution for 30 minutes at 37°C in a 5% CO₂ incubator, and protected from light, according to the vendor guidelines. A dead cell control was included by treating cells with 0.1% (w/v) saponin in 1x DPBS for 10 minutes at 37°C in the 5% CO₂ incubator, followed by staining with the dye solution using the same protocol as the normal cells. Cells were imaged using a Zeiss Observer.Z1 microscope at 100x and 200x magnifications within 30 minutes. Cells were analysed in duplicates.

2.2.9. Proliferation assay

Cell proliferation ability was assessed using a Click-iT™ EdU Imaging kit (Invitrogen, CAT# C10337) according to the vendor protocol. In this assay, cells incorporate 5-ethynyl-2'-deoxyuridine (EdU) at thymidine bases into newly synthesised DNA; thus, the presence of EdU indicates that cells have proliferated. Cells were incubated with EdU diluted 1:1000 in the culture media for 48 hours at 37°C in the 5% CO₂ incubator. After the incubation, cells were fixed with 4% (w/v) PFA for 15 minutes at RT and washed twice with 3% (w/v) BSA in 1x PBS. Cells were permeabilised with 0.1% Triton™ X-100 in 1x PBS for 10 minutes at RT to gain access to the DNA. Cells were washed twice with 3% (w/v) BSA in 1x PBS and incubated with Click-iT® reaction cocktail for 30 minutes at RT, in the dark. Nuclei were stained by incubating with 3 μ M DAPI in 1x PBS for 2 minutes at RT and protected from the light. The images were obtained using a Zeiss Observer.Z1 microscope at 100x and 200x magnifications. Cells were analysed in duplicates.

2.2.10. Gene expression analysis

2.2.10.1. RNA extraction

The total RNA was extracted and purified with a miRNeasy Micro kit (QIAGEN, CAT# 217084), according to the manufacturer's instructions. Cells were disrupted and homogenized with Qiazol Lysis reagent for 5 minutes at RT. Chloroform was added to the homogenate to isolate RNA, incubated at RT for 2 minutes, and centrifuged for 15 minutes at 12,000 $\times g$ at 4°C. RNA was collected from the upper aqueous phase, and then RNA was precipitated with 100% ethanol. After sequential washes using Buffer

RWT, Buffer RPE, and 80% ethanol, purified RNA was resuspended in 14 μL of RNase-free water. The concentration of RNA was detected using the NanoDrop 2000 Spectrophotometer (Thermo Fisher Scientific). The purity of the RNA was determined by the 260 nm/280 nm absorbance readings ratio and considered acceptable (devoid of DNA or protein contamination) for values of ~ 2 .

2.2.10.2. cDNA reverse transcription

A High-Capacity RNA-to-cDNA kit (Thermo Fisher Scientific, CAT# 4387406) was used to reverse-transcribe RNA to complementary DNA (cDNA). The reverse transcription mix was prepared following the manufacturer's protocol using 150 ng of RNA. Reaction tubes were incubated in a thermal cycler (Bio-Rad, T100) for 60 minutes at 37°C, followed by 5 minutes at 95°C. Synthesized cDNA was diluted with RNA-free water to obtain a final 7.5 ng cDNA/ μL solution and stored at -20°C.

2.2.10.3. Quantitative PCR

A quantitative reverse-transcription-polymerase chain reaction (qPCR) was used to amplify first-chain cDNA using a TaqMan™ Universal PCR Master Mix (Thermo Fisher Scientific, CAT# 4324018) and TaqMan probes (Thermo Fisher Scientific) on a QuantStudio® 5 Real-Time PCR Instrument for the following adipogenesis genes: *PPARG*, *FABP4* and adiponectin (*ADIPOQ*). Ubiquitin C (*UBC*) was used as a housekeeping gene. For each reaction, 7.5 ng cDNA was used. All reactions were performed in triplicates. Messenger RNA (mRNA) expression level was calculated using the $2^{-\Delta\Delta\text{Ct}}$ method [440]. The TaqMan probes used in the qPCR assay are listed in **Table 2-2**.

Gene	Species	Assay ID
<i>PPARG</i>	Human	Hs01115513_m1
<i>FABP4</i>	Human	Hs01086177_m1
<i>ADIPOQ</i>	Human	Hs00977214_m1
<i>UBC</i>	Human	Hs00824723_m1

Table 2-2 TaqMan probes used in qPCR assays.

2.2.11. Statistical analysis

Data are presented as individual values and mean \pm standard error of the mean (SEM). When applicable, the D'Agostino-Pearson and Kolmogorov-Smirnov normality tests were used to check for data normal distribution. Unpaired analyses were carried out. Continuous variables normally distributed were compared using the Student's t-test (two groups) or one-way analysis of variance (ANOVA) followed by Tukey's multiple comparison tests (three groups). Data not normally distributed were compared using non-parametric Mann-Whitney (two groups) or Kruskal-Wallis (three groups) tests, followed by Tukey or Dunn tests as appropriate. Two-way ANOVA was used to compare the mean differences between multiple groups for *in vitro* experiments with human cells. A p value < 0.05 was considered statistically significant. All analyses used GraphPad Prism 9.4.0 (San Diego, CA, USA).

2.3. Results

2.3.1. Sample collection and cell sorting

This study collected thirty-three BM samples from non-diabetes individuals and five from type 2 diabetes patients. Due to the inability to recruit patients during the COVID pandemic, the sample collection had to be suspended for a year, which prevented obtaining enough T2DM samples in time for the project's experiments. Therefore, all the experiments of this thesis were performed on non-diabetes patients' samples. The characteristics of donors are listed in **Table 2-3**. Twenty-nine non-diabetic samples were successfully processed to isolate and sort hBM-PCs. After immunomagnetic sorting (**Figure 2-2A**), $39.08 \pm 3.44\%$ of the total cells were represented by hBM-PCs, while the fraction of hBM-SCs was significantly lower ($18.15 \pm 2.39\%$) (**Figure 2-2B**). The CD45^{pos} cells were discarded as they showed HSCs phenotype characteristics, which were not the target population for this study. These results suggest that hBM-PCs took a vital part of hBM-MSCs from the quantity aspect.

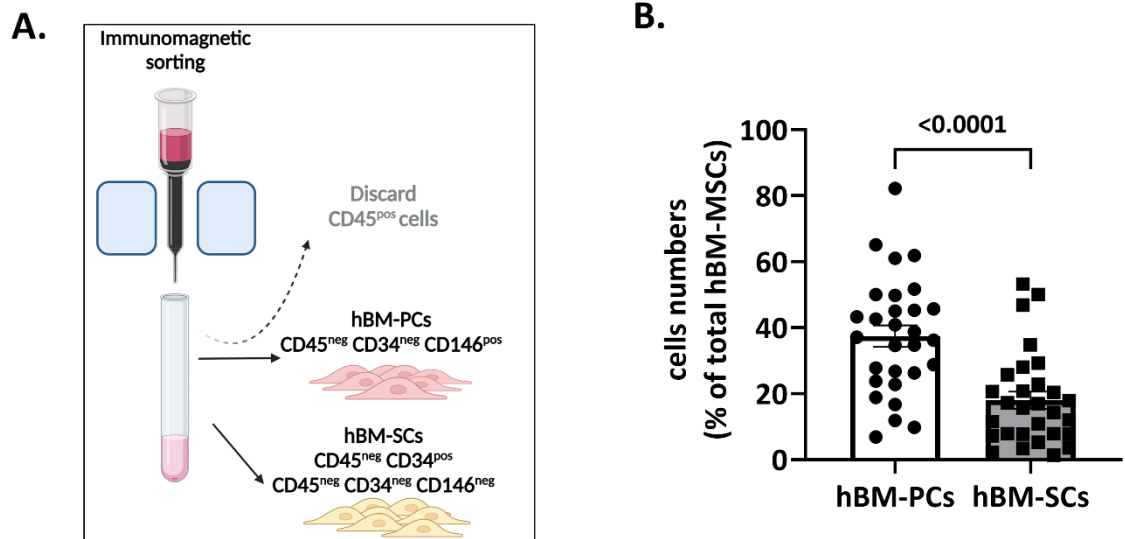


Figure 2-2 Human BM-PCs and BM-SCs sorting flow chart and results.

Image (A) shows the immunomagnetic sorting of hBM-PCs and hBM-SCs. Histogram (B) reports the fraction (%) of hBM-PCs and hBM-SCs in the total BM-MSCs. Data are shown as individual values and mean \pm SEM. Analysis: one-way ANOVA followed by unpaired t-test. $n = 29$ (nondiabetic) patients' cells/cell type. Abbreviations: hBM-PCs = human bone marrow pericytes; hBM-SCs = human bone marrow stromal cells, hBM-MSCs = human bone marrow mesenchymal stromal cells.

Sample NO.	Patient ID code	Collection date	Sex	Age	Diabetic	Sample quality	Experiment type						
							ICC Phenotype	Culture optimization	Passage Senescence	Dasatinib +senescent	Adipose differentiation	Dasatinib+ Differentiation	High glucose
BM01	22/15102020/R3	15/10/2020	Female	80-85	No	Good	√	√					√
BM02	22/31102020/R9	31/10/2020	Male	71	No	Good	√					√	
BM03	24/3122020/SW	03/12/2020	Female	72	No	Good	√				√	√	√
BM04	22/10122020/LB	10/12/2020	Female	67	No	Not good	x						
BM05	23/1032021/BM	10/03/2021	Male	70	No	Good	√			√	√	√	
BM06	22/2332021/WM	23/03/2021	Male	65	No	Good	√			√		√	√
BM07	23/2432021/DB	24/03/2021	Female	68	No	Good	√					√	
BM08	22/15042021/AS	15/04/2021	Female	81	No	Good	√						
BM09	22/15042021/MB	15/04/2021	Female	78	No	Good	√			√			√
BM10	24/22042021/TD	22/04/2021	Female	52	No	Good	√				√		
BM11	22/29042021/JR	29/04/2021	Male	58	No	Good	√			√			√
BM12	22/29042021/EM	29/04/2021	Female	68	No	Not good	x						
BM13	21/05052021/JE	05/05/2021	Female	72	No	Good	√				√	√	
BM14	22/09062021/SB	09/06/2021	Female	75	No	Good	√		√	√			
BM15	TH24/14062021IV	14/06/2021	Female	74	T2DM	Not good	x						
BM16	23/16062021/CP	16/06/2021	Male	63	No	Good	√		√			√	
BM17	22/29062021/DP	29/06/2021	Male	48	No	Good	√		√			√	
BM18	22/29062021/RP	29/06/2021	Female	67	No	Good	√		√			√	
BM19	22/7072021/RR	07/07/2021	Male	74	No	Good	√						
BM20	22/08072021/RR	08/07/2021	Male	72	No	Good	√		√				
BM21	22/02122021/MW	02/12/2021	Female	80	No	Good	√						
BM22	22/09122021/NM	09/12/2021	Female	55	No	Not good	x						
BM23	22/28012022/LP	28/01/2022	Male	72	No	Good	√					√	
BM24	21/31012022/CH	31/01/2022	Female	67	T2DM	Good	√						
BM25	21/31012022/PB	31/01/2022	Female	61	No	Good	√						
BM26	22/24022022/TB	24/02/2022	Male	63	No	Good	√						
BM27	24/16032022/RC	16/3/2022	Male	75	No	Good	√						
BM28	22/24032022/GT	24/3/2022	Female	86	No	Good	√						

BM29	22/26032022/PH	26/3/2022	Male	43	No	Good	√						
BM30	22/26032022/BA	26/3/2022	Male	67	No	Good	√						
BM31	22/26032022/PK	26/3/2022	Female	73	No	Good	√						
BM32	23/09062022/JE	9/6/2022	Male	53	T2DM	Good	√						
BM33	23/21072022/AC	21/7/2022	Male	59	No	Good	√						
BM34	24/2508/2022/AF	25/8/2022	Female	70	T2DM	Good	√						
BM35	24/2508/2022/PR	25/8/2022	Female	75	T2DM	Good	√						
BM36	19/14092022/BC	14/09/2022	Female	71	No	Good	√						
BM37	23/17092022/MH	17/09/2022	Male	60	No	Good	√						
BM38	24/22092022/TJ	22/09/2022	Male	72	No	Not good	x						

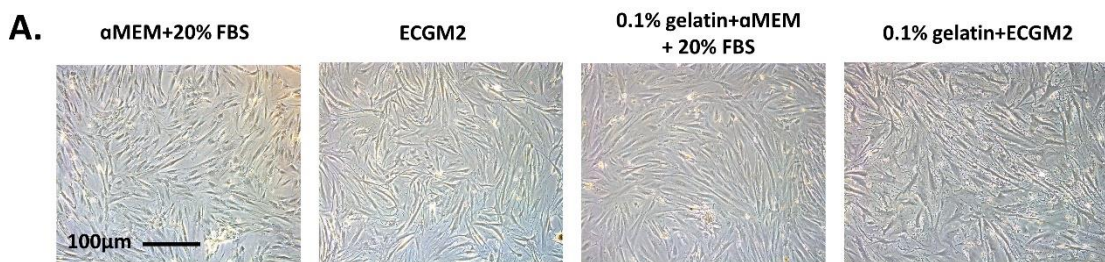
Table 2-3 Clinical characteristic of recruited patients and sample attribution to specific experiments.

* “Not good” means the cells isolated from the sample did not expand well *in vitro* and could not be used in experiments. These cell lines were not counted in the successfully isolated cells, so the total number of non-diabetic samples used in the project was 29.

2.3.2. Optimisation of human BM-PCs culture conditions

Since our group had established the culture conditions for hBM-PCs before [200, 302], only one primary cell line was used to confirm the protocol or for further optimisation.

The morphology and phenotype characteristics of hBM-PCs showed slight differences between different culture conditions. The hBM-PCs had a typical spindle shape under all four conditions (**Figure 2-3A**). Some of the cells cultured under α MEM + 20% (v/v) FBS condition were not expressing PDGFR β , and the cells cultured under ECGM2 did not all express PC maker NG2, whereas the cells cultured in the gelatin coated-flasks expansion in α MEM + 20% (v/v) FBS or ECGM2 medium were almost fully expressing the PC markers: CD146, NG2, and PDGFR β (**Figure 2-3B**). The cells expanded better in ECGM2 or α MEM + 20% (v/v) FBS with gelatin coating than in α MEM + 20% (v/v) FBS or ECGM2 without coating. The cells which were cultured with α MEM + 20% (v/v) FBS medium with/without the plate coated with gelatin had an increase of approximately one-fold in the proliferation ability compared with cells cultured in ECGM2 with/without gelatin coating (**Figure 2-3 C and D**). The viability of hBM-PCs was consistently more than 90% in all the culture conditions (**Figure 2-3 C and E**). This preliminary experiment suggested that hBM-PCs express typical PC antigens and grow better when cultured in α MEM supplemented with 20% (v/v) FBS on plates coated with 0.1% (w/v) gelatin. The extracellular matrix coating – an optimisation of the previous protocol – is likely to improve the cells' adhesion to the flask. Therefore, this culture protocol was adopted for all the subsequent studies.



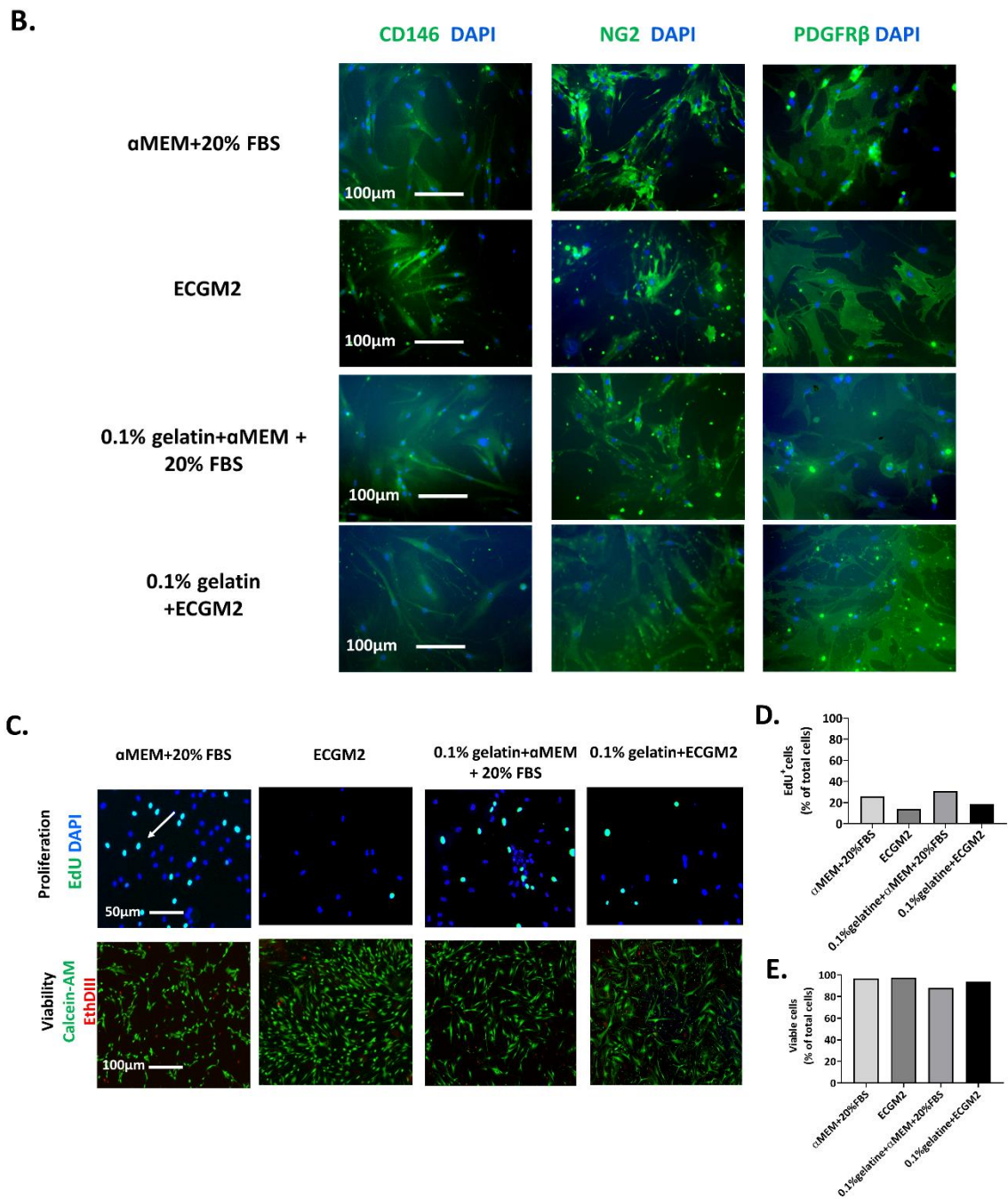


Figure 2-3 Morphology, phenotype, proliferation, and viability of human BM-PCs under different culture conditions.

HBM-PCs were expanded using four different culture conditions: 1) 20% (v/v) FBS + α MEM; 2) ECGM2; 3) plates pre-coated with 0.1% (w/v) gelatin solution and expansion in 20% (v/v) FBS + α MEM; or 4) plates pre-coated with 0.1% (w/v) gelatin solution and expansion in ECGM2. (A) Images indicate the morphological characteristics of the same hBM-PCs primary cell line expanded in the different culture conditions (1,500 cells/cm²). (B) Immunofluorescent images show the phenotype characteristics of hBM-PCs under the four culture conditions. HBM-PCs are positive for CD146 (green), NG2 (green) and PDGFR β (green). The nuclei were identified by DAPI (blue). Fluorescence images (C) show the cell proliferation and viability. The EdU staining (arrow, green) indicates proliferating cells, while DAPI labels nuclei in blue. The Calcein-AM staining (green)

labels live cells. Red fluorescence nuclear EthD-III staining indicates dead cells. Histograms (D&E) show the quantification of proliferating cells (D) or viable cells (E), expressed as a percentage of the total cells. n = 1 patients' cells/group. Abbreviations: CD = cluster of differentiation; NG2 = neural/glial antigen 2; PDGFR β = platelet-derived-growth factor beta; FBS = fetal bovine serum; α MEM = alpha minimum essential medium; ECGM2 = endothelial cell growth medium 2; hBM-PCs = human bone marrow pericytes; DAPI = 4',6-diamidino-2-phenylindole; EdU = 5-ethynyl-2' -deoxyuridine; EthDIII = Ethidium Homodimer III.

2.3.3. Characterisation of human BM-PCs

2.3.3.1. Phenotypic characteristics of human BM-PCs

The ICC staining confirmed that hBM-PCs were negative for CD34 (**Figure 2-4A**) while positive for CD146 (**Figure 2-4B**), PDGFR β (**Figure 2-4C**), and NG2 (**Figure 2-4D**).

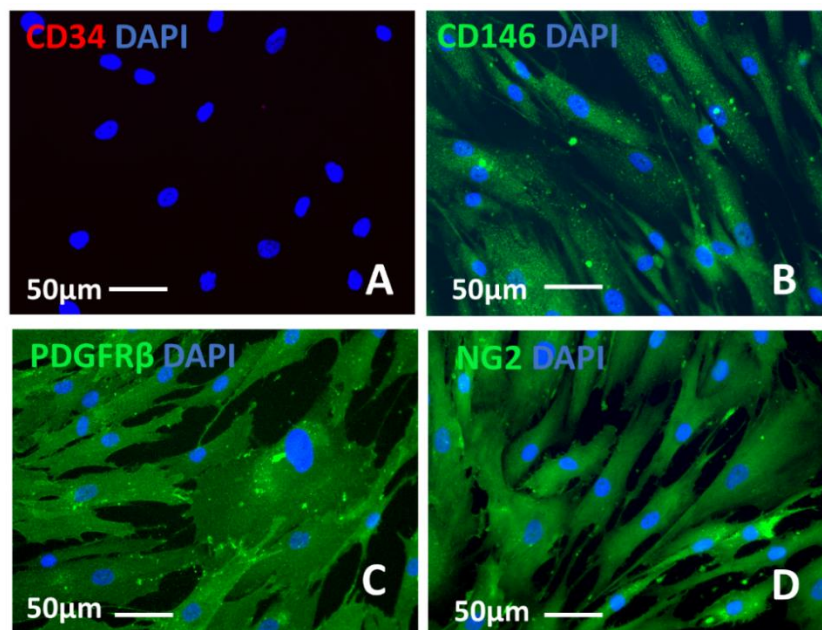
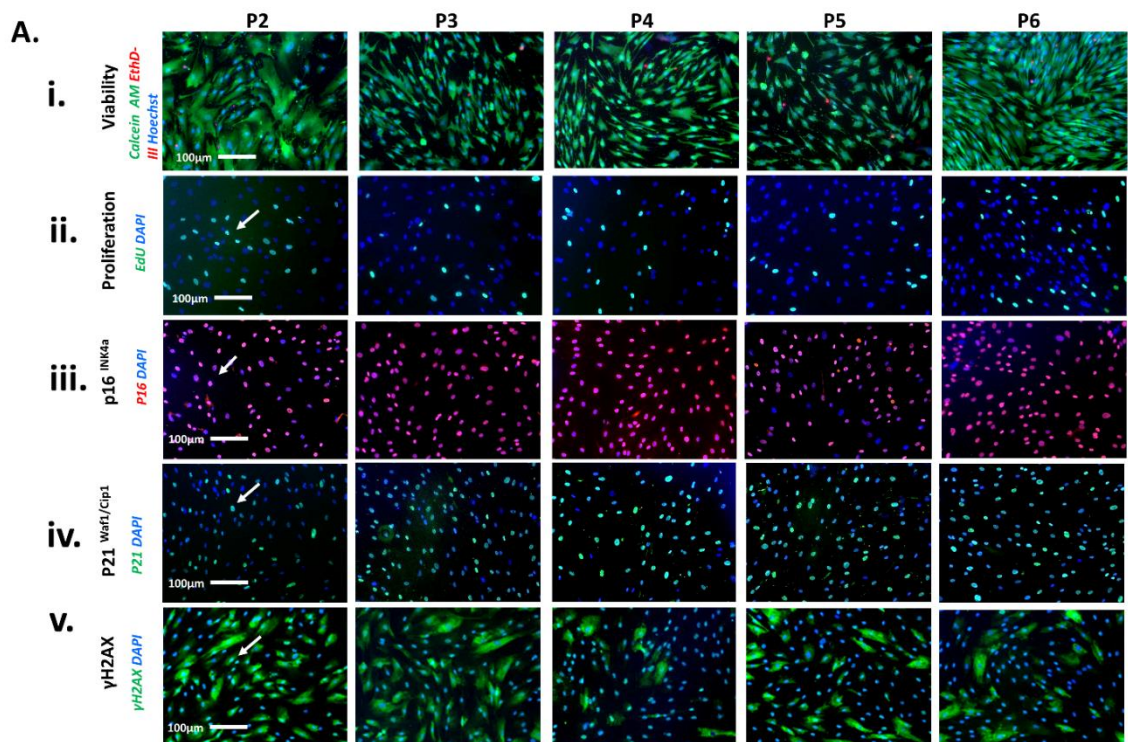


Figure 2-4 Human BM-PCs phenotypes are assessed using immunocytochemistry.

HBM-PCs were immunomagnetically sorted as the CD34^{neg}CD45^{neg}CD146^{pos} population. Images show stainings with antibodies: (A) anti-CD34, in red fluorescence, (B) anti-CD146, (C) anti-PDGFR β and (D) anti-NG2, in green fluorescence. Nuclei were identified by the blue fluorescence of DAPI. The cell phenotype was confirmed for all PC lines used in the study. Abbreviations: CD = cluster of differentiation; NG2 = neural/glial antigen 2; PDGFR β = platelet-derived-growth factor beta; hBM-PCs = human bone marrow pericytes; DAPI = 4',6-diamidino-2-phenylindole.

2.3.3.2. Senescence, proliferation ability and viability of human BM-PCs

The functional characteristics of hBM-PCs were measured in different cell lines from passage 2 to passage 6. More than 90% hBM-PCs were viable at each passage (**Figure 2-5 Ai and B**). Instead, the fraction of proliferating hBM-PCs decreased from $31 \pm 4.89\%$ (passage 2) to $20.4 \pm 4.89\%$ (passage 6), with this reduction being significantly different in passage 3 ($14.8 \pm 4.89\%$) and passage 5 ($12.4 \pm 4.89\%$) when compared with passage 2 (**Figure 2-5 Aii and C**). The fraction of cells expressing cell cycle arrest markers $p16^{INK4a}$ (**Figure 2-5 Aiii and D**) and $p21^{Waf1/Cip1}$ (**Figure 2-5 Aiv and E**) was constantly high (average $> 75\%$) throughout cell expansion. The expression of the double-stranded DNA breaks marker γ H2AX (**Figure 2-5 Av and F**) showed a tendency to increase over passages but was high since passage 2 (more than 67.42% positive cells), indicating most of the hBM-PCs were already senescent from the early passage.



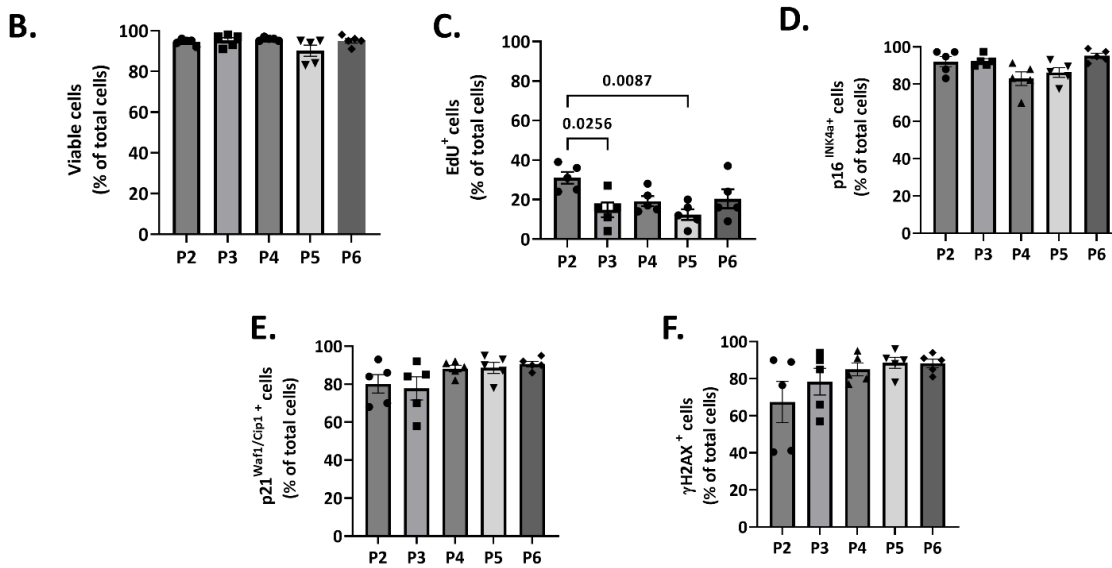


Figure 2-5 Cellular senescence, proliferation ability and viability at different passages.

Representative fluorescence images in hBM-PCs from passage 2 to passage 6 show (Ai) cells' viability (Calcein-AM, green, live cells; EthD-III, red, dead cells; Hoechst, blue, nuclei); (Aii) proliferation (EdU positive cells, arrow, green; nuclei, DAPI, blue); senescent cells: (Aiii) p16^{INK4a} positive (arrow, red), (Aiv) p21^{Waf1/Cip1} positive (arrow, green) and (Av) γH2AX positive (arrow, green). Nuclei were identified by DAPI (blue). The histograms in (B) and (C) show the quantitative results of the viable or proliferating cells, demonstrated as a percentage of the total cells. The histograms in (D) p16^{INK4a}, (E) p21^{Waf1/Cip1} and (F) γH2AX report the fraction (%) of cells positive for each senescence or DNA damage marker. Data are shown as individual values and mean ± SEM. Analysis: one-way ANOVA followed by Tukey's multiple comparisons tests. n = 5 patients' cells/passage. Abbreviations: P = passage; EdU = 5-ethynyl-2'-deoxyuridine; DAPI = 4',6-diamidino-2-phenylindole.

2.3.4. Phenotypic characteristics of human BM-SCs

ICC analyses were performed to analyse the antigenic profile of the hBM-SC population, which represents the remaining populations of hBM-MSCs after pericytes sorting. Results showed that only a small fraction of hBM-SCs express adventitial progenitor cells or PCs markers: CD34, CD146 and NG2 while highly expressing PDGFRβ and PDGFRα (**Figure 2-6 A to E**). This analysis confirms that hBM-SCs had typical mesenchymal cell characteristics that differ from hBM-PCs.

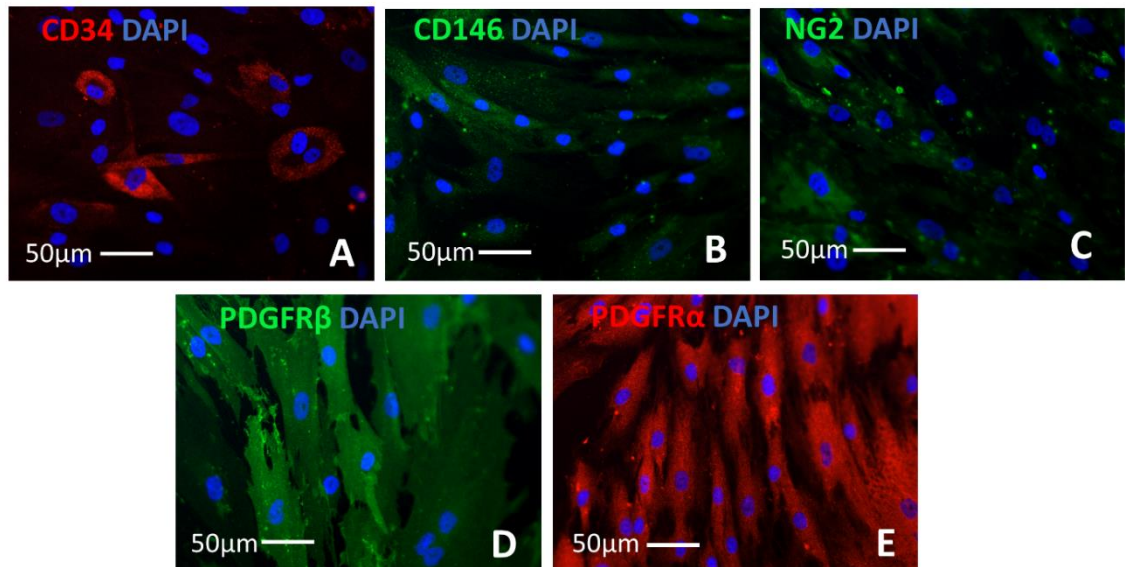


Figure 2-6 Phenotypic characteristics of the human BM-SCs populations (mixture of $CD45^{neg}CD34^{pos}$ and $CD45^{neg}CD34^{neg}CD146^{neg}$ cell populations) remaining after the human BM-PCs isolation.

Immunofluorescence images show cells labelled with antibodies: (A) anti-CD34, in red fluorescence; (B) anti-CD146, in green fluorescence; (C) anti-NG2, in green fluorescence; (D) anti-PDGFR β , in green fluorescence; and (E) anti-PDGFR α , in red fluorescence. Nuclei were identified by DAPI (blue). Abbreviations: CD = cluster of differentiation; NG2 = neural/glial antigen 2; PDGFR β = platelet-derived-growth factor beta; PDGFR α = platelet-derived-growth factor alpha; hBM-SCs = human bone marrow stromal cells; DAPI = 4',6-diamidino-2-phenylindole.

2.3.5. Propensity of human BM-PCs & BM-SCs differentiation into adipocytes

To investigate the hBM-SCs propensity to adipogenesis, I exposed hBM-PCs and hBM-SCs to a pro-adipogenic medium for 7, 14, and 21 days. The ORO staining showed that hBM-PCs started to differentiate into brown or beige adipocytes from day 7 and had a speedy eruption from day 14 to day 21. In contrast, hBM-SCs did not demonstrate a strong commitment to adipogenesis (**Figure 2-7A**). After 21 days of stimulation, the fraction of ORO-positive cells, expressed as a percentage of the total cells, showed that more hBM-PCs differentiated into adipocytes ($23.15 \pm 8.18\%$) than hBM-SCs ($0.087 \pm 0.087\%$) (**Figure 2-7B**). qPCR analyses indicated that during the adipose differentiation, both hBM-PCs and hBM-SCs upregulated the transcriptions of adipogenic mRNA: *PPARG*, *FABP4* and *ADIPOQ*, with no significant difference between the two cell

populations (**Figure 2-7 C to E**). These data suggest that hBM-PCs are the major source of adipocytes in culture.

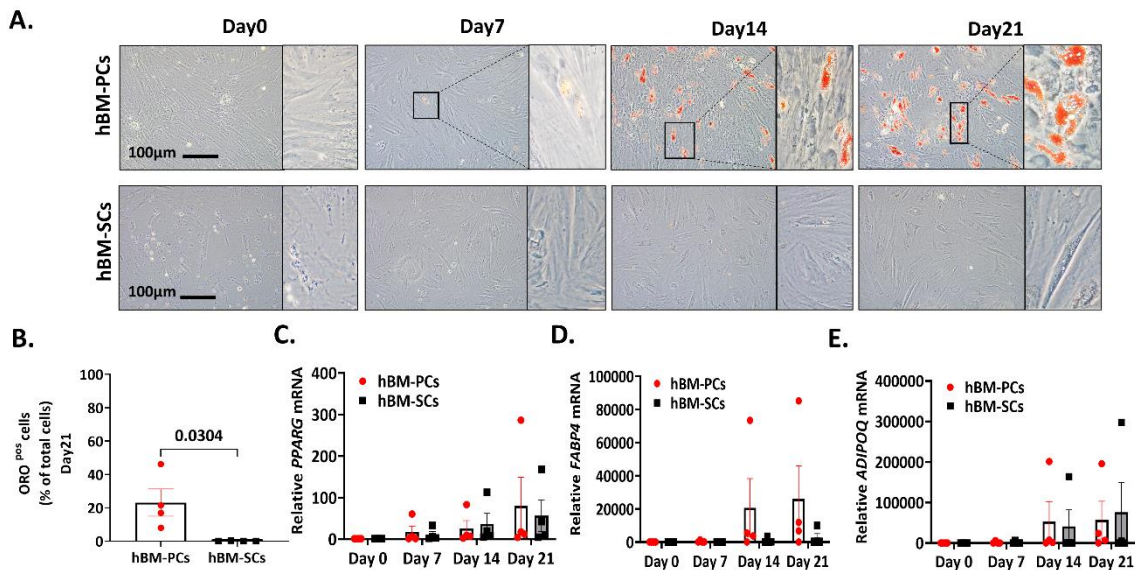


Figure 2-7 Adipogenic potential of human BM-PCs and BM-SCs.

HBM-PCs and hBM-SCs were compared for their differentiation potential into adipocytes. Bright-field images (A) show the adipocytes (red) stained with ORO in hBM-PCs and hBM-SCs after incubation with a pro-adipogenic medium for 7, 14, and 21 days. Histogram (B) shows the fraction of ORO-positive cells, demonstrated as a percentage of the total cells after stimulation for 21 days. Data are presented as individual values and means \pm SEM. Statistical analysis: unpaired t test. qPCR was performed to compare the relative expression of adipogenic differentiation-related mRNA (C) *PPARG*, (D) *FABP4*, and (E) *ADIPOQ* at different time points in hBM-PCs and hBM-SCs. Data are presented as individual values and means \pm SEM. Statistical analysis: Two-way ANOVA followed by Tukey's multiple comparisons tests. $n = 4$ patients' cells/group. Abbreviations: hBM-PCs = human bone marrow pericytes; hBM-SCs = human bone marrow stromal cells; ORO = oil red O; *PPARG* = peroxisome proliferator-activated receptor gamma; *FABP4* = fatty acid binding protein 4; *ADIPOQ* = adiponectin.

2.4. Conclusion

I collected and isolated thirty-eight human BM samples for the project. The culture condition of hBM-PCs was optimised as expansion cells in the α MEM medium supplementary with 20% (v/v) FBS on the plates pre-coated with 0.1% (w/v) gelatin. HBM-PC was positive for PC markers CD146, PDGFR β , and NG2 and negative for the hematopoietic cell marker CD34. These hBM-PCs showed high viability but low

proliferation ability and highly expressed senescence markers p16^{INK4a}, p21^{Waf1/Cip1}, and γ H2AX, indicating cellular senescence. Moreover, the hBM-SCs showed high expression of PDGFR β and PDGFR α and were partly positive for CD34, CD146, and NG2 markers. After 21 days of adipogenic differentiation, hBM-PCs demonstrated higher adipogenesis propensity than hBM-SCs.

Based on the results of this chapter, the following Chapter 5 investigates the effects of the senolytic agent Dasatinib on the function and senescence marker expression levels in hBM-PCs and the effects of Dasatinib on hBM-PCs & hBM-SCs adipogenic differentiation.

CHAPTER 3. EFFECTS OF SENOLYTIC AGENT DASATINIB ON HUMAN BM-PCS & BM-SCS

3.1. Introduction

This chapter aims to study the effects of the senolytic agent Dasatinib on hBM-PC adipogenesis and senescence. In Chapter 2, the results suggested that the hBM-PCs applied in this project were senescent and showed higher adipocyte differentiation ability than hBM-SCs. The senolytic agent Dasatinib targets to eliminate senescent preadipocytes and adipocytes. Therefore, in Chapter 3, it's worth understanding whether Dasatinib could eliminate senescent hBM-PCs and inhibit adipogenesis.

TKIs represent a milestone in cancer therapy. Recently, TKIs have been repurposed to treat non-cancer diseases, such as autoimmune arthritis [441]. Interestingly, recent clinical evidence suggests that TKIs can improve metabolic control in cancer patients with diabetes, preserving β cell function and mass, ameliorating insulin resistance, and allowing for discontinuation of antidiabetic therapy [442, 443]. Dasatinib is a second-generation TKI used to treat chronic myeloid leukemia and Philadelphia chromosome-positive acute lymphoblastic leukemia. It exhibits a more remarkable and extended kinase inhibitory potency than the first-generation TKIs [444]. In addition, Dasatinib is also used as a senolytic agent, which is found to primarily target preadipocytes and eliminate senescent cells by inducing cellular apoptosis [445].

3.2. Methods

3.2.1. Cell culture

HBM-PCs and hBM-SCs were isolated according to the methods in **section 2.2.2 & 2.2.3**. Both cell types were expanded in the α MEM + 20% (v/v) FBS medium on flasks coated with 0.1% (w/v) gelatin until 90% confluence. Then the cells were trypsinized with 1x 0.5% Trypsin-EDTA for 5 minutes, spun at 300 x g for 7 minutes. Cells were resuspended in the α MEM + 20% (v/v) FBS medium and seeded onto gelatin-coated 96- or 6-well plates for the following experiments.

3.2.2. Dasatinib treatment on human BM-PCs

The hBM-PCs were expanded in α MEM containing 20% (v/v) FBS until 90% confluence and then incubated with 1 μ M Dasatinib (Sigma Aldrich, CAT# CDS023389) for 48 hours, followed by 3-days recovery at 37°C in the 5% CO₂ incubator. DMSO, used to dissolve the drug, was employed as vehicle control at the same dilution as Dasatinib. After the treatment, viability, proliferation and TUNEL assays were performed as described above to measure the effects of Dasatinib on the function of hBM-PCs. ICC staining was used to analyse the expression of senescence markers: p16^{INK4a} and p21^{Waf1/Cip} in hBM-PCs.

3.2.3. Dasatinib treatment effects on human BM-PCs and BM-SCs adipose differentiation

To study the effects of Dasatinib treatment on adipogenic differentiation, hBM-PCs and hBM-SCs were incubated with the pro-adipogenic medium (1 μ M dexamethasone, 0.5 mM isobutylmethylxanthine, 10 μ g/mL insulin, and 1 μ M indomethacin in DMEM + 10% (v/v) FBS) and Dasatinib (1 μ M) for 21 days. In parallel, as controls, cells were either treated with an equal volume of DMSO (Vehicle group) or only stimulated with the pro-adipogenic differentiation media (CTRL group). Undifferentiated cells were assayed at the beginning of the protocol and served as a baseline. The differentiation protocol consisted of alternating 2 days of incubation with Dasatinib/vehicle and 3 days of

recovery without Dasatinib/vehicle for 21 days. The hBM-PCs and hBM-SCs were obtained from the same donor and used at the same passage.

After the treatment, ORO staining was performed on cells to analyse the adipocyte differentiation; RNA and proteins were harvested to measure the expression of relevant mRNAs and related proteins (PPAR γ , FABP4 and adiponectin); conditioned medium was collected for ELISA.

3.2.4. Immunocytochemistry

After Dasatinib treatment, cells were fixed with 4% (w/v) PFA and incubated with primary (anti-p16^{INK4a} and anti-p21^{Waf1/Cip1}) and secondary antibodies, according to the protocol in **section 2.2.6**. Images were acquired using Zeiss Observer.Z1 microscope under 10x and 20x objectives.

3.2.5. Oil red O staining on cells

After Dasatinib treatment and adipogenic induction on the hBM-PCs and hBM-SCs, cells were fixed. The ORO staining was performed to identify lipid droplets according to the methods in **section 2.2.7**.

3.2.6. Functional assays

3.2.6.1. Viability assay

The viability assay was performed using a Viability/Cytotoxicity Assay kit for Animal Live & Dead cells (Biotium, CAT# 30002-T) according to the vendor protocol, shown in **section 2.2.8**.

3.2.6.2. Proliferation assay

The proliferation assay was performed using a Click-iT™ EdU Imaging kit (Invitrogen, CAT# C10337) according to the vendor protocol in **section 2.2.9**.

3.2.6.3. TUNEL assay

Cellular apoptosis was measured by terminal deoxynucleotidyl transferase-mediated dUTP nick-end labelling (TUNEL) assay using the ApopTag® *In Situ* Apoptosis Detection kit (Millipore, CAT# S7165) according to the vendor protocol. This assay is based on the ability of the terminal deoxynucleotidyl transferase (TdT) enzyme to add nucleotides to the free double-stranded DNA breaks at sites of damage, thus labelling apoptotic cells. Cells were fixed with 1% (w/v) PFA for 10 minutes at RT and post-fixed with a precooled solution made of 2 parts of ethanol and 1 part of acetic acid for 5 minutes at -20°C. After washing with 1x DPBS three times, the equilibration buffer was applied to the cells for 10 seconds. Then, cells were incubated with the Working strength TdT enzyme solution for 1 hour at 37°C to label the damaged DNA with digoxigenin-conjugated dUTP. The reaction was stopped using the working strength stop/wash buffer and washed 3 times with 1x DPBS. Then, cells were incubated with anti-digoxigenin conjugated with a rhodamine fluorochrome for 30 minutes at RT, protected from light, to identify apoptotic cells. The nuclei were stained by 3 µM DAPI in 1x DPBS for 2 minutes at RT in the dark. The images were acquired using a Zeiss Observer.Z1 microscope at 200x magnification. Cells were analysed in duplicates.

3.2.7. Gene expression analysis

After Dasatinib treatment, RNA was extracted and collected for analysing the expression of adipogenic relevant genes (*FABP4*, *ADIPOQ*, and *PPARG*), according to the methods in **section 2.2.10**.

3.2.8. Western blot analysis

Western blotting (WB) was performed to assess protein expression levels. Confluent cells in a well of a 6-well plate were washed with cold 1x DPBS once and lysed with 100 µL cold lysis buffer prepared as follows: RIPA (Radioimmunoprecipitation assay) buffer (Sigma-Aldrich, CAT# R0278-500ML) supplemented with cocktails of Protease inhibitors (Dilution 1:50, Sigma-Aldrich, CAT# P8340) and Phosphatase inhibitors (Dilution 1:100, Sigma-Aldrich, CAT# P5726). The RIPA buffer contains three detergents (Triton-X100, sodium dodecyl sulfate (SDS), and sodium deoxycholate) which help disrupt cell

membranes. Two freezing-thawing cycles were performed to lyse cells and release intracellular proteins. Cell lysates were collected using a cell scraper, transferred to Eppendorf tubes, and centrifuged at 3,000 x *g* for 15 minutes at 4°C. The supernatant was collected, and the total protein concentration was quantified using a Bicinchoninic acid protein assay (BCA assay, Thermo Fisher Scientific, CAT# 23250) according to the vendor protocol and using BSA to generate a standard curve.

For samples preparation, 17 µg of total proteins were mixed with Laemmli SDS sample buffer (6x solution, from Thermo Fisher Scientific, CAT# J61337, used at a final concentration of 1x) and heated at 98°C for 8 minutes for protein denaturation. The Laemmli buffer is used to make the protein solution denser than the gel running buffer (due to glycerol) so that the samples sink into the wells of the gel; to label the solution with the tracking dye bromophenol blue to allow visualisation during migration; and to denature, reduce and negatively charge proteins thanks to the high content of SDS.

Samples were loaded into the wells of 12% precast polyacrylamide gel (Bio-Rad, CAT# 4561044) alongside the molecular weight (MW) ladder (10-180 kDa, Thermo Fisher Scientific, CAT# 26617). Proteins are separated based on MW through gel electrophoresis. 80 voltage (V) was applied for 20 minutes, then 150V for 1 hour. The electrophoresis chamber was filled with 1x running buffer (Invitrogen, CAT# LC2675-5). Since the MW of target proteins (PPAR γ : 53, 57kDa; FABP4: 15kDa; adiponectin: 27kDa) were small, a rapid semi-dry transfer blotting method was employed to transfer proteins onto 0.2 µm nitrocellulose membrane using Trans-Blot Turbo Transfer System (Bio-Rad). After transfer, the membrane was washed once with 1x Tris-buffered saline (Bio-Rad, CAT# 1706435)-0.05% (v/v) Tween-20 (TBS-T) and blocked with 5% non-fat dry milk diluted in 1x TBS-T for 1 hour at RT, and then rinsed with 1x TBS-T for 10 minutes. The membrane was incubated with primary antibodies diluted in 5% BSA/TBS-T or 5% non-fat dry milk/TBS-T overnight at 4°C. After the incubation, the membrane was washed with 1x TBS-T three times for 30 minutes and incubated with secondary antibodies: anti-rabbit (Cytiva, CAT# NA943V) or anti-mouse (Cytiva, CAT# NA9310V) conjugated with horseradish peroxidase (Dilution 1: 2000, diluted in blocking solution) for 1 hour at RT. After washing with 1x TBS-T, the membrane was incubated with ECL Prime WB Detection

Reagent (Cytiva, CAT# RPN2232) for 5 minutes in the dark. The chemiluminescence imaging was performed using the ChemiDoc™ MP system with Image Lab™ software (Bio-Rad). The antibodies used in WB analyses are listed in **Table 3-1**.

However, a pilot study was performed to test antibodies and found that anti-human FABP4 and anti-human adiponectin primary antibodies were not working, so the detection of FABP4 and adiponectin expression levels was replaced by using an enzyme-linked immunosorbent assay (ELISA) in below. Quantification of blots densitometry was performed using ImageJ. GAPDH was used as a housekeeping protein to normalise the densitometry data of assayed proteins and compare the relative protein abundance between samples.

Antibody	Reactivity	MW (kDa)	Source	Dilution	CAT#	Supplier
PPAR γ	Human	53, 57	Rabbit	1:1000	2435	Cell Signalling
FABP4	Human	15	Rabbit	1:1000	2120	Cell Signalling
Adiponectin	Human	27	Rabbit	1:1000	2789	Cell Signalling
Phospho-AKT (Ser473)	Human	60	Rabbit	1:1000	9271	Cell Signalling
AKT	Human	60	Mouse	1:2000	2920	Cell Signalling
GAPDH	Human	37	Mouse	1:1000	97166	Cell Signalling

Table 3-1 List of antibodies used for Western blot analyses.

3.2.9. ELISA assay

ELISA assay is a sensitive immunological assay to measure the levels of antibodies, antigens, proteins, and glycoproteins in biological samples. Since the WB failed to detect the protein expression of FABP4 and adiponectin, the ELISA assay was performed as a replacement. The FABP4 and adiponectin protein levels in the conditioned medium of hBM-PCs and hBM-SCs after adipogenesis differentiation were quantified using ELISA kits (R&D Systems, CAT# DY3150-05, #DY1065-05), following the vendor protocols. A 96-well high-binding plate was coated with Capture antibody for 16 hours at RT and blocked with Reagent Diluent for 1 hour. Samples and standards were added to the plate for 2 hours at RT. After washing the plate twice with an automated plate washer, samples and standards were incubated with a Detection antibody for 2 hours. Streptavidin-HRP working solution was added to each well and incubated for 20 minutes in the dark, followed by Substrate solution incubation. A Stop solution was used to stop the reaction, and the absorbance (optical density - OD) of each well was measured using a GloMax Microplate reader at 450 nm. The plate background, previously measured at 560 nm, was subtracted from the samples' OD. A standard curve was generated to derive the protein concentrations in each sample. Samples were assayed in triplicates.

3.2.10. Statistical analysis

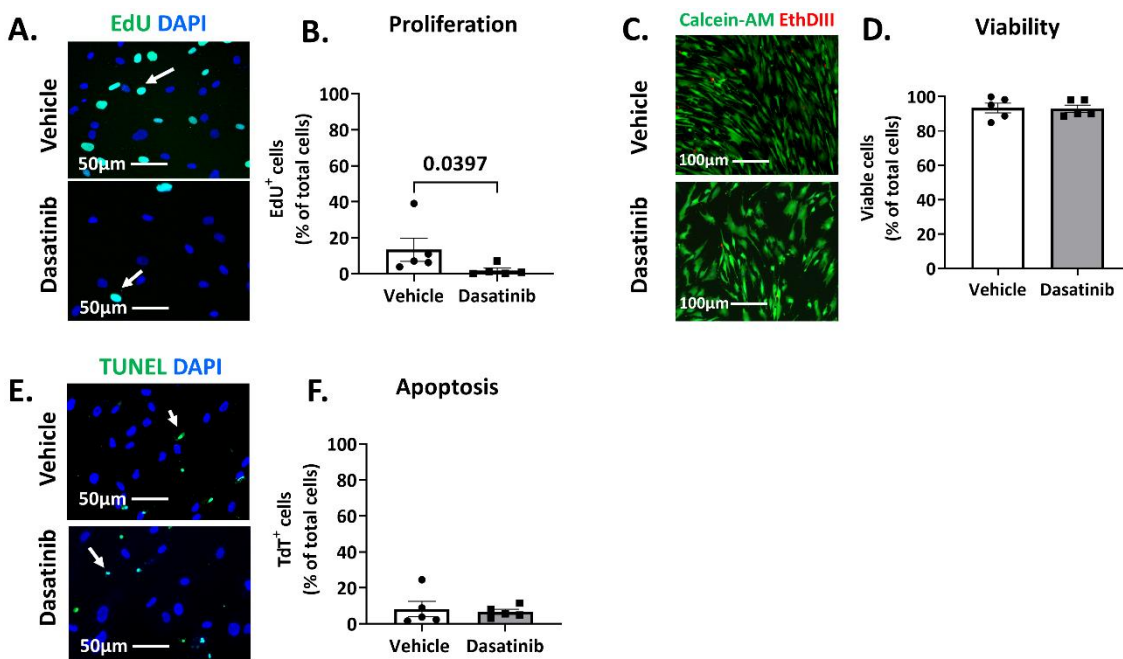
The statistical analysis was performed using the same methods as in **section 2.2.11**.

3.3. Results

3.3.1. Effects of Dasatinib on human BM-PCs

The effects of the senolytic agent Dasatinib on the senescent hBM-PCs were assessed by functional assays and ICC analysis. To this aim, I first performed a titration study to establish the suitable working, non-toxic concentration of Dasatinib (**Chapter 8. Appendix 8.1.2**), and the results of the pilot study suggested incubation cells with 1 μ M Dasatinib for 48 hours followed by 3 days recovery at 37°C in the 5% CO₂ incubator. Dasatinib-treated hBM-PCs proliferated less than the Vehicle-treated cells (**Figure 3-1 A**

and B). Conversely, Dasatinib treatment did not influence the viability (Figure 3-1 C and D) or apoptosis (Figure 3-1 E and F) of hBM-PCs. The hBM-PCs treated with Dasatinib tended to express fewer senescence markers, such as cyclin-dependent kinase inhibitor p16^{INK4a} (46.6 ± 11.8%) (Figure 3-1 G and H) and p21^{Waf1/Cip1} (55.6 ± 11.6%) (Figure 3-1 I and J), as compared to hBM-PCs in the Vehicle group (p16^{INK4a} = 60.6 ± 12.6%; p21^{Waf1/Cip1} = 74.5 ± 7.06%), although this difference was not statically significant. Altogether, these results suggest that a 48-hour treatment with 1 μM Dasatinib restrained cells' proliferation while tending to reduce the expression of senescence markers.



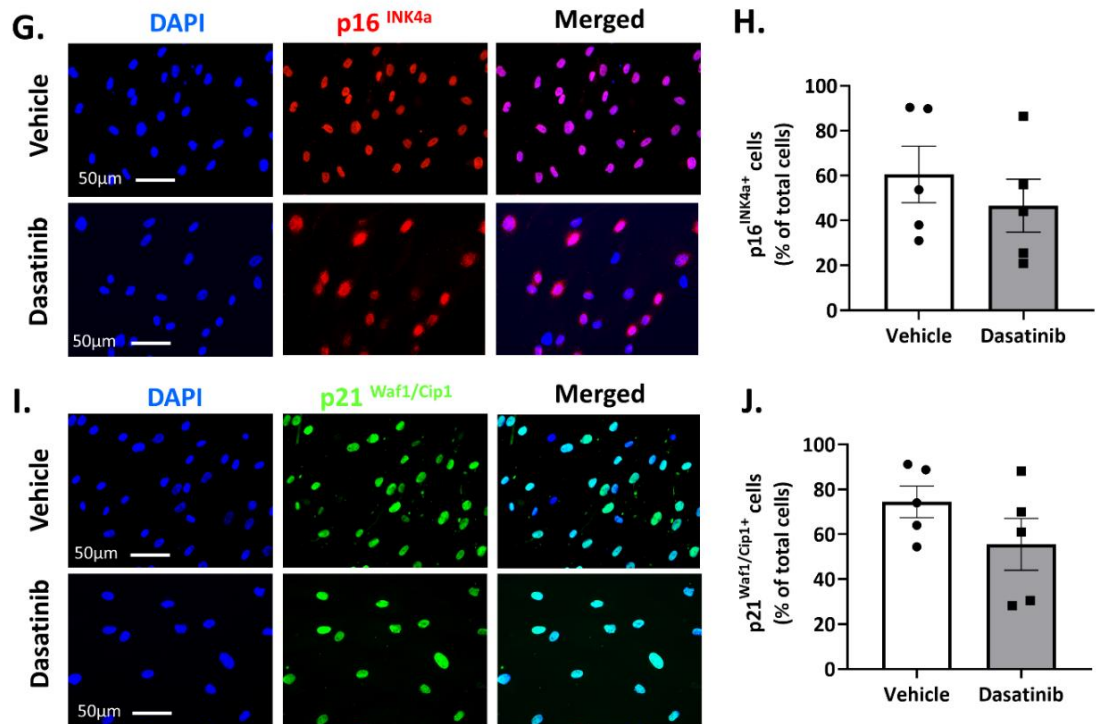


Figure 3-1 Effects of Dasatinib (1 μ M, 48 hours) or Vehicle (DMSO) treatment on human BM-PCs function and senescence.

Representative fluorescence images of (A) EdU positive (green nuclear staining) proliferating hBM-PCs, (C) Calcein-AM positive live (cytoplasmic green) / EthDIII-positive dead (nuclear red staining) cells, (E) TUNEL positive (green nuclear staining) apoptotic hBM-PCs, (G) p16^{INK4a} (red nuclear staining) and (I) p21^{Waf1/Cip1} (green nuclear staining) positive senescent hBM-PCs. DAPI labelled nuclei in blue. The bar graphs (B, D, F, H, and J) show the quantitative data (individual values and mean \pm SEM) of the above assays. n = 5 patients' cells /group. Analysis: unpaired t-test. Abbreviations: hBM-PCs = human bone marrow pericytes; EdU = 5-ethynyl-2' -deoxyuridine; EthD-III = Ethidium Homodimer III; DAPI = 4',6-diamidino-2-phenylindole.

3.3.2. Dasatinib blunts the adipose differentiation of human BM-PCs and BM-SCs

Next, I explored the effects of Dasatinib on the hBM-PCs and hBM-SCs differentiation into adipocytes. To this aim, I first performed a titration study to establish the best working, non-toxic concentration of Dasatinib. Three increasing concentrations of the drug - 0.25, 0.50, 1.00 μ M – were tested on hBM-PCs, and the effects on adipogenesis differentiation, senescence, and apoptosis were assessed (**Chapter 8. Appendix 8.1.3**). Based on these pilot data, I established that the best optimal dose was 1 μ M Dasatinib.

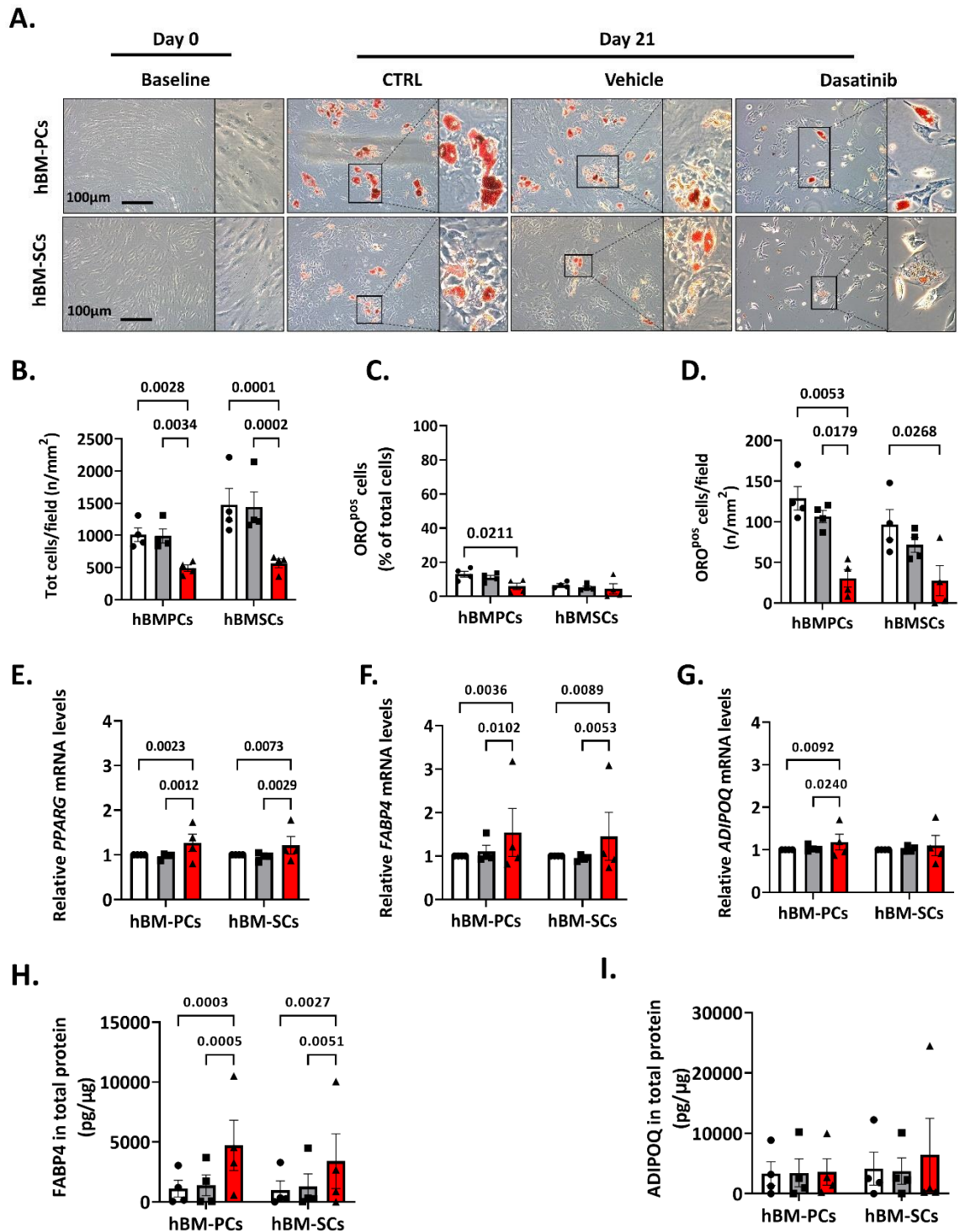
Used at this concentration, the drug reduced cellular senescence ($p21^{Waf1/Cip1} = 68.7 \pm 1.69\%$) while inducing apoptosis (**Figure 8-3**).

Bright-field images confirmed a stronger ORO staining in differentiated hBM-PCs than in hBM-SCs. Interestingly, compared with the CTRL and Vehicle groups, Dasatinib treatment reduced the number of total cells and the ability of the two cell populations to differentiate into adipocytes (**Figure 3-2A**). After 21 days, Dasatinib decreased the total cell numbers of hBM-PCs ($490 \pm 89.9/\text{field}$) and hBM-SCs ($565 \pm 89.9/\text{field}$) compared to the CTRL (hBM-PCs: $1010 \pm 89.9/\text{field}$, hBM-SCs: $1476 \pm 89.9/\text{field}$) and Vehicle (hBM-PCs: $990 \pm 89.9/\text{field}$, hBM-SCs: $1439 \pm 89.9/\text{field}$) groups (**Figure 3-2B**). Moreover, Dasatinib treatment reduced the fraction of hBM-PCs differentiated into adipocytes per total cells (**Figure 3-2C**) and the number of ORO-positive cells per microscopy field (**Figure 3-2D**).

Interestingly, the adipogenesis genes *PPARG* and *FABP4* transcription levels increased in Dasatinib-treated hBM-PCs and hBM-SCs (**Figure 3-2 E and F**). qPCR results also showed that Dasatinib-treated hBM-PCs expressed higher mRNA transcription levels of *ADIPOQ* (**Figure 3-2G**). Next, I investigated whether the relevant proteins had a similar tendency. Using ELISA, I measured secreted FABP4 and ADIPOQ levels in the conditioned medium after adipocyte differentiation. WB assessed the expression of PPAR γ in cells under different conditions, normalised by GAPDH. FABP4 was significantly increased in the conditioned medium of cells treated with Dasatinib (**Figure 3-2H**), whereas the levels of ADIPOQ remained unchanged (**Figure 3-2I**). Furthermore, the cellular expression of PPAR γ was also similar among all conditions tested (**Figure 3-2 J and K**).

These results indicate that Dasatinib treatment induced cellular apoptosis to eliminate senescent cells during adipogenic differentiation. At the same time, it promoted the transcription of adipogenesis-related mRNA *PPARG*, *FABP4* and *ADIPOQ* and upregulated the secretion of FABP4, thus inhibiting the mature adipocytes formation. The Dasatinib treatment may downregulate the expression of the pro-adipogenic factor TGF- β whilst regulating adipogenic-differentiation and -dedifferentiation relevant Wnt signalling pathway [446-448]. During differentiation, PPAR γ plays an essential role in

inducing the transcription of *ADIPOQ* and *FABP4* and promoting adipogenesis. However, high levels of *FABP4* reportedly inhibit the expression of *PPAR γ* to prevent adipocyte differentiation and instead activate apoptosis (**Figure 3-2L**) [449-451]. These results suggest a potential *PPAR γ* -*FABP4* feedback loop during Dasatinib treatment.



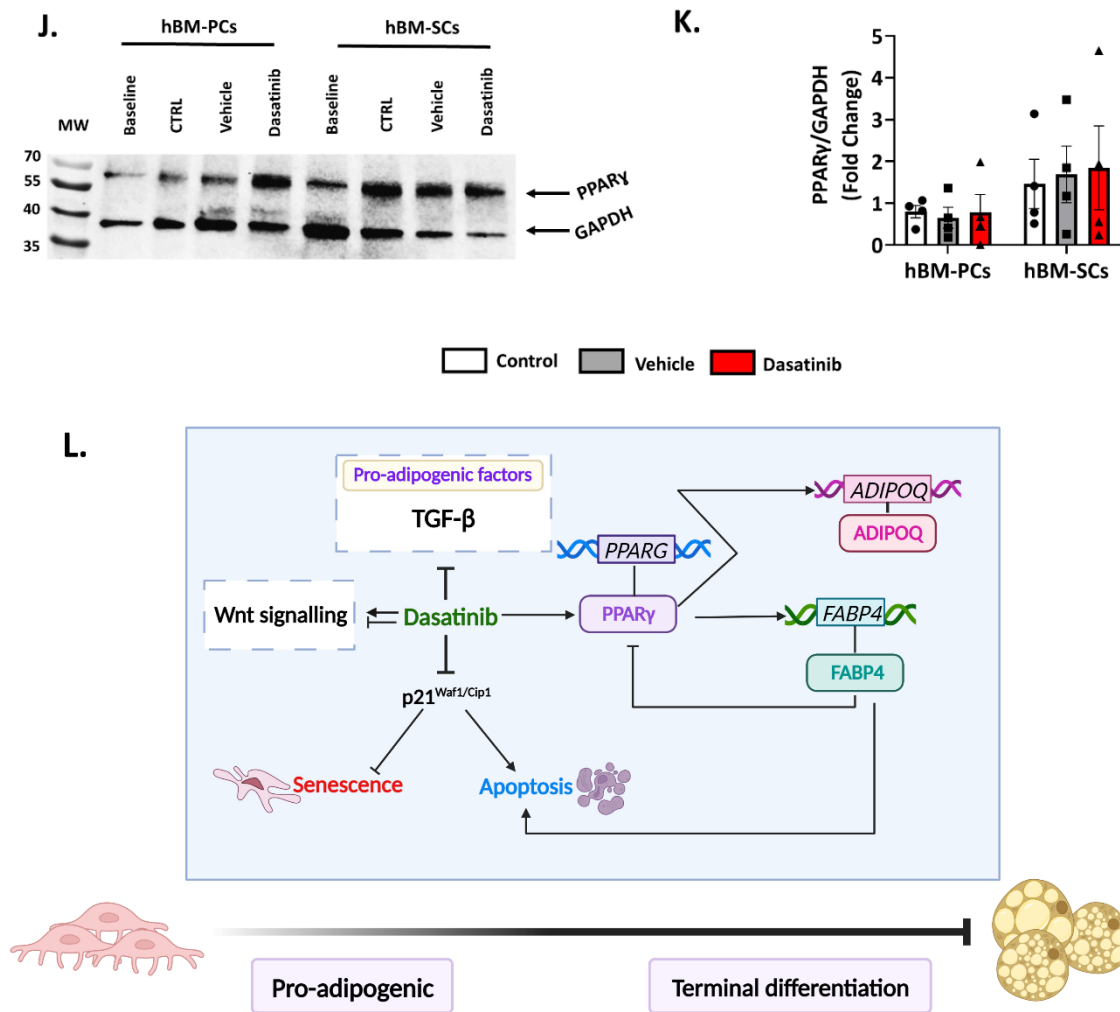


Figure 3-2 Effects of Dasatinib on the adipose differentiation of human BM-PCs and BM-SCs.

Bright-field images (A) show hBM-PCs and hBM-SCs differentiated into adipocytes (red ORO staining) after 21 days of treatment with CTRL / Dasatinib / vehicle. Histogram (B) shows the total cell number per field; histogram (C) shows the fraction of ORO-positive cells, demonstrated as a percentage of the total cells (quantification of the total cell number was performed using fluorescence images of cells stained with DAPI - images not shown); histogram (D) shows the quantitative data of ORO-positive cells per field. Bar graphs illustrate the qPCR results showing the relative expression of (E) *PPAR γ* ; (F) *FABP4*; and (G) *ADIPOQ* mRNA under different conditions. Histograms (H) and (I) show the secreted FABP4 and ADIPOQ protein levels in the conditioned medium of hBM-PCs and hBM-SCs under different treatments, as assessed by ELISA, and normalised versus the total cellular proteins. Representative Western blots (J) using cell extracts obtained from hBM-PCs and hBM-SCs. Membranes were incubated with antibodies directed against PPAR γ and GAPDH. Histogram (K) shows the results of the densitometry analysis. All the data were normalised versus the baseline (Day 0), presented as individual values and mean \pm SEM, as compared using two-way ANOVA followed by Tukey's multiple comparisons tests. $n = 4$ patients' cells/group. Cartoon (L) describes the mechanism of Dasatinib treatment. Dasatinib induces senescent cells' apoptosis by reducing the expression of p21^{Waf1/Cip1}; and inhibits adipogenesis by regulating PPAR γ -ADIPOQ

interaction and the PPAR γ -FABP4 feedback loop. Abbreviations: CTRL = control; hBM-PCs = human bone marrow pericytes; hBM-SCs = human bone marrow stromal cells; ORO = oil red O; PPAR γ /PPARG = peroxisome proliferator-activated receptor gamma; FABP4 = fatty acid binding protein 4; ADIPOQ = adiponectin.

3.4. Conclusion

The results in this chapter demonstrated that Dasatinib (1 μ M, 48 hours) treatment reduced the proliferation ability of hBM-PCs but maintained the viability and apoptosis of cells and showed no effects on improving cellular senescence. However, Dasatinib inhibited the adipogenic differentiation of hBM-PCs and hBM-SCs. The adipogenesis-related genes (*FABP4*, *PPARG*, and *ADIPOQ*) transcription levels were unpaired with their protein levels. The mechanism of Dasatinib blunting adipocyte differentiation of hBM-PCs and hBM-SCs is unclear, which is worthy of exploration in future studies.

Although Dasatinib could inhibit adipogenesis *in vitro*, its *in vivo* effects remain unknown, especially on T2DM obese models. Therefore, in Chapter 6, I investigated the effects of Dasatinib on Db/Db mice.

CHAPTER 4. *IN VIVO* EFFECTS OF DASATINIB TREATMENT ON T2DM OBESE MICE

4.1. Introduction

This chapter aims to explore the effects of *in vivo* administration of Dasatinib on T2DM obese mice heart and BM. Based on the results from Chapter 2 and Chapter 3, senolytic agent Dasatinib removed senescent hBM-PCs and blunted their adipogenic differentiation. These promising results encourage me to investigate the effects of *in vivo* administration of Dasatinib on diabetic obese mouse models, especially on the heart and BM steatosis and senescence.

T2DM is a prevalent risk factor for cardiovascular disease [163]. Early-stage cardiac remodelling in T2DM involves LV wall hypertrophy and reduced LV end-diastolic and end-systolic volumes. Underlying metabolic alterations include the loss of flexibility in myocardial substrate utilization, mitochondrial dysfunction, and the activation of inflammatory and fibrotic programs [452]. Progression of myocardial damage results in the development of heart failure, principally characterized by preserved ejection fraction [453, 454]. Cardiac steatosis, i.e., the intramyocardial accumulation of lipids, is a typical yet overlooked feature of diabetic cardiomyopathy [455].

T2DM is also associated with BM dysfunction [197]. Within T2DM, the fraction of BMAT among the total BM is significantly higher than in nondiabetic individuals, accompanied by the size increase of adipocytes in BM [198]. In Ferland-McCollough et al.'s study, hBM-MSCs from diabetic individuals showed higher adipogenesis propensity, consequently leading to fat accumulation in the BM [200]. BM microvascular remodelling was found in T2DM patients, which might relate to the hBM-PC dysfunction [302].

The combination of Dasatinib and the flavonoid Quercetin attenuated adipose tissue inflammation and senescence and improved systemic metabolic function in older mice [445, 456]. In a murine model of NAFLD, Dasatinib reportedly reduced liver steatosis, inflammation, fibrosis, and hepatocellular ballooning, by attenuating lipogenesis and inducing M2 macrophage polarization with anti-fibrotic activity [457]. Additionally, TKIs can improve the anti-lipolytic activity of insulin, thereby reducing the mobilization of FFAs from visceral fat depots [458]. Nonetheless, whether Dasatinib can halt or reverse cardiac or BM steatosis remains unknown.

4.2. Methods

4.2.1. Ethics

Animal studies were performed according to principles stated in the Animals (Scientific Procedures) Act, 1986 and the Guide for Care and Use of Laboratory Animals (Institute of Laboratory Animal Resources, 1996). Experimental protocols were covered by the UK Home Office (PPL number: PP1377882), the University of Bristol.

4.2.2. Experiment design

4.2.2.1. Short-term treatment of Dasatinib on T2DM obese mice

The *in vivo* studies were performed on 21-week-old male Db/Db mice (Envigo). Mice were fed a standard chow diet (LabDiet) and given water *ad libitum*. They were housed in conventional mouse cages in a bio-secure facility under a 12-hour light/dark cycle at 25°C. As I could not directly get 21-week-old Db/Db mice from the supplier, I had to order the younger mice (8 weeks old) and housing until they were 21 weeks old.

Two mice died during the acclimatization stage and before entering the study. Post-mortem analysis indicated the cause of death was likely a significant haemorrhage into the upper section of the small intestine, so the group size of this pilot experiment was reduced to 4 mice per group. Urine glucose levels (assessed using One+ Step® G strips)

and body weight of mice were measured during the maintenance period to confirm the stability of T2DM.

One week after baseline echocardiography, mice were randomly assigned to the two experimental groups. They received either Dasatinib (5 mg/kg) dissolved in 10% DMSO + 90% PEG300 [459] or only vehicle (10% DMSO + 90% PEG300) solvent *via* oral gavage once every 3 days for a week (Total administrations = 2). One week later, mice underwent a final echocardiography assessment under isoflurane-induced general anaesthesia (Anaesthesia with isoflurane: 2.5% for induction, 0.5-1.2% for maintenance) before being sacrificed by exsanguination (Withdrawal of blood by cardiac puncture under terminal anaesthesia, 4.0-4.5% isoflurane). Blood was collected into EDTA (0.5M, pH = 8.0, Invitrogen, CAT# AM9260G) coated Eppendorf tubes to obtain plasma. EDTA was used to prevent blood from clotting. Tubes were centrifuged at 3,500 x *g* for 10 minutes at 4°C to sediment the cells on the bottom of the tube. The supernatant - corresponding to plasma - was collected, transferred to new tubes, and stored at -80 °C until use. Urine was collected by direct aspiration from the bladder using a 25-Gauge needle and centrifuged at 4,000 x *g*, and the supernatant was transferred to a new tube and stored at -80°C. The heart, liver, spleen, visceral (pericardial and epididymal) and subcutaneous (inguinal) fats, femur and tibia were harvested. Half of each tissue was directly frozen in LN₂ and stored at -80°C for molecular biology analysis. The other half was fixed with 4% (w/v) PFA for histology study. Femur and tibia were also processed for isolating BM-SCs according to the methods in **section 4.2.4** for studying *in vitro* Dasatinib treatment effects (**see section 4.2.7**). The whole procedure of this short-term treatment experiment is shown in **Figure 4-1**. Detailed experimental procedures for the processing of animal tissues are described below.

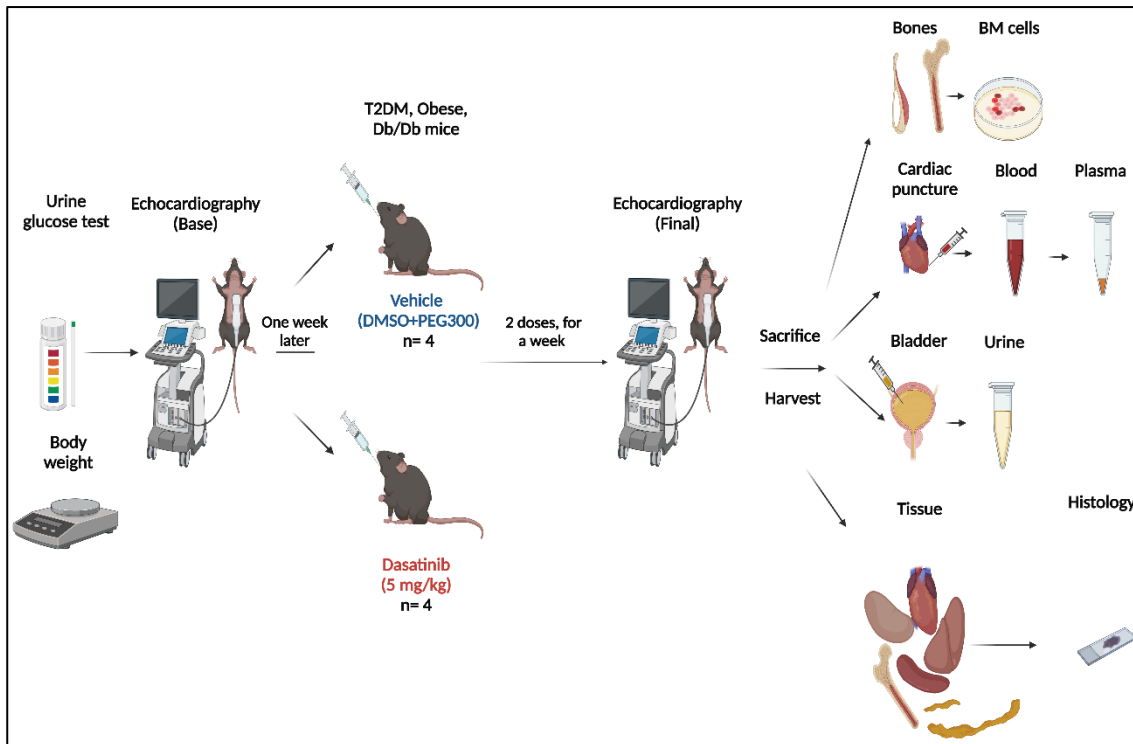


Figure 4-1 Scheme of short-term treatment of Dasatinib or Vehicle in T2DM obese mice.

4.2.2.2. Long-term treatment of Dasatinib on T2DM obese mice

The results of **section 4.2.2.1** of the short-term treatment study demonstrated that the Dasatinib treatment was safe and made us confident about investigating the benefit during a longer follow-up (**Figure 4-2**).

In this study, I introduced a NDM lean control of the same genetic background (C57BL/6) consisting of seven age- and sex-matched mice (Envigo). This C57BL/6 strain was used as a reference to confirm the deviation of diabetic mice from the healthy state. However, the primary question remained the comparison between Dasatinib and vehicle. Consequently, an unpaired statistical comparison was considered to determine the difference between the two diabetic groups. Db/Db mice were randomly allocated (as above) to receive Dasatinib (5 mg/kg) or vehicle (10%DMSO + 90% PEG300) (n = 9 mice per group) by oral gavage once per week and followed up for 4 weeks (Total administrations = 4). Urine glucose level was measured with strips as described above. At the end of follow-up 28 days after randomization, echocardiography was acquired with mice under general anaesthesia (isoflurane: 2.5% for induction, followed by 0.5-

1.2% for maintenance), and then mice were sacrificed under terminal anaesthesia (4.0-4.5% isoflurane), followed by heart and bladder puncture to collect blood, urine, and finally, harvested tissue. Plasma, urine, and half of the frozen tissue were stored at -80°C for molecular biology, and the other half of the tissues were fixed with 4% (w/v) PFA for histology. Total BM cells isolated from the femur and tibia were used for flow cytometry analysis (see section 4.2.8). Detailed experimental procedures for the processing of animal tissues are described below.

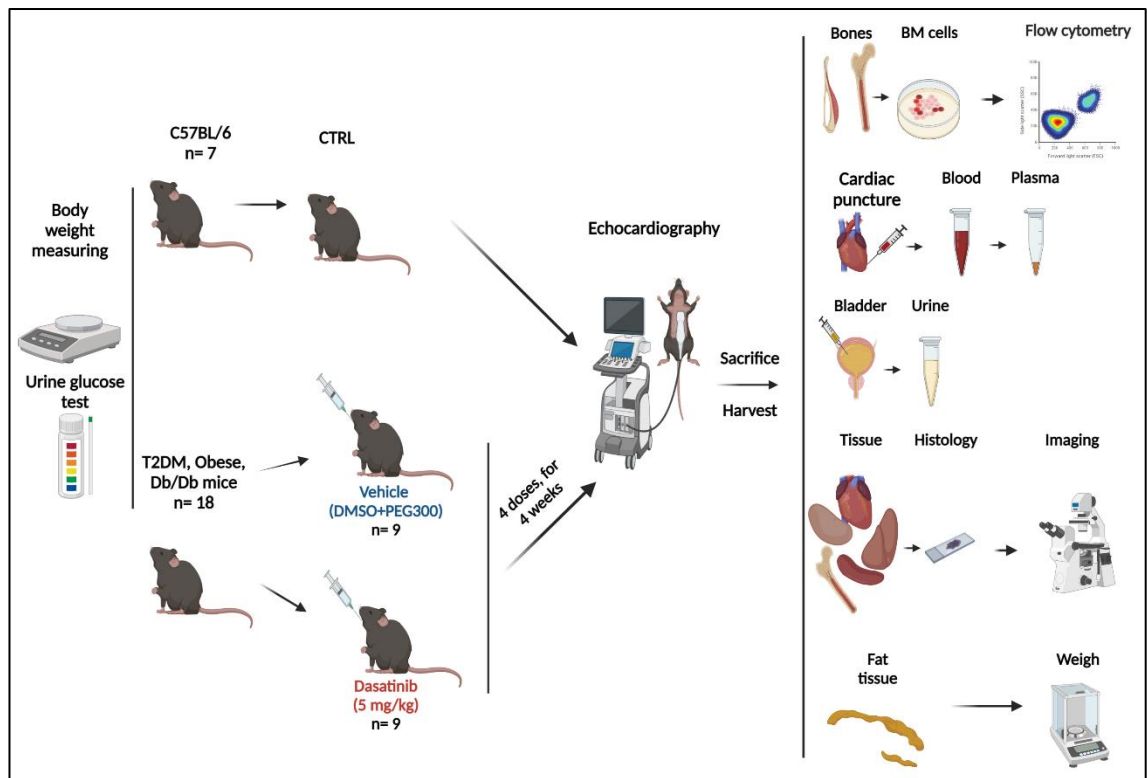


Figure 4-2 Scheme of long-term treatment of Dasatinib or Vehicle on T2DM obese mice.

4.2.3. Echocardiography

Echocardiography was performed to measure mice hearts' dimensional and functional parameters before sacrifice through the Vevo3100 echocardiography system (Fujifilm VisualSonics), using MX400 or MX550D transducers according to the body weight of the animal. The measurement was performed on the mice under isoflurane anaesthesia: 2.5% for induction, followed by 0.5-1.2% to maintain a heart rate close to 400-450 bpm. Before scanning, the animal's chest was shaved, and the pre-warmed ultrasound gel was

applied to the skin. Echocardiography images were obtained from the following views and planes: (1) parasternal long-axis (PSLAX) or parasternal short-axis (PSAX) brightness mode (B-mode); (2) PSLAX or PSAX motion mode (M-mode); (3) Apical four chamber (AP4) pulsed wave (PW) Doppler imaging and (4) AP4 tissue Doppler analysis.

The B-Mode and M-mode images acquired from PSLAX and PSAX views demonstrated the left ventricle (LV) systolic function and LV size. The following parameters were directly acquired from the M-mode or B-mode images both in systole (s) and diastole (d): heart rate (HR), left ventricular internal diameters (LVID; s and LVID; d), left ventricular anterior wall thickness (LVAW; s and LVAW; d) and left ventricular posterior wall thickness (LVPW; s and LVPW; d). Based on these values, other parameters could be calculated following the formulas [460] shown in **Table 4-1**, such as ejection fraction (EF), fractional shortening (FS), stroke volume (SV), left ventricular end-systolic and end-diastolic volumes (Volume; s and Volume; d), cardiac output (CO) and LV mass. In the case of differences in body weight, SV, Volume; s and Volume; d were normalized to body weight and expressed as SV correction (SV, Cor), Volume; s correction (Volume; s, Cor) and Volume; d correction (Volume; d, Cor) and CO was normalized to body surface area [461] and showed as a cardiac index (CI).

The AP4 PW Doppler and tissue Doppler images demonstrated the LV diastolic function of mice [460, 462] (**Table 4-1**). From PW-Doppler images, the LV filling velocity was evaluated by the following parameters: early (E) and late (A) diastolic transmitral Doppler flow velocities ratio (E/A), E wave deceleration time (DT), isovolumic relaxation time (IVRT), isovolumic contraction time (IVCT); myocardial performance index (MPI); non-flow time (NFT); aortic ejection time (AET) and mitral valve pressure half time (PHT). From tissue-Doppler images, the peak early diastolic annular velocity (e') was acquired to measure the myocardial motion in early diastole; the peak late diastolic annular velocity (a'); E/e' ratio was calculated to estimate the LV filling pressures, which was a crucial parameter in clinical diagnosis of heart failure with preserved EF (HFpEF) [463]. The image analyses and parameters calculation were performed using Vevo Lab 5.7.1 software.

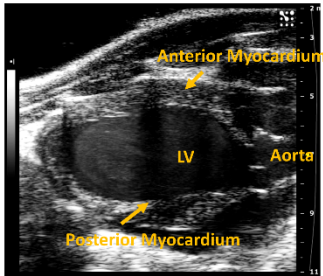
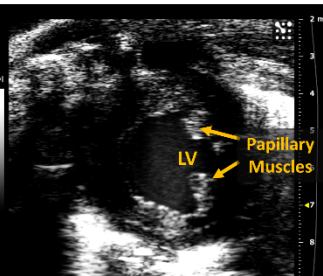
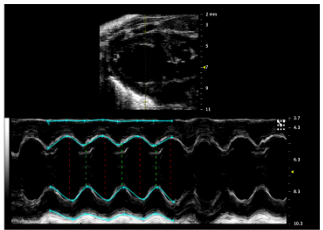
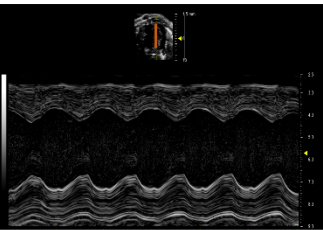
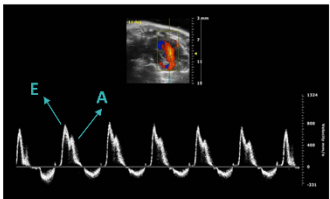
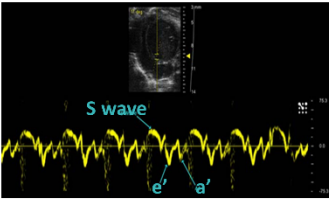
LV systolic function			
	PSLAX	PSAX	Measurements & Calculations
B-Mode			<ul style="list-style-type: none"> • HR • LVID • Wall thickness • FS (%)= (LVID;d-LVID;s)/LVID;d x 100 • Volume;s= (7/(2.4+LVID;s)) x LVID;s³ • Volume;d= (7/(2.4+LVID;d)) x LVID;d³ • SV= Volume;d - Volume;s • EF (%)= (Volume;d-Volume;s)/ Vol;d x 100 • CO= SV x HR • Body surface area= 9.82 x (body weight)^{2/3} (for C57/BL6 mouse) • Body surface area = 8.29 x (body weight)^{2/3} (for Db/Db mouse) • CI= CO/ Body surface area • LV mass= 1.04 [(LVID;d+LVAW;d+LVPW;d)³-LVIDd³]x0.8+0.6
M-Mode			
LV diastolic function			
	PW-Doppler	Tissue Doppler	Measurements & Calculations
			<ul style="list-style-type: none"> • E • A • e' • a' • E/A ratio= E/A • E/e' ratio= E/e' • e'/a' ratio= e'/a' • DT • IVRT • IVCT • AET • MPI = (IVRT+IVCT)/AET • PHT = 0.29 x DT • NFT

Table 4-1 Representative views of PSLAX B-mode & M-mode; PSAX B-mode & M-mode; PW Doppler and tissue Doppler and the parameters acquired from the above views.

Abbreviations: LV = left ventricle; PSLAX = parasternal long-axis; PSAX = parasternal short-axis; B-mode = brightness mode; M-mode = motion mode; Ap4 = apical four chamber; PW = pulsed wave; HR = heart rate; s = systole; d = diastole; LVID = left ventricular internal diameters; FS = fractional shortening; SV = stroke volume; EF = ejection fraction; CO = cardiac output; CI = cardiac index; E = early velocity; A = late velocity; e' = peak early diastolic annular velocity; a' = peak late diastolic annular velocity; DT = E wave deceleration time; IVRT = isovolumic relaxation time and IVCT = isovolumic contraction time; AET = aortic ejection time; NFT = non-flow time; MPI = myocardial performance index; PHT = mitral valve pressure half time. Echocardiograms source: <https://www.visualsonics.com/image-galle>.

4.2.4. Mouse BM cells isolation and expansion

4.2.4.1. Total BM cells isolation

Mouse BM cells were isolated according to Marianna et al.'s protocol [464]. The leg bones were collected during the final tissue harvest of animal experiments, put in sterile tubes containing 20 mL 1x DPBS, placed on ice and processed to collect BM cells within one hour. After removing muscle and skin from the bones, the proximal and distal ends were cut from the femur and tibia. The BM was flushed with 1x DPBS using syringes with 23-gauge needles until the bone cavity was empty and clean and centrifuged at 200 x *g* for 10 minutes at 25°C to separate the BM blood from the cellular component. Cell pellets, sedimented on the bottom of the tubes, were resuspended and incubated with 1x red blood cell (RBC) lysis buffer (Invitrogen, CAT# 00-4333-57) for 2 minutes at 4°C. This step was performed to remove unwanted erythrocytes. Cells were washed with 1x DPBS and centrifuged at 200 x *g* for 10 minutes. The pellet was resuspended in α MEM + 20% (v/v) FBS and counted. A total of 5×10^5 suspended BM cells were used in flow cytometry analysis (used in long-term treatment experiment, shown in **section 4.2.2.2**).

4.2.4.2. Mouse BM-SCs expansion

1×10^6 mouse BM cells isolated from **section 4.2.4.1** were seeded in a T25 flask and cultured with α MEM + 20% (v/v) FBS (used in the short-term treatment experiment, shown in **section 4.2.2.1**). After 48 hours of culture, the culture medium was changed from the seeded cells to remove the non-adherent HSCs. The remaining adherent cells were mouse BM-SCs (mBM-SCs) [465]. Then, the mBM-SCs were washed with 1x DPBS and cultured in α MEM + 20% (v/v) FBS at 37°C in the 5% CO₂ incubator.

4.2.5. Histology

4.2.5.1. General tissue processing

Heart, liver, spleen, and kidney tissues were harvested and directly fixed with 4% (w/v) PFA for 24 hours at 4°C, washed once in 1x PBS, and then transferred into 30% (w/v) sucrose (Sigma- Aldrich, CAT# S0389-1KG) for 48 hours at 4°C. Tissues were embedded

with Optimal Cutting Temperature compound (OCT, CellPath, CAT# KMA-0100-00A) and stored at -80°C . Heart samples were sectioned on the Cryostat STAR Nx50 (Thermo Fisher) at $6\ \mu\text{m}$ thickness. The rest of the organs' tissues were stored at -80°C for the possible experiment.

4.2.5.2. Bone processing

Femoral bones were collected and cleaned from the surrounding tissues, rinsed once with PBS, and fixed with 4% (w/v) PFA for 24 hours at 4°C . After fixation, tissues were decalcified with 10% (v/v) formic acid for 48 hours at RT. Bone decalcification is a process of softening bones by removing calcium ions and is necessary for bone sectioning and staining. An endpoint check of decalcification is used to test the residual calcium of specimens since a partially decalcified sample may cause poor staining [466]. The endpoint check of decalcification was performed by adding an equal volume of 5% (w/v) ammonium oxalate (Sigma-Aldrich, CAT# 221716-100G), 5% (w/v) ammonium hydroxide (Sigma-Aldrich, CAT# 09859-250ML) and decalcifying solution containing the bone specimens into a 1.5 mL Eppendorf tube to stand for 16 hours at RT. The decalcification was considered complete only if there was no precipitate. After decalcification, samples were washed with running water for 48 hours to remove the formic acid, placed in 30% (w/v) sucrose for 24 hours at 4°C , embedded with OCT, and sectioned at $12\ \mu\text{m}$ -thick.

4.2.5.3. Immunohistochemistry of mouse heart and BM sections

Frozen tissue sections were fixed with cold acetone (Sigma-Aldrich, CAT# 24201-2.5L-M) for 5 minutes at -20°C . After fixation, slides were air-dried at RT for 30 minutes, rehydrated with distilled water for 3 minutes, and washed with 1x PBS for 10 minutes. This step was followed by a heat-induced epitope retrieval (HIER) to expose epitopes that were masked during PFA fixation and allow epitope-antibody interaction. Sections were heated in 1x citrate buffer (pH = 6.0, Sigma-Aldrich, CAT# C9999-1000ML) using a microwave on low power for 11 minutes, cooled down to RT and washed 3 times in 1x PBS. Sections were incubated with 20% (v/v) goat serum (Vector Laboratories, CAT# S-

1000) in 1x PBS for 30 minutes at RT to block the unspecific binding sites. Serum is a blocking agent which contains antibodies that bind to the tissue's non-specific sites. Using serum matching the species of the secondary antibodies prevents non-specific binding of the secondary antibodies to the tissue. A pilot staining was performed to test the antibodies of senescence markers: p21^{Waf1/Cip1}, p16^{INK4a}, γ H2AX, and ki67 on mouse heart and BM specimens, and the results indicated only p16^{INK4a} antibody was working. Next, to assess cellular senescence, slides were incubated with anti-p16^{INK4a} (Dilution 1:50, Santa Cruz, CAT# sc-1661) primary antibody in 1% BSA (w/v) in 1x PBS overnight at 4°C, followed by an incubation in the oven for 30 minutes at 37°C. After washing three times with 1x PBS, sections were incubated with secondary antibody (Dilution 1:200, Alexa Fluor 568-conjugated goat anti-mouse IgG, Invitrogen, CAT# A11004) diluted in 1x PBS for 1 hour at 37°C, protected from light. This step was followed by three washes with 1x PBS. The nuclei were stained with 5 μ M DAPI in 1x PBS for 18 minutes at RT, protected from light. Slides were washed with 1x PBS for 15 minutes, rinsed once in distilled water for 3 minutes and mounted with Fluoromount-G (Invitrogen, CAT# 00-4958-02).

For the BM sections, the tissue autofluorescence was reduced by incubating slides with 0.1% (w/v) Sudan black (Sigma-Aldrich, CAT# 199664-25G) in 70% ethanol for 5 minutes at RT, followed by a rinse under running water for 30 minutes, a wash with distilled water for 15 minutes and mounting for imaging. Immunofluorescent images were acquired under 40x and 63x objectives of the Leica SP8 LIGHTNING confocal microscope. Controls omitting primary antibodies were performed for each slide to exclude the non-specific binding of secondary antibodies (images not shown). Since the host of p16^{INK4a} antibody is mouse, to rule out non-specific binding of the primary mouse antibody to the mouse tissue, I have performed stainings using a mouse IgG2a isotype control (same isotype as the anti-p16^{INK4a} mouse antibody, used at the same concentration (images not shown)). Details of the primary and secondary antibodies used in immunohistochemistry (IHC) are listed in **Table 4-2**. Two sections were analysed for each mouse.

Antigen	Host	Reactivity	Dilution (Working concentration)	Supplier & CAT#	2 nd Abs
P16 ^{INK4a}	Mouse	Mouse	1:50 (4 µg/mL)	Santa Cruz, SC-1661	Invitrogen, Alexa568 goat anti- mouse
Mouse IgG2a isotype control	Mouse / IgG2a	Mouse	1:250 (4 µg/mL)	Invitrogen, 02-6200	Invitrogen, Alexa568 goat anti- mouse

Table 4-2 Primary and secondary antibodies used in immunohistochemistry studies.

4.2.5.4. Oil red O staining on mouse heart and BM sections

The sections were equilibrated for 10 minutes at RT once removed from -20°C. Slides were covered with 1 mL ORO working solution (**described in section 2.2.7**) and incubated for 5 minutes for heart sections or 10 minutes for BM sections in a humid chamber. After incubation, slides were rinsed with running water for 30 minutes. Slides were mounted with Fluoromount-G and imaged within 24 hours at 400x and 600x magnification using an Olympus BX40 light microscope. Two sections were analysed for each mouse.

4.2.5.5. Azan Mallory staining on mouse heart sections

Myocardial interstitial fibrosis was identified using Azan Mallory staining [467]. The cryosections were post-fixed in acetone at -20°C for 5 minutes and then air-dried at RT. Sections were rehydrated with 1x PBS for 10 minutes and washed once in distilled water. Sections were stained by sequential incubations with the following solutions: 0.1% (w/v) Azocarmine G (Sigma-Aldrich, CAT# A1091-10g) at 60°C for 1.5 hours, followed by 5% (v/v) Phosphotungstic acid (Sigma-Aldrich, CAT# P4006-100g) at RT for 2 hours, and finally Mallory solution (0.5% (w/v) Methyl blue (Sigma-Aldrich, CAT# M5528-25g) + 2%

(w/v) Orange G (Sigma-Aldrich, CAT# O7252-100g) + 8% (v/v) Acetic acid (Sigma-Aldrich, CAT# A6283-500ml) in distilled water) at RT for 2 hours. After dehydration with d-Limonene (Mangnacol, d-Limonene-5L), sections were mounted with Eukitt® Quick-hardening mounting medium (Sigma-Aldrich, CAS# 25608-33-7). Images were acquired at 400x magnification using an Olympus BX40 light microscope.

4.2.5.6. Immunocytochemistry

After Dasatinib treatment (see **section 4.2.7**), mBM-SCs were fixed with 4% (w/v) PFA. Then cells were incubated with primary (anti-p16^{INK4a}, anti-p21^{Waf1/Cip1}, anti-γH2AX, and anti-ki67) and secondary antibodies (**Table 2-1**) according to the protocol described in **section 2.2.6**. Images were acquired using Zeiss Observer.Z1 microscope under 10x and 20x objectives.

4.2.6. Multiplex assay

A multiplex assay was performed with simultaneous quantification to assess the effects of Dasatinib treatment on multiple mouse plasma adipokines levels. Mouse plasma adiponectin, IL-6, insulin, leptin, MCP-1, PAI-1 total, resistin, and TNF-α expression levels were measured using a Milliplex Mouse Plasma Adipokine kit (Millipore, CAT# MADKMAG-71k), according to manufacturer's instructions. The plate was pre-coated with Assay buffer for 10 minutes at RT. Neat samples and standards were added to the plate, followed by incubation with mixed beads agitating on a plate shaker overnight at 4°C. After the incubation, the plate was placed on a magnet for 1 minute to allow the settling of magnetic beads and then washed with Wash buffer 3 times. Samples were incubated with Detection antibodies on the shaker for 30 minutes at RT, followed by Streptavidin-Phycoerythrin incubation. After washing, 100 μL of Sheath Fluid was added to all wells and fluorescence was detected using a Luminex MAGPIX system (Bio-RAD, Bio-Plex® MAGPIX™ Multiplex Reader). Each factor was analysed in duplicates.

4.2.7. *In vitro* Dasatinib treatment on mouse BM-SCs

Mouse BM-SCs were expanded in α MEM supplemented with 20% (v/v) FBS. Once approached 90% confluence, cells were incubated with Dasatinib (1 μ M) for 48 hours, and DMSO was used as vehicle control. After the treatment, ICC staining (methods shown in **section 4.2.5.6**) was used to analyse the expression of senescence markers (p16^{INK4a}, p21^{Waf1/Cip1}, γ H2AX) and a cell cycling marker (ki67).

4.2.8. Flow cytometry analyses on mouse BM cells

Flow cytometry analyses on total mouse BM cells were performed to assess the cellular senescence and the activity of mitochondria of the mBM-MSCs population. Total mouse BM cells were isolated from the mouse femur and tibia following the protocol in **section 4.2.4.1**.

A total of 500,000 cells were washed once with 1x DPBS, spun at 200 x *g* for 10 minutes, then stained with 100 μ L Zombie Aqua dye (Dilution 1:1000, diluted in 1x DPBS) for 20 minutes, at RT, protected from light, to assess cell viability. After washing with cold fluorescence-activated cell sorting (FACS) buffer, cells were incubated with TruStain FcX™ PLUS (anti-mouse CD16/32) antibody (Biolegend, CAT# 156603) for 10 minutes on ice at 1:200 dilution in 1x DPBS to inhibit the non-specific binding of the immunoglobulin to the Fc receptors. Next, cells were incubated with the following antibodies combinations to determine the antigenic profile: anti-mouse CD36, anti-mouse DPP4, anti-mouse CD29, anti-mouse CD45, anti-mouse CD73, anti-mouse Sca-1, anti-mouse CD11b in FACS buffer for 30 minutes, at 4°C, in the dark. After the staining of antibody combinations, MitoTracker® Deep Red (MDR) FM Mitochondrion-selective probes kit (Invitrogen, CAT# M46753) was performed to assess the activity of mitochondria by incubating cells with 25 nM working solution for 1 hour, at 37°C, spun at 300 x *g* for 7 minutes and wash once with 1x DPBS. After MDR staining, CellEvent™ Senescence Green Flow Cytometry Assay kit (SG, Thermo Fisher Scientific, CAT# C10841) was performed to detect senescent cells. After washing with 1x DPBS and spinning at 200 x *g* for 10 minutes, cells were fixed with 2% PFA (w/v) and then incubated with SG staining buffer (Dilution 1:1000, in FACS buffer) for 1 hour, at 37°C, without CO₂, protected from light,

to assess cell senescence. Fluorescence minus one (FMO) controls were included in the flow cytometry panels to confirm the specificity of the antibodies binding to the cells. The BD™ CompBead Plus Anti-Mouse Ig, κ beads (BD Bioscience, CAT# 560497) were used to optimize the fluorescence compensation settings for multicolour flow cytometric analyses. The BD LSR II Fortessa X20 (Becton Dickinson) and FlowJo v10.8.1 software were used to acquire the data for the following analyses. All the antibodies used in the mouse BM flow cytometry study are listed in **Table 4-3**.

To optimize the staining procedure, each antibody was titrated with four different dilutions (anti-CD36 antibody dilution: 1:10, 1:20, 1:40 and 1:80; anti-DPP4 antibody dilution: 1:20, 1:40, 1:80, and 1:160; anti-CD29 antibody dilution: 1:10, 1:20, 1:40 and 1:80; anti-CD45 antibody dilution: 1:40, 1:80, 1:160 and 1:320; anti-CD73 antibody dilution: 1:40, 1:80, 1:160 and 1:320; anti-Sca-1 antibody dilution: 1:20, 1:40, 1:80 and 1:160; anti-CD11b antibody dilution: 1:50, 1:100, 1:200 and 1:400 (data not shown). For all the kits used, the manufacturer’s guidelines were followed.

Antibody	Reactivity	Dilution	Fluorophores	Supplier
CD36	Mouse	1:30	Super Bright 600	eBioscience
DPP4	Mouse	1:20	PE	Biolegend
CD29	Mouse	1:10	APC-Vio 770	Miltenyi Biotec
CD45	Mouse	1:160	Brilliant Violet 785	Biolegend
CD73	Mouse	1:80	Super Bright 702	eBioscience
Sca-1	Mouse	1:40	Brilliant Violet 421	Biolegend
CD11b	Mouse	1:100	APC-Vio® 770, REAfinity™	Miltenyi Biotec

Table 4-3 List of antibodies used in mouse bone marrow cells flow cytometry analyses.

4.2.9. Statistical analysis

The statistical analysis was performed using the same methods as in **section 2.2.11**.

4.3. Results

4.3.1. *In vivo* effects of short-term Dasatinib treatment on T2DM obese mice

4.3.1.1. Animal model

Each mouse received two doses for one week (**Figure 4-3A**), and the final echocardiography was performed before the animals were sacrificed. Db/Db mice showed evident glycosuria (> 2000 (111) mg/dL (mmol/L), **Figure 4-3B**), confirming the stability of the diabetic status. Body weight was measured for each animal before each oral gavage to calculate the amount of Dasatinib administered during each treatment.

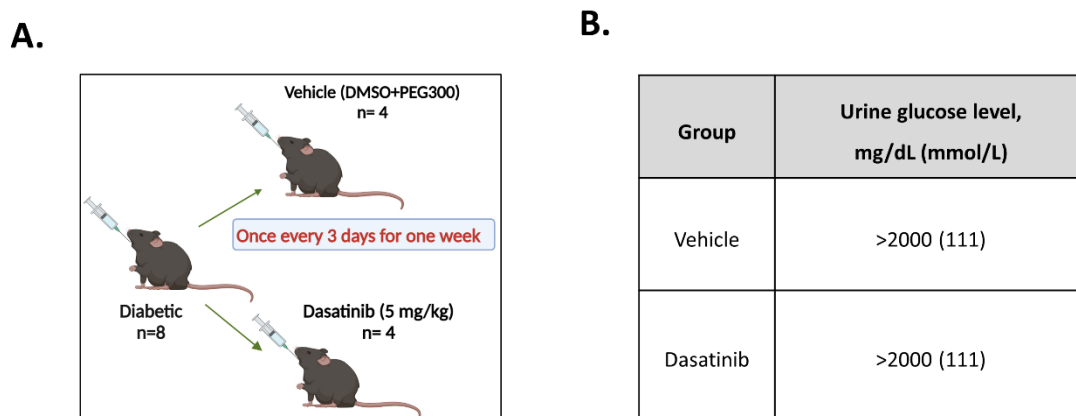


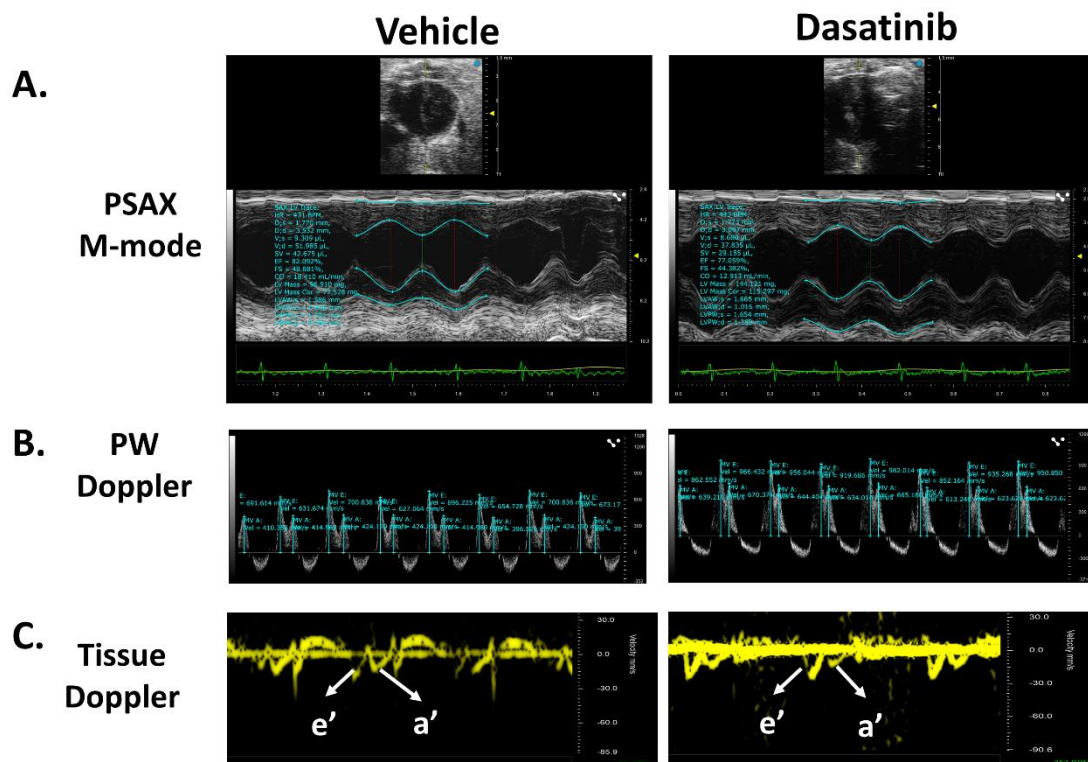
Figure 4-3 (A) Cartoon of short-term Dasatinib treatment on T2DM obese mice. (B) Table of glycosuria level in T2DM obese mice during the short-term Dasatinib treatment.

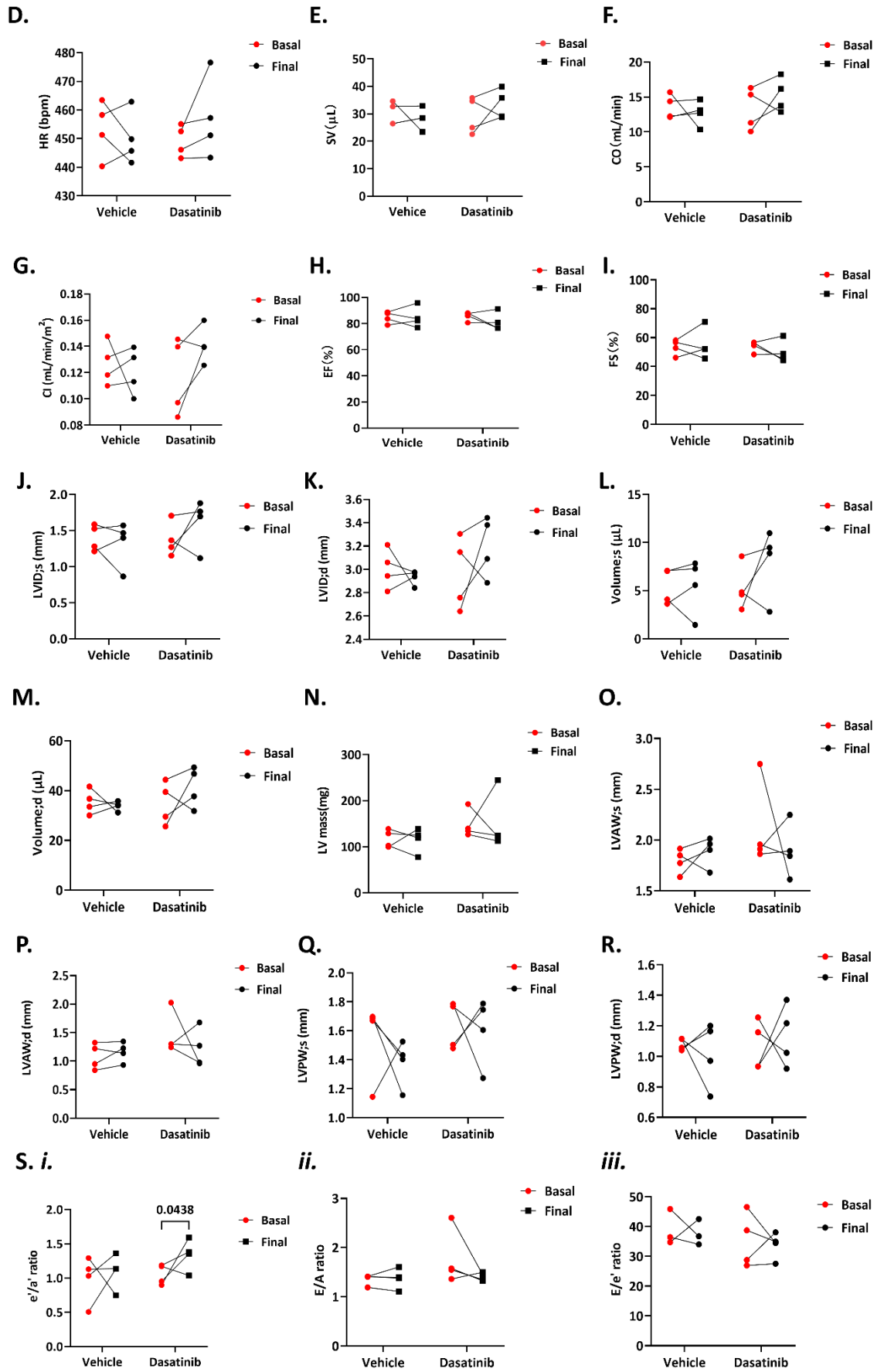
Eight Db/Db mice were randomly divided into two groups: the Vehicle group (10% DMSO + 90% PEG300) and the Dasatinib group (5 mg/kg) and received two gavages in one week. Urine glucose level was measured with parameter urine testing strips for all mice to confirm the stability of the diabetic model. $n = 4$ mice/group.

4.3.1.2. Effects of Dasatinib on T2DM obese mice cardiac function

Basal echocardiography was performed before treatment to compare the baseline and final cardiac function for all mice and compare the changes between the Vehicle and Dasatinib groups after one week of Dasatinib treatment (**Figure 4-4 A to C**). All the parameters were measured under similar HR (450 ± 2.97 bpm, **Figure 4-4D**). After

treatment, the hemodynamic parameters, such as SV, CO, and CI, remained comparable between the Dasatinib and Vehicle groups (**Figure 4-4 E to G**). Likewise, EF (**Figure 4-4H**) and FS (**Figure 4-4I**) were similar after treatment. The dimensional parameters, including LVID; s and LVID; d (**Figure 4-4 J and K**), end-systolic and end-diastolic volume (**Figure 4-4 L and M**), LV mass (**Figure 4-4 N**), LVAW and LVPW (**Figure 4-4 O to R**) showed no changes between Dasatinib and Vehicle groups. Moreover, the diastolic parameter, e'/a' ratio, increased in the Db/Db mice after Dasatinib treatment compared to the baseline ($p = 0.0438$) (**Figure 4-4 Si**). However, the other parameters did not show improvement after Dasatinib treatment (**Figure 4-4 Sii-Sx**). Altogether these data indicate that a one-week treatment with Dasatinib was not sufficient to improve the cardiac function of the T2DM mouse model.





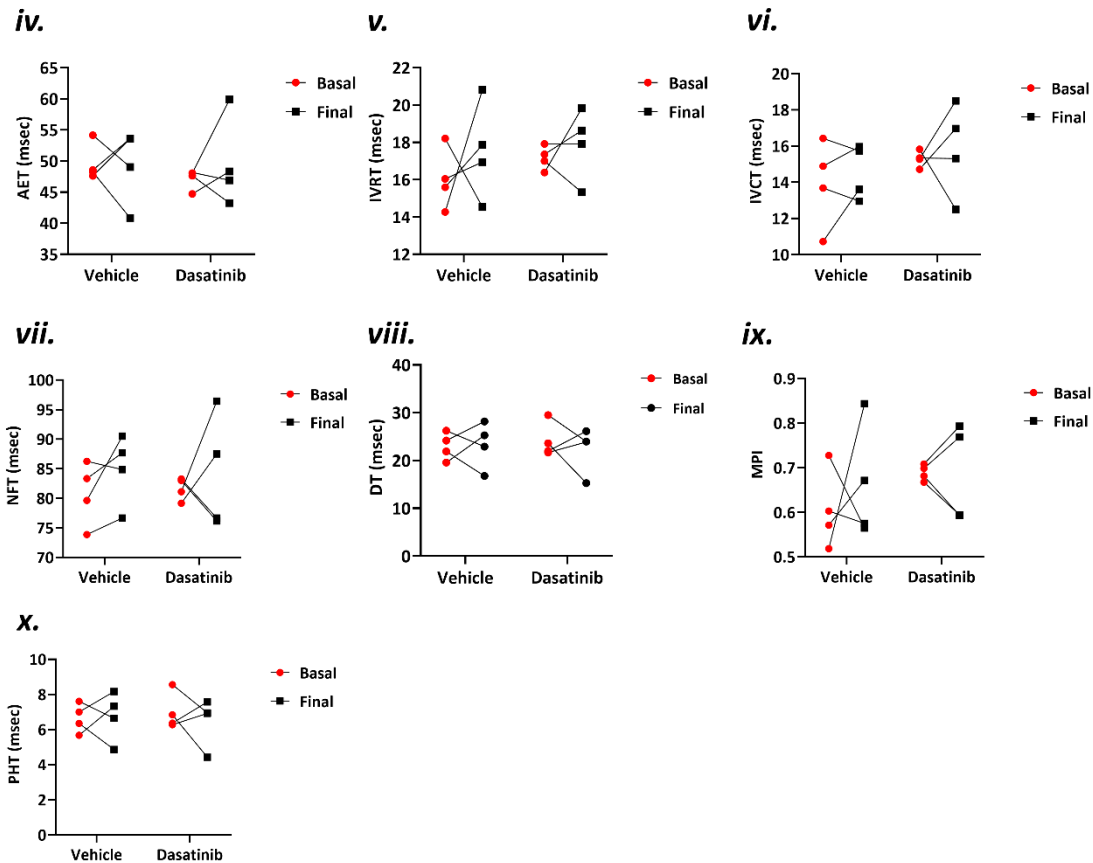


Figure 4-4 Cardiac function is evaluated by echocardiography in 21- and 22-week-old T2DM obese mice before and after the short-term Dasatinib treatment.

Representative echocardiograms of (A) PSAX M-mode traces, (B) PW Doppler and (C) tissue Doppler measurements. Graphs show the influence of Dasatinib on the following parameters of systolic function: (D) HR (bpm); (E) SV (μL); (F) CO (mL/min); (G) CI (ml/min/m²); (H) EF (%); (I) FS (%); (J) LVID; s (mm); (K) LVID; d (mm); (L) Volume; s (μL); (M) Volume; d (μL); (N) LV mass (mg); (O) LVAW; s (mm); (P) LVAW; d (mm); (Q) LVPW; s (mm); (R) LVPW; d (mm); and diastolic function (Si) e'/a' ratio; (Sii) E/A ratio; (Siii) E/e' ratio; (Siv) AET (msec); (Sv) IVRT (msec); (Svi) IVCT (msec); (Svii) NFT (msec); (Sviii) DT (msec); (Six) MPI; (Sx) PHT (msec). Data are presented as individual values and mean \pm SEM and were analysed using a two-way ANOVA followed by Tukey's multiple comparisons tests. $n = 4$ mice/group. The cardiac index is represented by the cardiac output normalised versus the body surface area. Abbreviations: NDM CTRL = non-diabetes mellitus control; T2DM = type 2 diabetes mellitus; HR = heart rate; SV = stroke volume; EF = ejection fraction; CO = cardiac output; CI = cardiac index; LVID = left ventricular internal diameters; DT = deceleration time; s = systolic; d = diastolic; LV = left ventricle; FS = fractional shortening; LVAW = left ventricular anterior wall thickness; LVPW = left ventricular posterior wall thickness; A = late mitral inflow peak velocity; a' = late mitral annulus peak velocity; E = early mitral inflow peak velocity; e' = early diastolic mitral annulus peak velocity; AET = aortic ejection time; NFT = non-flow time; IVCT = isovolumic contraction time; IVRT = isovolumic relaxation time; MPI = myocardial performance index; PHT = mitral valve pressure half time.

4.3.1.3. Effects of Dasatinib on T2DM obese mice plasma adipokines expression

Next, I performed multiplex assay to investigate whether Dasatinib treatment regulates the expression level of several adipokines in plasma. The results showed that IL-6 ($p = 0.07$, **Figure 4-5A**), MCP-1 ($p = 0.40$, **Figure 4-5B**), PAI-1 ($p = 0.11$, **Figure 4-5C**), insulin ($p = 0.98$, **Figure 4-5D**), resistin ($p = 0.96$, **Figure 4-5E**), and leptin ($p = 0.34$, **Figure 4-5F**) were not altered by Dasatinib treatment. The expression of TNF- α in circulation is reportedly lower in obese individuals [187], which explains why I found that the TNF- α expression level was not detected. Altogether, these data indicate that a short-term Dasatinib treatment of T2DM mice did not influence the plasma adipokines' expression.

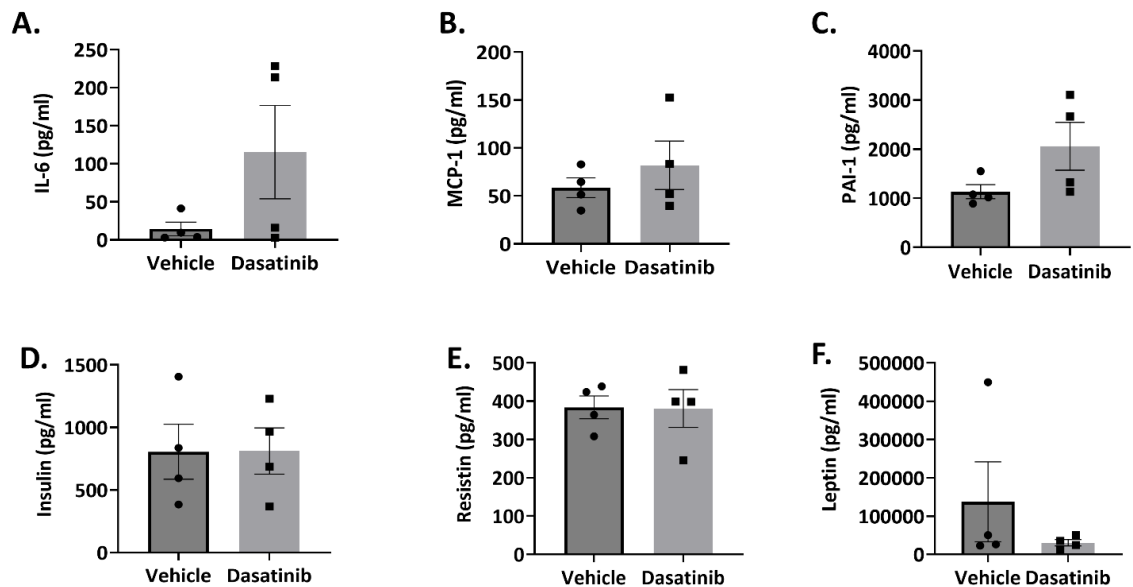


Figure 4-5 A short-term Dasatinib treatment does not alter the expression of plasma adipokines in T2DM obese mice.

Bar graphs show the plasma expression levels of the adipokines: (A) IL-6; (B) MCP-1; (C) PAI-1; (D) Insulin; (E) Resistin; and (F) Leptin, as assessed by a MILLIPLEX® Multiplex kit. Data are presented as individual values and mean \pm SEM and were analysed using an unpaired t-test. $n = 4$ mice/group. Abbreviations: IL-6 = Interleukin 6; MCP-1 = monocyte chemoattractant protein-1; PAI-1 = plasminogen activator inhibitor-1.

4.3.1.4. Dasatinib reduces lipid accumulation in the heart of T2DM obese mice

Histological assessment of ORO staining showed that Db/Db mice treated with Dasatinib had fewer ORO-positive cells in the heart tissue compared with the Vehicle group. The percentage of microscopic field area occupied by ORO-positive staining in the hearts of the Dasatinib group was $10 \pm 1.32\%$ ($p = 0.001$, **Figure 4-6 A and B**). These results indicate that a one-week treatment with Dasatinib reduced lipid accumulation in diabetic mice hearts.

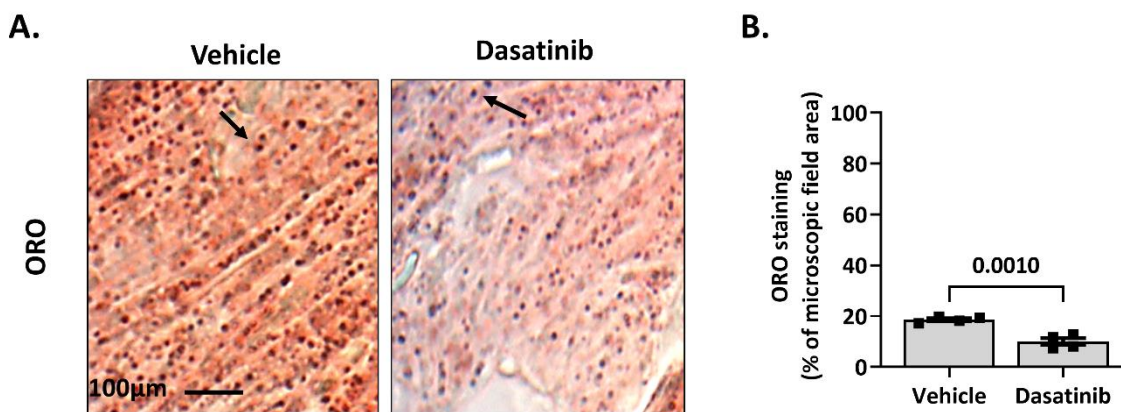


Figure 4-6 Short-term treatment with Dasatinib reduces lipid droplet accumulation in T2DM obese mice hearts.

Bright-field images (A) show the ORO-positive lipid droplet (arrow, red) distribution in Db/Db mice hearts. Bar graph (B) indicates the fraction of ORO positive staining per microscopic field area, demonstrated as a percentage of the total area. Data are presented as individual values and mean \pm SEM and were analysed using an unpaired t-test. $n = 4$ mice/group. Abbreviations: ORO = oil red O.

4.3.1.5. Dasatinib reduces lipid accumulation in the BM of T2DM obese mice

The ORO staining indicated that the short-term Dasatinib treatment reduced the lipid droplet accumulation in the BM of Db/Db mice (**Figure 4-7A**). The quantitative analysis demonstrated that the percentage of microscopic field area occupied by ORO-positive staining significantly decreased to $12.4 \pm 1.82\%$ with Dasatinib treatment ($p =$

0.018, **Figure 4-7B**). These data demonstrate the effective reduction of lipid accumulation in the BM of Db/Db mice after Dasatinib treatment.

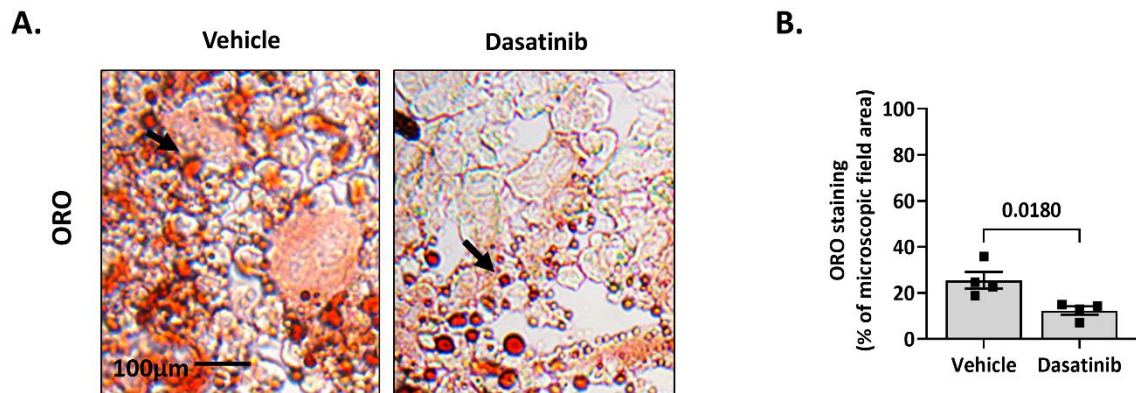


Figure 4-7 Short-term treatment with Dasatinib reduces lipid droplet accumulation in T2DM obese mice bone marrow.

Bright-field images (A) show the lipid droplets (arrow, red) stained with ORO in Db/Db mice BM from Vehicle and Dasatinib groups. Bar graph (B) indicates the fraction of ORO positive staining per microscopic field area, demonstrated as a percentage of the total area. Data are presented as individual values and mean \pm SEM and were analysed using an unpaired t-test. $n = 4$ mice/group. Abbreviations: ORO = oil red O.

4.3.1.6. Effects of Dasatinib on the expression of senescence markers in the heart of T2DM obese mice

The effects of Dasatinib treatment on the heart of Db/Db mice were assessed by IHC staining for p16^{INK4a}. Fluorescent images (**Figure 4-8A**) and the quantification of p16^{INK4a}-positive cells (**Figure 4-8B**) in the two groups showed that the one-week Dasatinib treatment did not impact the fraction of senescent cells in the heart.

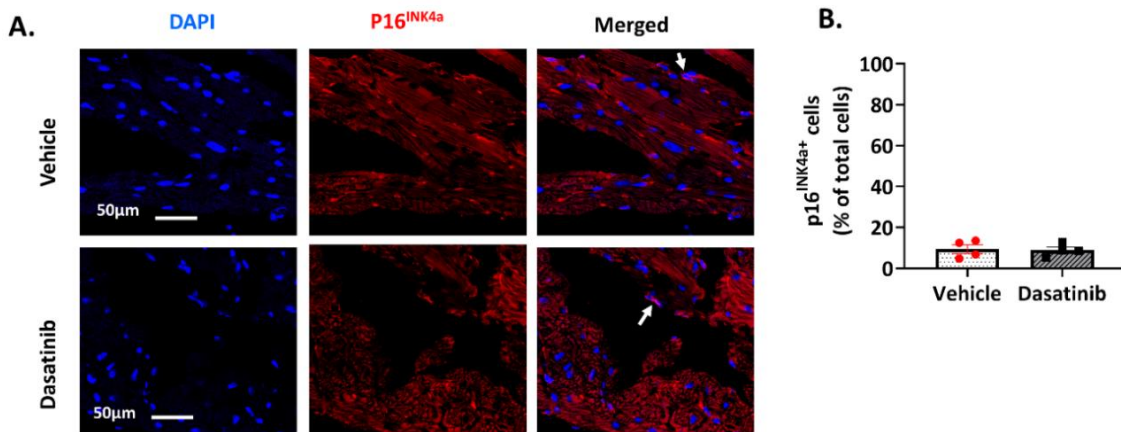


Figure 4-8 Effects of short-term Dasatinib treatment on the expression of senescence markers in the hearts of T2DM obese mice.

Representative confocal immunofluorescence images (A) show positive staining for p16^{INK4a} (arrow, red nuclear positivity) in Db/Db mice hearts. Histogram (B) indicates the percentage of p16^{INK4a} positive cells (% of the total cells). Data are presented as individual values and mean \pm SEM and analysed using an unpaired t-test. n = 4 mice /group. Abbreviations: DAPI = 4',6-diamidino-2-phenylindole.

4.3.1.7. Effects of Dasatinib on the expression of senescence markers in BM of T2DM obese mice

To study whether Dasatinib treatment could reduce the senescence of BM in Db/Db mice, I performed IHC staining to assess the expression level of the cell cycle arrest marker p16^{INK4a}. The results showed that one-week administration of Dasatinib in diabetic, obese mice slightly but not significantly decreased the ratio of senescent cells in BM ($p = 0.58$, **Figure 4-9 A and B**). The results suggest that short-term treatment of Dasatinib may not reduce the senescence of BM in 21-week-old Db/Db mice.

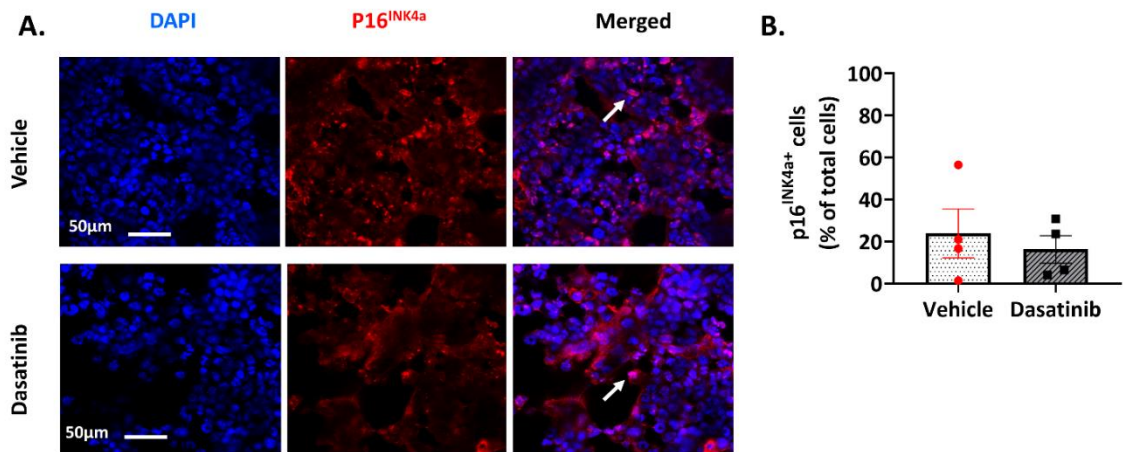


Figure 4-9 Short-term Dasatinib treatment influences T2DM obese mice bone marrow senescence.

Representative confocal images (A) show the expression of senescence marker p16^{INK4a} (arrow, red nuclear positivity) in Db/Db mice BM from Vehicle and Dasatinib group, while DAPI labelled nuclei in blue. Bar graph (B) shows the fraction of cells positive to the p16^{INK4a}. Data are presented as individual values and mean \pm SEM and were analysed using an unpaired t-test. n = 4 mice/group. Abbreviations: DAPI = 4',6-diamidino-2-phenylindole.

4.3.1.8. Effects of Dasatinib on T2DM obese mice BM-SCs

Next, I assessed the effects of Dasatinib on isolated mBM-SCs in culture. Incubation of mBM-SCs with Dasatinib or vehicle for 48 hours did not affect the expression of cyclin-dependent kinase inhibitor p16^{INK4a} (Dasatinib group: $89.8 \pm 3.3\%$ vs. Vehicle group: $88.1 \pm 5.8\%$) (**Figure 4-10 A and B**), while it reduced the expression of p21^{Waf1/Cip1} (Dasatinib group: $75.7 \pm 2.8\%$ vs. Vehicle group: $84.3 \pm 1.6\%$ $p = 0.0296$) (**Figure 4-10 C and D**). Moreover, Dasatinib did not change the frequency of cells expressing the DNA damage response maker γ H2AX but was negative for the marker of cycling cells ki67 ($57.17 \pm 6.92\%$, **Figure 4-10 E and F**). Moreover, Dasatinib-treated mBM-SCs were more proliferative than those treated with the Vehicle (Dasatinib group: $47.64 \pm 5.88\%$ vs. Vehicle group: $23.2 \pm 7.9\%$, $p = 0.0386$) (**Figure 4-10 G and H**). Finally, there was no significant difference in the total cell number per field in the two groups (**Figure 4-10I**). Altogether, these results indicate that *in vitro* treatment of mBM-SCs with Dasatinib reduced the expression of p21^{Waf1/Cip1} and increased cell proliferation.

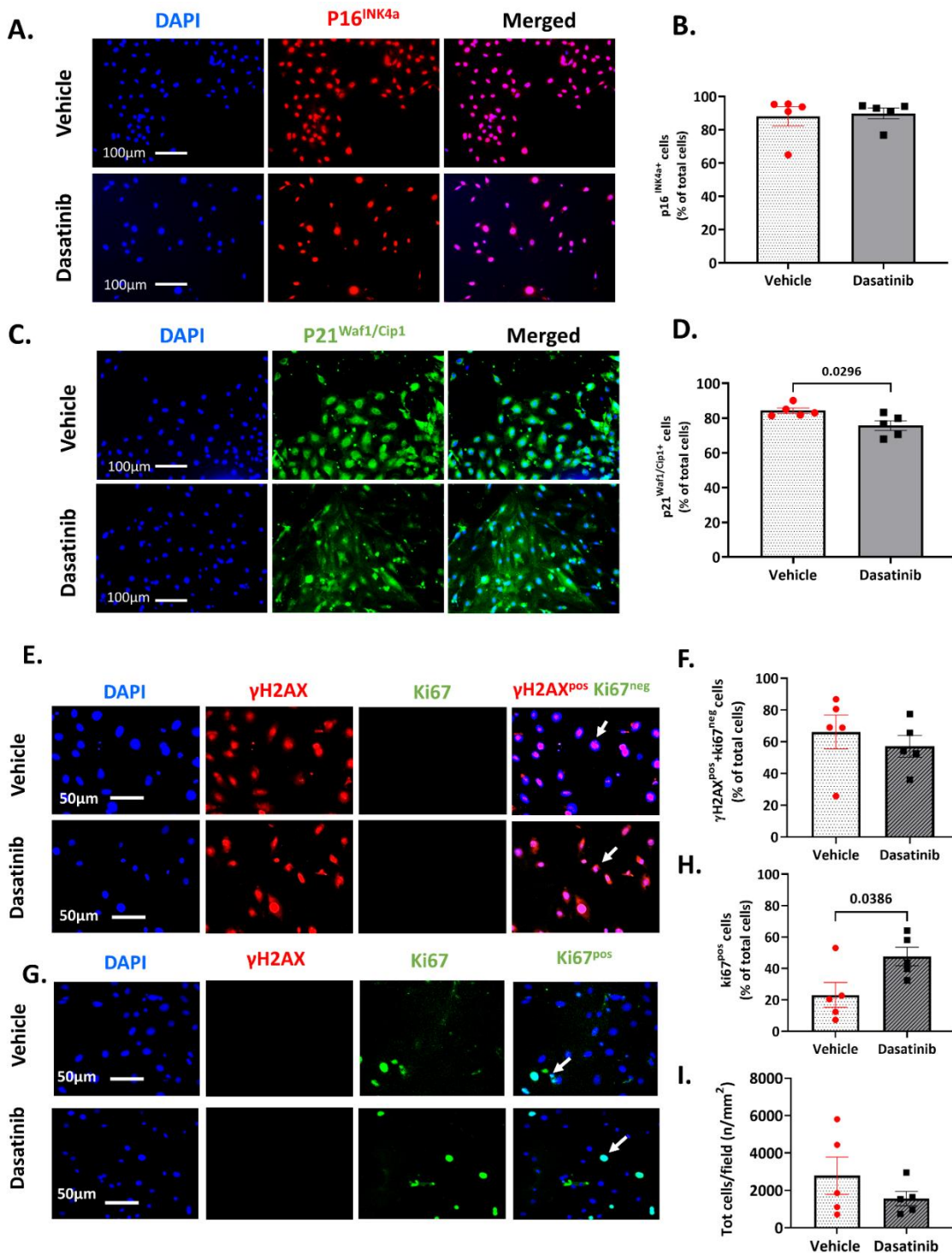


Figure 4-10 Effects of *in vitro* treatment with Dasatinib on mouse BM-SCs isolated from T2DM obese mice.

After isolating BM-SCs from Db/Db mice treated with Dasatinib (5 mg/kg) or Vehicle (10% DMSO + 90% PEG300) for one week, cells were expanded for one month and incubated with Dasatinib (1 μM) or Vehicle (DMSO) for 48 hours to enhance the effect of the drug. Immunofluorescence images of (A) p16^{INK4a} positive (red nuclear positivity), (C) p21^{Waf1/Cip1} positive (green nuclear positivity) and (E) γH2AX positive (red nuclear positivity) + ki67 negative cells show senescent mBM-SCs, while (G) ki67 positive (green nuclear positivity) cells indicate cycling mBM-SCs. Bar graphs (B, D, F, and H) show the

quantitative analysis of p16^{INK4a} positive cells; p21^{Waf1/Cip1} positive cells; γ H2AX positive + ki67 negative cells; and ki67 positive cells, demonstrated as a percentage of total cells (nuclei were identified by DAPI, blue). Bar graph (I) indicates the density of total cells per microscopy field. Data are presented as individual values and mean \pm SEM and were analysed using an unpaired t test. n = 5 mice cells/group. Abbreviations: mBM-SCs = mouse bone marrow stromal cells; DMSO = Dimethyl sulfoxide; PEG300 = polyethylene glycol 300; DAPI = 4',6-diamidino-2-phenylindole.

4.3.2. *In vivo* effects of long-term Dasatinib treatment on T2DM obese mice

4.3.2.1. Animal model

The results of the short-term treatment of Db/Db mice with Dasatinib indicated that the treatment was safe and encouraged us to investigate the benefits during a longer-term treatment. The eighteen Db/Db male mice were randomly assigned to the Vehicle or Dasatinib-treatment group and administered with vehicle solvent (10% DMSO + 90% PEG300) or Dasatinib (5 mg/kg) by oral gavage once per week for four weeks (**Figure 4-11A**). Measurements of urine glucose levels confirmed the stability of the diabetic status in the Dasatinib and Vehicle groups. Db/Db mice showed overt glycosuria (> 2000 (111) mg/dL (mmol/L)). Non-diabetic control, C57BL/6 mice were evaluated in parallel for reference and showed normal urine glucose level (<100 (5.5) mg/dL (mmol/L)) (**Figure 4-11B**).

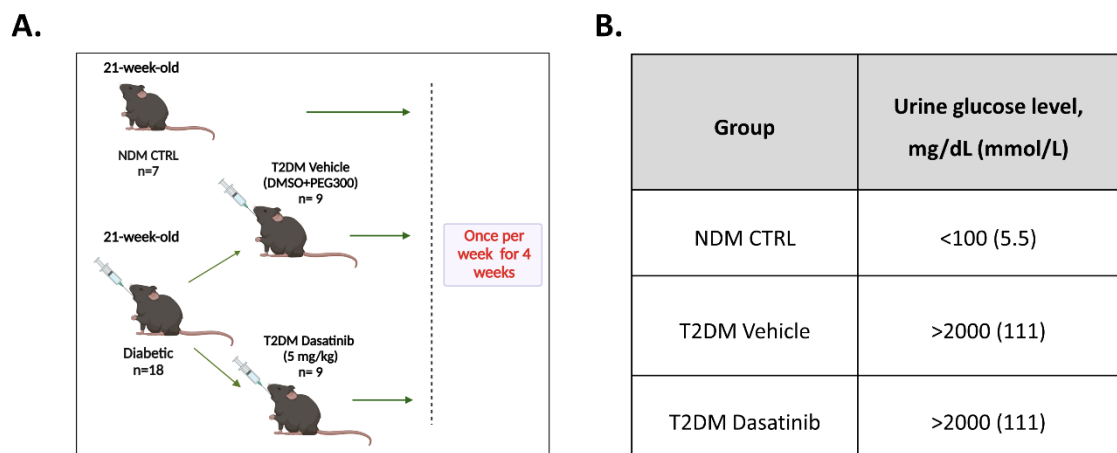


Figure 4-11 Confirmation of the diabetic status in T2DM obese mice used for the long-term treatment study with Dasatinib.

Cartoon (A) of long-term Dasatinib treatment on Db/Db mice. (B) Table of glycosuria level in Db/Db mice during the long-term Dasatinib treatment.

4.3.2.2. Effects of Dasatinib on T2DM obese mice body weight and fat pad weight

During the 4-week treatment, no significant body weight changes were found between the Vehicle and Dasatinib groups, whereas, as expected, the weight of animals in the CTRL group was lighter than that of diabetic mice (**Figure 4-12A**). At termination, the weight of pericardial (**Figure 4-12B**), epididymal (**Figure 4-12C**) and inguinal (**Figure 4-12D**) fat tissue was similar between the two diabetic groups but significantly increased compared with non-diabetic mice. Since these fat tissues are the typical WAT, these results suggest that Dasatinib did not impact the level of lipids in WAT located in other tissue depots.

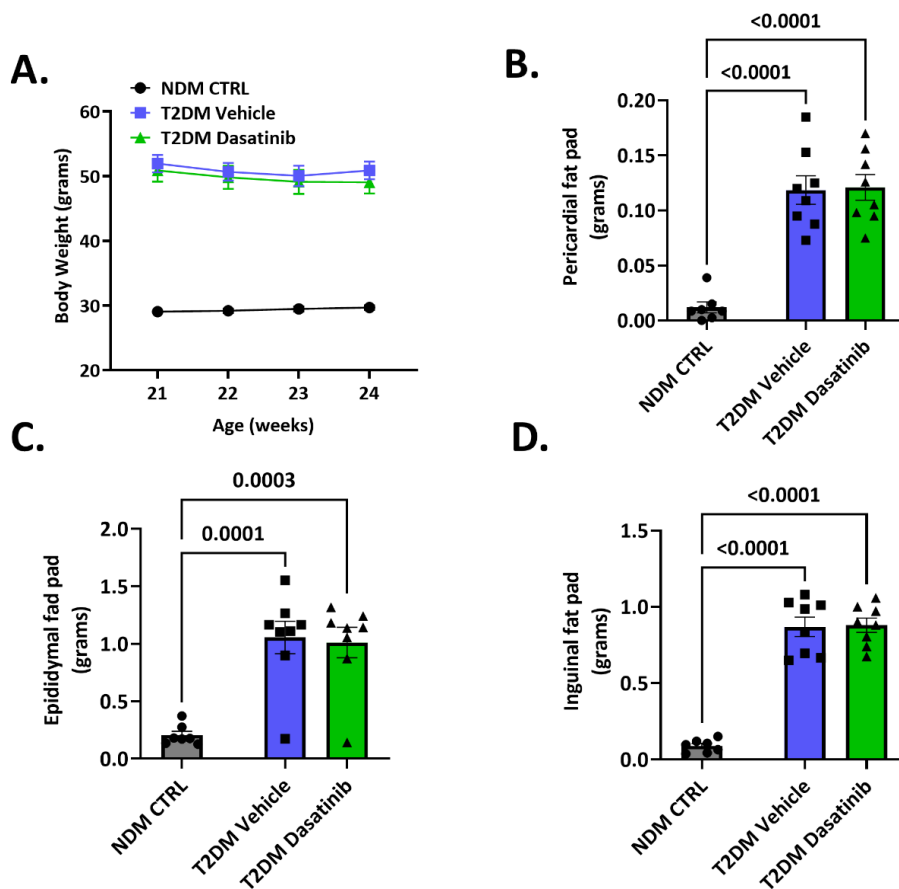


Figure 4-12 Long-term treatment with Dasatinib does not impact the body weight and fat pad weight of T2DM obese mice.

Treatment was started on 21-week-old mice for 4 weeks. Graph (A) shows the body weight progression during the 4 weeks of treatment for mice from different groups: NDM CTRL (C57BL/6 mice, reference control); T2DM Vehicle (Db/Db mice treated with 10% DMSO + 90% PEG300, oral gavage); and T2DM Dasatinib (Db/Db mice treated with Dasatinib, 5 mg/kg, oral gavage). Histograms show the (B) pericardial, (C) epididymal and (D) inguinal fat pad weight at the end of the study. Data are presented as individual values and mean \pm SEM. Group pairs were compared using one-way ANOVA followed by Tukey's multiple comparisons tests. $n = 7$ (NDM CTRL group) and 8 (T2DM Vehicle and T2DM Dasatinib groups) mice/group. Abbreviations: T2DM = type 2 diabetes mellitus; NDM CTRL = non-diabetes mellitus control.

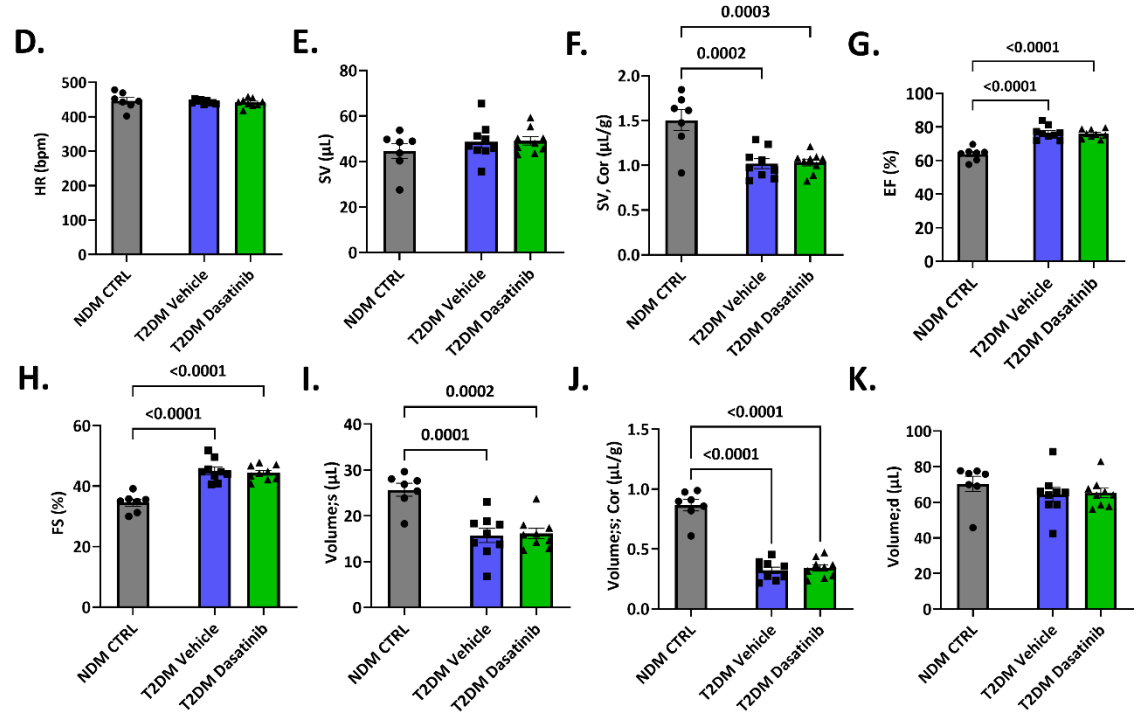
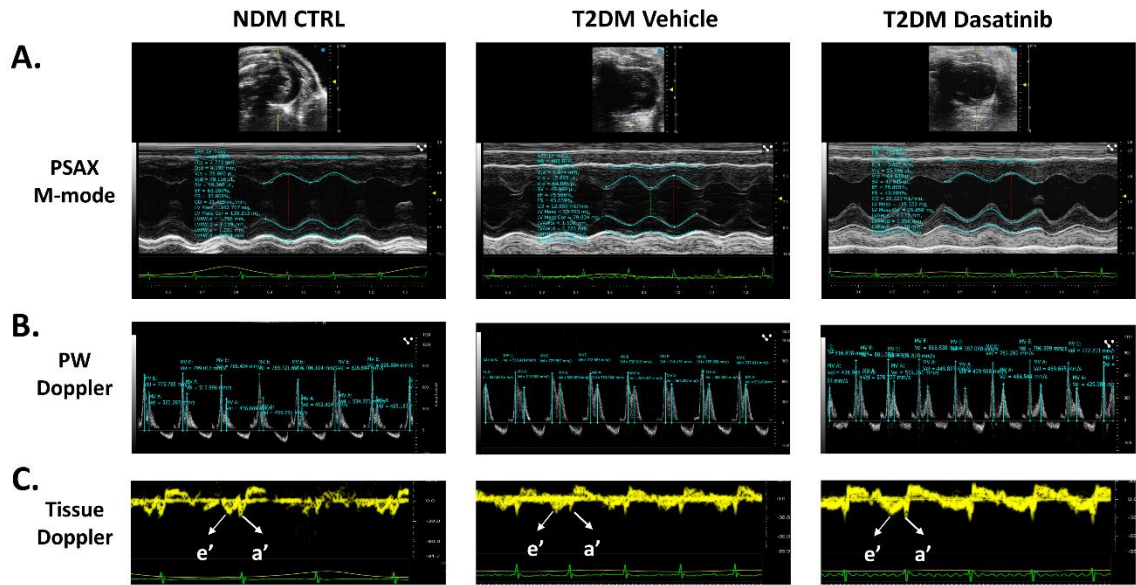
4.3.2.3. Effects of Dasatinib on T2DM obese mice cardiac function

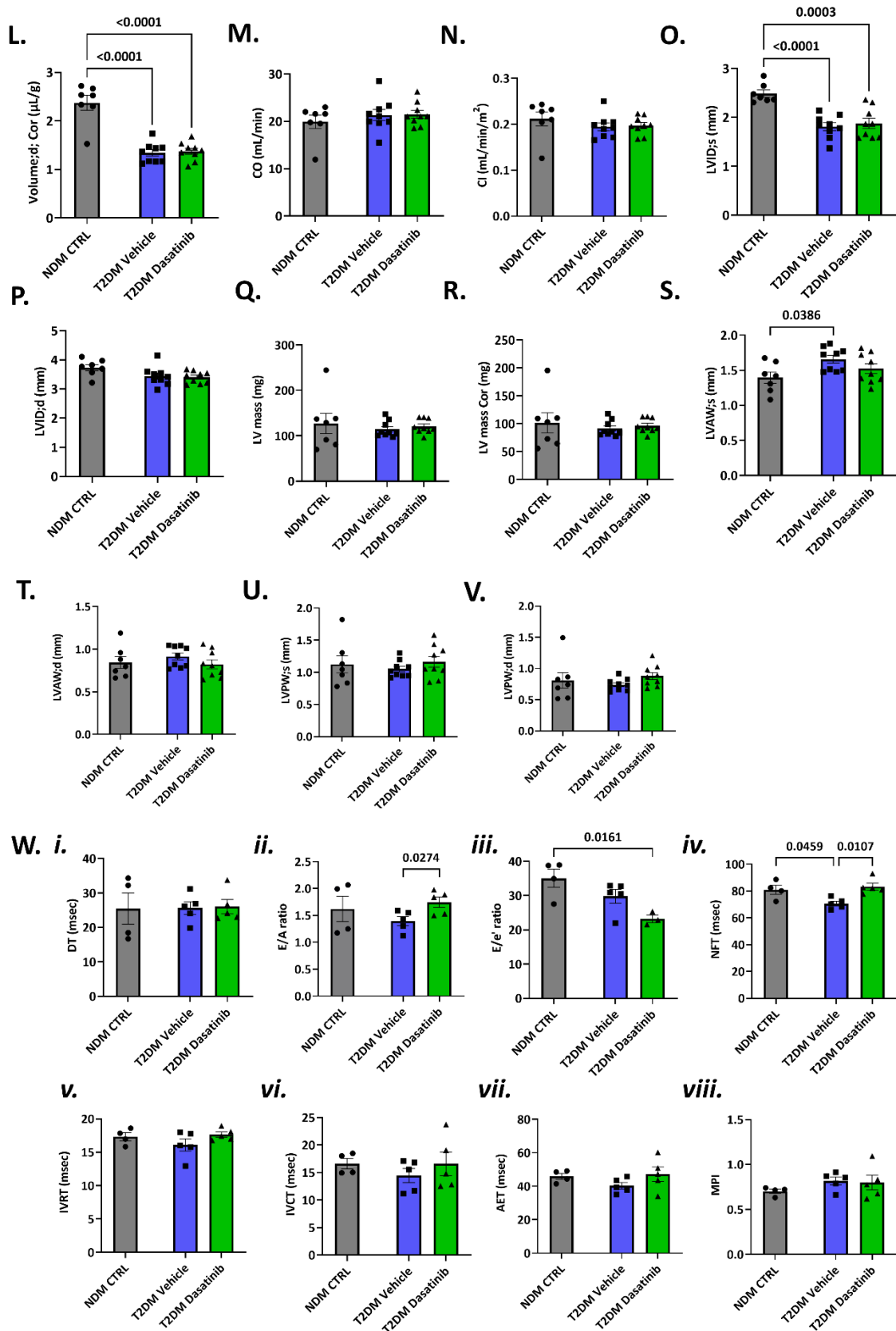
Echocardiography was performed at termination to assess the cardiac function in animals from different groups. For this experiment, baseline echocardiography was not performed due to technical issues since it was difficult to find the correct imaging view of the obese mouse heart within one hour (more than one-hour anaesthesia may be harmful to animals and will also influence the following experiment). Therefore, diabetic mice treated with Dasatinib were directly compared to the Vehicle treatment group and the wild-type control. Representative echocardiograms for animals in the three groups are shown in **Figure 4-13 A to C**.

All the echocardiographic measurements were performed on mice at similar heart rate values (443.8 ± 5.23 bpm, **Figure 4-13D**). At the 25-week assessment (termination), diabetic mice showed similar SV, regardless of treatment (**Figure 4-13E**). However, after correction of the SV for body mass, both the diabetic groups showed a similar reduction in indexed SV compared with nondiabetic controls ($p = 0.0002$ vs T2DM Vehicle, $p = 0.0003$ vs T2DM Dasatinib, **Figure 4-13F**), which is suggestive of concentric inward LV remodelling in the T2DM groups. This means the ventricular mass remains like the nondiabetic animals, but the volume inside is reduced relative to mass. Diabetic mice in both Vehicle and Dasatinib treatment groups showed similar systolic abnormalities in EF and FS, significantly increasing compared to NDM CTRL mice (**Figure 4-13 G and H**). The left ventricular end systolic and diastolic volume (**Figure 4-13 I and K**) were normalised by the body mass (**Figure 4-13 J and L**) and showed similar values in T2DM treated or untreated animals while they were lower than those of control mice. These data indicate

that the heart undergoes an adaptive remodelling characterised by preserving the systolic function through inward remodelling. This is a feature of HFpEF manifested in individuals with T2DM. CO and CI showed no apparent changes in diabetic mice after treatment with Dasatinib (**Figure 4-13 M and N**). The cardiac dimensional parameters showed no differences between the T2DM mice in the two treatment groups (**Figure 4-13 O to R**). The left ventricular anterior wall thickness at systolic was thicker in T2DM Vehicle group compared with CTRL group (**Figure 4-13S**) and the left ventricular anterior wall thickness at diastolic and left ventricular posterior wall thickness at systolic and diastolic showed no difference between T2DM Vehicle and Dasatinib groups (**Figure 4-13 T to V**).

The diastolic function was assessed by using PW Doppler and tissue Doppler traces. The DT showed no difference after Dasatinib treatment in diabetic mice (**Figure 4-13Wi**). Importantly, the blood flow across the mitral valve (E/A ratio) was improved in the T2DM Dasatinib group compared with the T2DM Vehicle group (**Figure 4-13Wii**). The E/e' ratio was decreased in diabetic mice, especially in the Dasatinib-treated groups versus the NDM CTRL mice ($p = 0.0161$) (**Figure 4-13Wiii**). The NFT index was reduced in vehicle-treated diabetic mice compared with NDM CTRL mice ($p = 0.0459$). Interestingly, T2DM mice treated with Dasatinib had significantly improved NFT compared with the Vehicle group ($p = 0.0107$) (**Figure 4-13Wiv**). However, other parameters of diastolic function (e.g., IVRT, IVCT, AET, MPI, e'/a' and PHT) (**Figure 4-13 Wv to Wx**) were not affected by the treatment, although IVRT (**Figure 4-13 Wv**), IVCT (**Figure 4-13 Wvi**) and AET (**Figure 4-13 Wvii**) showed the same trend as NFT. Altogether, these data suggests that the hearts of T2DM obese mice showed a typical cardiac remodelling and that one-month treatment with Dasatinib improved cardiac diastolic function.





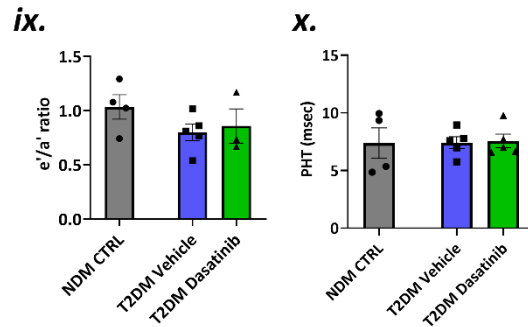


Figure 4-13 Results of echocardiography analysis in 25-week-old T2DM obese mice undergoing long-term treatment with Dasatinib.

Representative echocardiograms of (A) PSAX M-mode traces, (B) PW Doppler and (C) tissue Doppler measurements. Graphs show the influence of Dasatinib on the parameters of systolic function: (D) HR (bpm); (E) SV (μL); (F) SV, Cor ($\mu\text{L/g}$); (G) EF (%); (H) FS (%); (I) Volume; s (μL); (J) Volume; s, Cor (μL); (K) Volume; d (μL); (L) Volume; d, Cor (μL); (M) CO (mL/min); (N) CI (mL/min/m²); (O) LVID; s (mm); (P) LVID; d (mm); (Q) LV mass (mg); (R) LV mass Cor (mg); (S) LVAW; s (mm); (T) LVAW; d (mm); (U) LVPW; s (mm); (V) LVPW; d (mm); and diastolic function (Wi) DT (msec); (Wii) E/A ratio; (Wiii) E/e' ratio; (Wiv) NFT (msec); (Wv) IVRT (msec); (Wvi) IVCT (msec); (Wvii) AET (msec); (Wviii) MPI; (Wix) e'/a' ratio; (Wx) PHT (msec). Data are presented as individual values and mean \pm SEM. Group pairs were compared using one-way ANOVA followed by Tukey's multiple comparisons tests. n = 7 (NDM CTRL group) and 8 (T2DM Vehicle and T2DM Dasatinib group) mice/group. The cardiac index is the normalisation of cardiac output by body surface area. Due to a technical problem, PW and tissue Doppler images could be analysed only in a subgroup of animals. Abbreviations: NDM CTRL = non-diabetes mellitus control; T2DM = type 2 diabetes mellitus; PW Doppler = pulsed wave Doppler; HR = heart rate; SV = stroke volume; Cor = corrected; EF = ejection fraction; CO = cardiac output; CI = cardiac index; s = systolic; DT = deceleration time; d = diastolic; LV = left ventricle; FS = fractional shortening; LVAW, s = left ventricular anterior wall thickness, systolic; LVAW, d = left ventricular anterior wall thickness, diastolic; LVPW, s = left ventricular posterior wall thickness, systolic; LVPW, d = left ventricular posterior wall thickness, diastolic; LVID = left ventricular internal diameters; E = left ventricular relaxation in early diastole velocity; A = left ventricular relaxation in late diastole velocity; e' = early diastolic mitral annular velocity; a' = late mitral annulus peak velocity; AET = aortic ejection time; NFT = non-flow time; IVCT = isovolumic contraction time; IVRT = isovolumic relaxation time; MPI = myocardial performance index; PHT = mitral valve pressure half time.

4.3.2.4. Effects of Dasatinib on T2DM obese mice plasma adipokines

Next, multiplex assays were performed to measure the levels of adipokines released in the peripheral blood. IL-6 and insulin plasma levels showed no changes between the CTRL and T2DM mice, either with or without Dasatinib treatment (**Figure 4-14 A and B**). Moreover, the secreted levels of leptin and MCP-1 were enriched in the T2DM mice,

with no changes between the Vehicle and Dasatinib groups (**Figure 4-14 C and D**). The serine protease inhibitor PAI-1, which is a major target of the TGF- β 1/p53 senescence signalling pathway [468], was elevated in vehicle-treated diabetic mice. However, its level in the Dasatinib-treated group was not different from T2DM mice given vehicle (**Figure 4-14E**). The mice in the diabetic groups expressed less resistin than the nondiabetic mice, with no changes induced by Dasatinib (**Figure 4-14F**). The plasma TNF- α levels were lower than those detectable within the assay standard curve. Altogether, these results indicate that the administration of Dasatinib did not influence the plasma adipokines levels after one month of treatment.

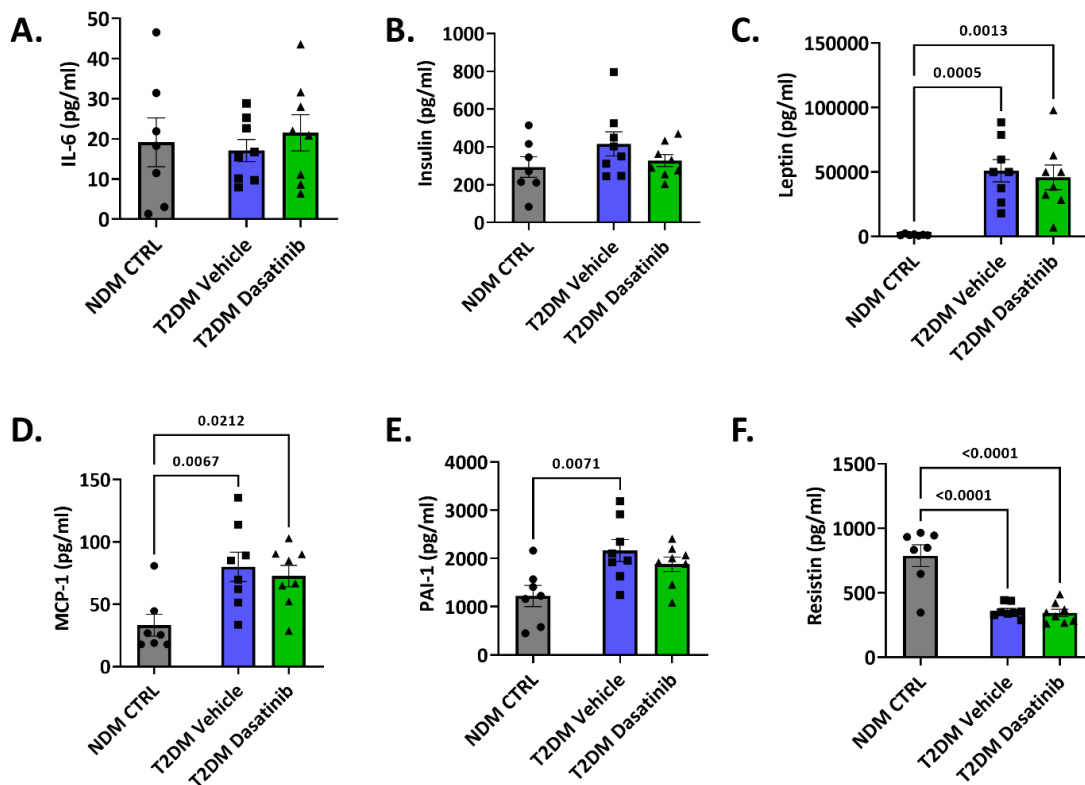


Figure 4-14 Long-term treatment with Dasatinib does not affect the concentrations of adipokines in T2DM obese mice plasma.

Histograms indicate the secreted level of (A) IL-6, (B) Insulin, (C) Leptin, (D) MCP-1, (E) PAI-1, and (F) Resistin in mice plasma from NDM CTRL, T2DM Vehicle, and T2DM Dasatinib groups, as assessed by MILLIPLEX® Multiplex kit. Data are presented as individual values and mean \pm SEM. Group pairs were compared using one-way ANOVA followed by Tukey's multiple comparisons tests. $n = 7$ (NDM CTRL group) and 8 (T2DM Vehicle and T2DM Dasatinib group) mice/group. Abbreviations: NDM CTRL = non-diabetes mellitus control; T2DM = type 2 diabetes mellitus, IL-6 = Interleukin 6; MCP-1 = monocyte chemoattractant protein-1; PAI-1 = plasminogen activator inhibitor-1.

4.3.2.5. Dasatinib reduces the lipid accumulation in the heart of T2DM obese mice

Next, I assessed whether Dasatinib treatment reduced lipid accumulation in the heart of T2DM mice. As expected, there was a significant increase in lipid accumulation in the hearts of both diabetic groups when compared with the NDM CTRL group. Interestingly, the area occupied by ORO^{pos} lipid droplets in the hearts of Dasatinib-treated T2DM mice ($13.83 \pm 2.45\%$) was lower than that in the Vehicle group ($24.52 \pm 4.08\%$) (**Figure 4-15 A and B**). These results indicate that long-term treatment with Dasatinib reduced lipid accumulation in the hearts of T2DM mice.

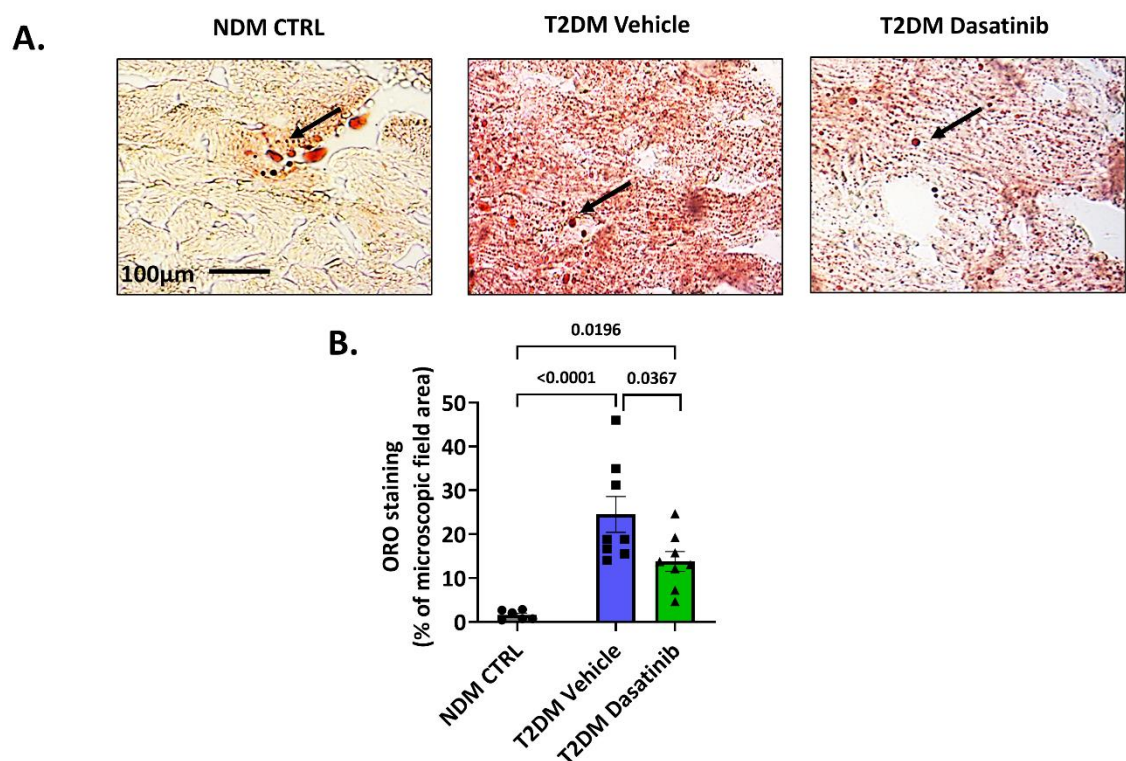


Figure 4-15 Long-term treatment with Dasatinib reduces the lipid accumulation in the hearts of T2DM obese mice.

Bright-field images (A) show the ORO-positive lipid droplets (arrow, red) in the hearts of mice from NDM CTRL, T2DM Vehicle, and T2DM Dasatinib groups. Histogram (B) indicates the percentage of microscopy field area occupied by ORO-positive lipid droplets. Data are presented as individual values and mean \pm SEM. Group pairs were compared using one-way ANOVA followed by Tukey's multiple comparisons tests. $n = 6$ (NDM CTRL group) and 8 (T2DM Vehicle and T2DM Dasatinib group) mice/group. Abbreviations: ORO = oil red O; NDM CTRL = non-diabetes mellitus control; T2DM = type 2 diabetes mellitus.

4.3.2.6. Dasatinib reduces the lipid accumulation in the BM of T2DM obese mice

Next, I studied the effects of Dasatinib treatment on lipid accumulation in the BM of T2DM mice. Compared with the nondiabetic mice, as expected, there was a significant lipid enrichment in all the T2DM animals. Interestingly, the quantification of the ORO staining showed fewer ORO^{pos} lipid droplets per microscopy field in the BM from T2DM mice treated with Dasatinib ($37.9 \pm 3.91\%$) than in the Vehicle group ($58.04 \pm 6.85\%$) (Figure 4-16 A and B). These results indicate that T2DM induced the accumulation of lipid droplets in the BM, with this phenotype being improved by Dasatinib treatment.

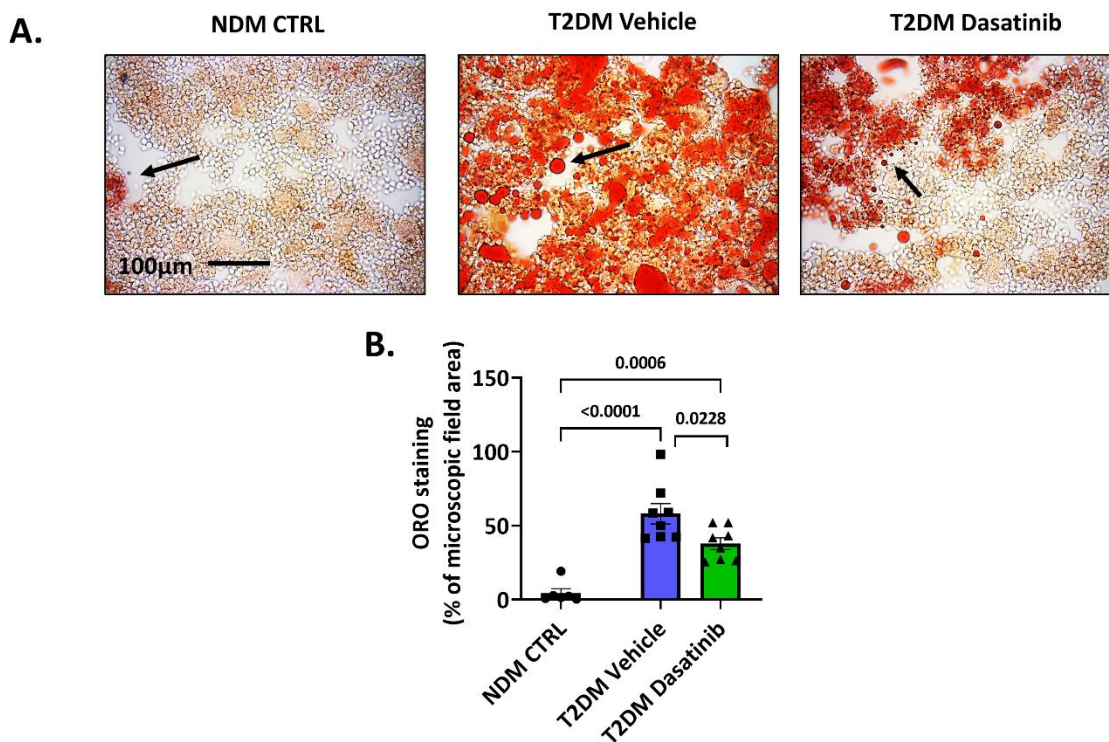


Figure 4-16 Long-term treatment with Dasatinib reduces the lipid accumulation in the bone marrow of T2DM obese mice.

Bright-field images (A) show the ORO-positive lipid droplet (arrow, red) accumulation in the BM of mice from NDM CTRL, T2DM Vehicle, and T2DM Dasatinib groups. Bar graph (B) shows the percentage of microscopy field area positive for ORO staining. Data are presented as individual values and mean \pm SEM. Group pairs were compared using one-way ANOVA followed by Tukey's multiple comparisons tests. $n = 7$ (NDM CTRL group) and 8 (T2DM Vehicle and T2DM Dasatinib group) mice/group. Abbreviations: BM = bone marrow; ORO = oil red O; NDM CTRL= non-diabetes mellitus control; T2DM = type 2 diabetes mellitus.

4.3.2.7. Correlation between BM & heart lipid accumulation and heart lipid accumulation & cardiac function

Next, I performed a simple linear regression analysis of BM and heart lipid accumulation using the ORO results from **section 4.3.2.6** and **section 4.3.2.5** and a simple linear regression analysis between heart lipid accumulation and E/A ratio (**Figure 4-13Wii**). The results of this analysis demonstrate a direct correlation between the content of lipids in the BM and heart in all the groups of animals ($p < 0.0001$, $R^2 = 0.599$, **Figure 4-17A**). Moreover, there is a direct correlation between the abundance of lipids in the BM and hearts of T2DM mice ($p < 0.02$, $R^2 = 0.32$, **Figure 4-17B**). However, the discrimination between diabetic animals given vehicle or Dasatinib shows that the senolytic agent reduces both organs' fat, whereas the correlation between heart and BM fat content is lost after Dasatinib treatment (**Figure 4-17C**). Moreover, the number of intramyocardial lipids was inversely correlated with the E/A ratio ($p = 0.05$, $R^2 = 0.36$) in all the groups of animals (**Figure 4-17D**).

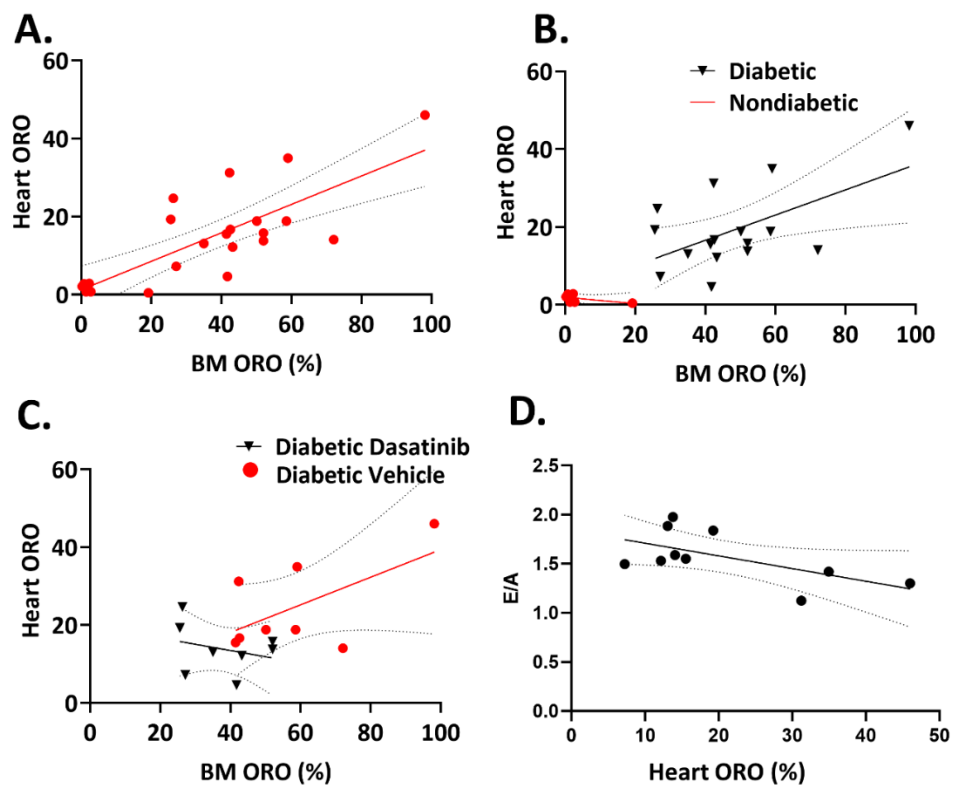


Figure 4-17 Regression analysis of bone marrow and heart lipid accumulation and cardiac function.

Linear regression analysis was performed to analyse the correlation between the respective BM and heart ORO-positive lipid deposits (Figures 6-16 and 6-15) in nondiabetic and T2DM mice treated with vehicle or Dasatinib or the correlation between heart ORO-positive lipid deposits and E/A ratio (Figure 6-13Wii). Graphs show the correlation between heart and BM lipid accumulation (A) in all groups, (B) in T2DM or NDM mice, (C) in diabetic mice treated with vehicle or Dasatinib, and (D) lipid content in the heart and E/A ratio of all animals. Simple linear regression. n = 6 (NDM CTRL group) and 8 (T2DM Vehicle and T2DM Dasatinib group) mice/group. Abbreviations: BM = bone marrow; ORO = oil red O; T2DM = type 2 diabetes mellitus; NDM = non-diabetes mellitus.

4.3.2.8. Dasatinib reduces myocardial interstitial fibrosis in T2DM obese mice

Next, I assessed the myocardial interstitial fibrosis using Azan Mallory staining (**Figure 4-18A**). As expected, there was an increase in myocardial interstitial fibrosis in the hearts of diabetic mice given vehicle compared with NDM CTRL mice ($p = 0.0038$) (**Figure 4-18 A and B**). Interestingly, the percentage of tissue area occupied by fibrosis was significantly reduced in the hearts of diabetic animals receiving Dasatinib ($p = 0.0456$) (**Figure 4-18 A and B**). The results suggest that Dasatinib treatment ameliorated myocardial interstitial fibrosis in diabetic mice.

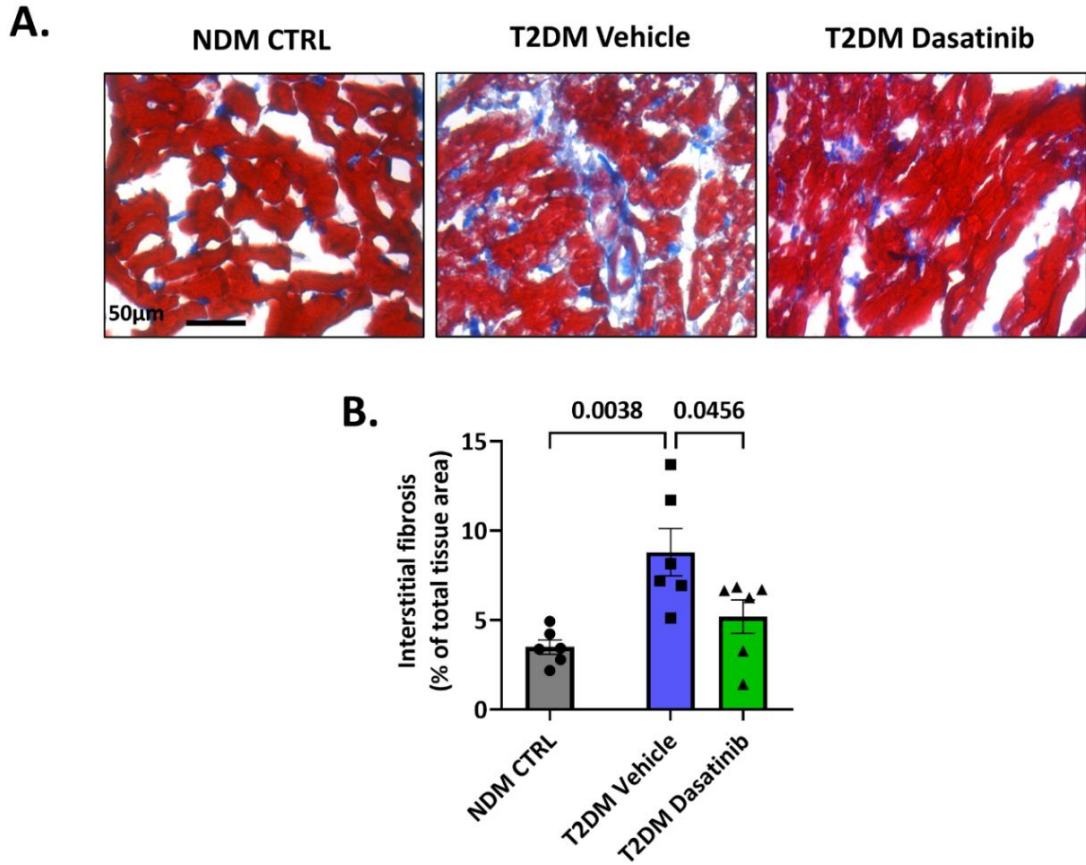


Figure 4-18 Long-term treatment with Dasatinib reduces the myocardial interstitial fibrosis of T2DM obese mice.

Representative Azan Mallory images (blue: fibrosis) (A) and a bar graph (B) showing the effect of diabetes and Dasatinib on myocardial interstitial fibrosis from NDM CTRL, T2DM Vehicle, and T2DM Dasatinib groups. Data are presented as individual values and mean \pm SEM. Group pairs were compared using one-way ANOVA followed by Tukey's multiple comparisons tests. $n = 6$ mice/group. Abbreviations: NDM CTRL = non-diabetes mellitus control; T2DM = type 2 diabetes mellitus.

4.3.2.9. Dasatinib reduces cellular senescence in the heart of T2DM obese mice

Next, I assessed the levels of cardiac senescence in mice from different groups. Quantification of IHC staining showed a decrease in the senescence maker p16^{INK4a} in the heart of Dasatinib-treated T2DM mice ($7.904 \pm 1.43\%$ nuclei) compared with the vehicle ($18.65 \pm 3.81\%$ nuclei, $p = 0.0193$). Moreover, the levels of p16^{INK4a} in T2DM Vehicle group mice hearts were significantly higher than the non-diabetic controls

($6.319 \pm 2.84\%$) ($p = 0.0132$, **Figure 4-19 A and B**). These results indicate that Dasatinib reduced cardiac senescence in T2DM obese mice.

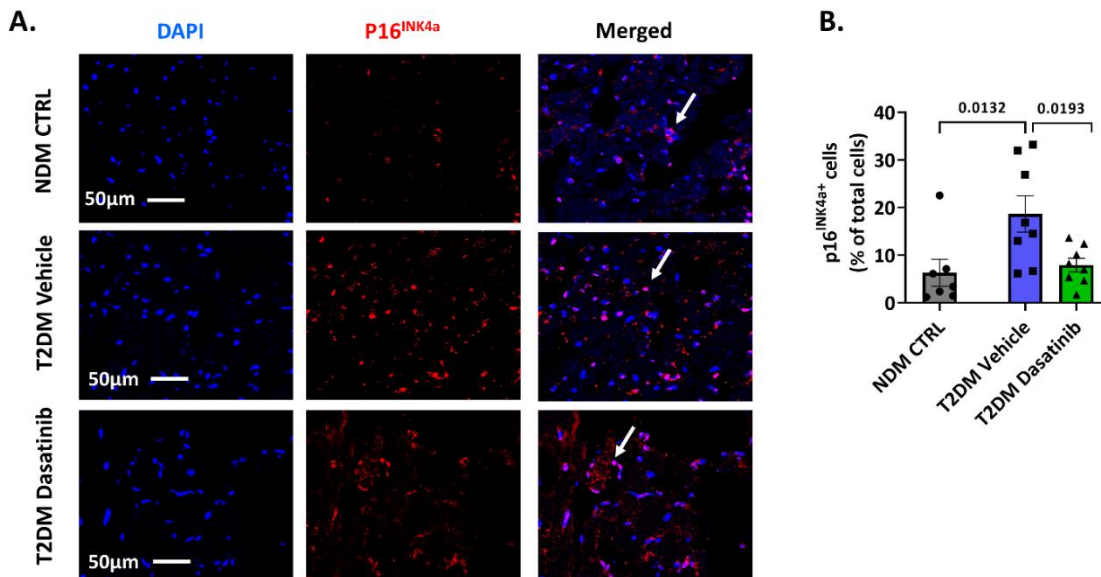


Figure 4-19 Long-term treatment with Dasatinib reduces cardiac senescence of T2DM obese mice.

Representative confocal immunofluorescence images (A) show expression of p16^{INK4a} (arrow, red nuclear positivity) in the murine heart from NDM CTRL, T2DM Vehicle, and T2DM Dasatinib groups. Nuclei were stained with DAPI. Bar graph (B) shows the fraction of p16^{INK4a} positive cells, demonstrates as a percentage of total cells. Data are presented as individual values and mean \pm SEM. Group pairs were compared using one-way ANOVA followed by Tukey's multiple comparisons tests. $n = 7$ (NDM CTRL group) and 8 (T2DM Vehicle and T2DM Dasatinib group) mice/group. Abbreviations: NDM CTRL= non-diabetes mellitus control; T2DM = type 2 diabetes mellitus; DAPI = 4',6-diamidino-2-phenylindole.

4.3.2.10. Effects of Dasatinib on cellular senescence in the BM of T2DM obese mice

The effects of Dasatinib on cell senescence in the BM of T2DM mice were assessed by IHC. Compared with NDM CTRL mice, diabetic mice receiving the vehicle showed a significant increase in the fraction of BM cells expressing the cell senescence maker p16^{INK4a} ($p = 0.0117$) (**Figure 4-20 A and B**). While the diabetic animals that received one-month drug treatment showed a trend of reducing expression of p16^{INK4a} ($4.94 \pm 1.57\%$) compared with the diabetic Vehicle group ($9.07 \pm 1.31\%$), this difference was not

significant (**Figure 4-20 A and B**). Unlike the results demonstrated in the heart, the long-term treatment with Dasatinib did not reduce cell senescence in the BM of Db/Db mice.

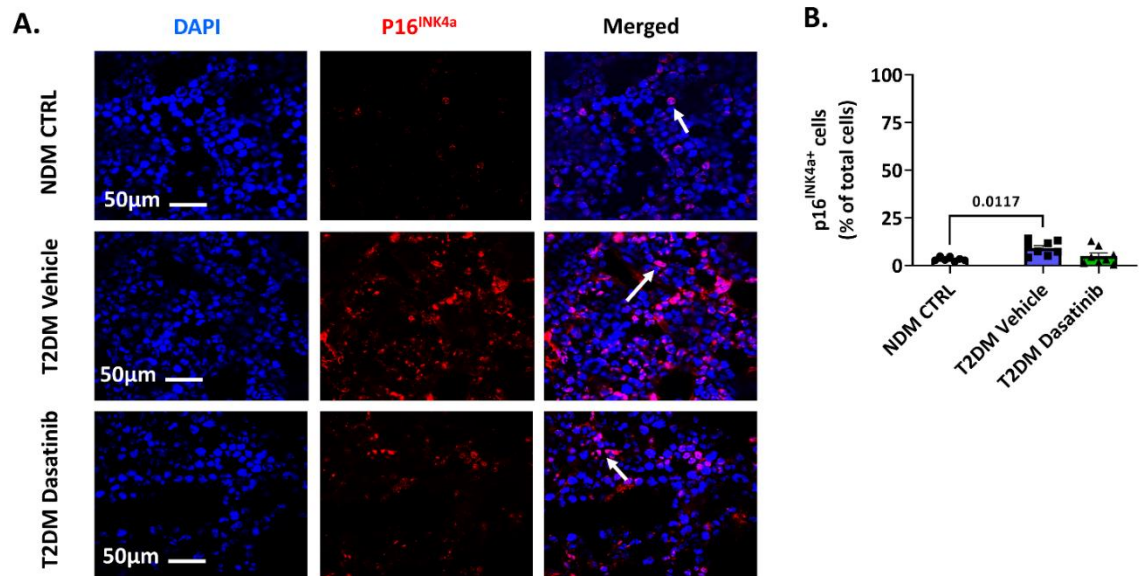


Figure 4-20 Effects of long-term treatment with Dasatinib on bone marrow senescence of T2DM obese mice.

Representative confocal immunofluorescence images (A) show the p16^{INK4a} expression (arrow, red nuclear positivity) in mice BM from NDM CTRL, T2DM Vehicle and T2DM Dasatinib groups. Nuclei were stained by DAPI. Histogram (B) shows the fraction of p16^{INK4a} positive cells demonstrates as a percentage of total BM cells. Data are presented as individual values and mean ± SEM. Group pairs were compared using one-way ANOVA followed by Tukey's multiple comparisons tests. n = 7 (NDM CTRL group) and 8 (T2DM Vehicle and T2DM Dasatinib group) mice/group. Abbreviations: BM = bone marrow; NDM CTRL= non-diabetes mellitus control; T2DM = type 2 diabetes mellitus; DAPI = 4',6-diamidino-2-phenylindole.

4.3.2.11. Effects of Dasatinib treatment on T2DM obese mice BM- MSCs

I next assessed if Dasatinib reduced the relative abundance and the senescence levels of mouse BM-MSCs, the population that gives rise to adipocytes. Using flow cytometry, I verified that both CD45^{neg}CD11b^{neg}CD29^{pos} cells, as well as the subfractions that express Sca-1 or CD73, were similarly abundant in the BM of NDM CTRL and T2DM mice and were not modified by Dasatinib (**Figure 4-21 Ai to Avi & Bi to Bii & C to E**). Looking at function-related markers, BM-MSCs from T2DM mice showed an increased frequency

of the scavenger receptor CD36, which reportedly labels cells with an activated SASP [469] (Figure 4-21 Avii, Biii, and F), and a decreased frequency of DPP4, a regulator of chemokine-induced stem cell mobilization [470], in the Dasatinib group (Figure 4-21 Avii, Biv, and G). In addition, the fluorescence signalling associated with β -galactosidase, a biomarker of replicative senescence, was upregulated in BM-MSCs of diabetic mice receiving vehicle compared with NDM CTRL mice (Figure 4-21 Aviii and H), while there was no difference between the two diabetic groups. The MitoTracker Deep red fluorescence intensity, which labels mitochondria of live cells, was similar between the three groups (Figure 4-21 Aviii and I).

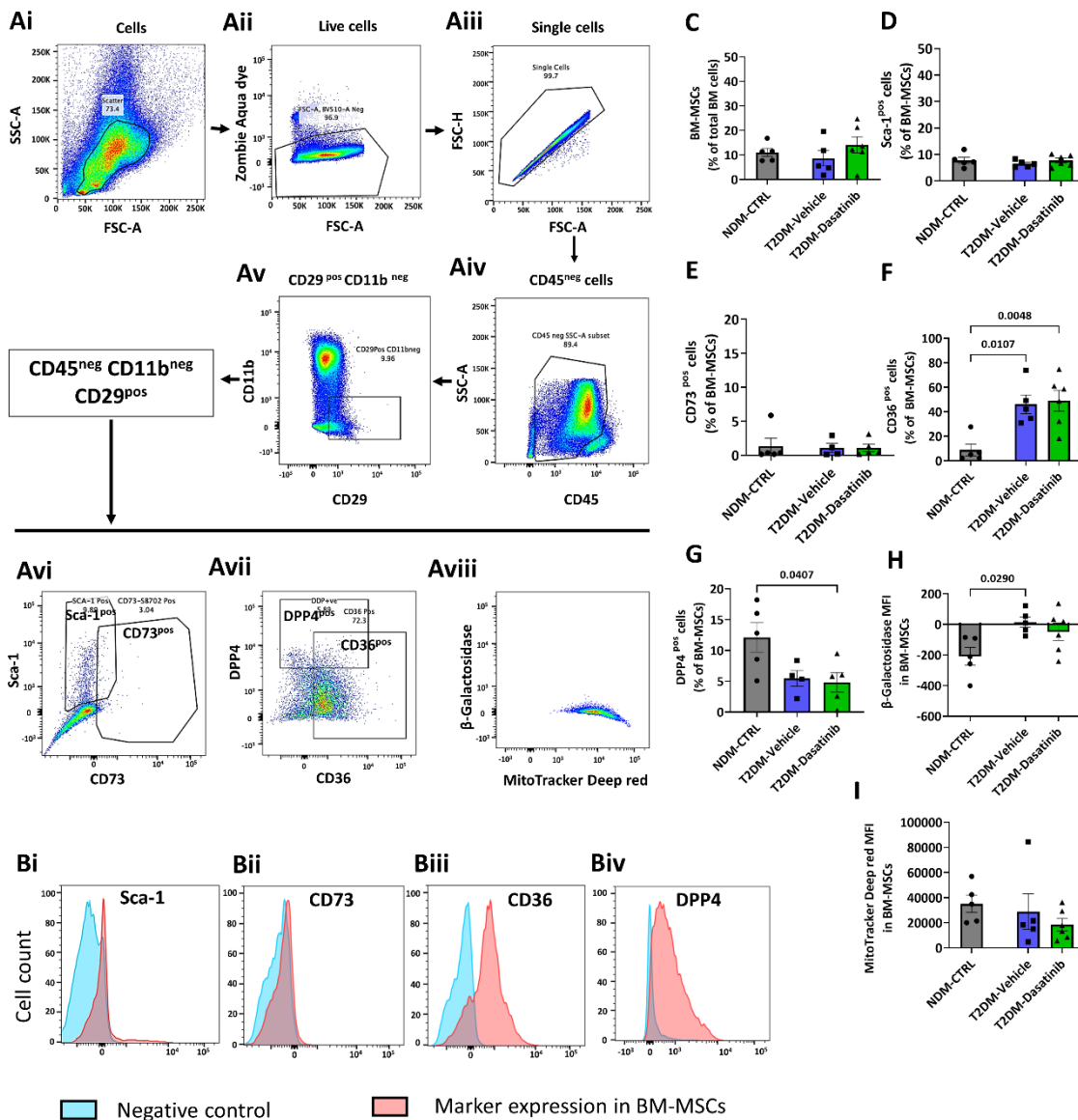


Figure 4-21 Flow cytometry analysis of mouse bone marrow mesenchymal stromal cells.

Freshly isolated mouse total BM cells were analysed by flow cytometry for identifying (A-E) BM-MSCs (gating for CD45, CD11b, CD29, Sca-1 and CD73), and next for detecting senescence (gating for CD36 and β -galactosidase Senescence Green) (F&H), mobilisation potential (gating for DPP4 (CD26)) (G) and mitochondrial activity in live cells (gating for MitoTracker Deep red) (I). The gating strategies (Ai-Aiii) consisted of selecting live singlet populations, (Aiv-Av) sorting for CD45^{neg}CD11b^{neg}CD29^{pos} MSCs, followed by (Avi & Avii) examining the ratio of cell fractions positive for Sca-1, CD73, DPP4, and CD36, and finally (Aviii) detecting the median fluorescence intensity (MFI) of β -galactosidase Senescence Green and MitoTracker Deep red in BM-MSCs. Representative histograms (Bi-Biv) showing markers expression in BM-MSCs (red) and their FMO controls (blue). The fluorescence intensity of β -galactosidase Senescence Green data is displayed on Bi-exponential plots. This is a hybrid scale where it is logarithmic for both positive and negative values until the 1st decade (-10 to +10), which is displayed as linear. Bar graphs show individual values and means \pm SEM. n = 4 to 6 mice/group. Group pairs were compared using one-way ANOVA followed by Tukey's multiple comparisons tests. Abbreviation: BM-MSCs = bone marrow mesenchymal stromal cells, CD = cluster of differentiation, Sca-1 = stem cells antigen-1, DPP4 = dipeptidyl peptidase 4, SSC-A = side scatter area, FSC-H = forward scatter height, FSC-A = forward scatter area, MFI = median fluorescence intensity, NDM CTRL = non-diabetes mellitus control, T2DM = type 2 diabetes mellitus.

4.4. Conclusion

The results of this chapter showed that the short-term treatment of Dasatinib reduced lipid accumulation in the heart and BM without ameliorating cardiac function, regulating plasma adipokines expression, or reducing the expression of p16^{INK4a}. However, the *in vitro* treatment of Dasatinib could decrease the expression of p21^{Waf1/Cip1} in mBM-SCs.

The long-term treatment of Dasatinib decreased the lipid accumulation in the T2DM mice heart, improved cardiac LV diastolic function, reduced myocardial interstitial fibrosis, and decreased the cardiac p16^{INK4a} expression levels. Likewise, the lipid accumulation in the T2DM mice BM was decreased within the long-duration treatment of Dasatinib, but the cellular senescence in BM did not improve. Furthermore, the expression levels of CD36 and DPP4 and the activity of mitochondria were similar in the mouse BM-MSCs, but the level of β -galactosidase was attenuated after Dasatinib treatment.

CHAPTER 5. DISCUSSION

Main Results

The *in vitro* study confirms the ratio of human BM-derived PCs (39.08%) among BM-MSCs, phenotype characteristics of hBM-PCs, viability, proliferation, apoptosis and senescent of hBM-PCs and their adipogenic differentiation capability, and the effects of senolytic agent Dasatinib on adipogenesis of hBM-PCs. The results demonstrated that hBM-PC was a primary adipogenic differentiation cellular source of human BM. Dasatinib induced cellular apoptosis by downregulating the expression levels of p21^{Waf1/Cip1} and inhibited viability and adipogenesis commitment of human BM-MSCs. The *in vivo* study confirms the presence of BM adiposity, cardiac steatosis and interstitial fibrosis, and LV remodelling in a murine model of T2DM. Importantly, I demonstrated for the first time that the TKI Dasatinib reduced lipid accumulation in the BM and heart of diabetic mice without affecting other adipose tissue depots or altering glycosuria. Dasatinib also attenuated cardiac fibrosis. Moreover, Dasatinib-treated mice had lower levels of p16^{INK4a} in the heart, suggesting an inhibitory impact of the drug on the senescence signalling pathway.

Optimisation of BM cell culture

Human BM-MSCs were reported to show valuable therapeutic potential for cell therapy and regenerative medication, but the limited cell number restricts its clinical application. *In vitro*, cellular expansion is the only strategy to increase cell numbers. However, the cell divisions are restricted, and all the cells will access replicative senescence [320]. This permanent cell cycle arrest reduces cellular proliferation ability and subsequently limits *in vitro* cell expansion. The cell culture surface coated with extracellular matrix (ECM) proteins, including gelatin, laminin, fibronectin, and collagen, improved the BM-MSCs doubling rate and the final cell numbers without effects the cellular senescence. Compared to all the tested ECM proteins coated plates, the cells on gelatin-coated plates showed higher proliferation ability [471]. Since our hBM-PCs were already involved in senescence, culturing in a gelatin-coated plate could help with their expansion which

was beneficial for us to have enough cells for the study. Therefore, I optimised the culture conditions for hBM-PCs by coating plates with 0.1% (w/v) gelatin.

Pericytes are enriched in human bone marrow

In human BM, some subpopulations of MSCs show the features of PCs, like highly expressed NG2, PDGFR β , CD146 and lower expression for HSCs marker CD45, CD34 and endothelial marker CD31 [299, 301, 302]. Most PCs have a similar multipotent differentiation ability to MSCs, such as adipogenic, osteogenic and myogenic [288]. In addition to the multipotent differentiation capability, hBM-PCs and hBM-MSCs share some crucial phenotype characteristics, suggesting that MSCs may establish the BM environment. For instance, mouse BM-MSCs have populations showing PDGFR α ^{pos} Sca-1^{pos}, LepR^{pos}, PDGFR α ^{pos}CD51^{pos}, CD45^{neg}Tie2^{neg}CD90^{neg}CD51^{pos}CD105^{pos}, and Nestin-GFP^{pos} phenotypes and CXCL12-abundant reticular (CAR) cells. Among these mouse BM-MSCs populations, some Nestin-GFP^{pos} subsets are positive expressing PC marker NG2 but lacking leptin receptors and distribute around arterioles [300]. However, unlike MSCs, PCs are usually distributed enwrapping vessel walls, specifically, BM-derived PCs located around the arterioles and sinusoids [300]. The arteriolar niche hBM-PCs were found to participate in HSCs quiescence [472], while the sinusoidal niche PCs contributed to HSCs proliferation [473].

The hBM-PCs population in our study was isolated from the BM-MSCs two times the remaining hBM-SCs. This indicates that the hBM-PC is the main subpopulation, a quantities aspect apart from the CD45^{pos} HSCs. Adipogenic differentiation results of our study demonstrated that the CD34^{neg}CD45^{neg}CD146^{pos} PC population had higher adipogenic capabilities than the hBM-SCs. This phenomenon indicates that hBM-PCs are the main subsets of human BM-MSCs responsible for adipogenesis. Previous studies from our group demonstrated that T2DM induced dysfunction in human CD146^{pos} BM-PCs by reducing cell viability, migration, and proliferation ability and leading to apoptosis while decreasing cellular angiogenesis support capacity *in vitro*. Furthermore, downregulation of AKT-relevant angiocrine signalling pathways was found in the hBM-PCs from diabetic individuals, which was associated with lower expression of CXCL12, fibroblast growth factor-2 and increased expression of the angiogenesis inhibitor

angiopoietin 2 [302]. Although I was unable to get suitable diabetic human BM samples to study the differences in adipogenesis ability of hBM-PCs between diabetic and nondiabetic, the previous study from our group showed that the BM-MSCs from T2DM patients had high adipogenesis propensity than non-diabetic individuals [200]. It would be interesting to investigate the effects of T2DM on hBM-PCs adipogenesis in future studies.

In vitro effect of Dasatinib on BM cell senescence and adipogenesis

Cellular senescence is an irreversible cell-cycle arrested stage. The senescent cells show a hypertrophic morphology and reduced proliferation ability [319]. Unlike cellular quiescence, which occurs in G₀, senescence usually occurs in G₁ and possibly in the G₂ phase during the cell cycle [350]. Senescent cells remain alive, but their metabolic activity and gene expression are altered, creating complicated SASPs. Cellular senescence impairs tissue repair and regeneration and consequently develops aging [350]. To date, there is no specific marker to identify senescent cells. Cellular senescence is usually evaluated by combining several hallmarks from different signalling pathways. The cyclin-dependent kinase inhibitor p16^{INK4a} is a crucial marker for assessing senescence, as p16^{INK4a} is essential for maintaining the senescence state by inhibiting the phosphorylation of Rb. In addition, TGF- β may also contribute to senescence as it keeps Rb at a hypophosphorylated stage and then induces cycle arrest of lung epithelial cells in G₁ [350].

The activation of p53/p21^{Waf1/Cip1} signalling results in DNA damage induced by multiple reasons, including proliferation exhaustion, oncogene activation, and genotoxic stress or mitochondrial dysfunction-induced oxidative stress. P53 is a central mediator of cellular senescence, and it can be directly activated by DDR, AMP-activated protein kinase (AMPK), p38 MAPK, and mTOR signalling pathways; subsequently, the upregulation of p53 elevates the downstream p21^{Waf1/Cip1} [350]. During cell cycle progression, a high level of cell cycle arrest marker p21^{Waf1/Cip1} prevents the kinase activity of cyclin D/CDK4,6 complexes causing cell cycle inhibition [350]. DNA impairment is another essential character of senescent cells, and the DDR marker γ H2AX expression level is elevated, indicating unrepaired DNA damage [352].

Moreover, the SASP factors are considered crucial hallmarks of cellular senescence. The composition of SASP is complex and differs in various cell types, including proinflammatory factors, chemokines, bioactive lipids, angiogenic factors, and MMP. Among these SASP factors, IGFBP3, IGFBP4, and IGFBP7 are reported essential in inducing senescence via paracrine signalling. Moreover, the capability of IGFBP3 in promoting cellular senescence is regulated by PAI-1. Furthermore, PAI-1 is reported as a crucial downstream factor of p53, which participates in leading to replicative senescence. The proinflammatory cytokines NF- κ B, IL-6, and IL-8 also get involved in mediating cellular senescence [350]. In the present study, more than 70% of hBM-PCs expressed senescence markers p16^{INK4a}, p21^{Waf1/Cip1} and γ H2AX and showed low proliferation ability, indicating our cells were senescence. The senolytic agent Dasatinib reduced the expression of p21^{Waf1/Cip1} and induced cellular apoptosis after 21 days of coincubation with adipogenic medium (Figure 8-3A). However, the Dasatinib (1 μ M, 48 hours) treated only showed no effects on p16^{INK4a} and p21^{Waf1/Cip1} expression levels apart from reduced proliferation ability of cells.

Adipogenesis is the progress of adipocyte formation by preadipocyte differentiation [474]. Many genes get involved in regulating adipogenic differentiation, among which the transcription factor PPAR γ plays an indispensable role in adipocyte lineage and maintenance of the phenotype of adipocytes [475]. An *in vitro* study found that the activation of PPAR γ increased adipogenesis and lipid metabolism in brown adipocytes [476]. In the progression of adipogenesis, activated PPAR γ is a transcription factor for various genes expression in mature adipocytes, such as FABP4, adiponectin, CD36, and lipoprotein lipase [477]. The lipid transporter, *FABP4*, is the primary target gene of PPAR γ . However, Garin-Shkolnik et al. reported that FABP4 reduced adipogenic differentiation and PPAR γ and was negatively correlated with PPAR γ in adipose tissue. The preadipocytes and macrophages from the FABP4-null mice had higher expression levels of PPAR γ , and in macrophages, compensation with FABP4 could reverse the upregulation of the expression of FABP4. Meanwhile, the FABP4-lacking preadipocytes demonstrated higher adipogenesis capability than the normal preadipocytes [478].

Since PPAR γ is a crucial promotor for adipogenesis, which subsequently increases the production of small insulin-sensitive adipocytes and improves insulin sensitivity, consequently reducing the risk of insulin resistance and the onset of T2DM. Adipose tissue is vital in mediating PPAR γ on insulin sensitivity [479]. Therefore, high expression levels of FABP4 could reduce insulin sensitivity, leading to insulin resistance or even developing into T2DM. Moreover, FABP4 participates in the proinflammatory state. Therefore, the negative feedback loop between FABP4 and PPAR γ explains the higher level of FABP4 in obese T2DM patients compared with nondiabetics. Furthermore, compared with SAT, VAT shows a higher FABP4 level and a lower level of PPAR γ , and the VAT/SAT ratio is increased in people with T2DM [478]. Franczyk et al.'s study demonstrated that VAT removal could reduce insulin resistance in the liver, skeletal muscle, and adipose tissue of male C57BL/6J mice [65]. Our studies showed that inhibition of adipogenesis by Dasatinib was reflected by increased RNA transcripts for *PPARG* and *ADIPOQ* genes, whereas protein expression remained unaltered. On the other hand, FABP4 was upregulated at both mRNA and secreted protein levels in hBM-PCs & BM-SCs.

Interestingly, Dasatinib has been reported to increase the expression levels of PPAR γ and induce adipogenesis in human BM-MSCs, which conflicts with our results. In Borriello et al.'s study, Dasatinib-induced hBM-MSCs adipogenesis potential mechanisms were by inhibiting MAPK signalling pathways through Erk1/2 phosphorylation inhibition [480]. The contrasting conclusions from Borriello et al. and our studies are worth further exploration in the future. Since Dasatinib is a TKI, usually used to treat chronic myeloid leukaemia, its possible effects on BM-derived MSCs or PCs adipogenesis may influence bone turnover and haematopoiesis. Moreover, Dasatinib can block the TGF- β signalling pathways [481], and TGF- β is an important pro-adipogenic factor [482]. Combined with the literature's conclusions and findings, I hypothesise a potential special PPAR γ -FABP4 related mechanism during Dasatinib treatment on hBM-PCs & hBM-SCs adipogenesis (Figure 5-2L).

Dasatinib improves heart and BM steatosis with positive consequences for cardiac function in diabetic mice

Enlargement of white fat depots occurs during periods of caloric excess and is associated with increased risks for diabetes, insulin resistance, and CVD. Visceral fat accumulation is associated with increased resistance against the anti-lipolytic action of insulin. Accelerated lipolysis in visceral fat leads to free fatty acid mobilisation, resulting in hyperglycaemia and hepatic insulin resistance [483]. In addition, patients with T2DM develop an intraparenchymal accumulation of lipids in organs that usually contain minor amounts of fat, with harmful clinical consequences as in the case of metabolic dysfunction-associated fatty liver disease [484].

Less is known about the pathophysiological relevance of fat surrounding and infiltrating the heart. Accumulation of pericardial and epicardial fat, which is a white adipose tissue but also displays brown-fat like or beige fat features, has been associated with an increased risk for HFpEF, coronary artery disease, and arrhythmias [485-487]. Lipids can also accumulate in cardiomyocytes, as initially shown in explanted hearts of patients with end-stage non-ischemic cardiomyopathy, arrhythmogenic right ventricular cardiomyopathy, and healed myocardial infarction [488]. Obesity and T2DM exacerbate this phenomenon [489]. Significantly, cardiac adiposopathy can precede but also contribute to the evolution of diabetic cardiomyopathy into heart failure [490]. A retrospective study on T2DM patients who underwent cardiovascular computed tomography imaging demonstrated that those with more myocardial lipids had more severe LV systolic and diastolic dysfunction [491]. The circulation represents the primary source of fatty acids that become stored as TG droplets within cardiomyocytes, with epicardial fat representing a secondary source. This latter assumption is based on a reported correlation between epicardial fat volume and myocardial fat content, a combination often associated with higher LV mass, interstitial fibrosis, and worse LV performance in healthy subjects and heart failure patients [430, 492, 493]. Therefore, reducing lipid accumulation in the heart is an urgent therapeutic target in patients with T2DM. Caloric restriction reportedly reduced myocardial lipid content in non-diabetic obese and T2DM patients [494, 495], whereas pioglitazone or metformin was ineffective [496]. In present study, the Dasatinib treatment reduced lipid accumulation in the diabetic mice heart at both treatment durations. Remarkably, the LV diastolic function

and the cardiac interstitial fibrosis were improved after long-term treatment with Dasatinib.

Cellular senescence is closely related to cardiovascular disorders. The myocardium p53 expression level increased in patients with end-stage heart failure and those with hypertrophic or dilated cardiomyopathy. Moreover, a high level of SASP factor, IGFBP7, influenced the prognosis of patients with HFpEF [325]. Cellular senescence in mouse cardiomyocytes increased the production of ROS, resulting in increased LV mass and cardiomyocyte volume while reducing the number of cardiomyocytes [497]. Senolytic agents were reported to eliminate p16^{INK4a}-positive cells in cardiomyocytes. For instance, in a premature aging mouse model, the senolytic agent AP20187 treatment removed p16^{INK4a}-positive cells, resulting in increased cardiomyocyte number but showed no improvement in cardiac function [498]. Moreover, Dasatinib + Quercetin treatment ameliorated cardiac ejection fraction in aged C57BL/6 mice [499]. Another study on aged INK-ATTAC mice showed that the Dasatinib + Quercetin treatment removed senescent cells, activated cardiac progenitor cells, and increased the proliferation ability of remaining cardiomyocytes [500]. These studies suggest that senolytic agents could selectively eliminate senescent cardiomyocytes and preserve the regenerative capability of cardiac progenitor cells. Our study demonstrated that the long duration of Dasatinib treatment reduced senescent marker p16^{INK4a} levels in the murine hearts and improved the diastolic function of the heart.

Interestingly, senolytic therapy also showed sufficient effects on those tissues with limited regenerative capacity. For instance, senolytic agent ganciclovir was found to eliminate senescent astrocytes in Parkinsonian Substantia Nigra pars compacta of p16-3MR mice (an aged mouse model), consequently ameliorating motor function and recovered adult neurogenesis in these aged mice [501]. Recently, Salam et al. have shown that ganciclovir treatment removed p16^{INK4a}-positive senescent malignant cells in the p16-3MR glioblastoma mice model, improving the survival of female glioblastoma-bearing mice [502]. In addition, senolytic agents may be crucial in tissue remodelling and organ repair as well. Senolytic drug ABT-263 administration via oral gavage eliminated senescent neurons in spinal-cord-injured mice model, reduced the

levels of prof-fibrotic (e.g., amphiregulin, IGFBP-3, serpin E1) and pro-inflammatory (e.g., IL-15, TNF- α) factors and ameliorated the motor, sensory, and bladder function of animals [503].

BMAT is crucial for energy storage and bone homeostasis maintenance [94]. BMAT is an endocrine fat depot that regulates energy metabolism and skeleton homeostasis by producing adipokines, growth factors, inflammation factors, peptides, and fatty acids [101]. Unlike the subcutaneous and visceral fat, the BM fat shows both characteristics of white and brown adipocytes [504] and exists in constitutive and regulated forms [94]. Emerging evidence indicates that BM fat accumulation may increase cardiovascular complication risk [198]. BM adipocytes originate from BM-MSCs, and regulate adipogenesis progress by PPAR γ [316]. BM adipocytes are similar to white adipocytes, but the lipid composition changes with aging, and the nucleus is replaced by lipid droplets [316]. T2DM is a risk factor causing BM fat overloading and breaking the balance between BM adipocytes and osteoblasts, leading to decreased bone mineral density and osteoporosis [193, 196]. The morphometric analysis results demonstrated that the number and size of BM adipocytes were increased in diabetic patients compared to nondiabetic individuals [198]. T2DM is reported to induce BM remodelling by decreasing the number of microvessels and sensory nerves, increasing CD34^{pos} HSCs apoptosis, and promoting fat accumulation.

Moreover, BM adiposity is positive-correlated with HbA1c [198]. The abundance of BMAT in the T2DM population promotes the senescence progress of the whole body, as senescent BMAT could expand senescence through the entire system via endocrine characteristics [198]. In the previous study from our group, researchers found that the BM-MSCs from T2DM patients showed higher transcription levels of adipogenesis markers, including PPAR γ , FABP4, adiponectin, and C/EBP α , than nondiabetic cells [200]. The present study demonstrated that either one-week or four-week Dasatinib treatment could reduce lipid accumulation in diabetic mice BM. However, the BM-MSCs isolated from T2DM mouse BM showed no improvement in reducing CD36, the adipogenic marker, and DPP4 [470], a regulator of chemokine-induced stem cell mobilization. CD36 is a membrane glycoprotein on the surface of adipocytes, platelets,

myocytes, mononuclear phagocytes, and hepatocytes. It has been reported that CD36 contributed to promoting chronic inflammation of adipocytes and macrophages, consequently leading to insulin resistance in obesity [505]. Moreover, CD36 is a target gene of PPAR γ , and the expression of CD36 and PPAR γ are positively correlated [506]. DPP4, also termed CD26, is an enzyme that acts on incretin hormones, especially promoting the inactivation of GLP1, subsequently caused decreasing in insulin secretion, and inducing hyperglycemia [507]. Moreover, DPP4 also plays a crucial role in regulating the mobilization of BM stem cells by mediating granulocyte-colony stimulating factor and CXCL12. Different from the high level of DPP4 in the circulation system, the activity and expression levels of DPP4 are decreased in diabetic BM, consequently influencing BM stem cell mobilization [470]. In contrast to heart and BM, Dasatinib did not reduce classical white fat depots, thus suggesting a distinct action on the heart and BM.

Accumulating evidence suggests that TKI therapy benefits dysmetabolic disease. Imatinib, a first-generation TKI, reportedly preserved β cell function in adult patients with recent-onset T1DM [508]. An association therapy of Dasatinib, a second-generation TKI, and the flavonoid Quercetin attenuated adipose tissue inflammation and improved systemic metabolic function in older mice [445]. In addition, this drug combination had senolytic effects in WAT, as evidenced by a reduction in the expression of SA- β -gal, p16^{INK4a}, and p21^{Waf1/Cip1} [456]. The present study found that the four-week treatment of Dasatinib trended to attenuate the p16^{INK4a} level in diabetic mice BM and attenuated their BM-MSCs senescent phenotype, β -galactosidase.

Different mechanisms could be implicated in the observed cardiac benefits. Cardiomyocyte senescence is associated with disruption of the tight balance between lipid availability and oxidation [509, 510]. Studies have previously shown that anti-aging treatments protect the heart from T2DM-induced damage through subtle modifications in mitochondrial-related proteins and lipid metabolism [467, 511]. Dasatinib may act as a senolytic agent eliminating lipid-bearing senescent cardiomyocytes, as suggested by the reduction in p16^{INK4a} expression, along with an improved metabolic performance of remaining cardiomyocytes. Senolytic agents can alleviate multiple senescence-related phenotypes, including activation of local and systemic SASP signalling [512]. However,

in our study, Dasatinib therapy of diabetic mice did not alter the plasma levels of inflammatory adipokines.

A direct effect of Dasatinib on metabolic pathways is suggested by the previous finding that the TKI protected against glucose intolerance through the upregulation of PGC-1 α expression in WAT [513]. Induction of PGC-1 α has anti-fibrotic and cardioprotective effects in T2DM [514]. Additionally, TKIs can improve the anti-lipolytic activity of insulin, thereby reducing the mobilization of FFAs from visceral fat depots [458]. In a murine model of NAFLD, Dasatinib reportedly reduced liver steatosis, inflammation, fibrosis, and hepatocellular ballooning, by attenuating lipogenesis and inducing M2 macrophage polarization with antifibrotic activity [457]. In this latter study, the TKI was given at the dosage of 4 or 8 mg/kg once daily for four weeks [457]. I preferred to use intermittent treatment schedules to reduce potential toxic effects while preserving clinical efficacy [515].

In the present study, although the results showed some statistically significant improvement in diabetic mice after Dasatinib treatment, it's still far from translation to clinical application. There were several limitations in the study: 1) the group size of animals was small; 2) the diabetic model was a transgenic mouse model, which did not fully mimic the pathophysiological conditions of human diabetes; 3) the study was just the first step of exploring the senolytic effect of Dasatinib on diabetic mice, which needed further deeply preclinical work to understand the potential mechanisms. Therefore, it would be better to increase the group size of animals, study the effects of Dasatinib on other models, such as the high-fat diet-induced diabetes model and further explore the potential mechanisms of Dasatinib treatment before clinical study.

CHAPTER 6. FUTURE PERSPECTIVES

In this study, the optimised culture condition of hBM-PC plays an important role in maintaining the function and phenotype characteristics of pericytes, which is beneficial for the *in vitro* expansion of hBM-PCs, especially in the cells come from elderly donors showing the features of senescence.

The work investigating the adipogenic differentiation propensity in the human BM-MSCs subpopulation demonstrates that hBM-PC is the primary subset adipocyte source in the BM-MSCs, which gives us a further understanding of the multipotent capacity of BM-MSCs. This finding suggests that hBM-PCs may be a novel target for exploring the mechanisms of BM adiposopathy or T2DM-related BM steatosis. In the previous study of our group, I found that T2DM human BM-MSCs had higher adipogenesis capacity than nondiabetic cells [200]. However, due to the shortage of diabetic BM samples caused by the COVID-19 pandemic, this project was only performed on nondiabetic cell lines. Whether the diabetes conditions will influence this phenomenon is still unclear and worth exploring in future studies. Meantime, the transcription levels of adipogenesis-related genes and their protein levels show no statistical difference between hBM-PCs and hBM-SCs. Therefore, future studies on hBM-PCs adipogenic differentiation will be performed on more cell lines and will compare T2DM and healthy samples.

The work exploring the effects of the senolytic agent Dasatinib on hBM-PCs and hBM-SCs shows that Dasatinib blunts the adipogenic differentiation of both populations. Although histological results of ORO staining indicated that Dasatinib inhibited adipocytes differentiation in hBM-PCs and hBM-SCs, the molecular biology analysis showed that the transcription levels of adipogenesis genes *FABP4*, *PPARG*, and *ADIPOQ* were not consistent with their protein levels. *FABP4* was upregulated at both mRNA and secreted protein levels. Despite lacking a typical secretory signal peptide, *FABP4* is reportedly released from adipocytes in a non-classical lipolytic pathway, possibly acting as an adipokine [516]. Therefore, I propose a potential *FABP4*-PPAR γ feedback loop to explain this phenomenon. However, the Borriello et al. study [480] reported that

Dasatinib increased adipogenic differentiation in human BM-MSCs, which was inverse to our conclusions. The differences between MSCs and PCs may cause this. Consequently, I will have two experiments in future studies to investigate the mechanisms of Dasatinib on the adipogenic differentiation of hBM-PCs:

1. **Study 1.** Effects of Dasatinib on human BM-MSCs and BM-PCs adipogenic differentiation.
2. **Study 2.** Effects of FABP4 inhibitor (BMS309403) on Dasatinib-treated hBM-PCs adipogenic differentiation.

The *in vivo* Dasatinib treatment on T2DM obese mice study demonstrates that Dasatinib treatment reduces lipid accumulation in both heart and BM. The results indicated that long-duration administration of Dasatinib reduced cardiac steatosis and fibrosis and improved diastolic function in obese, type 2 diabetic mice and decreased the expression of the cyclin-dependent kinase inhibitor p16^{INK4a}. The treatment did not affect body weight, the size of WAT depots, or altered glycosuria. Since CVD represents the leading cause of mortality in T2DM, I propose a new project to targeting improve T2DM cardiomyopathy based on the findings of this study as follows.

Pemafibrate, a PPAR α agonist, has beneficial effects on dyslipidaemia but not cardiac function [517]. Dasatinib, a TKI, improves mitochondrial biogenesis and triglyceride utilisation via activation of PGC-1 α , a co-regulator of PPAR α [513]. Acting as a senolytic agent, Dasatinib eradicates senescent and pro-inflammatory cells in the diabetic heart. Therefore, I hypothesise that the combination of Pemafibrate and Dasatinib exerts synergistic benefits on systemic metabolic control and cardiac steatosis to protect from the development of diabetic cardiomyopathy. I will test this hypothesis under the following specific objectives, developed in 3 interconnected studies:

1. **Study 1.** Demonstrate that combined treatment with intermittent Dasatinib plus Pemafibrate improves cardiac function in two distinct models of T2DM with similar benefits in both sexes.

2. **Study 2.** Characterise the metabolic improvement at the systemic and cardiac levels.
3. **Study 3.** Investigate the molecular mechanisms restoring the PPAR α and PGC-1 α balance in the diabetic heart.

CHAPTER 7. CONCLUSION

The table below summarises the findings of each chapter.

Chapter	Main Findings
Chapter 2. Cellular source of adipocytes in human bone marrow	<ul style="list-style-type: none"> • Thirty-eight human BM samples were collected and isolated. • Optimised culture conditions of hBM-PCs: culturing cells in 20% (v/v) FBS + αMEM medium and seeded on plates coated with 0.1% (w/v) gelatin. • The hBM-PCs were highly expressed senescence markers and had low proliferation ability, indicating senescence of these cells. • The hBM-PCs showed high adipocyte differentiation capability than hBM-SCs, indicating that hBM-PC was the primary source of adipocytes.
Chapter 3. Effects of Senolytic agent Dasatinib on hBM-PCs & hBM-SCs	<ul style="list-style-type: none"> • Dasatinib treatment reduced the proliferation ability of hBM-PCs. • Dasatinib treatment blunted adipogenesis of hBM-PCs along with decreasing p21^{Waf1/Cip1} levels and inducing apoptosis.
Chapter 4. <i>In vivo</i> effects of Dasatinib-treatment on T2DM obese mice	<ul style="list-style-type: none"> • Short-term treatment of Dasatinib only reduced lipid accumulation in the heart and BM. • Long-term treatment of Dasatinib reduced lipid accumulation in the heart and expression levels of p16^{INK4a} and myocardial interstitial fibrosis and ameliorated cardiac diastolic function. • Long-term treatment of Dasatinib decreased lipid accumulation in the BM and tended to attenuate senescence in mouse BM-MSCs. • Short- or long-term treatment of Dasatinib showed no effects on adipokines (resistin, leptin, IL-6, PAI-1, MCP-1, and insulin) circulation levels.

Table 7-1 Summary of the findings.

This study was based on the previous findings in our group, an MCP-1 feedback loop between BM-derived MSCs and adipocytes that can be enhanced with T2DM. Since the subpopulations of BM-MSCs vary, the subset responsible for adipogenesis remains unknown. Therefore, the first objective of this project was to explore the adipogenesis

population. Unfortunately, the pandemic of COVID-19 caused suppression of patient recruitment for 10 months, primarily influencing the recruitment of diabetic samples. Therefore, after discussing with Prof. *Paolo Madeddu*, we decided to keep investigating the adipogenesis capability of hBM-PCs without T2DM conditions. Fortunately, the nondiabetic hBM-PCs showed characteristics of senescence, which encouraged us to investigate the effects of senolytic agent Dasatinib on the adipogenesis of hBM-PCs. Prior to this work, our group had established the protocol for hBM-PCs isolation and expansion. However, the senescent PCs detached from the culture surface within the original conditions, so I had to optimise the culture conditions to grow the cells. Although the *in vitro* study was not performed on diabetic samples, the effects of TKI Dasatinib on senescent hBM-PCs were meaningful to explore, as aging was closely associated with T2DM.

In vivo study aimed to investigate the effects of Dasatinib on T2DM obese mice BM and cardiac function. Since the supplier did not have suitable Db/Db mice, I had to order younger mice (8-week-olds) and house them until 21 weeks old. I had three trials for this study, but the first trial was forced to stop due to the laboratory closure during the COVID-19 pandemic. The animals for the first trial were sacrificed at 20 weeks old without entering the experiments, and tissues were harvested for backup. Considering the welfare of animals and budget saving, I performed a pilot study to select suitable ages of the Db/Db mice to understand whether I could start the treatment at an early age of the animal. An ORO staining was used to measure the lipid accumulation in Db/Db mice hearts from different ages. The results showed higher ORO positive cell distribution in the 20-week-old mice heart, suggesting a better obese model than other ages of animals. Next, a short-term treatment of Dasatinib model was applied to study the safety and effects of the drug. The results demonstrated that short-term treatment of Dasatinib was safe for animals and could reduce cardiac and BM steatosis but no alteration in cardiac function or cellular senescence. The results of short-term treatment encouraged us to prolong the administration of Dasatinib duration for further analysis. The long-term treatment of Dasatinib findings suggests that Dasatinib can help combat heart steatosis and fibrosis. I can only speculate about the mechanisms underlying this benefit, which may involve Dasatinib's metabolic and senolytic activities.

Based on the findings of this study, my first-author manuscript entitled “*The tyrosine kinase inhibitor Dasatinib reduces cardiac steatosis and fibrosis in obese, type 2 diabetic mice*” is published by *Cardiovascular Diabetology*. (<https://doi.org/10.1186/s12933-023-01955-9>).

In summary, this study successfully found that hBM-PC was the primary adipocyte source in BM, and Dasatinib could blunt PC adipogenic differentiation. Meanwhile, Dasatinib could reduce cardiac steatosis, fibrosis, and BM obesity in obese, type 2 diabetic mice. Finally, future works are necessary to confirm the findings of this study and investigate deeply mechanisms.

CHAPTER 8. APPENDIX

8.1. Supplementary data

8.1.1. Positive control of cellular senescence

Before obtaining BM samples to isolate hBM-PCs, the DNA damage agent Etoposide was used in preliminary experiments to induce cellular senescence in human primary cardiac pericytes (hCPs). This was considered as a positive control to test methods to detect cell senescence. hCPs were stimulated with 40 μ M or 60 μ M Etoposide for 48 or 72 hours. After the incubation, ICC staining (methods shown in **section 2.2.6**) was performed to analyse the senescence marker p21^{Waf1/Cip1} expression levels in all the conditions (**Figure 8-1A**). Senescence- β -galactosidase assay (methods according to the vendor's protocol, Cell Signaling, CAT#9860) was used to analyse the expression of β -galactosidase, but results could not be quantified due to technical issues since it was difficult to focus the cells under the microscope and the positive signal was unclear (**Figure 8-1B**). The results showed that cells stimulated with 40 μ M Etoposide for 72 hours had a high expression of p21^{Waf1/Cip1} (71.25%) compared with the other conditions (**Figure 8-1C**). Because later, I found that more than 80% of hBM-PCs were senescent (**Figure 2-5**), there was no need to use a positive control of cell senescence in the *in vitro* studies with BM cells.

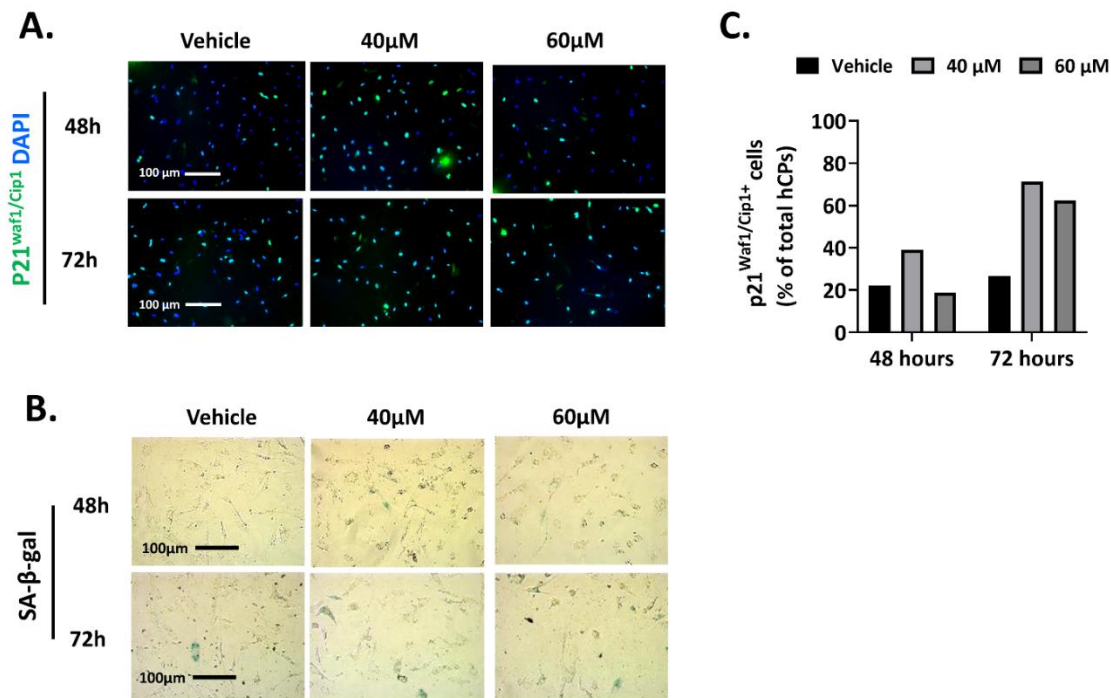


Figure 8-1 Etoposide-induced human CPs senescence as a positive control of cellular senescence.

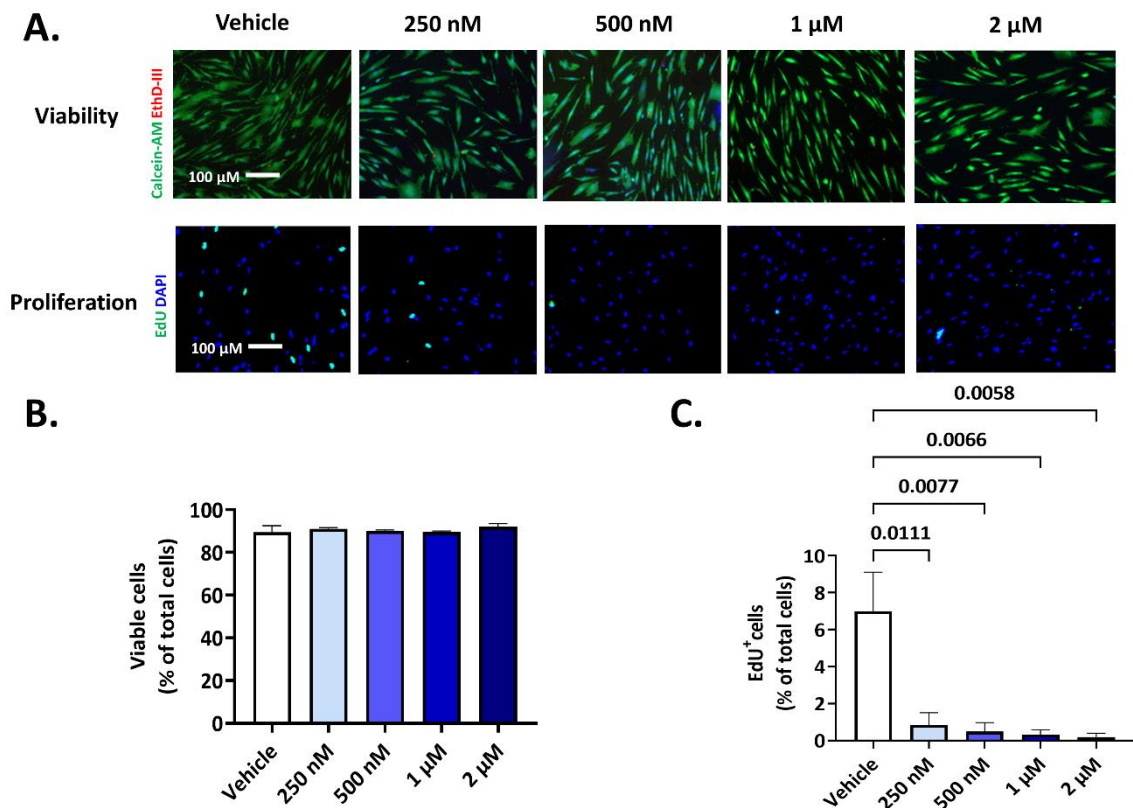
Human CPs (n = 1 cell line/group) were stimulated with 40 μM or 60 μM Etoposide or vehicle (DMSO) for 48 or 72 hours. Immunofluorescence images (A) show p21^{Waf1/Cip1} (green nuclear positivity) positive senescent hCPs. Nuclei were stained with DAPI (blue). Bar graph (C) shows the p21^{Waf1/Cip1} positive cell fraction (expressed as % of total cells) under different conditions. Bright-field images (B) show the β-galactosidase activity (blue) in hCPs in the Vehicle group and 40 μM and 60 μM Etoposide groups. Abbreviations: hCPs = human cardiac pericytes, DMSO = Dimethyl sulfoxide; SA-β-gal = senescence-β-galactosidase; DAPI = 4',6-diamidino-2-phenylindole.

8.1.2. Optimisation of Dasatinib concentration for *in vitro* treatment of human BM-PCs

Before assessing the effects of Dasatinib on senescent hBM-PCs, a titration of increasing concentrations of Dasatinib was used to establish the optimal dosage of the drug. hBM-PCs were incubated with four different concentrations of Dasatinib, including 250 nM, 500 nM, 1 μM and 2 μM for 48 hours, followed by 3 days of recovery in a drug-free medium; DMSO was used as a vehicle. At the end of the protocol, hBM-PC viability, proliferation (EdU), and expression of senescence makers p16^{INK4a}, γH2AX^{pos} + ki67^{neg},

and p21^{Waf1/Cip1} were assessed to measure the cellular function. Antibodies using this experiment are listed in **Table 2-1**.

The viability assay showed more than 90% viable cells in each experimental condition (**Figure 8-2 A and B**). Moreover, hBM-PCs treated with Dasatinib had fewer EdU-positive cells than the Vehicle-treated cells, indicating that the drug suppresses cell proliferation (**Figure 8-2 A and C**). While Dasatinib did not significantly affect the expression of senescence markers, I observed a trend to reduce the expression of p16^{INK4a} and p21^{Waf1/Cip1} in cells treated with 1 μ M Dasatinib (**Figure 8-2 D to F**). However, the fraction of γ H2AX^{pos} + ki67^{neg} cells remained similar in all the treatment groups (**Figure 8-2G**). Altogether, these data suggest that a 48-hour treatment with 1 μ M Dasatinib, followed by a 3-day recovery, may reduce hBM-PC proliferation ability, and potentially decrease cellular senescence whilst not affecting cell viability. Therefore, I will adopt this concentration for all the experiments performed in this thesis.



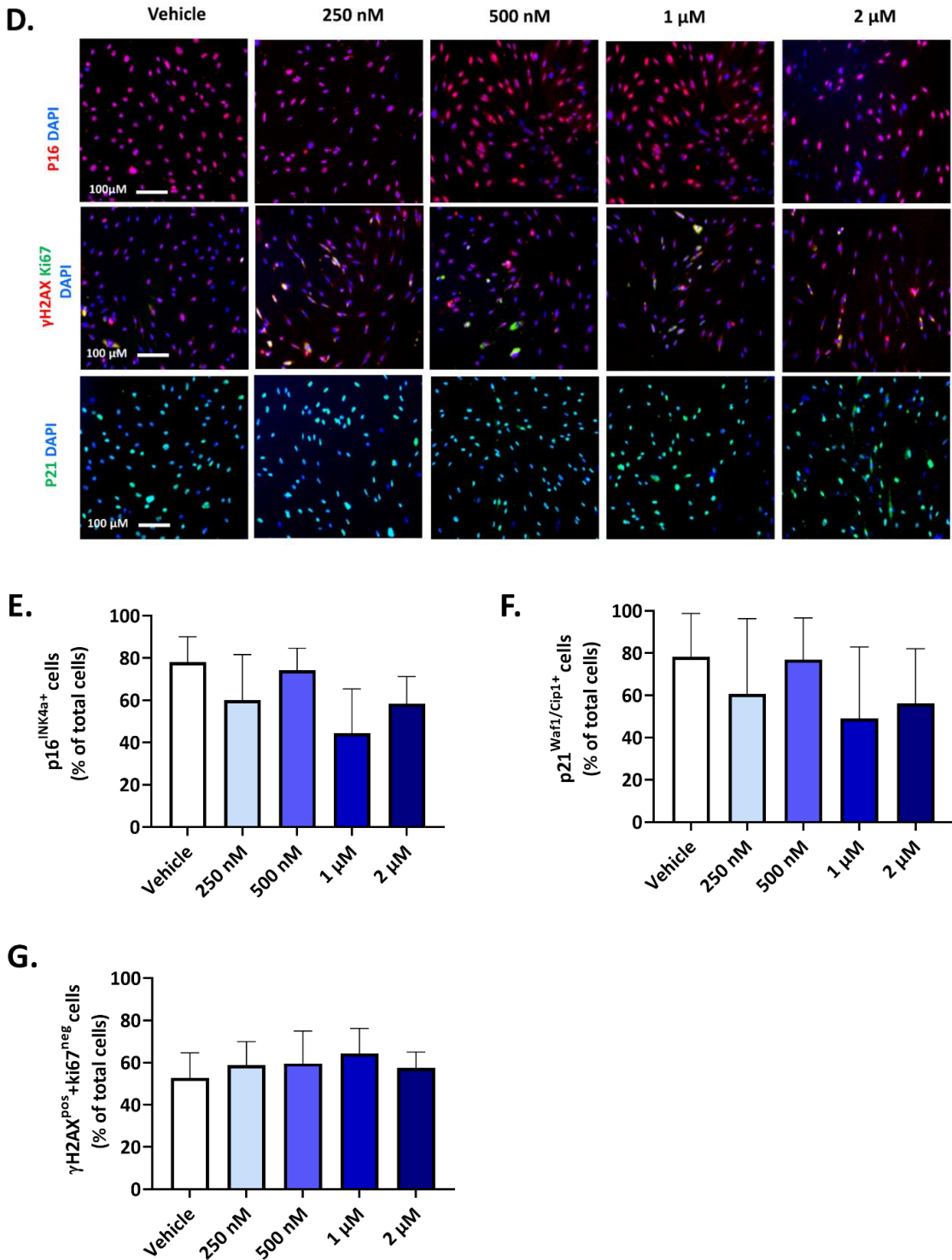


Figure 8-2 Optimisation of Dasatinib concentration for *in vitro* treatment of human BM-PCs.

Cells were treated with 250 nM, 500 nM, 1 μM and 2 μM Dasatinib or vehicle (DMSO) for 48 hours and left to recover for three days. Fluorescence images (A) show the viable (Calcein-AM, live cell = green fluorescence; EthD-III, dead cell = red fluorescence) and proliferating cells (EdU positive cells = green fluorescence) after Dasatinib treatment. Bar graphs show the fraction of viable cells (B) and EdU-positive proliferating cells (C), demonstrated as a percentage of the total cells. Immunofluorescence images show (D)

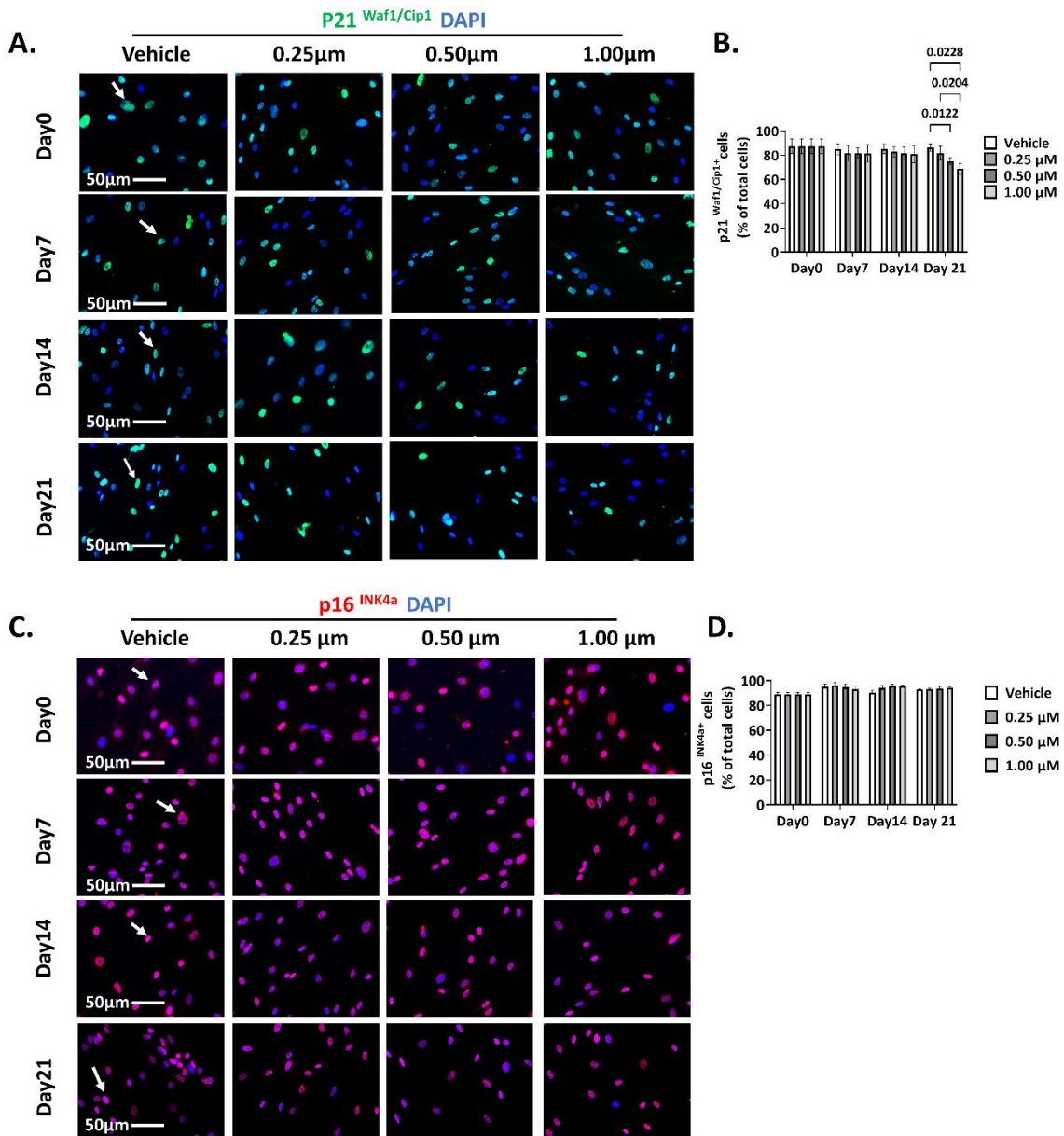
the presence of p16^{INK4a} (red nuclear positivity), p21^{Waf1/Cip1} (green nuclear positivity), and γ H2AX^{pos} + ki67^{neg} (γ H2AX = red nuclear positivity; ki67 = green nuclear positivity) senescent hBM-PCs in the total cell numbers. Nuclei were stained with DAPI (blue). Bar graphs (E, F, and G) show the fraction (%) of p16^{INK4a}, p21^{Waf1/Cip1} and γ H2AX^{pos} + ki67^{neg} cells. Data are presented as mean \pm SEM and were analysed using one-way ANOVA followed by Tukey's multiple comparisons tests. n = 3 patients' cells/group. Abbreviations: hBM-PCs = human bone marrow pericytes; DMSO = dimethyl sulfoxide; DAPI = 4',6-diamidino-2-phenylindole.

8.1.3. Optimisation of the Dasatinib concentration for *in vitro* induction of human BM-PC adipocyte differentiation

Before exploring the effects of Dasatinib on senescent hBM-PC adipogenic differentiation, a pilot study was performed to select the optimal concentration for Dasatinib. HBM-PCs were stimulated with a pro-adipogenic medium, including 1 μ M dexamethasone, 0.5 mM isobutylmethylxanthine, 10 μ g/mL insulin, and 1 μ M indomethacin in DMEM + 10% (v/v) FBS for 21 days. The medium was supplemented with three different concentrations of Dasatinib (0.25 μ M, 0.50 μ M, and 1.00 μ M). The differentiation protocol consisted of alternating 2 days of incubation with Dasatinib/vehicle and 3 days of recovery without Dasatinib/vehicle for 21 days. ICC staining (methods shown in **section 2.2.6**) was used to assess the expression levels of senescence markers p16^{INK4a} and p21^{Waf1/Cip1} (antibodies listed in **Table 2-1**), ORO staining (methods shown in **section 2.2.7**) was performed to measure the adipocyte differentiation (methods shown in **section 3.2.3**), and TUNEL assay (methods shown in **section 3.2.6.3**) was used to evaluate the cell apoptosis.

The results indicated that after 21 days of stimulation with the pro-adipogenic medium, treatment with 0.5 μ M or 1 μ M Dasatinib reduced the fraction of p21^{Waf1/Cip1}-positive cells (**Figure 8-3 A and B**) when compared with the Vehicle group. The p16^{INK4a} expression levels (**Figure 8-3 C and D**) were similar in all the treatment conditions. The ORO quantification indicated a trend towards reduced adipocyte differentiation in hBM-PCs treated with higher concentrations of Dasatinib (**Figure 8-3 E and F**). After 21 days,

1 μM Dasatinib treatment induced significant apoptosis in the hBM-PCs compared with the Vehicle group (Figure 8-3 G and H). Altogether, these results suggest that 1 μM Dasatinib treatment may inhibit adipogenic differentiation by activating apoptosis and downregulating the expression of p21^{Waf1/Cip1}. Therefore, this concentration (1 μM) of the drug will be used for the following studies.



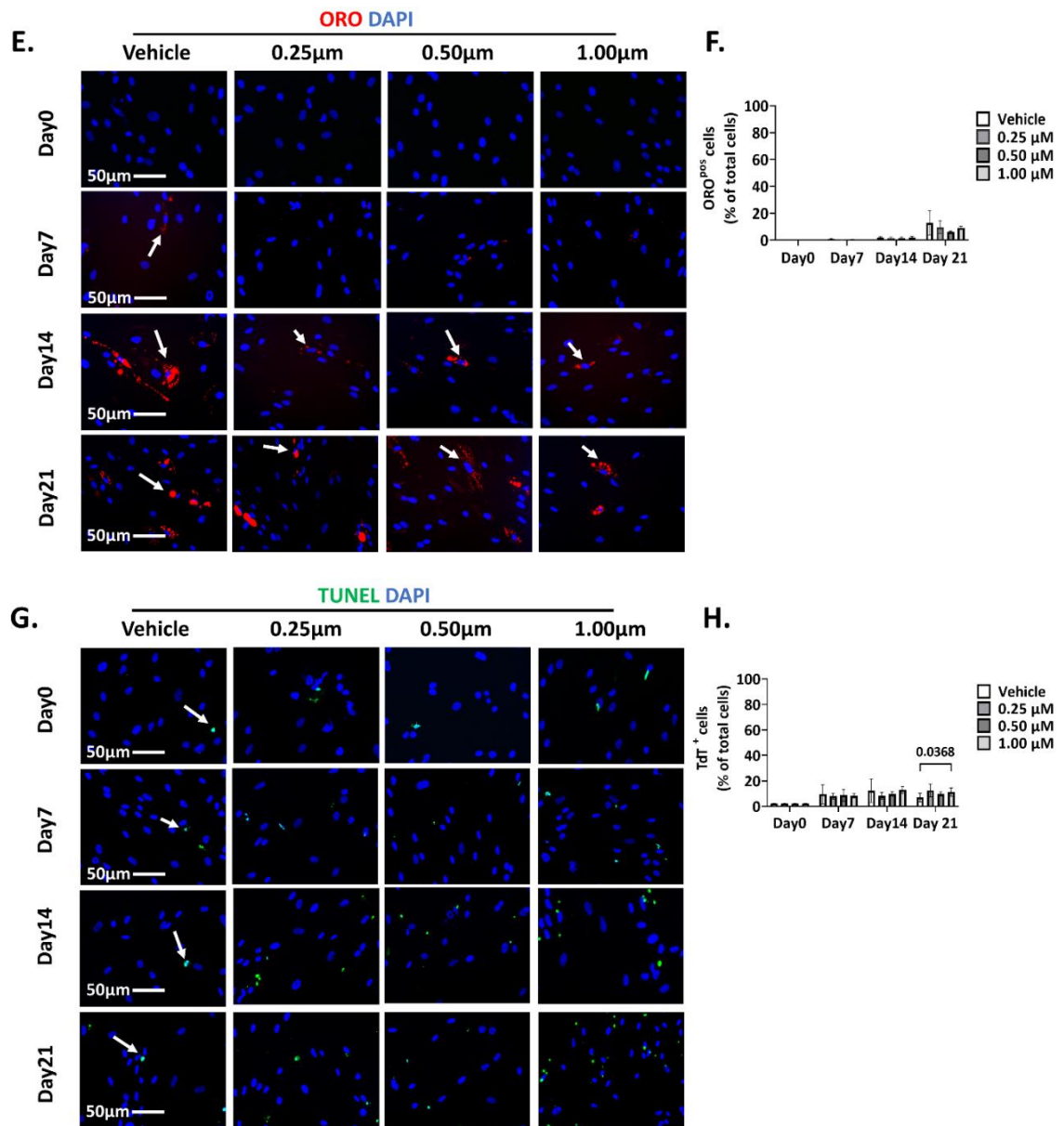


Figure 8-3 Optimisation of the Dasatinib concentration for experiments of adipogenesis differentiation of human BM-PCs.

Immunofluorescence images show the nuclear expression of the senescence markers: (A) p21^{Waf1/Cip1} (arrow, green) and (C) p16^{INK4a} (arrow, red) in hBM-PCs; (E) the presence of adipocytes is shown by ORO-positive staining (arrow, red); and (G) the presence of apoptotic hBM-PCs is shown by positivity to TUNEL (arrow, green). Nuclei were stained with DAPI (blue). Bar graphs (B, D, F, and H) show the fraction of cells (demonstrated as a percentage of total cells) positive to the above-described fluorescence stainings. Data are presented as mean \pm SEM and were analysed using two-way ANOVA followed by Tukey's multiple comparisons tests. n = 3 patients' cells/group. Abbreviations: hBM-PCs = human bone marrow pericytes; DMSO = dimethyl sulfoxide; DAPI = 4',6-diamidino-2-phenylindole; TdT = terminal deoxynucleotidyl transferase.

8.2. *In vitro* insulin resistance models

8.2.1. High glucose induced insulin resistance *in vitro*

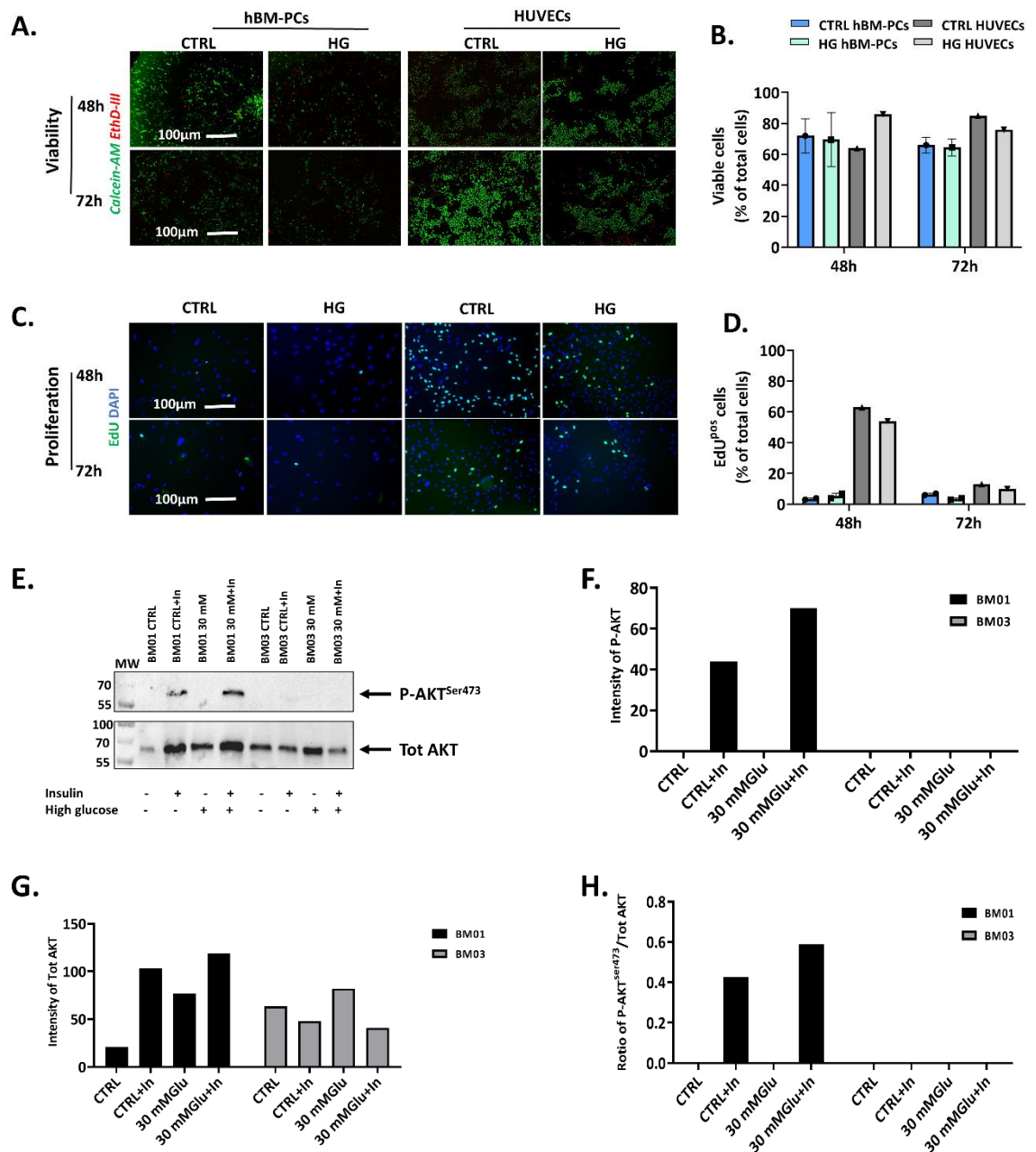
8.2.1.1. Experiment design

Due to the difficulty of collecting human T2DM BM samples, I performed a pilot experiment to mimic insulin resistance *in vitro*. HUVECs were used as a positive control [224]. Both hBM-PCs (n = 2) and HUVECs (n = 1) were stimulated with α MEM containing either the regular concentration of glucose used for optimal cell growth (CTRL, 5.5 mM) or a high glucose concentration (HG, 30 mM) to mimic insulin resistance, for 48 or 72 hours. After the incubation, cells were cultured with α MEM only in the absence or presence of 100 nM insulin for 30 minutes at 37°C before being processed for WB (methods shown in **section 3.2.8**) or ICC (methods shown in **section 2.2.6**). Functional assays included cell viability (methods shown in **section 2.2.8**), proliferation (EdU incorporation) (methods shown in **section 2.2.9**), expression of the senescence marker p21^{Waf1/Cip1} by ICC, AKT activation/phosphorylation (P-Akt^{Ser473}) using WB.

8.2.1.2. Results

The results showed that HG did not influence either HUVEC or hBM-PC viability (**Figure 8-4 A and B**). However, after 72 hours of stimulation, compared with the 48-hour time point, I observed a decrease in the proliferation ability of HUVECs in both control and HG groups, while there were no changes for hBM-PCs (**Figure 8-4 C and D**). Because a decrease in the ratio between P-AKT^{Ser473} and Total AKT indicates insulin resistance [518], I analysed how P-AKT^{Ser473}/Tot AKT changed in hBM-PCs after the incubation with different media. Due to the limited availability of hBM-PCs, I performed this pilot study using only two cell lines. Interestingly, after insulin stimulation, one cell line showed a tendency to a higher P-AKT^{Ser473}/Total AKT ratio in the HG than in the CTRL treatment, which was in contrast with what was reported in the literature, while the other cell line did not express P-AKT^{Ser473} (**Figure 8-4 E to H**). Moreover, the ICC results showed that 69% of cells were p21^{WAF1/CIP1}-positive in the CTRL group, indicating that hBM-PCs were

already senescent at baseline (**Figure 8-4 I and J**). This finding is consistent with the results of **section 2.3.3.2**. These results suggest that senescent hBM-PCs are not sensitive to high glucose. Therefore, HG cannot be used to induce insulin resistance.



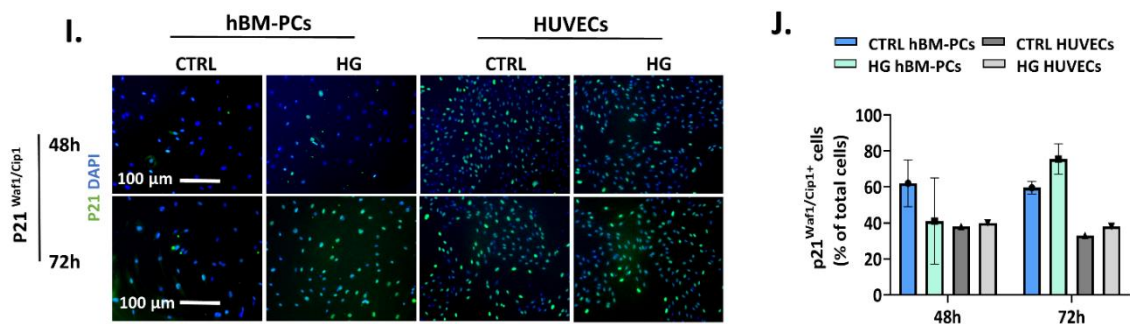


Figure 8-4 *In vitro* model of high glucose-induced insulin resistance in human BM-PCs and HUVECs.

Cells were incubated with either regular (5 mM) or high glucose (30 mM) concentrations for 48 or 72 hours. HUVECs were used as the positive control according to the literature. Fluorescence images show the (A) viability (Calcein-AM, live cell = green, EthD-III, dead cell = red) and (C) proliferation ability (EdU nuclear positivity, green) of hBM-PCs and HUVECs. Histograms (B and D) show the fraction of cells (% of total cells) positive for the indicated markers. (E) Western blots using cell extracts obtained from hBM-PCs (other blots performed using HUVECs and hBM-PCs did not technically work, so results are not shown). Membranes were incubated with antibodies directed against P-AKT^{Ser473} and Total AKT. Histograms (F and G) show the intensity of P-AKT^{Ser473} and Total AKT (measured as mean grey values) in hBM-PCs. Histogram (H) shows the ratio between P-AKT^{Ser473} and Total AKT. Immunofluorescence images (I) show the nuclear expression of the senescence marker p21^{Waf1/Cip1} (green) in hBM-PCs and HUVECs. Nuclei were stained by DAPI (blue). Histogram (J) shows the fraction of cells positive for p21^{Waf1/Cip1} (% of total cells). Data are shown as mean \pm SEM and were analysed using two-way ANOVA followed by Tukey's multiple comparisons tests. n = 2 (hBM-PCs) or 1 (HUVECs) biological replicates/group. Abbreviations: hBM-PCs = human bone marrow pericytes; HUVECs = human umbilical vein endothelial cells; DAPI = 4',6-diamidino-2-phenylindole; P-AKT^{Ser473} = phosphor-protein kinase B ser473; AKT = protein kinase B; In = insulin; Glu = glucose.

8.2.2. High glucose and glucosamine induced insulin resistance *in vitro*

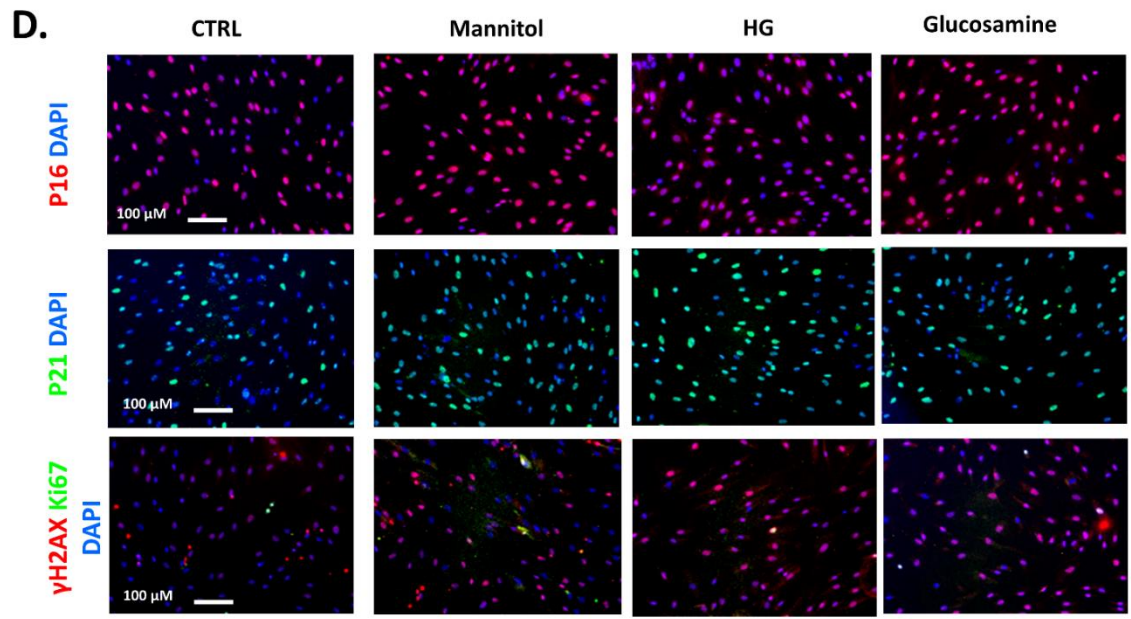
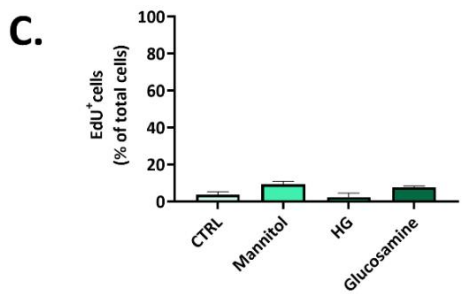
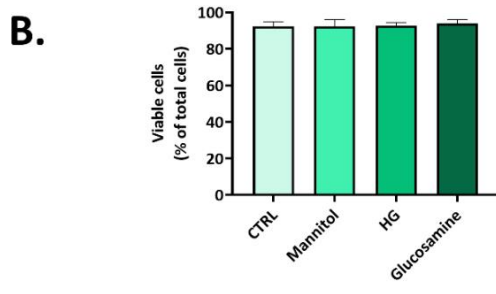
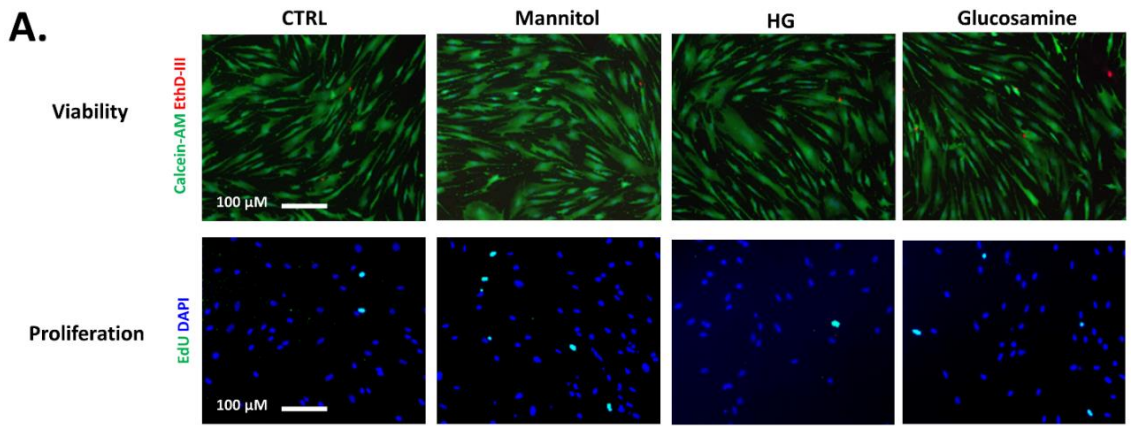
8.2.2.1. Experiment design

Moving on from the previous study (section 8.2.1), which indicated that senescent hBM-PCs were not sensitive to HG, I decided to test whether glucosamine [224] can induce insulin resistance in hBM-PCs. To exclude the osmotic effect of D-glucose on cells, D-mannitol served as an osmotic control to optimise the experiment [519]. HBM-PCs were stimulated with 10 mM glucosamine, 30 mM D-mannitol, 30 mM D-glucose or 5.5 mM

D-glucose (CTRL) for 48 hours. After treatment, half of the cells were processed for function assays and ICC staining, and the other half of hBM-PCs were incubated with α MEM supplemented with/without 100 nM insulin for 30 minutes at 37°C to collect proteins for WB to measure the ratio P-AKT^{Ser473} / Total AKT.

8.2.2.2 Results

The functional assays demonstrated that the hBM-PCs treated with either HG or glucosamine showed similar fractions of viable and proliferative cells (**Figure 8-5 A to C**). Moreover, cells in the different treatment conditions showed similar high expression levels of senescence markers p16^{INK4a}, γ H2AX^{pos} + ki67^{neg}, and p21^{Waf1/Cip1}, which reflected the cellular senescence of baseline hBM-PCs with no changes given by treatment (**Figure 8-5 D to G**). Likewise, the cell cycle marker ki67 showed no changes between the treatment or baseline groups (**Figure 8-5H**). The WB results are not shown here as I could not detect any P-AKT^{Ser473} or AKT expression in this experiment. This result may be induced by cellular senescence, which limits proliferation, resulting in the cell numbers being too low to collect enough proteins for WB detection. Altogether, these results suggest that senescent hBM-PCs were not sensitive to HG or glucosamine. Therefore, I cannot establish an *in vitro* model of insulin resistance.



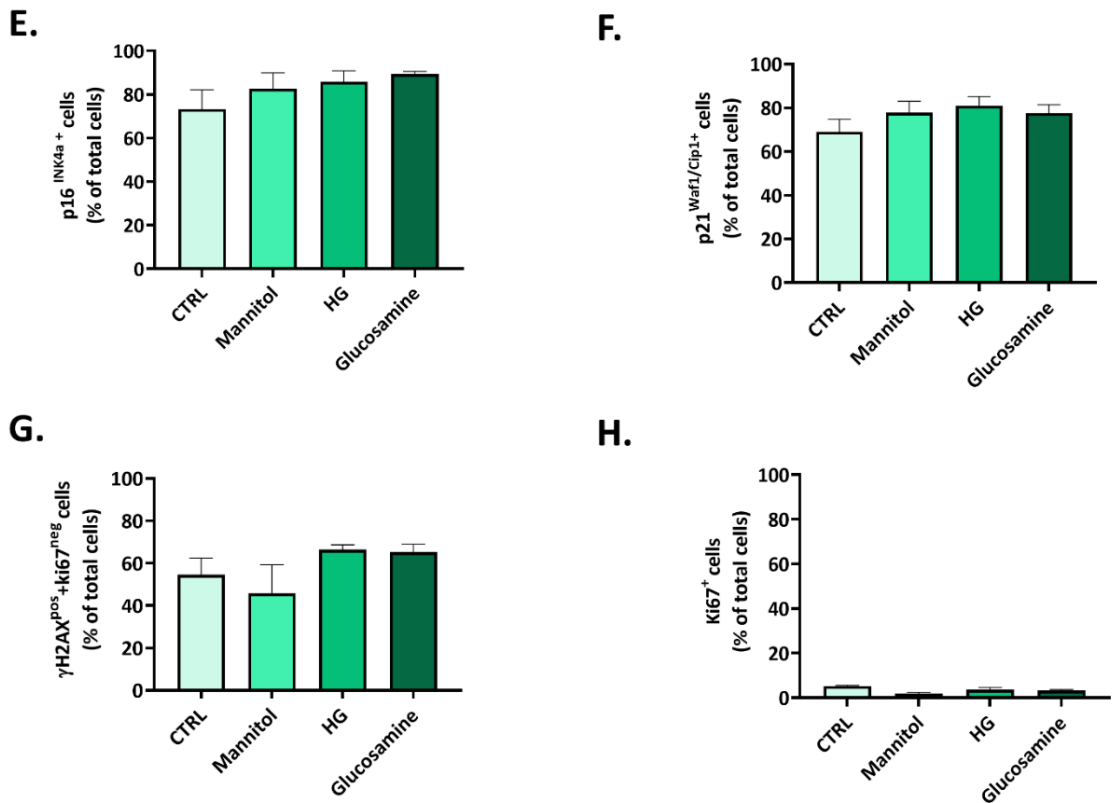


Figure 8-5 *In vitro* model of high glucose and glucosamine-induced insulin resistance in human BM-PCs.

HBM-PCs were incubated with either D-mannitol or D-glucose (both 30 mM) or glucosamine (10 mM) or CTRL (5.5 mM D-glucose) for 48 hours. (A) Fluorescence images show the viability (Calcein-AM, live cell = green, EthD-III, dead cell = red) and proliferation ability (EdU nuclear positivity, green) of hBM-PCs under different treatments. Bar graphs (B and C) show data on quantifying viable and EdU-positive cells (expressed as % of total nuclei/cells). ICC images (D) show the expression of senescence markers p16^{INK4a} (red), γ H2AX^{pos} + ki67^{neg} (red only), p21^{Waf1/Cip1} (green) and ki67^{pos} (green only) in hBM-PCs from different groups. Bar graphs (E, F, and G) show the fraction of p16^{INK4a}-, γ H2AX^{pos} + ki67^{neg}-, and p21^{Waf1/Cip1}-positive cells (% of total cells) and (H) shows the fraction of ki67 positive cells (% of total cells). Nuclei were identified by DAPI (blue). Data are presented as mean \pm SEM and were analysed using one-way ANOVA followed by Tukey's multiple comparisons tests. n = 3 patients' cells/group. Abbreviations: hBM-PCs = human bone marrow pericytes; DAPI = 4',6-diamidino-2-phenylindole; EdU = 5-ethynyl-2'-deoxyuridine; HG = high glucose; CTRL = control.

8.3. T2DM obese mice age selection

8.3.1. Experiment design

To ensure animal welfare and reduce the stress on animals while addressing the scope of the project, I decided to perform the study using the youngest animals showing the properties of diabetic obese individuals. ORO staining (methods shown in **section 4.2.5.4**) was used to analyse the lipid accumulation in the heart of mice from four different age groups to decide the most suitable Db/Db mice age representing a model of obesity (The Db/Db mouse heart samples were from the excessive tissues of other projects in our group). The liver was used as a positive control for the staining.

8.3.2. Results

The results indicated that ORO-positive lipid deposits in the hearts significantly increased in 21-week-old Db/Db mice (**Figure 8-6 A and B**), which aligns with literature and the Jackson Laboratory reports [520, 521]. Therefore, these 21-week-old mice were used in the *in vivo* studies of this thesis.

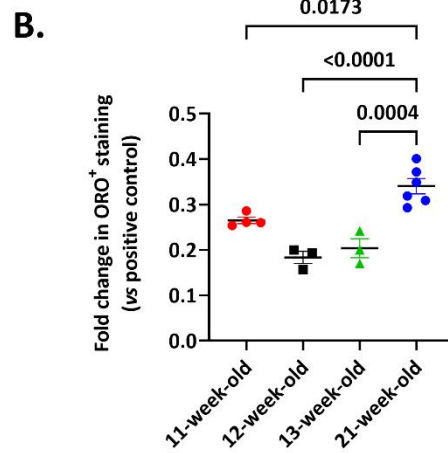
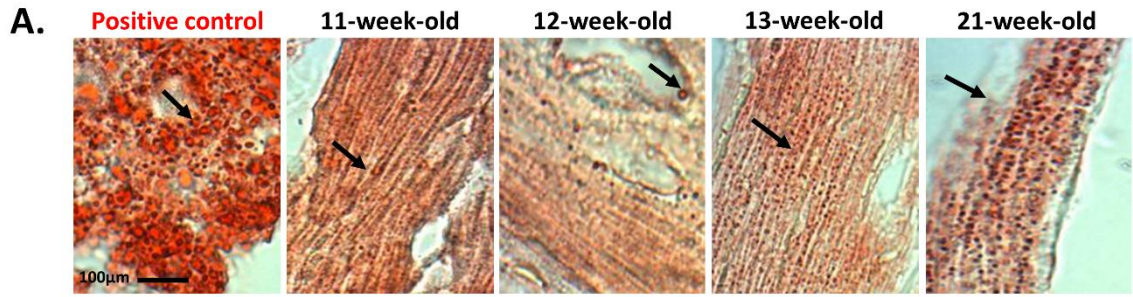


Figure 8-6 Lipid droplet accumulation in T2DM obese mice hearts at different ages.

Bright-field images (A) show lipid droplets stained with ORO (arrow, red) in Db/Db mice hearts. Liver tissue was used as a positive control for ORO staining. Scatter plot (B) shows the fold change of ORO positive staining in heart tissue versus the positive control. Data are presented as individual values and mean \pm SEM and were analysed using one-way ANOVA followed by Tukey's multiple comparisons tests. $n = 3$ to 6 mice/group. Abbreviations: ORO = oil red O.

BIBLIOGRAPHY

1. American Diabetes, A., *Diagnosis and classification of diabetes mellitus*. Diabetes Care, 2009. **32 Suppl 1**(Suppl 1): p. S62-7.
2. American Diabetes Association Professional Practice, C., *2. Classification and Diagnosis of Diabetes: Standards of Medical Care in Diabetes-2022*. Diabetes Care, 2022. **45**(Suppl 1): p. S17-S38.
3. Magliano, D.J. and E.J. Boyko, *IDF DIABETES ATLAS, in IDF DIABETES ATLAS*. 2021: Brussels.
4. Ahlqvist, E., et al., *Novel subgroups of adult-onset diabetes and their association with outcomes: a data-driven cluster analysis of six variables*. Lancet Diabetes Endocrinol, 2018. **6**(5): p. 361-369.
5. Forouhi, N.G. and N.J. Wareham, *Epidemiology of diabetes*. Medicine, 2019. **47**(1): p. 22-27.
6. Ogle, G.D., et al., *Global estimates of incidence of type 1 diabetes in children and adolescents: Results from the International Diabetes Federation Atlas, 10th edition*. Diabetes Res Clin Pract, 2022. **183**: p. 109083.
7. Chan, J.C.N., et al., *The Lancet Commission on diabetes: using data to transform diabetes care and patient lives*. Lancet, 2021. **396**(10267): p. 2019-2082.
8. Toplak, H., et al., [*"Diabesity"-Obesity and type 2 diabetes (Update 2019)*]. Wien Klin Wochenschr, 2019. **131**(Suppl 1): p. 71-76.
9. Organization, W.H. *Diabetes*. 2022 [cited 2022 16 September]; Available from: <https://www.who.int/news-room/fact-sheets/detail/diabetes>.
10. Bikbov, M.M., et al., *Prevalence, awareness and control of diabetes in Russia: The Ural Eye and Medical Study on adults aged 40+ years*. PLoS One, 2019. **14**(4): p. e0215636.
11. Edmonds, M., C. Manu, and P. Vas, *The current burden of diabetic foot disease*. J Clin Orthop Trauma, 2021. **17**: p. 88-93.
12. Zhu, B. and S. Qu, *The Relationship Between Diabetes Mellitus and Cancers and Its Underlying Mechanisms*. Front Endocrinol (Lausanne), 2022. **13**: p. 800995.
13. Banting, F.G. and C.H. Best, *The Journal of Laboratory and Clinical Medicine: The Internal Secretion of the Pancreas*. Nutrition Reviews, 1987. **45**(4): p. 55-57.
14. Rizza, R.A., *Pathogenesis of fasting and postprandial hyperglycemia in type 2 diabetes: implications for therapy*. Diabetes, 2010. **59**(11): p. 2697-707.
15. Wilcox, G., *Insulin and insulin resistance*. Clin Biochem Rev, 2005. **26**(2): p. 19-39.
16. Ormazabal, V., et al., *Association between insulin resistance and the development of cardiovascular disease*. Cardiovasc Diabetol, 2018. **17**(1): p. 122.
17. Freeman, A.M. and N. Pennings, *Insulin Resistance, in StatPearls*. 2023: Treasure Island (FL).
18. Lee, S.H., S.Y. Park, and C.S. Choi, *Insulin Resistance: From Mechanisms to Therapeutic Strategies*. Diabetes Metab J, 2022. **46**(1): p. 15-37.
19. Randle, P.J., et al., *The glucose fatty-acid cycle. Its role in insulin sensitivity and the metabolic disturbances of diabetes mellitus*. Lancet, 1963. **1**(7285): p. 785-9.

20. Petersen, K.F., et al., *Increased prevalence of insulin resistance and nonalcoholic fatty liver disease in Asian-Indian men*. Proc Natl Acad Sci U S A, 2006. **103**(48): p. 18273-7.
21. Chavez, J.A. and S.A. Summers, *A ceramide-centric view of insulin resistance*. Cell Metab, 2012. **15**(5): p. 585-94.
22. Ozcan, U., et al., *Chemical chaperones reduce ER stress and restore glucose homeostasis in a mouse model of type 2 diabetes*. Science, 2006. **313**(5790): p. 1137-40.
23. Wellen, K.E. and G.S. Hotamisligil, *Inflammation, stress, and diabetes*. J Clin Invest, 2005. **115**(5): p. 1111-9.
24. Roberts, C.K., A.L. Hevener, and R.J. Barnard, *Metabolic syndrome and insulin resistance: underlying causes and modification by exercise training*. Compr Physiol, 2013. **3**(1): p. 1-58.
25. Nagy, C. and E. Einwallner, *Study of In Vivo Glucose Metabolism in High-fat Diet-fed Mice Using Oral Glucose Tolerance Test (OGTT) and Insulin Tolerance Test (ITT)*. J Vis Exp, 2018(131).
26. Li, M., et al., *Trends in insulin resistance: insights into mechanisms and therapeutic strategy*. Signal Transduct Target Ther, 2022. **7**(1): p. 216.
27. Stumvoll, M., et al., *Use of the oral glucose tolerance test to assess insulin release and insulin sensitivity*. Diabetes Care, 2000. **23**(3): p. 295-301.
28. Zhang, Y., et al., *The Optimized Calculation Method for Insulin Dosage in an Insulin Tolerance Test (ITT): A Randomized Parallel Control Study*. Front Endocrinol (Lausanne), 2020. **11**: p. 202.
29. Tam, C.S., et al., *Defining insulin resistance from hyperinsulinemic-euglycemic clamps*. Diabetes Care, 2012. **35**(7): p. 1605-10.
30. Giannarelli, R., et al., *Reducing insulin resistance with metformin: the evidence today*. Diabetes Metab, 2003. **29**(4 Pt 2): p. 6S28-35.
31. MacDonald, P.E., et al., *The multiple actions of GLP-1 on the process of glucose-stimulated insulin secretion*. Diabetes, 2002. **51 Suppl 3**: p. S434-42.
32. Deacon, C.F., *Physiology and Pharmacology of DPP-4 in Glucose Homeostasis and the Treatment of Type 2 Diabetes*. Front Endocrinol (Lausanne), 2019. **10**: p. 80.
33. Hattori, S., *Omarigliptin decreases inflammation and insulin resistance in a pleiotropic manner in patients with type 2 diabetes*. Diabetol Metab Syndr, 2020. **12**: p. 24.
34. Richter, B., et al., *Dipeptidyl peptidase-4 (DPP-4) inhibitors for type 2 diabetes mellitus*. Cochrane Database Syst Rev, 2008. **2008**(2): p. CD006739.
35. Yang, A. and E.P. Mottillo, *Adipocyte lipolysis: from molecular mechanisms of regulation to disease and therapeutics*. Biochem J, 2020. **477**(5): p. 985-1008.
36. Zimmermann, R., et al., *Fat mobilization in adipose tissue is promoted by adipose triglyceride lipase*. Science, 2004. **306**(5700): p. 1383-6.
37. Haemmerle, G., et al., *Hormone-sensitive lipase deficiency in mice changes the plasma lipid profile by affecting the tissue-specific expression pattern of lipoprotein lipase in adipose tissue and muscle*. J Biol Chem, 2002. **277**(15): p. 12946-52.
38. Shi, F. and S. Collins, *Second messenger signaling mechanisms of the brown adipocyte thermogenic program: an integrative perspective*. Horm Mol Biol Clin Investig, 2017. **31**(2).

39. Miki, H., et al., *Essential role of insulin receptor substrate 1 (IRS-1) and IRS-2 in adipocyte differentiation*. Mol Cell Biol, 2001. **21**(7): p. 2521-32.
40. Moro, C., et al., *Atrial natriuretic peptide contributes to physiological control of lipid mobilization in humans*. FASEB J, 2004. **18**(7): p. 908-10.
41. Jepson, C.A. and S.J. Yeaman, *Inhibition of hormone-sensitive lipase by intermediary lipid metabolites*. FEBS Lett, 1992. **310**(2): p. 197-200.
42. Henry, B.A. and I.J. Clarke, *Chapter 14 - Animal Models for Manipulation of Thermogenesis*, in *Animal Models for the Study of Human Disease*, P.M. Conn, Editor. 2013, Academic Press: Boston. p. 305-330.
43. Giralt, M. and F. Villarroya, *White, brown, beige/brite: different adipose cells for different functions?* Endocrinology, 2013. **154**(9): p. 2992-3000.
44. Bielczyk-Maczynska, E., *White Adipocyte Plasticity in Physiology and Disease*. Cells, 2019. **8**(12).
45. Sanchez-Gurmaches, J., C.M. Hung, and D.A. Guertin, *Emerging Complexities in Adipocyte Origins and Identity*. Trends Cell Biol, 2016. **26**(5): p. 313-326.
46. Bini, S., et al., *The Interplay between Angiopoietin-Like Proteins and Adipose Tissue: Another Piece of the Relationship between Adiposopathy and Cardiometabolic Diseases?* Int J Mol Sci, 2021. **22**(2).
47. Kwok, K.H., K.S. Lam, and A. Xu, *Heterogeneity of white adipose tissue: molecular basis and clinical implications*. Exp Mol Med, 2016. **48**(3): p. e215.
48. Gil, A., et al., *Is adipose tissue metabolically different at different sites?* Int J Pediatr Obes, 2011. **6 Suppl 1**: p. 13-20.
49. Frigolet, M.E. and R. Gutierrez-Aguilar, *The colors of adipose tissue*. Gac Med Mex, 2020. **156**(2): p. 142-149.
50. Huh, J.Y., et al., *Crosstalk between adipocytes and immune cells in adipose tissue inflammation and metabolic dysregulation in obesity*. Mol Cells, 2014. **37**(5): p. 365-71.
51. Nguyen, H.P., et al., *Aging-dependent regulatory cells emerge in subcutaneous fat to inhibit adipogenesis*. Dev Cell, 2021. **56**(10): p. 1437-1451 e3.
52. Acosta, J.R., et al., *Increased fat cell size: a major phenotype of subcutaneous white adipose tissue in non-obese individuals with type 2 diabetes*. Diabetologia, 2016. **59**(3): p. 560-70.
53. Reyes-Farias, M., et al., *White adipose tissue dysfunction in obesity and aging*. Biochemical Pharmacology, 2021. **192**.
54. McLaughlin, T., et al., *Preferential fat deposition in subcutaneous versus visceral depots is associated with insulin sensitivity*. J Clin Endocrinol Metab, 2011. **96**(11): p. E1756-60.
55. Kloting, N., et al., *Insulin-sensitive obesity*. Am J Physiol Endocrinol Metab, 2010. **299**(3): p. E506-15.
56. Palmer, A.K., et al., *Targeting senescent cells alleviates obesity-induced metabolic dysfunction*. Aging Cell, 2019. **18**(3): p. e12950.
57. Ibrahim, M.M., *Subcutaneous and visceral adipose tissue: structural and functional differences*. Obes Rev, 2010. **11**(1): p. 11-8.
58. Spalding, K.L., et al., *Dynamics of fat cell turnover in humans*. Nature, 2008. **453**(7196): p. 783-7.

59. Barchetta, I., et al., *Sick fat: the good and the bad of old and new circulating markers of adipose tissue inflammation*. J Endocrinol Invest, 2019. **42**(11): p. 1257-1272.
60. Ito, A., et al., *Role of MAPK phosphatase-1 in the induction of monocyte chemoattractant protein-1 during the course of adipocyte hypertrophy*. J Biol Chem, 2007. **282**(35): p. 25445-52.
61. Reyes-Farias, M., et al., *White adipose tissue dysfunction in obesity and aging*. Biochem Pharmacol, 2021. **192**: p. 114723.
62. Alkhoury, N., et al., *Adipocyte apoptosis, a link between obesity, insulin resistance, and hepatic steatosis*. J Biol Chem, 2010. **285**(5): p. 3428-38.
63. Gabriely, I., et al., *Removal of visceral fat prevents insulin resistance and glucose intolerance of aging: an adipokine-mediated process?* Diabetes, 2002. **51**(10): p. 2951-8.
64. Chen, P., et al., *Abdominal subcutaneous adipose tissue: a favorable adipose depot for diabetes?* Cardiovasc Diabetol, 2018. **17**(1): p. 93.
65. Franczyk, M.P., M. He, and J. Yoshino, *Removal of Epididymal Visceral Adipose Tissue Prevents Obesity-Induced Multi-organ Insulin Resistance in Male Mice*. J Endocr Soc, 2021. **5**(5): p. bvab024.
66. Canello, R. and K. Clement, *Is obesity an inflammatory illness? Role of low-grade inflammation and macrophage infiltration in human white adipose tissue*. BJOG, 2006. **113**(10): p. 1141-7.
67. Cinti, S., *Adipose Organ Development and Remodeling*. Compr Physiol, 2018. **8**(4): p. 1357-1431.
68. Donato, A.J., et al., *The impact of ageing on adipose structure, function and vasculature in the B6D2F1 mouse: evidence of significant multisystem dysfunction*. J Physiol, 2014. **592**(18): p. 4083-96.
69. Schosserer, M., et al., *Age-Induced Changes in White, Brite, and Brown Adipose Depots: A Mini-Review*. Gerontology, 2018. **64**(3): p. 229-236.
70. Cannon, B. and J. Nedergaard, *Brown adipose tissue: function and physiological significance*. Physiol Rev, 2004. **84**(1): p. 277-359.
71. Marlatt, K.L. and E. Ravussin, *Brown Adipose Tissue: an Update on Recent Findings*. Curr Obes Rep, 2017. **6**(4): p. 389-396.
72. Chait, A. and L.J. den Hartigh, *Adipose Tissue Distribution, Inflammation and Its Metabolic Consequences, Including Diabetes and Cardiovascular Disease*. Front Cardiovasc Med, 2020. **7**: p. 22.
73. Cao, W., et al., *beta-Adrenergic activation of p38 MAP kinase in adipocytes: cAMP induction of the uncoupling protein 1 (UCP1) gene requires p38 MAP kinase*. J Biol Chem, 2001. **276**(29): p. 27077-82.
74. Mirbolooki, M.R., et al., *Quantitative assessment of brown adipose tissue metabolic activity and volume using 18F-FDG PET/CT and β -adrenergic receptor activation*. EJNMMI Res, 2011. **1**(1): p. 30.
75. Mirbolooki, M.R., et al., *Adrenergic pathway activation enhances brown adipose tissue metabolism: a [18 F]FDG PET/CT study in mice*. Nucl Med Biol, 2014. **41**(1): p. 10-6.
76. Virtanen, K.A., et al., *Functional brown adipose tissue in healthy adults*. N Engl J Med, 2009. **360**(15): p. 1518-25.

77. Barbatelli, G., et al., *The emergence of cold-induced brown adipocytes in mouse white fat depots is determined predominantly by white to brown adipocyte transdifferentiation*. *Am J Physiol Endocrinol Metab*, 2010. **298**(6): p. E1244-53.
78. Kiefer, F.W., *Browning and thermogenic programming of adipose tissue*. *Best Pract Res Clin Endocrinol Metab*, 2016. **30**(4): p. 479-485.
79. Bartelt, A., et al., *Brown adipose tissue activity controls triglyceride clearance*. *Nat Med*, 2011. **17**(2): p. 200-5.
80. Hanssen, M.J., et al., *Short-term cold acclimation improves insulin sensitivity in patients with type 2 diabetes mellitus*. *Nat Med*, 2015. **21**(8): p. 863-5.
81. Shimizu, I., et al., *Vascular rarefaction mediates whitening of brown fat in obesity*. *J Clin Invest*, 2014. **124**(5): p. 2099-112.
82. Kotzbeck, P., et al., *Brown adipose tissue whitening leads to brown adipocyte death and adipose tissue inflammation*. *J Lipid Res*, 2018. **59**(5): p. 784-794.
83. Shimizu, I. and K. Walsh, *The Whitening of Brown Fat and Its Implications for Weight Management in Obesity*. *Curr Obes Rep*, 2015. **4**(2): p. 224-9.
84. Cypess, A.M., et al., *Anatomical localization, gene expression profiling and functional characterization of adult human neck brown fat*. *Nat Med*, 2013. **19**(5): p. 635-9.
85. Jespersen, N.Z., et al., *A classical brown adipose tissue mRNA signature partly overlaps with brite in the supraclavicular region of adult humans*. *Cell Metab*, 2013. **17**(5): p. 798-805.
86. Wu, J., et al., *Beige adipocytes are a distinct type of thermogenic fat cell in mouse and human*. *Cell*, 2012. **150**(2): p. 366-76.
87. Seale, P., et al., *PRDM16 controls a brown fat/skeletal muscle switch*. *Nature*, 2008. **454**(7207): p. 961-7.
88. Shao, M., et al., *Cellular Origins of Beige Fat Cells Revisited*. *Diabetes*, 2019. **68**(10): p. 1874-1885.
89. Cheng, L., et al., *Brown and beige adipose tissue: a novel therapeutic strategy for obesity and type 2 diabetes mellitus*. *Adipocyte*, 2021. **10**(1): p. 48-65.
90. Yao, L., et al., *Cold-Inducible SIRT6 Regulates Thermogenesis of Brown and Beige Fat*. *Cell Rep*, 2017. **20**(3): p. 641-654.
91. de Jong, J.M.A., et al., *The beta(3)-adrenergic receptor is dispensable for browning of adipose tissues*. *Am J Physiol Endocrinol Metab*, 2017. **312**(6): p. E508-E518.
92. Desjardins, E.M. and G.R. Steinberg, *Emerging Role of AMPK in Brown and Beige Adipose Tissue (BAT): Implications for Obesity, Insulin Resistance, and Type 2 Diabetes*. *Curr Diab Rep*, 2018. **18**(10): p. 80.
93. Zwick, R.K., et al., *Anatomical, Physiological, and Functional Diversity of Adipose Tissue*. *Cell Metab*, 2018. **27**(1): p. 68-83.
94. Pachon-Pena, G. and M.A. Bredella, *Bone marrow adipose tissue in metabolic health*. *Trends Endocrinol Metab*, 2022. **33**(6): p. 401-408.
95. Scheller, E.L., et al., *Region-specific variation in the properties of skeletal adipocytes reveals regulated and constitutive marrow adipose tissues*. *Nat Commun*, 2015. **6**: p. 7808.
96. Li, Z., et al., *Development, regulation, metabolism and function of bone marrow adipose tissues*. *Bone*, 2018. **110**: p. 134-140.

97. Bredella, M.A., et al., *Increased bone marrow fat in anorexia nervosa*. J Clin Endocrinol Metab, 2009. **94**(6): p. 2129-36.
98. Ambrosi, T.H., et al., *Adipocyte Accumulation in the Bone Marrow during Obesity and Aging Impairs Stem Cell-Based Hematopoietic and Bone Regeneration*. Cell Stem Cell, 2017. **20**(6): p. 771-784 e6.
99. Yu, E.W., et al., *Marrow adipose tissue composition in adults with morbid obesity*. Bone, 2017. **97**: p. 38-42.
100. Baum, T., et al., *Does vertebral bone marrow fat content correlate with abdominal adipose tissue, lumbar spine bone mineral density, and blood biomarkers in women with type 2 diabetes mellitus?* J Magn Reson Imaging, 2012. **35**(1): p. 117-24.
101. Sulston, R.J. and W.P. Cawthorn, *Bone marrow adipose tissue as an endocrine organ: close to the bone?* Horm Mol Biol Clin Investig, 2016. **28**(1): p. 21-38.
102. Rahman, S., et al., *Inducible brown adipose tissue, or beige fat, is anabolic for the skeleton*. Endocrinology, 2013. **154**(8): p. 2687-701.
103. Liu, L.F., et al., *Characterization of age-related gene expression profiling in bone marrow and epididymal adipocytes*. BMC Genomics, 2011. **12**: p. 212.
104. Rudin, E. and N. Barzilai, *Inflammatory peptides derived from adipose tissue*. Immun Ageing, 2005. **2**(1): p. 1.
105. Tabe, Y., et al., *Bone Marrow Adipocytes Facilitate Fatty Acid Oxidation Activating AMPK and a Transcriptional Network Supporting Survival of Acute Monocytic Leukemia Cells*. Cancer Res, 2017. **77**(6): p. 1453-1464.
106. Rosen, C.J., et al., *Marrow fat and the bone microenvironment: developmental, functional, and pathological implications*. Crit Rev Eukaryot Gene Expr, 2009. **19**(2): p. 109-24.
107. Aaron, N., et al., *The Implications of Bone Marrow Adipose Tissue on Inflammaging*. Front Endocrinol (Lausanne), 2022. **13**: p. 853765.
108. Miggitsch, C., et al., *Human bone marrow adipocytes display distinct immune regulatory properties*. EBioMedicine, 2019. **46**: p. 387-398.
109. Le Jemtel, T.H., et al., *Epicardial Adipose Tissue and Cardiovascular Disease*. Curr Hypertens Rep, 2019. **21**(5): p. 36.
110. Piche, M.E. and P. Poirier, *Obesity, ectopic fat and cardiac metabolism*. Expert Rev Endocrinol Metab, 2018. **13**(4): p. 213-221.
111. Sacks, H.S., et al., *Uncoupling protein-1 and related messenger ribonucleic acids in human epicardial and other adipose tissues: epicardial fat functioning as brown fat*. J Clin Endocrinol Metab, 2009. **94**(9): p. 3611-5.
112. Antonopoulos, A.S. and C. Antoniades, *The role of epicardial adipose tissue in cardiac biology: classic concepts and emerging roles*. J Physiol, 2017. **595**(12): p. 3907-3917.
113. Iacobellis, G., D. Corradi, and A.M. Sharma, *Epicardial adipose tissue: anatomic, biomolecular and clinical relationships with the heart*. Nat Clin Pract Cardiovasc Med, 2005. **2**(10): p. 536-43.
114. Yudkin, J.S., E. Eringa, and C.D. Stehouwer, *"Vasocrine" signalling from perivascular fat: a mechanism linking insulin resistance to vascular disease*. Lancet, 2005. **365**(9473): p. 1817-20.
115. Ansaldo, A.M., et al., *Epicardial adipose tissue and cardiovascular diseases*. Int J Cardiol, 2019. **278**: p. 254-260.

116. Mancio, J., et al., *Epicardial adipose tissue volume assessed by computed tomography and coronary artery disease: a systematic review and meta-analysis*. Eur Heart J Cardiovasc Imaging, 2018. **19**(5): p. 490-497.
117. Villasante Fricke, A.C. and G. Iacobellis, *Epicardial Adipose Tissue: Clinical Biomarker of Cardio-Metabolic Risk*. Int J Mol Sci, 2019. **20**(23).
118. Haemers, P., et al., *Atrial fibrillation is associated with the fibrotic remodelling of adipose tissue in the subepicardium of human and sheep atria*. Eur Heart J, 2017. **38**(1): p. 53-61.
119. Doukbi, E., et al., *Browning Epicardial Adipose Tissue: Friend or Foe?* Cells, 2022. **11**(6).
120. Li, Y., et al., *Epicardial fat tissue in patients with diabetes mellitus: a systematic review and meta-analysis*. Cardiovasc Diabetol, 2019. **18**(1): p. 3.
121. Noyes, A.M., et al., *Cardiac adipose tissue and its relationship to diabetes mellitus and cardiovascular disease*. World J Diabetes, 2014. **5**(6): p. 868-76.
122. Iacobellis, G. and H.J. Willens, *Echocardiographic epicardial fat: a review of research and clinical applications*. J Am Soc Echocardiogr, 2009. **22**(12): p. 1311-9; quiz 1417-8.
123. Malavazos, A.E., et al., *Relation of echocardiographic epicardial fat thickness and myocardial fat*. Am J Cardiol, 2010. **105**(12): p. 1831-5.
124. Friedman, D.J., et al., *Pericardial fat is associated with atrial conduction: the Framingham Heart Study*. J Am Heart Assoc, 2014. **3**(2): p. e000477.
125. Horckmans, M., et al., *Pericardial Adipose Tissue Regulates Granulopoiesis, Fibrosis, and Cardiac Function After Myocardial Infarction*. Circulation, 2018. **137**(9): p. 948-960.
126. Hatem, S.N., A. Redheuil, and E. Gandjbakhch, *Cardiac adipose tissue and atrial fibrillation: the perils of adiposity*. Cardiovasc Res, 2016. **109**(4): p. 502-9.
127. Yang, F.S., et al., *High pericardial and peri-aortic adipose tissue burden in pre-diabetic and diabetic subjects*. BMC Cardiovasc Disord, 2013. **13**: p. 98.
128. Cavalcante, J.L., et al., *Association of epicardial fat, hypertension, subclinical coronary artery disease, and metabolic syndrome with left ventricular diastolic dysfunction*. Am J Cardiol, 2012. **110**(12): p. 1793-8.
129. Hachiya, K., et al., *Relation of epicardial fat to central aortic pressure and left ventricular diastolic function in patients with known or suspected coronary artery disease*. Int J Cardiovasc Imaging, 2014. **30**(7): p. 1393-8.
130. Hajer, G.R., T.W. van Haeften, and F.L. Visseren, *Adipose tissue dysfunction in obesity, diabetes, and vascular diseases*. Eur Heart J, 2008. **29**(24): p. 2959-71.
131. Su, X. and D. Chang, *Role of adiposopathy and physical activity in cardio-metabolic disorder diseases*. Clin Chim Acta, 2020. **511**: p. 243-247.
132. Bays, H.E., et al., *Pathogenic potential of adipose tissue and metabolic consequences of adipocyte hypertrophy and increased visceral adiposity*. Expert Rev Cardiovasc Ther, 2008. **6**(3): p. 343-68.
133. Bays, H. and C. Ballantyne, *Adiposopathy: why do adiposity and obesity cause metabolic disease?* Future Lipidology, 2017. **1**(4): p. 389-420.
134. Morrison, R.F. and S.R. Farmer, *Hormonal signaling and transcriptional control of adipocyte differentiation*. J Nutr, 2000. **130**(12): p. 3116S-3121S.
135. Yang, J., J. Kang, and Y. Guan, *The mechanisms linking adiposopathy to type 2 diabetes*. Front Med, 2013. **7**(4): p. 433-44.

136. Bays, H.E., *Adiposopathy, diabetes mellitus, and primary prevention of atherosclerotic coronary artery disease: treating "sick fat" through improving fat function with antidiabetes therapies.* Am J Cardiol, 2012. **110**(9 Suppl): p. 4B-12B.
137. Christofides, E.A. and J.M. Gonzalez-Campoy, *Adiposopathy*, in *Bariatric Endocrinology*. 2019. p. 99-120.
138. Bays, H., N. Abate, and M. Chandalia, *Adiposopathy: sick fat causes high blood sugar, high blood pressure and dyslipidemia.* Future Cardiol, 2005. **1**(1): p. 39-59.
139. Roden, M., et al., *Mechanism of free fatty acid-induced insulin resistance in humans.* J Clin Invest, 1996. **97**(12): p. 2859-65.
140. Storgaard, H., et al., *Insulin secretion after short- and long-term low-grade free fatty acid infusion in men with increased risk of developing type 2 diabetes.* Metabolism, 2003. **52**(7): p. 885-94.
141. Cnop, M., *Fatty acids and glucolipotoxicity in the pathogenesis of Type 2 diabetes.* Biochem Soc Trans, 2008. **36**(Pt 3): p. 348-52.
142. Boden, G., et al., *Effect of a low-carbohydrate diet on appetite, blood glucose levels, and insulin resistance in obese patients with type 2 diabetes.* Ann Intern Med, 2005. **142**(6): p. 403-11.
143. Kim, J.K., et al., *Tissue-specific overexpression of lipoprotein lipase causes tissue-specific insulin resistance.* Proc Natl Acad Sci U S A, 2001. **98**(13): p. 7522-7.
144. Kershaw, E.E. and J.S. Flier, *Adipose tissue as an endocrine organ.* J Clin Endocrinol Metab, 2004. **89**(6): p. 2548-56.
145. Rakatzi, I., et al., *Adiponectin counteracts cytokine- and fatty acid-induced apoptosis in the pancreatic beta-cell line INS-1.* Diabetologia, 2004. **47**(2): p. 249-58.
146. Kriketos, A.D., et al., *Exercise increases adiponectin levels and insulin sensitivity in humans.* Diabetes Care, 2004. **27**(2): p. 629-30.
147. Lau, C.H. and S. Muniandy, *Novel adiponectin-resistin (AR) and insulin resistance (IRAR) indexes are useful integrated diagnostic biomarkers for insulin resistance, type 2 diabetes and metabolic syndrome: a case control study.* Cardiovasc Diabetol, 2011. **10**: p. 8.
148. Bays, H.E., et al., *Is adiposopathy (sick fat) an endocrine disease?* Int J Clin Pract, 2008. **62**(10): p. 1474-83.
149. Bays, H.E., *Adiposopathy is "sick fat" a cardiovascular disease?* J Am Coll Cardiol, 2011. **57**(25): p. 2461-73.
150. Bravo, P.E., et al., *Leptin and hypertension in obesity.* Vasc Health Risk Manag, 2006. **2**(2): p. 163-9.
151. Duntas, L. and D. Micic, *Adiposopathy and thyroid disease: tracing the pathway to cardiovascular risk.* Expert Rev Cardiovasc Ther, 2012. **10**(6): p. 797-803.
152. Bailey, M.A., *11beta-Hydroxysteroid Dehydrogenases and Hypertension in the Metabolic Syndrome.* Curr Hypertens Rep, 2017. **19**(12): p. 100.
153. Umemura, S., et al., *Plasma angiotensinogen concentrations in obese patients.* Am J Hypertens, 1997. **10**(6): p. 629-33.
154. Giacchetti, G., et al., *Gene expression of angiotensinogen in adipose tissue of obese patients.* Int J Obes Relat Metab Disord, 2000. **24 Suppl 2**: p. S142-3.
155. de Jongh, R.T., et al., *Free fatty acid levels modulate microvascular function: relevance for obesity-associated insulin resistance, hypertension, and microangiopathy.* Diabetes, 2004. **53**(11): p. 2873-82.

156. Yanai, H. and H. Yoshida, *Beneficial Effects of Adiponectin on Glucose and Lipid Metabolism and Atherosclerotic Progression: Mechanisms and Perspectives*. Int J Mol Sci, 2019. **20**(5).
157. Larigauderie, G., et al., *Adipophilin enhances lipid accumulation and prevents lipid efflux from THP-1 macrophages: potential role in atherogenesis*. Arterioscler Thromb Vasc Biol, 2004. **24**(3): p. 504-10.
158. Choy, E.H., et al., *Translating IL-6 biology into effective treatments*. Nat Rev Rheumatol, 2020. **16**(6): p. 335-345.
159. Nystoriak, M.A. and A. Bhatnagar, *Cardiovascular Effects and Benefits of Exercise*. Front Cardiovasc Med, 2018. **5**: p. 135.
160. Lee, H.Y., J.P. Despres, and K.K. Koh, *Perivascular adipose tissue in the pathogenesis of cardiovascular disease*. Atherosclerosis, 2013. **230**(2): p. 177-84.
161. Liu, S., et al., *Transplantation of adipose tissue lacking PAI-1 improves glucose tolerance and attenuates cardiac metabolic abnormalities in high-fat diet-induced obesity*. Adipocyte, 2020. **9**(1): p. 170-178.
162. Maeda, N., et al., *Adiponectin, a unique adipocyte-derived factor beyond hormones*. Atherosclerosis, 2020. **292**: p. 1-9.
163. Henning, R.J., *Type-2 diabetes mellitus and cardiovascular disease*. Future Cardiol, 2018. **14**(6): p. 491-509.
164. Emerging Risk Factors, C., et al., *Diabetes mellitus, fasting blood glucose concentration, and risk of vascular disease: a collaborative meta-analysis of 102 prospective studies*. Lancet, 2010. **375**(9733): p. 2215-22.
165. Glovaci, D., W. Fan, and N.D. Wong, *Epidemiology of Diabetes Mellitus and Cardiovascular Disease*. Curr Cardiol Rep, 2019. **21**(4): p. 21.
166. Scirica, B.M., *Prevalence, incidence, and implications of silent myocardial infarctions in patients with diabetes mellitus*. Circulation, 2013. **127**(9): p. 965-7.
167. Khan, M.M., et al., *Prevalence and predictors of stroke among individuals with prediabetes and diabetes in Florida*. BMC Public Health, 2022. **22**(1): p. 243.
168. Petrie, J.R., T.J. Guzik, and R.M. Touyz, *Diabetes, Hypertension, and Cardiovascular Disease: Clinical Insights and Vascular Mechanisms*. Can J Cardiol, 2018. **34**(5): p. 575-584.
169. Jia, G., M.A. Hill, and J.R. Sowers, *Diabetic Cardiomyopathy: An Update of Mechanisms Contributing to This Clinical Entity*. Circ Res, 2018. **122**(4): p. 624-638.
170. Toto, R.D., *Defining Hypertension: Role of New Trials and Guidelines*. Clin J Am Soc Nephrol, 2018. **13**(10): p. 1578-1580.
171. Whelton, P.K., et al., 2017 ACC/AHA/AAPA/ABC/ACPM/AGS/APhA/ASH/ASPC/NMA/PCNA Guideline for the Prevention, Detection, Evaluation, and Management of High Blood Pressure in Adults: Executive Summary: A Report of the American College of Cardiology/American Heart Association Task Force on Clinical Practice Guidelines. J Am Coll Cardiol, 2018. **71**(19): p. 2199-2269.
172. Niiranen, T.J., et al., *Relative Contributions of Arterial Stiffness and Hypertension to Cardiovascular Disease: The Framingham Heart Study*. J Am Heart Assoc, 2016. **5**(11).
173. Saxena, T., A.O. Ali, and M. Saxena, *Pathophysiology of essential hypertension: an update*. Expert Rev Cardiovasc Ther, 2018. **16**(12): p. 879-887.

174. Ning, B., et al., *Hypertension Enhances Advanced Atherosclerosis and Induces Cardiac Death in Watanabe Heritable Hyperlipidemic Rabbits*. Am J Pathol, 2018. **188**(12): p. 2936-2947.
175. Guzik, T.J. and R.M. Touyz, *Oxidative Stress, Inflammation, and Vascular Aging in Hypertension*. Hypertension, 2017. **70**(4): p. 660-667.
176. Duarte, D.A., et al., *The concomitance of hypertension and diabetes exacerbating retinopathy: the role of inflammation and oxidative stress*. Curr Clin Pharmacol, 2013. **8**(4): p. 266-77.
177. Yannoutsos, A., et al., *Clinical relevance of aortic stiffness in end-stage renal disease and diabetes: implication for hypertension management*. J Hypertens, 2018. **36**(6): p. 1237-1246.
178. McFarlane, S.I., D.A. Sica, and J.R. Sowers, *Stroke in patients with diabetes and hypertension*. J Clin Hypertens (Greenwich), 2005. **7**(5): p. 286-92; quiz 293-4.
179. Birkenhager, W.H., et al., *Effects of antihypertensive treatment on endpoints in the diabetic patients randomized in the Systolic Hypertension in Europe (Syst-Eur) trial*. J Nephrol, 2000. **13**(3): p. 232-7.
180. Gallagher, D., et al., *Healthy percentage body fat ranges: an approach for developing guidelines based on body mass index*. Am J Clin Nutr, 2000. **72**(3): p. 694-701.
181. Piche, M.E., A. Tchernof, and J.P. Despres, *Obesity Phenotypes, Diabetes, and Cardiovascular Diseases*. Circ Res, 2020. **126**(11): p. 1477-1500.
182. Rana, M.N. and I.J. Neeland, *Adipose Tissue Inflammation and Cardiovascular Disease: An Update*. Curr Diab Rep, 2022. **22**(1): p. 27-37.
183. Bailey, R.R., M.C. Serra, and R.P. McGrath, *Obesity and diabetes are jointly associated with functional disability in stroke survivors*. Disabil Health J, 2020. **13**(3): p. 100914.
184. Zhu, J., et al., *The incidence of acute myocardial infarction in relation to overweight and obesity: a meta-analysis*. Arch Med Sci, 2014. **10**(5): p. 855-62.
185. Jung, U.J. and M.S. Choi, *Obesity and its metabolic complications: the role of adipokines and the relationship between obesity, inflammation, insulin resistance, dyslipidemia and nonalcoholic fatty liver disease*. Int J Mol Sci, 2014. **15**(4): p. 6184-223.
186. Khafagy, R. and S. Dash, *Obesity and Cardiovascular Disease: The Emerging Role of Inflammation*. Front Cardiovasc Med, 2021. **8**: p. 768119.
187. Rohm, T.V., et al., *Inflammation in obesity, diabetes, and related disorders*. Immunity, 2022. **55**(1): p. 31-55.
188. Zanolli, L., et al., *Vascular consequences of inflammation: a position statement from the ESH Working Group on Vascular Structure and Function and the ARTERY Society*. J Hypertens, 2020. **38**(9): p. 1682-1698.
189. Esmon, C.T., *The interactions between inflammation and coagulation*. Br J Haematol, 2005. **131**(4): p. 417-30.
190. England, P.H., *Adult obesity and type 2 diabetes*. 2014, Public Health England.
191. Einarson, T.R., et al., *Prevalence of cardiovascular disease in type 2 diabetes: a systematic literature review of scientific evidence from across the world in 2007-2017*. Cardiovasc Diabetol, 2018. **17**(1): p. 83.

192. Ciumarnean, L., et al., *Cardiovascular Risk Factors and Physical Activity for the Prevention of Cardiovascular Diseases in the Elderly*. Int J Environ Res Public Health, 2021. **19**(1).
193. Vestergaard, P., *Discrepancies in bone mineral density and fracture risk in patients with type 1 and type 2 diabetes--a meta-analysis*. Osteoporos Int, 2007. **18**(4): p. 427-44.
194. Bilha, S.C., et al., *Bone mineral density predictors in long-standing type 1 and type 2 diabetes mellitus*. BMC Endocr Disord, 2021. **21**(1): p. 156.
195. Kim, T.Y. and A.L. Schafer, *Diabetes and Bone Marrow Adiposity*. Curr Osteoporos Rep, 2016. **14**(6): p. 337-344.
196. Schwartz, A.V., *Marrow fat and bone: review of clinical findings*. Front Endocrinol (Lausanne), 2015. **6**: p. 40.
197. Fadini, G.P., et al., *Concise review: diabetes, the bone marrow niche, and impaired vascular regeneration*. Stem Cells Transl Med, 2014. **3**(8): p. 949-57.
198. Santopaolo, M., et al., *Bone marrow fat: friend or foe in people with diabetes mellitus?* Clin Sci (Lond), 2020. **134**(8): p. 1031-1048.
199. Spinetti, G., et al., *Global remodeling of the vascular stem cell niche in bone marrow of diabetic patients: implication of the microRNA-155/FOXO3a signaling pathway*. Circ Res, 2013. **112**(3): p. 510-22.
200. Ferland-McCollough, D., et al., *MCP-1 Feedback Loop Between Adipocytes and Mesenchymal Stromal Cells Causes Fat Accumulation and Contributes to Hematopoietic Stem Cell Rarefaction in the Bone Marrow of Patients With Diabetes*. Diabetes, 2018. **67**(7): p. 1380-1394.
201. Tchkonja, T., et al., *Fat tissue, aging, and cellular senescence*. Aging Cell, 2010. **9**(5): p. 667-84.
202. Khosla, S., et al., *Update on the pathogenesis and treatment of skeletal fragility in type 2 diabetes mellitus*. Nat Rev Endocrinol, 2021. **17**(11): p. 685-697.
203. Coppe, J.P., et al., *The senescence-associated secretory phenotype: the dark side of tumor suppression*. Annu Rev Pathol, 2010. **5**: p. 99-118.
204. Eckhardt, B.A., et al., *Accelerated osteocyte senescence and skeletal fragility in mice with type 2 diabetes*. JCI Insight, 2020. **5**(9).
205. Ahmad, E., et al., *Type 2 diabetes*. Lancet, 2022. **400**(10365): p. 1803-1820.
206. Tan, S.Y., et al., *Type 1 and 2 diabetes mellitus: A review on current treatment approach and gene therapy as potential intervention*. Diabetes Metab Syndr, 2019. **13**(1): p. 364-372.
207. Balducci, S., et al., *Physical exercise as therapy for type 2 diabetes mellitus*. Diabetes Metab Res Rev, 2014. **30 Suppl 1**: p. 13-23.
208. Pfeiffer, A.F. and H.H. Klein, *The treatment of type 2 diabetes*. Dtsch Arztebl Int, 2014. **111**(5): p. 69-81; quiz 82.
209. Hu, F.B., et al., *Diet, lifestyle, and the risk of type 2 diabetes mellitus in women*. N Engl J Med, 2001. **345**(11): p. 790-7.
210. Davies, M.J., et al., *Management of Hyperglycemia in Type 2 Diabetes, 2022. A Consensus Report by the American Diabetes Association (ADA) and the European Association for the Study of Diabetes (EASD)*. Diabetes Care, 2022. **45**(11): p. 2753-2786.

211. American Diabetes Association Professional Practice, C., *9. Pharmacologic Approaches to Glycemic Treatment: Standards of Medical Care in Diabetes-2022*. Diabetes Care, 2022. **45**(Suppl 1): p. S125-S143.
212. Ahmad, E., et al., *Where Does Metformin Stand in Modern Day Management of Type 2 Diabetes?* Pharmaceuticals (Basel), 2020. **13**(12).
213. DeFronzo, R.A., *Combination therapy with GLP-1 receptor agonist and SGLT2 inhibitor*. Diabetes Obes Metab, 2017. **19**(10): p. 1353-1362.
214. Davies, M., et al., *Semaglutide 2.4 mg once a week in adults with overweight or obesity, and type 2 diabetes (STEP 2): a randomised, double-blind, double-dummy, placebo-controlled, phase 3 trial*. Lancet, 2021. **397**(10278): p. 971-984.
215. Adams, T.D., et al., *Weight and Metabolic Outcomes 12 Years after Gastric Bypass*. N Engl J Med, 2017. **377**(12): p. 1143-1155.
216. Abdul-Ghani, M.A. and R.A. DeFronzo, *Pathogenesis of insulin resistance in skeletal muscle*. J Biomed Biotechnol, 2010. **2010**: p. 476279.
217. Yudhani, R.D., et al., *In Vitro Insulin Resistance Model: A Recent Update*. J Obes, 2023. **2023**: p. 1964732.
218. Krako Jakovljevic, N., et al., *In vitro models of insulin resistance: Mitochondrial coupling is differently affected in liver and muscle cells*. Mitochondrion, 2021. **61**: p. 165-173.
219. Garg, R., et al., *Pancreastatin inhibitor PSTi8 prevents free fatty acid-induced oxidative stress and insulin resistance by modulating JNK pathway: In vitro and in vivo findings*. Life Sci, 2022. **289**: p. 120221.
220. Achard, C.S. and D.R. Laybutt, *Lipid-induced endoplasmic reticulum stress in liver cells results in two distinct outcomes: adaptation with enhanced insulin signaling or insulin resistance*. Endocrinology, 2012. **153**(5): p. 2164-77.
221. Zhang, Q., et al., *Mangiferin Improved Palmitate-Induced-Insulin Resistance by Promoting Free Fatty Acid Metabolism in HepG2 and C2C12 Cells via PPARalpha: Mangiferin Improved Insulin Resistance*. J Diabetes Res, 2019. **2019**: p. 2052675.
222. Li, H.B., et al., *Silibinin improves palmitate-induced insulin resistance in C2C12 myotubes by attenuating IRS-1/PI3K/Akt pathway inhibition*. Braz J Med Biol Res, 2015. **48**(5): p. 440-6.
223. Luo, W., et al., *High glucose inhibits myogenesis and induces insulin resistance by down-regulating AKT signaling*. Biomed Pharmacother, 2019. **120**: p. 109498.
224. Mammi, C., et al., *Sildenafil reduces insulin-resistance in human endothelial cells*. PLoS One, 2011. **6**(1): p. e14542.
225. Giri, B., et al., *Chronic hyperglycemia mediated physiological alteration and metabolic distortion leads to organ dysfunction, infection, cancer progression and other pathophysiological consequences: An update on glucose toxicity*. Biomed Pharmacother, 2018. **107**: p. 306-328.
226. Catalano, K.J., et al., *Insulin resistance induced by hyperinsulinemia coincides with a persistent alteration at the insulin receptor tyrosine kinase domain*. PLoS One, 2014. **9**(9): p. e108693.
227. Houstis, N., E.D. Rosen, and E.S. Lander, *Reactive oxygen species have a causal role in multiple forms of insulin resistance*. Nature, 2006. **440**(7086): p. 944-8.
228. Tan, Y., et al., *Diabetic downregulation of Nrf2 activity via ERK contributes to oxidative stress-induced insulin resistance in cardiac cells in vitro and in vivo*. Diabetes, 2011. **60**(2): p. 625-33.

229. Heydemann, A., *An Overview of Murine High Fat Diet as a Model for Type 2 Diabetes Mellitus*. J Diabetes Res, 2016. **2016**: p. 2902351.
230. Kottaisamy, C.P.D., et al., *Experimental animal models for diabetes and its related complications-a review*. Lab Anim Res, 2021. **37**(1): p. 23.
231. King, A.J., *The use of animal models in diabetes research*. Br J Pharmacol, 2012. **166**(3): p. 877-94.
232. Aras, M., B.G. Tchang, and J. Pape, *Obesity and Diabetes*. Nurs Clin North Am, 2021. **56**(4): p. 527-541.
233. Zhang, Y., et al., *Positional cloning of the mouse obese gene and its human homologue*. Nature, 1994. **372**(6505): p. 425-32.
234. Hummel, K.P., M.M. Dickie, and D.L. Coleman, *Diabetes, a new mutation in the mouse*. Science, 1966. **153**(3740): p. 1127-8.
235. river, C. *In Vivo Models for Type 2 Diabetes Studies*. Available from: <https://www.criver.com/products-services/discovery-services/pharmacology-studies/cardiovascular-metabolic-disease-models/type-2-diabetes-services?region=3696>.
236. Srinivasan, K. and P. Ramarao, *Animal models in type 2 diabetes research: an overview*. Indian J Med Res, 2007. **125**(3): p. 451-72.
237. Wang, B., P.C. Chandrasekera, and J.J. Pippin, *Leptin- and leptin receptor-deficient rodent models: relevance for human type 2 diabetes*. Curr Diabetes Rev, 2014. **10**(2): p. 131-45.
238. Surwit, R.S., et al., *Diet-induced type II diabetes in C57BL/6J mice*. Diabetes, 1988. **37**(9): p. 1163-7.
239. Winzell, M.S. and B. Ahren, *The high-fat diet-fed mouse: a model for studying mechanisms and treatment of impaired glucose tolerance and type 2 diabetes*. Diabetes, 2004. **53 Suppl 3**: p. S215-9.
240. Mosser, R.E., et al., *High-fat diet-induced beta-cell proliferation occurs prior to insulin resistance in C57Bl/6J male mice*. Am J Physiol Endocrinol Metab, 2015. **308**(7): p. E573-82.
241. Asha, G.V., et al., *Male mice are susceptible to high fat diet-induced hyperglycaemia and display increased circulatory retinol binding protein 4 (RBP4) levels and its expression in visceral adipose depots*. Arch Physiol Biochem, 2016. **122**(1): p. 19-26.
242. Clee, S.M. and A.D. Attie, *The genetic landscape of type 2 diabetes in mice*. Endocr Rev, 2007. **28**(1): p. 48-83.
243. Haskell, B.D., et al., *The diabetes-prone NZO/HlLt strain. I. Immunophenotypic comparison to the related NZB/BINJ and NZW/LacJ strains*. Lab Invest, 2002. **82**(7): p. 833-42.
244. Ramasubramanian, B., et al., *Protective Effects of Chaya against Mitochondrial and Synaptic Toxicities in the Type 2 Diabetes Mouse Model TallyHO*. Cells, 2022. **11**(4).
245. McDonald, S., et al., *Heterogeneity and altered beta-cell identity in the TallyHo model of early-onset type 2 diabetes*. Acta Histochem, 2022. **124**(7): p. 151940.
246. Travlos, G.S., *Normal structure, function, and histology of the bone marrow*. Toxicol Pathol, 2006. **34**(5): p. 548-65.

247. Davé, U.P. and M.J. Koury, *Structure of the Marrow and the Hematopoietic Microenvironment*, in *Williams Hematology, 9e*, K. Kaushansky, et al., Editors. 2015, McGraw-Hill Education: New York, NY.
248. Murphy, D.T., et al., *Bone marrow*. *Magn Reson Imaging Clin N Am*, 2010. **18**(4): p. 727-35.
249. Nees, S., et al., *Wall structures of myocardial precapillary arterioles and postcapillary venules reexamined and reconstructed in vitro for studies on barrier functions*. *Am J Physiol Heart Circ Physiol*, 2012. **302**(1): p. H51-68.
250. Pinho, S. and P.S. Frenette, *Haematopoietic stem cell activity and interactions with the niche*. *Nat Rev Mol Cell Biol*, 2019. **20**(5): p. 303-320.
251. Horton, P.D., S. Dumbali, and P.L. Wenzel, *Mechanoregulation in hematopoiesis and hematologic disorders*. *Curr Stem Cell Rep*, 2020. **6**(3): p. 86-95.
252. Crane, G.M., E. Jeffery, and S.J. Morrison, *Adult haematopoietic stem cell niches*. *Nat Rev Immunol*, 2017. **17**(9): p. 573-590.
253. Lucas, D., *Structural organization of the bone marrow and its role in hematopoiesis*. *Curr Opin Hematol*, 2021. **28**(1): p. 36-42.
254. Bianco, P., et al., *The meaning, the sense and the significance: translating the science of mesenchymal stem cells into medicine*. *Nat Med*, 2013. **19**(1): p. 35-42.
255. Kandarakov, O., A. Belyavsky, and E. Semenova, *Bone Marrow Niches of Hematopoietic Stem and Progenitor Cells*. *Int J Mol Sci*, 2022. **23**(8).
256. Naveiras, O., et al., *Bone-marrow adipocytes as negative regulators of the haematopoietic microenvironment*. *Nature*, 2009. **460**(7252): p. 259-63.
257. Yu, V.W. and D.T. Scadden, *Hematopoietic Stem Cell and Its Bone Marrow Niche*. *Curr Top Dev Biol*, 2016. **118**: p. 21-44.
258. Calvi, L.M. and D.C. Link, *Cellular complexity of the bone marrow hematopoietic stem cell niche*. *Calcif Tissue Int*, 2014. **94**(1): p. 112-24.
259. Anthony, B.A. and D.C. Link, *Regulation of hematopoietic stem cells by bone marrow stromal cells*. *Trends Immunol*, 2014. **35**(1): p. 32-7.
260. Heideveld, E. and E. van den Akker, *Digesting the role of bone marrow macrophages on hematopoiesis*. *Immunobiology*, 2017. **222**(6): p. 814-822.
261. Maryanovich, M., S. Takeishi, and P.S. Frenette, *Neural Regulation of Bone and Bone Marrow*. *Cold Spring Harb Perspect Med*, 2018. **8**(9).
262. Wilson, A. and A. Trumpp, *Bone-marrow haematopoietic-stem-cell niches*. *Nat Rev Immunol*, 2006. **6**(2): p. 93-106.
263. Ohlstein, B., et al., *The stem cell niche: theme and variations*. *Curr Opin Cell Biol*, 2004. **16**(6): p. 693-9.
264. Venezia, T.A., et al., *Molecular signatures of proliferation and quiescence in hematopoietic stem cells*. *PLoS Biol*, 2004. **2**(10): p. e301.
265. Hanoun, M., et al., *Neural regulation of hematopoiesis, inflammation, and cancer*. *Neuron*, 2015. **86**(2): p. 360-73.
266. Pongratz, G. and R.H. Straub, *Role of peripheral nerve fibres in acute and chronic inflammation in arthritis*. *Nat Rev Rheumatol*, 2013. **9**(2): p. 117-26.
267. Sampaio-Pinto, V., et al., *Bone marrow contribution to the heart from development to adulthood*. *Semin Cell Dev Biol*, 2021. **112**: p. 16-26.

268. Tan, Y., et al., *Mechanisms of diabetic cardiomyopathy and potential therapeutic strategies: preclinical and clinical evidence*. Nat Rev Cardiol, 2020. **17**(9): p. 585-607.
269. Altara, R., et al., *Targeting Obesity and Diabetes to Treat Heart Failure with Preserved Ejection Fraction*. Front Endocrinol (Lausanne), 2017. **8**: p. 160.
270. Yin, T. and L. Li, *The stem cell niches in bone*. J Clin Invest, 2006. **116**(5): p. 1195-201.
271. Cooper, B., *The origins of bone marrow as the seedbed of our blood: from antiquity to the time of Osler*. Proc (Bayl Univ Med Cent), 2011. **24**(2): p. 115-8.
272. Spencer, J.A., et al., *Direct measurement of local oxygen concentration in the bone marrow of live animals*. Nature, 2014. **508**(7495): p. 269-73.
273. Jang, Y.Y. and S.J. Sharkis, *A low level of reactive oxygen species selects for primitive hematopoietic stem cells that may reside in the low-oxygenic niche*. Blood, 2007. **110**(8): p. 3056-63.
274. Takubo, K., et al., *Regulation of the HIF-1alpha level is essential for hematopoietic stem cells*. Cell Stem Cell, 2010. **7**(3): p. 391-402.
275. Forristal, C.E., et al., *Pharmacologic stabilization of HIF-1alpha increases hematopoietic stem cell quiescence in vivo and accelerates blood recovery after severe irradiation*. Blood, 2013. **121**(5): p. 759-69.
276. Holmes, C. and W.L. Stanford, *Concise review: stem cell antigen-1: expression, function, and enigma*. Stem Cells, 2007. **25**(6): p. 1339-47.
277. Silva, W.N., et al., *Hematopoietic stem cell stretches and moves in its bone marrow niche*. Crit Rev Oncol Hematol, 2021. **163**: p. 103368.
278. McKinney-Freeman, S.L., et al., *Surface antigen phenotypes of hematopoietic stem cells from embryos and murine embryonic stem cells*. Blood, 2009. **114**(2): p. 268-78.
279. FRIEDENSTEIN, A.J., et al., *HETEROTOPIC TRANSPLANTS OF BONE MARROW*. Transplantation, 1968. **6**(2): p. 230-247.
280. Kobolak, J., et al., *Mesenchymal stem cells: Identification, phenotypic characterization, biological properties and potential for regenerative medicine through biomaterial micro-engineering of their niche*. Methods, 2016. **99**: p. 62-8.
281. Payushina, O.V., E.I. Domaratskaya, and V.I. Starostin, *Mesenchymal stem cells: Sources, phenotype, and differentiation potential*. Biology Bulletin, 2006. **33**(1): p. 2-18.
282. Qiao, C., et al., *Human mesenchymal stem cells isolated from the umbilical cord*. Cell Biol Int, 2008. **32**(1): p. 8-15.
283. Dominici, M., et al., *Minimal criteria for defining multipotent mesenchymal stromal cells. The International Society for Cellular Therapy position statement*. Cytotherapy, 2006. **8**(4): p. 315-7.
284. Bara, J.J., et al., *Concise review: Bone marrow-derived mesenchymal stem cells change phenotype following in vitro culture: implications for basic research and the clinic*. Stem Cells, 2014. **32**(7): p. 1713-23.
285. Baker, N., L.B. Boyette, and R.S. Tuan, *Characterization of bone marrow-derived mesenchymal stem cells in aging*. Bone, 2015. **70**: p. 37-47.
286. da Silva Meirelles, L., A.I. Caplan, and N.B. Nardi, *In search of the in vivo identity of mesenchymal stem cells*. Stem Cells, 2008. **26**(9): p. 2287-99.

287. Sacchetti, B., et al., *Self-renewing osteoprogenitors in bone marrow sinusoids can organize a hematopoietic microenvironment*. Cell, 2007. **131**(2): p. 324-36.
288. Crisan, M., et al., *A perivascular origin for mesenchymal stem cells in multiple human organs*. Cell Stem Cell, 2008. **3**(3): p. 301-13.
289. Lv, F.J., et al., *Concise review: the surface markers and identity of human mesenchymal stem cells*. Stem Cells, 2014. **32**(6): p. 1408-19.
290. Karaoz, E., et al., *Characterization of mesenchymal stem cells from rat bone marrow: ultrastructural properties, differentiation potential and immunophenotypic markers*. Histochem Cell Biol, 2009. **132**(5): p. 533-46.
291. Wang, C., et al., *Isolation and culturation, phenotype detection of rat bone marrow mesenchymal stem cells*. Xi Bao Yu Fen Zi Mian Yi Xue Za Zhi, 2007. **23**(5): p. 466-8.
292. Rostovskaya, M. and K. Anastassiadis, *Differential expression of surface markers in mouse bone marrow mesenchymal stromal cell subpopulations with distinct lineage commitment*. PLoS One, 2012. **7**(12): p. e51221.
293. Short, B., et al., *Mesenchymal stem cells*. Arch Med Res, 2003. **34**(6): p. 565-71.
294. Soleimani, M. and S. Nadri, *A protocol for isolation and culture of mesenchymal stem cells from mouse bone marrow*. Nat Protoc, 2009. **4**(1): p. 102-6.
295. Yusop, N., et al., *Isolation and Characterisation of Mesenchymal Stem Cells from Rat Bone Marrow and the Endosteal Niche: A Comparative Study*. Stem Cells Int, 2018. **2018**: p. 6869128.
296. Lotfy, A., et al., *Characterization of mesenchymal stem cells derived from rat bone marrow and adipose tissue: a comparative study*. Int J Stem Cells, 2014. **7**(2): p. 135-42.
297. Gu, Y., et al., *Cell Therapy for Critical Limb Ischemia: Advantages, Limitations, and New Perspectives for Treatment of Patients with Critical Diabetic Vasculopathy*. Curr Diab Rep, 2021. **21**(3): p. 11.
298. Attwell, D., et al., *What is a pericyte?* J Cereb Blood Flow Metab, 2016. **36**(2): p. 451-5.
299. Alvino, V.V., et al., *Approaches for the isolation and long-term expansion of pericytes from human and animal tissues*. Front Cardiovasc Med, 2022. **9**: p. 1095141.
300. Kunisaki, Y., *Pericytes in Bone Marrow*. Adv Exp Med Biol, 2019. **1122**: p. 101-114.
301. Mangialardi, G., A. Cordaro, and P. Madeddu, *The bone marrow pericyte: an orchestrator of vascular niche*. Regen Med, 2016. **11**(8): p. 883-895.
302. Mangialardi, G., et al., *Bone marrow pericyte dysfunction in individuals with type 2 diabetes*. Diabetologia, 2019. **62**(7): p. 1275-1290.
303. Cathery, W., et al., *Umbilical Cord Pericytes Provide a Viable Alternative to Mesenchymal Stem Cells for Neonatal Vascular Engineering*. Front Cardiovasc Med, 2020. **7**: p. 609980.
304. Armulik, A., G. Genove, and C. Betsholtz, *Pericytes: developmental, physiological, and pathological perspectives, problems, and promises*. Dev Cell, 2011. **21**(2): p. 193-215.
305. Path, G., et al., *Stem cells in the treatment of diabetes mellitus - Focus on mesenchymal stem cells*. Metabolism, 2019. **90**: p. 1-15.

306. Navarro, R., et al., *Immune Regulation by Pericytes: Modulating Innate and Adaptive Immunity*. Front Immunol, 2016. **7**: p. 480.
307. Armulik, A., et al., *Pericytes regulate the blood-brain barrier*. Nature, 2010. **468**(7323): p. 557-61.
308. Schepers, K., et al., *Myeloproliferative neoplasia remodels the endosteal bone marrow niche into a self-reinforcing leukemic niche*. Cell Stem Cell, 2013. **13**(3): p. 285-99.
309. Hanoun, M., et al., *Acute myelogenous leukemia-induced sympathetic neuropathy promotes malignancy in an altered hematopoietic stem cell niche*. Cell Stem Cell, 2014. **15**(3): p. 365-375.
310. Arranz, L., et al., *Neuropathy of haematopoietic stem cell niche is essential for myeloproliferative neoplasms*. Nature, 2014. **512**(7512): p. 78-81.
311. Bukowska, J., et al., *Bone Marrow Adipocyte Developmental Origin and Biology*. Curr Osteoporos Rep, 2018. **16**(3): p. 312-319.
312. Tencerova, M., M. Ferencakova, and M. Kassem, *Bone marrow adipose tissue: Role in bone remodeling and energy metabolism*. Best Pract Res Clin Endocrinol Metab, 2021. **35**(4): p. 101545.
313. de Paula, F.J.A. and C.J. Rosen, *Structure and Function of Bone Marrow Adipocytes*. Compr Physiol, 2017. **8**(1): p. 315-349.
314. de Paula, F.J.A. and C.J. Rosen, *Marrow Adipocytes: Origin, Structure, and Function*. Annu Rev Physiol, 2020. **82**: p. 461-484.
315. Horowitz, M.C., et al., *Bone marrow adipocytes*. Adipocyte, 2017. **6**(3): p. 193-204.
316. Piotrowska, K. and M. Tarnowski, *Bone Marrow Adipocytes-Role in Physiology and Various Nutritional Conditions in Human and Animal Models*. Nutrients, 2021. **13**(5).
317. Kawai, T., M.V. Autieri, and R. Scalia, *Adipose tissue inflammation and metabolic dysfunction in obesity*. Am J Physiol Cell Physiol, 2021. **320**(3): p. C375-C391.
318. Chaib, S., T. Tchkonja, and J.L. Kirkland, *Cellular senescence and senolytics: the path to the clinic*. Nat Med, 2022. **28**(8): p. 1556-1568.
319. Gorgoulis, V., et al., *Cellular Senescence: Defining a Path Forward*. Cell, 2019. **179**(4): p. 813-827.
320. Ogrodnik, M., *Cellular aging beyond cellular senescence: Markers of senescence prior to cell cycle arrest in vitro and in vivo*. Aging Cell, 2021. **20**(4): p. e13338.
321. Wang, E., *Senescent human fibroblasts resist programmed cell death, and failure to suppress bcl2 is involved*. Cancer Res, 1995. **55**(11): p. 2284-92.
322. Mohamad Kamal, N.S., et al., *Aging of the cells: Insight into cellular senescence and detection Methods*. Eur J Cell Biol, 2020. **99**(6): p. 151108.
323. Hayflick, L. and P.S. Moorhead, *The serial cultivation of human diploid cell strains*. Exp Cell Res, 1961. **25**: p. 585-621.
324. Nassrally, M.S., et al., *Cell cycle arrest in replicative senescence is not an immediate consequence of telomere dysfunction*. Mech Ageing Dev, 2019. **179**: p. 11-22.
325. Shimizu, I. and T. Minamino, *Cellular senescence in cardiac diseases*. J Cardiol, 2019. **74**(4): p. 313-319.
326. Ginzberg, M.B., R. Kafri, and M. Kirschner, *Cell biology. On being the right (cell) size*. Science, 2015. **348**(6236): p. 1245075.

327. Ogrodnik, M., et al., *Cellular senescence drives age-dependent hepatic steatosis*. Nat Commun, 2017. **8**: p. 15691.
328. Ogrodnik, M., H. Salmonowicz, and V.N. Gladyshev, *Integrating cellular senescence with the concept of damage accumulation in aging: Relevance for clearance of senescent cells*. Aging Cell, 2019. **18**(1): p. e12841.
329. Unterluggauer, H., et al., *Premature senescence of human endothelial cells induced by inhibition of glutaminase*. Biogerontology, 2008. **9**(4): p. 247-59.
330. Zwerschke, W., et al., *Metabolic analysis of senescent human fibroblasts reveals a role for AMP in cellular senescence*. Biochem J, 2003. **376**(Pt 2): p. 403-11.
331. Nacarelli, T., et al., *NAD(+) metabolism governs the proinflammatory senescence-associated secretome*. Nat Cell Biol, 2019. **21**(3): p. 397-407.
332. Carroll, B., et al., *Persistent mTORC1 signaling in cell senescence results from defects in amino acid and growth factor sensing*. J Cell Biol, 2017. **216**(7): p. 1949-1957.
333. d'Adda di Fagagna, F., *Living on a break: cellular senescence as a DNA-damage response*. Nat Rev Cancer, 2008. **8**(7): p. 512-22.
334. Ksiazek, K., et al., *Vulnerability to oxidative stress and different patterns of senescence in human peritoneal mesothelial cell strains*. Am J Physiol Regul Integr Comp Physiol, 2009. **296**(2): p. R374-82.
335. Hornsby, P.J., *Senescence and life span*. Pflugers Arch, 2010. **459**(2): p. 291-9.
336. Dumont, P., et al., *Appearance of biomarkers of in vitro ageing after successive stimulation of WI-38 fibroblasts with IL-1alpha and TNF-alpha: senescence associated beta-galactosidase activity and morphotype transition*. J Anat, 2000. **197 Pt 4**(Pt 4): p. 529-37.
337. Chen, Q.M., *Replicative senescence and oxidant-induced premature senescence. Beyond the control of cell cycle checkpoints*. Ann N Y Acad Sci, 2000. **908**: p. 111-25.
338. Ma, W., et al., *Psoralen plus UVA (PUVA) induced premature senescence as a model for stress-induced premature senescence*. Exp Gerontol, 2002. **37**(10-11): p. 1197-201.
339. Pomatto, L.C.D. and K.J.A. Davies, *Adaptive homeostasis and the free radical theory of ageing*. Free Radic Biol Med, 2018. **124**: p. 420-430.
340. Liu, Y., et al., *New Insights for Cellular and Molecular Mechanisms of Aging and Aging-Related Diseases: Herbal Medicine as Potential Therapeutic Approach*. Oxid Med Cell Longev, 2019. **2019**: p. 4598167.
341. Surova, O. and B. Zhivotovsky, *Various modes of cell death induced by DNA damage*. Oncogene, 2013. **32**(33): p. 3789-97.
342. Zhu, H., et al., *Oncogene-induced senescence: From biology to therapy*. Mech Ageing Dev, 2020. **187**: p. 111229.
343. Fan, D.N.Y. and C.A. Schmitt, *Genotoxic Stress-Induced Senescence*. Methods Mol Biol, 2019. **1896**: p. 93-105.
344. Teng, Y.N., et al., *Etoposide Triggers Cellular Senescence by Inducing Multiple Centrosomes and Primary Cilia in Adrenocortical Tumor Cells*. Cells, 2021. **10**(6).
345. Sung, J.Y., et al., *Prednisolone suppresses adriamycin-induced vascular smooth muscle cell senescence and inflammatory response via the SIRT1-AMPK signaling pathway*. PLoS One, 2020. **15**(9): p. e0239976.

346. Lasry, A. and Y. Ben-Neriah, *Senescence-associated inflammatory responses: aging and cancer perspectives*. Trends Immunol, 2015. **36**(4): p. 217-28.
347. Mikula-Pietrasik, J., et al., *Mechanisms and significance of therapy-induced and spontaneous senescence of cancer cells*. Cell Mol Life Sci, 2020. **77**(2): p. 213-229.
348. Kudlova, N., J.B. De Sanctis, and M. Hajdich, *Cellular Senescence: Molecular Targets, Biomarkers, and Senolytic Drugs*. Int J Mol Sci, 2022. **23**(8).
349. Hernandez-Segura, A., J. Nehme, and M. Demaria, *Hallmarks of Cellular Senescence*. Trends Cell Biol, 2018. **28**(6): p. 436-453.
350. Kumari, R. and P. Jat, *Mechanisms of Cellular Senescence: Cell Cycle Arrest and Senescence Associated Secretory Phenotype*. Front Cell Dev Biol, 2021. **9**: p. 645593.
351. Itahana, K., J. Campisi, and G.P. Dimri, *Methods to detect biomarkers of cellular senescence: the senescence-associated beta-galactosidase assay*. Methods Mol Biol, 2007. **371**: p. 21-31.
352. Liao, C.M., et al., *Induction of Stress-Induced Renal Cellular Senescence In Vitro: Impact of Mouse Strain Genetic Diversity*. Cells, 2021. **10**(6).
353. Swanson, E.C., et al., *Higher-order unfolding of satellite heterochromatin is a consistent and early event in cell senescence*. J Cell Biol, 2013. **203**(6): p. 929-42.
354. Narita, M., et al., *Rb-mediated heterochromatin formation and silencing of E2F target genes during cellular senescence*. Cell, 2003. **113**(6): p. 703-16.
355. Hewitt, G., et al., *Telomeres are favoured targets of a persistent DNA damage response in ageing and stress-induced senescence*. Nat Commun, 2012. **3**: p. 708.
356. Narasimhan, A., et al., *Role of Cellular Senescence in Type II Diabetes*. Endocrinology, 2021. **162**(10).
357. Palmer, A.K., et al., *Cellular Senescence in Type 2 Diabetes: A Therapeutic Opportunity*. Diabetes, 2015. **64**(7): p. 2289-98.
358. Robertson, R.P., et al., *Beta-cell glucose toxicity, lipotoxicity, and chronic oxidative stress in type 2 diabetes*. Diabetes, 2004. **53 Suppl 1**: p. S119-24.
359. Teta, M., et al., *Very slow turnover of beta-cells in aged adult mice*. Diabetes, 2005. **54**(9): p. 2557-67.
360. Gregg, B.E., et al., *Formation of a human beta-cell population within pancreatic islets is set early in life*. J Clin Endocrinol Metab, 2012. **97**(9): p. 3197-206.
361. Helman, A., et al., *p16(Ink4a)-induced senescence of pancreatic beta cells enhances insulin secretion*. Nat Med, 2016. **22**(4): p. 412-20.
362. Xu, H., et al., *Chronic inflammation in fat plays a crucial role in the development of obesity-related insulin resistance*. J Clin Invest, 2003. **112**(12): p. 1821-30.
363. Vigouroux, C., et al., *Molecular mechanisms of human lipodystrophies: from adipocyte lipid droplet to oxidative stress and lipotoxicity*. Int J Biochem Cell Biol, 2011. **43**(6): p. 862-76.
364. Bluher, M., *Adipose tissue dysfunction in obesity*. Exp Clin Endocrinol Diabetes, 2009. **117**(6): p. 241-50.
365. Palmer, A.K., et al., *Cellular senescence: at the nexus between ageing and diabetes*. Diabetologia, 2019. **62**(10): p. 1835-1841.
366. Narasimhan, A., et al., *Cellular Senescence in Obesity and Associated Complications: a New Therapeutic Target*. Curr Diab Rep, 2022. **22**(11): p. 537-548.

367. Palmer, A.K., et al., *Senescence in obesity*, in *Cellular Senescence in Disease*. 2022. p. 289-308.
368. Liu, Z., et al., *The role of adipose tissue senescence in obesity- and ageing-related metabolic disorders*. Clin Sci (Lond), 2020. **134**(2): p. 315-330.
369. Minamino, T., et al., *A crucial role for adipose tissue p53 in the regulation of insulin resistance*. Nat Med, 2009. **15**(9): p. 1082-7.
370. Mundstock, E., et al., *Effect of obesity on telomere length: Systematic review and meta-analysis*. Obesity (Silver Spring), 2015. **23**(11): p. 2165-74.
371. Kim, K.S., et al., *Induction of cellular senescence by insulin-like growth factor binding protein-5 through a p53-dependent mechanism*. Mol Biol Cell, 2007. **18**(11): p. 4543-52.
372. Khamzina, L., et al., *Increased activation of the mammalian target of rapamycin pathway in liver and skeletal muscle of obese rats: possible involvement in obesity-linked insulin resistance*. Endocrinology, 2005. **146**(3): p. 1473-81.
373. Khan, M.T., M. Nieuwdorp, and F. Backhed, *Microbial modulation of insulin sensitivity*. Cell Metab, 2014. **20**(5): p. 753-760.
374. Kim, E.C. and J.R. Kim, *Senotherapeutics: emerging strategy for healthy aging and age-related disease*. BMB Rep, 2019. **52**(1): p. 47-55.
375. Schafer, M.J., et al., *Exercise Prevents Diet-Induced Cellular Senescence in Adipose Tissue*. Diabetes, 2016. **65**(6): p. 1606-15.
376. Tang, X., P.H. Li, and H.Z. Chen, *Cardiomyocyte Senescence and Cellular Communications Within Myocardial Microenvironments*. Front Endocrinol (Lausanne), 2020. **11**: p. 280.
377. Evangelou, K., et al., *Cellular senescence and cardiovascular diseases: moving to the "heart" of the problem*. Physiol Rev, 2023. **103**(1): p. 609-647.
378. Papaconstantinou, J., *The Role of Signaling Pathways of Inflammation and Oxidative Stress in Development of Senescence and Aging Phenotypes in Cardiovascular Disease*. Cells, 2019. **8**(11).
379. Fyhrquist, F., O. Saijonmaa, and T. Strandberg, *The roles of senescence and telomere shortening in cardiovascular disease*. Nat Rev Cardiol, 2013. **10**(5): p. 274-83.
380. Anderson, R., et al., *Length-independent telomere damage drives post-mitotic cardiomyocyte senescence*. EMBO J, 2019. **38**(5).
381. Hu, C., et al., *Cellular Senescence in Cardiovascular Diseases: A Systematic Review*. Aging Dis, 2022. **13**(1): p. 103-128.
382. Nakamura, K. and T. Shichita, *Cellular and molecular mechanisms of sterile inflammation in ischaemic stroke*. J Biochem, 2019. **165**(6): p. 459-464.
383. Hsieh, C.C. and J. Papaconstantinou, *The effect of aging on p38 signaling pathway activity in the mouse liver and in response to ROS generated by 3-nitropropionic acid*. Mech Ageing Dev, 2002. **123**(11): p. 1423-35.
384. Hsieh, C.C., J.I. Rosenblatt, and J. Papaconstantinou, *Age-associated changes in SAPK/JNK and p38 MAPK signaling in response to the generation of ROS by 3-nitropropionic acid*. Mech Ageing Dev, 2003. **124**(6): p. 733-46.
385. Xie, F., et al., *The endoplasmic reticulum stress-autophagy pathway is involved in apelin-13-induced cardiomyocyte hypertrophy in vitro*. Acta Pharmacol Sin, 2017. **38**(12): p. 1589-1600.

386. Zeng, Z., et al., *CTCF inhibits endoplasmic reticulum stress and apoptosis in cardiomyocytes by upregulating RYR2 via inhibiting S100A1*. *Life Sci*, 2020. **242**: p. 117158.
387. Nishimura, A., et al., *Hypoxia-induced interaction of filamin with Drp1 causes mitochondrial hyperfission-associated myocardial senescence*. *Sci Signal*, 2018. **11**(556).
388. Kirkland, J.L. and T. Tchkonina, *Senolytic drugs: from discovery to translation*. *J Intern Med*, 2020. **288**(5): p. 518-536.
389. Wilson, W.H., et al., *Navitoclax, a targeted high-affinity inhibitor of BCL-2, in lymphoid malignancies: a phase 1 dose-escalation study of safety, pharmacokinetics, pharmacodynamics, and antitumour activity*. *Lancet Oncol*, 2010. **11**(12): p. 1149-59.
390. Zhu, Y., et al., *New agents that target senescent cells: the flavone, fisetin, and the BCL-X(L) inhibitors, A1331852 and A1155463*. *Aging (Albany NY)*, 2017. **9**(3): p. 955-963.
391. Liu, X., et al., *Senolytic activity of piperlongumine analogues: Synthesis and biological evaluation*. *Bioorg Med Chem*, 2018. **26**(14): p. 3925-3938.
392. Zoico, E., et al., *Senolytic effects of quercetin in an in vitro model of pre-adipocytes and adipocytes induced senescence*. *Sci Rep*, 2021. **11**(1): p. 23237.
393. Syed, D.N., et al., *Inhibition of Akt/mTOR signaling by the dietary flavonoid fisetin*. *Anticancer Agents Med Chem*, 2013. **13**(7): p. 995-1001.
394. Yousefzadeh, M.J., et al., *Fisetin is a senotherapeutic that extends health and lifespan*. *EBioMedicine*, 2018. **36**: p. 18-28.
395. Huang, Y., et al., *Senolytic Peptide FOXO4-DRI Selectively Removes Senescent Cells From in vitro Expanded Human Chondrocytes*. *Front Bioeng Biotechnol*, 2021. **9**: p. 677576.
396. Moiseeva, O., et al., *Metformin inhibits the senescence-associated secretory phenotype by interfering with IKK/NF-kappaB activation*. *Aging Cell*, 2013. **12**(3): p. 489-98.
397. Chen, D., et al., *Metformin protects against apoptosis and senescence in nucleus pulposus cells and ameliorates disc degeneration in vivo*. *Cell Death Dis*, 2016. **7**(10): p. e2441.
398. Sasaki, N., Y. Itakura, and M. Toyoda, *Rapamycin promotes endothelial-mesenchymal transition during stress-induced premature senescence through the activation of autophagy*. *Cell Commun Signal*, 2020. **18**(1): p. 43.
399. Liu, Y., X. Li, and A. Jin, *Rapamycin Inhibits Nf-KappaB Activation by Autophagy to Reduce Catabolism in Human Chondrocytes*. *J Invest Surg*, 2020. **33**(9): p. 861-873.
400. Xu, M., et al., *JAK inhibition alleviates the cellular senescence-associated secretory phenotype and frailty in old age*. *Proc Natl Acad Sci U S A*, 2015. **112**(46): p. E6301-10.
401. Fuhrmann-Stroissnigg, H., et al., *SA-beta-Galactosidase-Based Screening Assay for the Identification of Senotherapeutic Drugs*. *J Vis Exp*, 2019(148).
402. Weiland, T., et al., *Enhanced killing of therapy-induced senescent tumor cells by oncolytic measles vaccine viruses*. *Int J Cancer*, 2014. **134**(1): p. 235-43.
403. Chen, Z., et al., *Senescent cells re-engineered to express soluble programmed death receptor-1 for inhibiting programmed death receptor-1/programmed*

- death ligand-1 as a vaccination approach against breast cancer. Cancer Sci, 2018. 109(6): p. 1753-1763.*
404. Munoz-Espin, D., et al., *A versatile drug delivery system targeting senescent cells. EMBO Mol Med, 2018. 10(9).*
405. Nakagami, H., *Cellular senescence and senescence-associated T cells as a potential therapeutic target. Geriatr Gerontol Int, 2020. 20(2): p. 97-100.*
406. Chaib, S., T. Tchkonja, and J.L. Kirkland, *Obesity, Senescence, and Senolytics. Handb Exp Pharmacol, 2022. 274: p. 165-180.*
407. Yosef, R., et al., *Directed elimination of senescent cells by inhibition of BCL-W and BCL-XL. Nat Commun, 2016. 7: p. 11190.*
408. Watanabe, Y., et al., *Navitoclax improves acute-on-chronic liver failure by eliminating senescent cells in mice. Hepatol Res, 2023. 53(5): p. 460-472.*
409. Cang, S., et al., *ABT-199 (venetoclax) and BCL-2 inhibitors in clinical development. J Hematol Oncol, 2015. 8: p. 129.*
410. Liu, Z., et al., *BH4 domain of Bcl-2 as a novel target for cancer therapy. Drug Discov Today, 2016. 21(6): p. 989-96.*
411. Wang, Y., et al., *Discovery of piperlongumine as a potential novel lead for the development of senolytic agents. Aging (Albany NY), 2016. 8(11): p. 2915-2926.*
412. Ozsoy, S., et al., *Quercetin-Mediated Apoptosis and Cellular Senescence in Human Colon Cancer. Anticancer Agents Med Chem, 2020. 20(11): p. 1387-1396.*
413. Kim, S.G., et al., *Fisetin-induced PTEN expression reverses cellular senescence by inhibiting the mTORC2-Akt Ser473 phosphorylation pathway in vascular smooth muscle cells. Exp Gerontol, 2021. 156: p. 111598.*
414. Elsallabi, O., et al., *Fisetin as a Senotherapeutic Agent: Biopharmaceutical Properties and Crosstalk between Cell Senescence and Neuroprotection. Molecules, 2022. 27(3).*
415. Robbins, P.D., et al., *Senolytic Drugs: Reducing Senescent Cell Viability to Extend Health Span. Annu Rev Pharmacol Toxicol, 2021. 61: p. 779-803.*
416. Lindauer, M. and A. Hochhaus, *Dasatinib. Recent Results Cancer Res, 2018. 212: p. 29-68.*
417. Cortes, J.E., et al., *Final 5-Year Study Results of DASISION: The Dasatinib Versus Imatinib Study in Treatment-Naive Chronic Myeloid Leukemia Patients Trial. J Clin Oncol, 2016. 34(20): p. 2333-40.*
418. Breccia, M. and G. Alimena, *Activity and safety of dasatinib as second-line treatment or in newly diagnosed chronic phase chronic myeloid leukemia patients. BioDrugs, 2011. 25(3): p. 147-57.*
419. Hickson, L.J., et al., *Senolytics decrease senescent cells in humans: Preliminary report from a clinical trial of Dasatinib plus Quercetin in individuals with diabetic kidney disease. EBioMedicine, 2019. 47: p. 446-456.*
420. Gao, Z., et al., *Dasatinib causes keratinocyte apoptosis via inhibiting high mobility group Box 1-mediated mitophagy. Toxicol Lett, 2023. 373: p. 22-32.*
421. Dalgic, C.T., et al., *Investigating the Role of JAK/STAT Pathway on Dasatinib-Induced Apoptosis for CML Cell Model K562. Clin Lymphoma Myeloma Leuk, 2015. 15 Suppl: p. S161-6.*
422. Park, N.S., et al., *Anti-growth and pro-apoptotic effects of dasatinib on human oral cancer cells through multi-targeted mechanisms. J Cell Mol Med, 2021. 25(17): p. 8300-8311.*

423. Elsayed, H.R.H., et al., *Enhanced Autophagic Flux, Suppressed Apoptosis and Reduced Macrophage Infiltration by Dasatinib in Kidneys of Obese Mice*. *Cells*, 2022. **11**(4).
424. Saccon, T.D., et al., *Senolytic Combination of Dasatinib and Quercetin Alleviates Intestinal Senescence and Inflammation and Modulates the Gut Microbiome in Aged Mice*. *J Gerontol A Biol Sci Med Sci*, 2021. **76**(11): p. 1895-1905.
425. Novais, E.J., et al., *Long-term treatment with senolytic drugs Dasatinib and Quercetin ameliorates age-dependent intervertebral disc degeneration in mice*. *Nat Commun*, 2021. **12**(1): p. 5213.
426. Ryu, K.Y., et al., *Dasatinib regulates LPS-induced microglial and astrocytic neuroinflammatory responses by inhibiting AKT/STAT3 signaling*. *J Neuroinflammation*, 2019. **16**(1): p. 190.
427. Li, C., et al., *Senolytic therapy ameliorates renal fibrosis postacute kidney injury by alleviating renal senescence*. *FASEB J*, 2021. **35**(1): p. e21229.
428. Justice, J.N., et al., *Senolytics in idiopathic pulmonary fibrosis: Results from a first-in-human, open-label, pilot study*. *EBioMedicine*, 2019. **40**: p. 554-563.
429. Li, H., et al., *Isolation and characterization of primary bone marrow mesenchymal stromal cells*. *Ann N Y Acad Sci*, 2016. **1370**(1): p. 109-18.
430. Ng, A.C.T., et al., *Impact of Epicardial Adipose Tissue, Left Ventricular Myocardial Fat Content, and Interstitial Fibrosis on Myocardial Contractile Function*. *Circ Cardiovasc Imaging*, 2018. **11**(8): p. e007372.
431. Sarjeant, K. and J.M. Stephens, *Adipogenesis*. *Cold Spring Harb Perspect Biol*, 2012. **4**(9): p. a008417.
432. Zubiria, M.G., et al., *Dexamethasone primes adipocyte precursor cells for differentiation by enhancing adipogenic competency*. *Life Sci*, 2020. **261**: p. 118363.
433. Zilberfarb, V., et al., *Effect of dexamethasone on adipocyte differentiation markers and tumour necrosis factor-alpha expression in human PAZ6 cells*. *Diabetologia*, 2001. **44**(3): p. 377-86.
434. Styner, M., et al., *Indomethacin promotes adipogenesis of mesenchymal stem cells through a cyclooxygenase independent mechanism*. *J Cell Biochem*, 2010. **111**(4): p. 1042-50.
435. Mitic, R., et al., *A simplified and defined serum-free medium for cultivating fat across species*. *iScience*, 2023. **26**(1): p. 105822.
436. Klemm, D.J., et al., *Insulin-induced adipocyte differentiation. Activation of CREB rescues adipogenesis from the arrest caused by inhibition of prenylation*. *J Biol Chem*, 2001. **276**(30): p. 28430-5.
437. Ramirez-Zacarias, J.L., F. Castro-Munozledo, and W. Kuri-Harcuch, *Quantitation of adipose conversion and triglycerides by staining intracytoplasmic lipids with Oil red O*. *Histochemistry*, 1992. **97**(6): p. 493-7.
438. Mehlem, A., et al., *Imaging of neutral lipids by oil red O for analyzing the metabolic status in health and disease*. *Nat Protoc*, 2013. **8**(6): p. 1149-54.
439. Reusch, J.E. and D.J. Klemm, *Inhibition of cAMP-response element-binding protein activity decreases protein kinase B/Akt expression in 3T3-L1 adipocytes and induces apoptosis*. *J Biol Chem*, 2002. **277**(2): p. 1426-32.

440. Livak, K.J. and T.D. Schmittgen, *Analysis of relative gene expression data using real-time quantitative PCR and the 2(-Delta Delta C(T)) Method*. *Methods*, 2001. **25**(4): p. 402-8.
441. Guo, K., et al., *Treatment Effects of the Second-Generation Tyrosine Kinase Inhibitor Dasatinib on Autoimmune Arthritis*. *Front Immunol*, 2018. **9**: p. 3133.
442. Althubiti, M., *Tyrosine Kinase Targeting: A Potential Therapeutic Strategy for Diabetes*. *Saudi J Med Med Sci*, 2022. **10**(3): p. 183-191.
443. Fountas, A., L.N. Diamantopoulos, and A. Tsatsoulis, *Tyrosine Kinase Inhibitors and Diabetes: A Novel Treatment Paradigm?* *Trends Endocrinol Metab*, 2015. **26**(11): p. 643-656.
444. Chen, R. and B. Chen, *The role of dasatinib in the management of chronic myeloid leukemia*. *Drug Des Devel Ther*, 2015. **9**: p. 773-9.
445. Islam, M.T., et al., *Senolytic drugs, dasatinib and quercetin, attenuate adipose tissue inflammation, and ameliorate metabolic function in old age*. *Aging Cell*, 2023. **22**(2): p. e13767.
446. Kanemaru, R., et al., *Dasatinib Suppresses TGFbeta-Mediated Epithelial-Mesenchymal Transition in Alveolar Epithelial Cells and Inhibits Pulmonary Fibrosis*. *Lung*, 2018. **196**(5): p. 531-541.
447. Zaafan, M.A. and A.M. Abdelhamid, *Dasatinib ameliorates thioacetamide-induced liver fibrosis: modulation of miR-378 and miR-17 and their linked Wnt/beta-catenin and TGF-beta/smads pathways*. *J Enzyme Inhib Med Chem*, 2022. **37**(1): p. 118-124.
448. Henry, S.L., et al., *White adipocytes: More than just fat depots*. *International Journal of Biochemistry & Cell Biology*, 2012. **44**(3): p. 435-440.
449. Deng, T., et al., *FABP4 silencing ameliorates hypoxia reoxygenation injury through the attenuation of endoplasmic reticulum stress-mediated apoptosis by activating PI3K/Akt pathway*. *Life Sci*, 2019. **224**: p. 149-156.
450. Li, B., et al., *SnapShot: FABP Functions*. *Cell*, 2020. **182**(4): p. 1066-1066 e1.
451. Wang, B., et al., *Fatty acid-binding protein 4 is a therapeutic target for septic acute kidney injury by regulating inflammatory response and cell apoptosis*. *Cell Death & Disease*, 2022. **13**(4).
452. Peterson, L.R. and R.J. Gropler, *Metabolic and Molecular Imaging of the Diabetic Cardiomyopathy*. *Circ Res*, 2020. **126**(11): p. 1628-1645.
453. Mordi, I.R., *Non-Invasive Imaging in Diabetic Cardiomyopathy*. *J Cardiovasc Dev Dis*, 2019. **6**(2).
454. McHugh, K., et al., *Heart Failure With Preserved Ejection Fraction and Diabetes: JACC State-of-the-Art Review*. *J Am Coll Cardiol*, 2019. **73**(5): p. 602-611.
455. Schulze, P.C., K. Drosatos, and I.J. Goldberg, *Lipid Use and Misuse by the Heart*. *Circ Res*, 2016. **118**(11): p. 1736-51.
456. Murakami, T., N. Inagaki, and H. Kondoh, *Cellular Senescence in Diabetes Mellitus: Distinct Senotherapeutic Strategies for Adipose Tissue and Pancreatic beta Cells*. *Front Endocrinol (Lausanne)*, 2022. **13**: p. 869414.
457. Elsayed, H.R.H., et al., *Can Dasatinib Ameliorate the Hepatic changes, Induced by Long Term Western Diet, in Mice?* *Ann Anat*, 2021. **234**: p. 151626.
458. Duggan, B.M., et al., *Tyrosine kinase inhibitors of Ripk2 attenuate bacterial cell wall-mediated lipolysis, inflammation and dysglycemia*. *Sci Rep*, 2017. **7**(1): p. 1578.

459. Vandyke, K., et al., *The tyrosine kinase inhibitor dasatinib dysregulates bone remodeling through inhibition of osteoclasts in vivo*. *J Bone Miner Res*, 2010. **25**(8): p. 1759-70.
460. Zacchigna, S., et al., *Towards standardization of echocardiography for the evaluation of left ventricular function in adult rodents: a position paper of the ESC Working Group on Myocardial Function*. *Cardiovasc Res*, 2021. **117**(1): p. 43-59.
461. Cheung, M.C., et al., *Body surface area prediction in normal, hypermuscular, and obese mice*. *J Surg Res*, 2009. **153**(2): p. 326-31.
462. Cuijpers, I., et al., *The effect of different anaesthetics on echocardiographic evaluation of diastolic dysfunction in a heart failure with preserved ejection fraction model*. *Sci Rep*, 2020. **10**(1): p. 15701.
463. Hamdani, N., et al., *Myocardial titin hypophosphorylation importantly contributes to heart failure with preserved ejection fraction in a rat metabolic risk model*. *Circ Heart Fail*, 2013. **6**(6): p. 1239-49.
464. Santopalo, M., et al., *Activation of Bone Marrow Adaptive Immunity in Type 2 Diabetes: Rescue by Co-stimulation Modulator Abatacept*. *Front Immunol*, 2021. **12**: p. 609406.
465. Maridas, D.E., et al., *Isolation, Culture, and Differentiation of Bone Marrow Stromal Cells and Osteoclast Progenitors from Mice*. *J Vis Exp*, 2018(131).
466. Callis, G.M., *18 - Bone*, in *Theory and Practice of Histological Techniques (Sixth Edition)*, J.D. Bancroft and M. Gamble, Editors. 2008, Churchill Livingstone: Edinburgh. p. 333-363.
467. Dang, Z., et al., *Transfer of a human gene variant associated with exceptional longevity improves cardiac function in obese type 2 diabetic mice through induction of the SDF-1/CXCR4 signalling pathway*. *Eur J Heart Fail*, 2020. **22**(9): p. 1568-1581.
468. Samarakoon, R., et al., *The TGF-beta1/p53/PAI-1 Signaling Axis in Vascular Senescence: Role of Caveolin-1*. *Biomolecules*, 2019. **9**(8).
469. Chong, M., et al., *CD36 initiates the secretory phenotype during the establishment of cellular senescence*. *EMBO Rep*, 2018. **19**(6).
470. Fadini, G.P., et al., *Stem cell compartmentalization in diabetes and high cardiovascular risk reveals the role of DPP-4 in diabetic stem cell mobilopathy*. *Basic Res Cardiol*, 2013. **108**(1): p. 313.
471. Mogha, P., S. Iyer, and A. Majumder, *Extracellular matrix protein gelatin provides higher expansion, reduces size heterogeneity, and maintains cell stiffness in a long-term culture of mesenchymal stem cells*. *Tissue Cell*, 2023. **80**: p. 101969.
472. Kunisaki, Y., et al., *Arteriolar niches maintain haematopoietic stem cell quiescence*. *Nature*, 2013. **502**(7473): p. 637-43.
473. Asada, N., et al., *Differential cytokine contributions of perivascular haematopoietic stem cell niches*. *Nat Cell Biol*, 2017. **19**(3): p. 214-223.
474. Datta, P., et al., *Chapter 5 - The Role of Adipokines and Adipogenesis in the Pathogenesis of Osteoarthritis*, in *Cytokine Effector Functions in Tissues*, M. Foti and M. Locati, Editors. 2017, Academic Press. p. 99-107.
475. Bae, K.H., W.K. Kim, and S.C. Lee, *Involvement of protein tyrosine phosphatases in adipogenesis: new anti-obesity targets?* *BMB Rep*, 2012. **45**(12): p. 700-6.

476. Tai, T.A., et al., *Activation of the nuclear receptor peroxisome proliferator-activated receptor gamma promotes brown adipocyte differentiation*. J Biol Chem, 1996. **271**(47): p. 29909-14.
477. Tontonoz, P. and B.M. Spiegelman, *Fat and beyond: the diverse biology of PPARgamma*. Annu Rev Biochem, 2008. **77**: p. 289-312.
478. Garin-Shkolnik, T., et al., *FABP4 attenuates PPARgamma and adipogenesis and is inversely correlated with PPARgamma in adipose tissues*. Diabetes, 2014. **63**(3): p. 900-11.
479. Leonardini, A., et al., *Cross-Talk between PPARgamma and Insulin Signaling and Modulation of Insulin Sensitivity*. PPAR Res, 2009. **2009**: p. 818945.
480. Borriello, A., et al., *The tyrosine kinase inhibitor dasatinib induces a marked adipogenic differentiation of human multipotent mesenchymal stromal cells*. PLoS One, 2011. **6**(12): p. e28555.
481. Bartscht, T., et al., *Dasatinib blocks transcriptional and promigratory responses to transforming growth factor-beta in pancreatic adenocarcinoma cells through inhibition of Smad signalling: implications for in vivo mode of action*. Molecular Cancer, 2015. **14**(1): p. 199.
482. Zhang, K., et al., *Molecular Mechanism of Stem Cell Differentiation into Adipocytes and Adipocyte Differentiation of Malignant Tumor*. Stem Cells Int, 2020. **2020**: p. 8892300.
483. Carmen, G.Y. and S.M. Victor, *Signalling mechanisms regulating lipolysis*. Cell Signal, 2006. **18**(4): p. 401-8.
484. Morieri, M.L., et al., *Prevalence of hepatic steatosis in patients with type 2 diabetes and response to glucose-lowering treatments. A multicenter retrospective study in Italian specialist care*. J Endocrinol Invest, 2021. **44**(9): p. 1879-1889.
485. Iacobellis, G. and A.C. Bianco, *Epicardial adipose tissue: emerging physiological, pathophysiological and clinical features*. Trends Endocrinol Metab, 2011. **22**(11): p. 450-7.
486. Kenchaiah, S., et al., *Pericardial Fat and the Risk of Heart Failure*. J Am Coll Cardiol, 2021. **77**(21): p. 2638-2652.
487. Milanese, G., et al., *Validity of epicardial fat volume as biomarker of coronary artery disease in symptomatic individuals: Results from the ALTER-BIO registry*. Int J Cardiol, 2020. **314**: p. 20-24.
488. da Silva, R.M.S. and R.J.V. de Mello, *Fat deposition in the left ventricle: descriptive and observational study in autopsy*. Lipids Health Dis, 2017. **16**(1): p. 86.
489. Dong, X., et al., *Impact of body mass index and diabetes on myocardial fat content, interstitial fibrosis and function*. Int J Cardiovasc Imaging, 2023. **39**(2): p. 379-390.
490. Izzo, P., *Myocardial, perivascular, and epicardial fat*. Diabetes Care, 2011. **34 Suppl 2**(Suppl 2): p. S371-9.
491. Kashiwagi-Takayama, R., et al., *Myocardial fat accumulation is associated with cardiac dysfunction in patients with type 2 diabetes, especially in elderly or female patients: a retrospective observational study*. Cardiovasc Diabetol, 2023. **22**(1): p. 48.

492. Szczepaniak, L.S., et al., *Myocardial triglycerides and systolic function in humans: in vivo evaluation by localized proton spectroscopy and cardiac imaging*. *Magn Reson Med*, 2003. **49**(3): p. 417-23.
493. Liao, P.A., et al., *Myocardial triglyceride content at 3 T cardiovascular magnetic resonance and left ventricular systolic function: a cross-sectional study in patients hospitalized with acute heart failure*. *J Cardiovasc Magn Reson*, 2016. **18**: p. 9.
494. Hammer, S., et al., *Prolonged caloric restriction in obese patients with type 2 diabetes mellitus decreases myocardial triglyceride content and improves myocardial function*. *J Am Coll Cardiol*, 2008. **52**(12): p. 1006-12.
495. Viljanen, A.P., et al., *Effect of caloric restriction on myocardial fatty acid uptake, left ventricular mass, and cardiac work in obese adults*. *Am J Cardiol*, 2009. **103**(12): p. 1721-6.
496. van der Meer, R.W., et al., *Pioglitazone improves cardiac function and alters myocardial substrate metabolism without affecting cardiac triglyceride accumulation and high-energy phosphate metabolism in patients with well-controlled type 2 diabetes mellitus*. *Circulation*, 2009. **119**(15): p. 2069-77.
497. Torella, D., et al., *Cardiac stem cell and myocyte aging, heart failure, and insulin-like growth factor-1 overexpression*. *Circ Res*, 2004. **94**(4): p. 514-24.
498. Baker, D.J., et al., *Naturally occurring p16(Ink4a)-positive cells shorten healthy lifespan*. *Nature*, 2016. **530**(7589): p. 184-9.
499. Zhu, Y., et al., *The Achilles' heel of senescent cells: from transcriptome to senolytic drugs*. *Aging Cell*, 2015. **14**(4): p. 644-58.
500. Lewis-McDougall, F.C., et al., *Aged-senescent cells contribute to impaired heart regeneration*. *Aging Cell*, 2019. **18**(3): p. e12931.
501. Chinta, S.J., et al., *Cellular Senescence Is Induced by the Environmental Neurotoxin Paraquat and Contributes to Neuropathology Linked to Parkinson's Disease*. *Cell Rep*, 2018. **22**(4): p. 930-940.
502. Salam, R., et al., *Cellular senescence in malignant cells promotes tumor progression in mouse and patient Glioblastoma*. *Nat Commun*, 2023. **14**(1): p. 441.
503. Paramos-de-Carvalho, D., et al., *Targeting senescent cells improves functional recovery after spinal cord injury*. *Cell Rep*, 2021. **36**(1): p. 109334.
504. Krings, A., et al., *Bone marrow fat has brown adipose tissue characteristics, which are attenuated with aging and diabetes*. *Bone*, 2012. **50**(2): p. 546-52.
505. Nicholls, H.T., et al., *Hematopoietic cell-restricted deletion of CD36 reduces high-fat diet-induced macrophage infiltration and improves insulin signaling in adipose tissue*. *Diabetes*, 2011. **60**(4): p. 1100-10.
506. Christiaens, V., et al., *CD36 promotes adipocyte differentiation and adipogenesis*. *Biochim Biophys Acta*, 2012. **1820**(7): p. 949-56.
507. Capuano, A., et al., *Dipeptidyl peptidase-4 inhibitors in type 2 diabetes therapy--focus on alogliptin*. *Drug Des Devel Ther*, 2013. **7**: p. 989-1001.
508. Gitelman, S.E., et al., *Imatinib therapy for patients with recent-onset type 1 diabetes: a multicentre, randomised, double-blind, placebo-controlled, phase 2 trial*. *Lancet Diabetes Endocrinol*, 2021. **9**(8): p. 502-514.
509. Ogrodnik, M., et al., *Cellular senescence drives age-dependent hepatic steatosis*. *Nature Communications*, 2017. **8**(1): p. 15691.

510. Correia-Melo, C., et al., *Mitochondria are required for pro-ageing features of the senescent phenotype*. The EMBO Journal, 2016. **35**(7): p. 724-742.
511. Faulkner, A., et al., *Multi-Omics Analysis of Diabetic Heart Disease in the db/db Model Reveals Potential Targets for Treatment by a Longevity-Associated Gene*. Cells, 2020. **9**(5).
512. Kirkland, J.L. and T. Tchkonina, *Cellular Senescence: A Translational Perspective*. EBioMedicine, 2017. **21**: p. 21-28.
513. Sylow, L., et al., *The Cancer Drug Dasatinib Increases PGC-1alpha in Adipose Tissue but Has Adverse Effects on Glucose Tolerance in Obese Mice*. Endocrinology, 2016. **157**(11): p. 4184-4191.
514. Ihm, S.H., et al., *Peroxisome proliferator-activated receptor-gamma activation attenuates cardiac fibrosis in type 2 diabetic rats: the effect of rosiglitazone on myocardial expression of receptor for advanced glycation end products and of connective tissue growth factor*. Basic Res Cardiol, 2010. **105**(3): p. 399-407.
515. La Rosee, P., et al., *Improved tolerability by a modified intermittent treatment schedule of dasatinib for patients with chronic myeloid leukemia resistant or intolerant to imatinib*. Ann Hematol, 2013. **92**(10): p. 1345-50.
516. Furuhashi, M., et al., *Fatty Acid-Binding Protein 4 (FABP4): Pathophysiological Insights and Potent Clinical Biomarker of Metabolic and Cardiovascular Diseases*. Clin Med Insights Cardiol, 2014. **8**(Suppl 3): p. 23-33.
517. Das Pradhan, A., et al., *Triglyceride Lowering with Pemafibrate to Reduce Cardiovascular Risk*. N Engl J Med, 2022. **387**(21): p. 1923-1934.
518. Shao, J., et al., *Decreased Akt kinase activity and insulin resistance in C57BL/KsJ-Leprdb/db mice*. J Endocrinol, 2000. **167**(1): p. 107-15.
519. Jia, Y., et al., *SIRT1 is a regulator in high glucose-induced inflammatory response in RAW264.7 cells*. PLoS One, 2015. **10**(3): p. e0120849.
520. Laboratory, T.J. *PHENOTYPE INFORMATION FOR BKS-DB (000642)*. Available from: <https://www.jax.org/jax-mice-and-services/solutions-by-therapeutic-area/metabolic-diseases/featured-mice-for-type-2-and-obesity/phenotype-information-for-000642>.
521. Lin, H., et al., *Non/mini-invasive monitoring of diabetes-induced myocardial damage by Fourier transform infrared spectroscopy: Evidence from biofluids*. Biochim Biophys Acta Mol Basis Dis, 2022. **1868**(9): p. 166445.